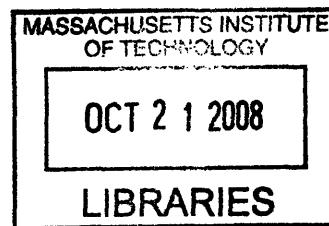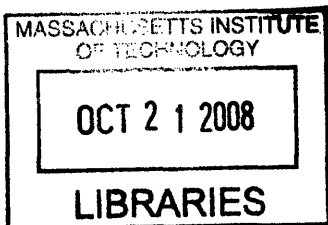# Reservoir Monitoring Using Induced Seismicity at a Petroleum Field

in Oman

by

Sudipta Sarkar

Submitted to the Department of Earth, Atmospheric, and Planetary Sciences
in partial fulfillment of the requirements for the degree of

DOCTOR OF PHILOSOPHY

at the

MASSACHUSETTS INSTITUTE OF TECHNOLOGY

September 2008

© 2008 Massachusetts Institute of Technology. All Rights Reserved.

Signature of Author: _____

Department of Earth, Atmospheric and Planetary Sciences

August 26, 2008

Certified by: _____

M. Nafi Toksöz

Robert R. Shrock Professor of Geophysics

Thesis Supervisor

Accepted by: _____

Maria Zuber

E.A. Griswold Professor of Geophysics

Department Head

ARCHIVES

Reservoir Monitoring using Induced Seismicity at a Petroleum Field in Oman

by

Sudipta Sarkar

Abstract

This thesis presents methods of analysis and results from a petroleum reservoir monitoring application using induced seismicity data. The dissertation work is comprised of four major studies, each focusing on a different aspect of induced seismicity. First, methods and issues in location of induced seismicity are discussed, and strategies are proposed for determining accurate hypocenters of induced events. The importance of velocity model and how it impacts the depth determination of reservoir-induced events are demonstrated with real field data. A location method that is better-suited than other existing methods for this application is proposed. The accuracy and efficiency of this proposed location method is demonstrated with field data application.

Secondly, event locations and interpretations are presented for about 1300 induced events recorded by a near-surface network over a seven year period at a petroleum field in Oman. The event hypocenters delineate two major northeast-southwest striking faults in the field, which are consistent with fault maps derived from reflection seismic interpretations. Spatiotemporal analysis of induced event locations reveals ongoing large scale fault reactivation in the field, and also suggests compaction of the gas reservoir as the major cause and water injection in the oil reservoir as the secondary cause for inducing seismicity in the field.

Thirdly, event locations and interpretations are presented for a different set of induced seismicity data recorded by a deep-borehole network over an 11-month period at the same field. About 5400 events are located and analyzed, and detailed mapping of faults and fractures using the event hypocenters are presented. Patterns of seismicity also reveal faults and fracture systems previously unmapped by reflection seismic. While this dataset allows for much finer

interpretation, the results between the two network data are found to be consistent and comparable.

Finally, the double-difference relocation and tomography method is applied for event relocation and imaging of the reservoir. Better correlation of relocated events with faults is observed from application of this method to the surface-network events, and detailed velocity and structure images for the reservoir are obtained from application of tomography with the deep-network events.

Thesis Advisor: **M. Nafi Toksöz**

Title: Robert R. Shrock Professor of Geophysics, MIT.

Contents

3.   Passive Seismic Monitoring using data from Near-Surface Network

4

Chapter 1

Introduction

1.1 Objective

The main purpose of this dissertation work is to make scientific contributions and technological advancements in the application of induced seismicity for reservoir monitoring and characterization. Induced seismicity[1] refers to *typically* minor earthquakes and tremors that are caused by human activities that alter the stresses and strains on the Earth's crust. In petroleum reservoirs, seismicity is generally induced due to production and/or injection operations. Depending on the causes of seismicity in the field, this data can be used for various purposes, such as: identification of faults and fractures and detection of changes over time, monitoring of flow, identification of zones of threats to wellbore stability and potential drilling hazard. Since this seismicity data is of *passive* type, the first and foremost important task in any application that uses induced seismicity data is to locate these events with high accuracy. One of the main objectives of this thesis is to study the location issues of induced seismicity in detail and develop efficient methods for improving the location accuracy. The methods and strategies are then applied on two extensive induced seismicity datasets acquired through passive seismic monitoring of a petroleum field. Locations of these induced events are used to identify faults and

---

[1] Two other terms that are often used interchangeably (in the literature and in this thesis) and essentially carry the same meaning as induced seismicity are "passive seismic", and "microseismic".

fractures, and monitored over time to detect structural changes in the reservoir. And the last but not the least objective of this thesis is to explore reservoir imaging from induced seismicity, using the field data available for this study.

1.2 Background

Over the last several decades, induced seismicity has been observed in connection with numerous human activities and at various geologic settings. Examples include oil and gas extraction (Grasso, 1992), well stimulation (Phillips *et al.*, 2002), enhanced oil recovery (Maxwell *et al.*, 1998), impoundment of water reservoirs in the vicinity of dams (Gupta, 1992), mining activity (Gibowicz and Lasocki, 2001), fluid injection and disposal (Tabeli and Cornet, 1987), geothermal operations (Baria *et al.*, 1999), underground nuclear explosions (Boucher et al., 1969), and CO_2 sequestration (Maxwell *et al.*, 2004). In the petroleum industry, some of the major application areas in which induced seismicity has been used as a monitoring tool are – hydraulic fracturing (e.g. Rutledge and Phillips, 2003), well/casing failure (e.g. Kristansen *et al.*, 2000), fault mapping (e.g. Maxwell *et al.*, 1998), mapping fluid movements (e.g. Rutledge et al., 1998), mapping compaction strains (e.g. Grasso, 1992), mapping thermal fronts (e.g. McGillivray, 2004), tracking fluid injection (e.g. Deflandre *et al.*, 1995), and mapping waste disposals (e.g. Keck and Withers, 1994). At present, the majority of induced seismicity applications in the petroleum industry are concerned with monitoring hydraulic fracturing or

stimulation of wells, and the number is rapidly growing. Hydraulic fracturing is commonly used to increase the permeability near the borehole through intentional creation of new fractures that extend from the borehole into rock formations. Monitoring of the associated microseismicity during a fracturing operation can give important insight into the fracture pattern and fluid migration. Similarly, monitoring of the seismic events that may be "unintentionally" triggered or induced during the production-cycle of the field can be used to obtain valuable information about various hydrodynamic processes and reservoir property changes that occur at some distance from the boreholes, in the reservoir. Although the number of such applications is very limited at the moment, with improvements in data acquisition and processing technology and better understanding of reservoir physics, usage of induced seismicity as a tool for reservoir monitoring and characterization is likely to flourish. A summary of some of the important case studies that demonstrate the value of field-scale reservoir monitoring using induced seismicity (Wilson *et al.*, 2004) is given by the following paragraph.

In 1993 a production monitoring study was carried out in Clinton County, Kentucky, where over 3000 induced events were detected. Locations from that dataset defined a shallow dipping structure interpreted as a reverse-slip fracture zone, previously undetected from seismic reflection data (Rutledge and Phillips, 1994). In 1997, a passive seismic monitoring study of the Ekofisk reservoir in the North Sea was carried out, where 3000 microseismic events were recorded during only 19 days of monitoring. After further processing using a collapsing algorithm (Jones and Stewart, 1997), those location data were shown to map out a series of structures that parallel known fault trends within the reservoir (Maxwell *et al.*, 1998). These structures had never previously been imaged because of an overlying gas cap. Another

9

monitoring project was carried out in the North Sea during 1998 in the Valhall field (Dyer et al., 1999), in which over 500 microseismic events were detected and 324 located. Subsequent shear wave analysis of these data demonstrated a temporal change in the shear wave anisotropy believed to be associated with reservoir drawdown (Teanby *et al.*, 2004). By combining the microseismic data from Valhall and Ekofisk with in situ stress and pore pressure data, (Zoback and Zinke, 2002), it was shown how production induced normal faulting is believed to have spread out from the crest of the structures onto the flanks. In recent years, a number of major national and international oil companies have started passive seismic monitoring studies in some of their producing fields. Examples of these fields include Ghawar (Dasgupta, 2005), Valhall (Barkved, 2002), Tengiz (Raymer et al., 2004), Peace River (McGillivray, 2004), and Cold Lake (Talebi *et al.*, 1998).

1.3 The Field of Study

The induced seismicity data that are used for this dissertation work come from a producing petroleum field that has undergone passive seismic monitoring for a long period of time. The field is located in the Sultanate of Oman and operated by Petroleum Development Oman (PDO). Figure 1.1 shows the location of the field (white box) in Oman along with the distribution of local and regional *natural* earthquakes around the Arabian Peninsula.
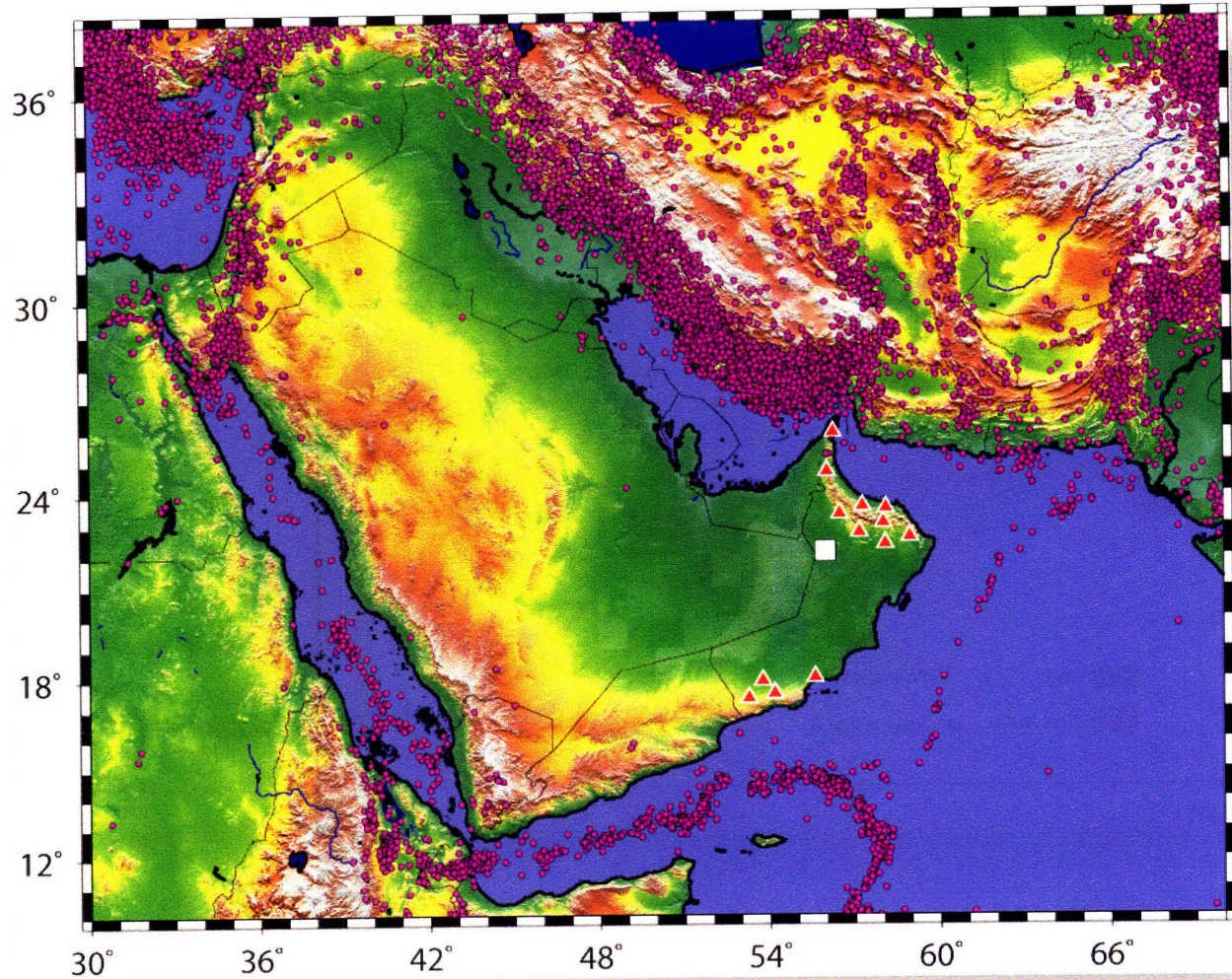
Figure 1.1: Geologic map of the Middle East and its surrounding region, showing country borders and regional seismicity around the Arabian Peninsula reported by the USGS PDE catalog. Locations of earthquakes having magnitudes >= 3 from the period 1973 – 2007 are plotted in purple filled dots. Red triangles show seismic stations from Oman national network. The white box indicates the location of the petroleum field discussed in this study, which lies in a relatively *aseismic* zone.
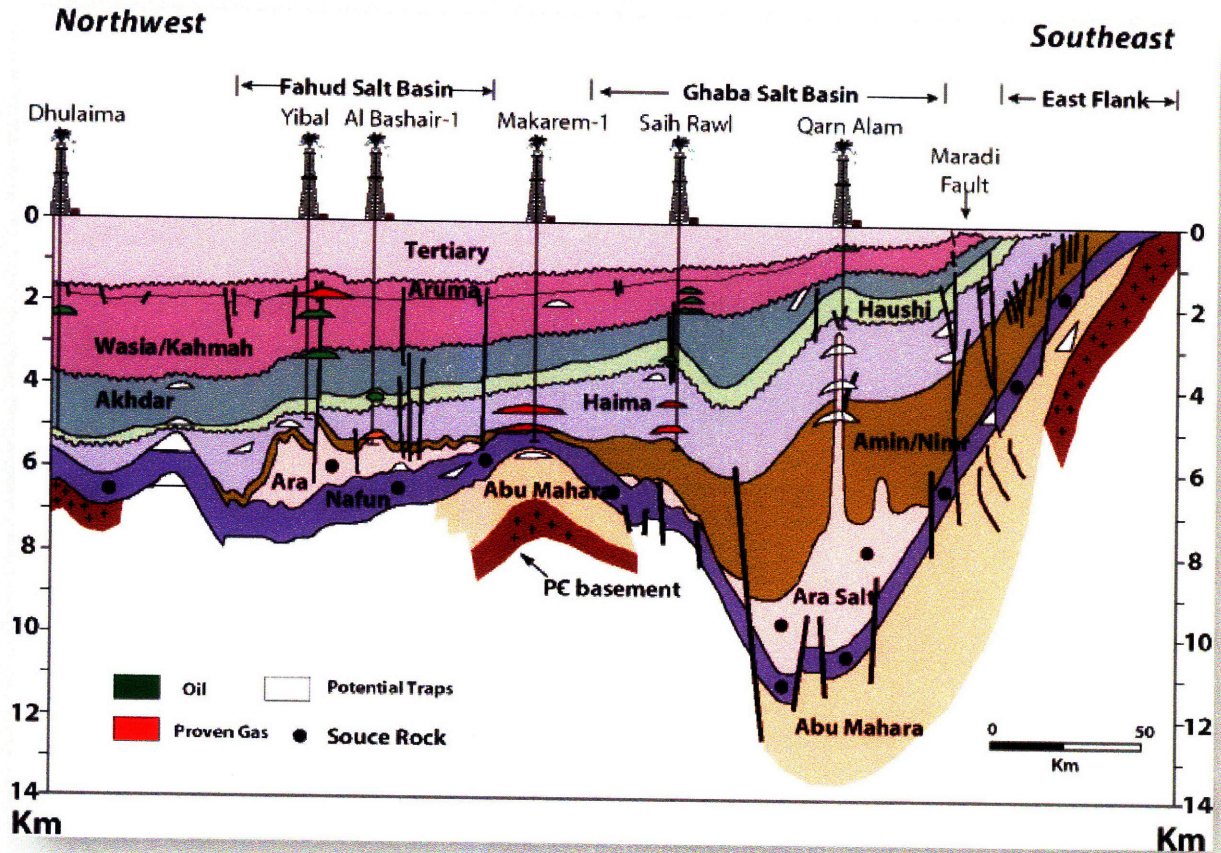
Figure 1.2: Generalized northwest-southeast cross-section across northern Oman and the Ghaba Salt Basin, Central Oman Platform, and Fahud Salt Basin showing major oil and gas fields, proven occurrences, and potential traps (adopted from Pollastro, 1999)

Figure 1.2 summarizes the geologic structure, major oil and gas fields and salt basins of Oman. The following is a summary of the oil and gas field studied for this dissertation work from Sze (2005); a more detailed description of the geology of the region and of the field can be found in the Appendices of Sze (2005).

The petroleum field used to study induced seismicity for this thesis is located in the north-central group of fields in the Fahud salt basin. It was discovered in 1962 and put into production in 1969. Structurally the field is a large anticline created by deep-seated salt movement (Blaskovich *et al.*, 1985). The dome is about 15 × 20 km in size with a northeast-southwest axial elongation that is probably a result of regional deformation. A seismic section of a broader region that also covers our field is given by Figure 1.3. Dips along the flanks are 4 to 5 degrees. The structure is dominated by a major central graben and two major systems of extensive tensional faulting with two preferred directions (southeast-northwest and northeast-southwest) that affect the trapping mechanism in the oil reservoir. All faults are high-angle normal faults. The northeast-southwest major network of faults and fractures partially connects all parts of the fields together. Porosities range from 30 to 35 percent. The matrix permeability is low (1 – 100 mD). Permeabilities in fault and fracture zones are believed to be orders of magnitude higher than the average matrix permeability. The main oil production is from the Lower Cretaceous Shuaiba chalk overlain disconformably by Nahr Umr shale, while gas is produced from the shallower Natih Formation overlain by the Fiqa shale Formation. A structural cross-section of the field showing the major producing units is given by Figure 1.4. Structural faults in the Shuaiba reservoir are known to be very permeable and water conductive. The Shuaiba reservoir, which is located at a depth of ~ 1420 m (relative to the surface; surface is ~110 m above the Mean Sea Level used in this study), is in pressure communication with the underlying Khuff formation. The oil column has a maximum thickness of 100 m with no primary gascap present. The Shuaiba chalk is a soft, fine-textured limestone of marine origin, consisting almost wholly of calcite formed by the moderately shallow-water accumulation of skeletal debris. The Natih Formation is part of the Mesozoic platform carbonate succession deposited on

the southeastern Arabian Peninsula. The age of Natih is middle Cretaceous (late Albian to Cenomanian/early Turonian), and its deposition was terminated by early Turonian uplift (Hitchings and Potters, 2000). As a result of eustatic sea level changes, the Natih Formation is cyclic with a succession of coarsening-upward cycles of deeper marine shales and mudstones grading to shallow marine rudistid packstones and grainstones, each terminated by an emergence surface. A stratigraphic column chart of the field is given by Figure 1.5. Gas from Natih has been extracted by depletion drive; as reported in 2000, pressure had dropped from 10,120 KPa to 7,920 KPa since 1973 (van Driel *et al.*, 2000). The Shuaiba oil reservoir was initially produced by natural depletion, and thus the field had suffered from rapid reservoir pressure depletion. Water injection based on a five-spot water flooding pattern was introduced in 1972 to maintain reservoir pressure, which was subsequently expanded to an inverted nine spot pattern (500 m well spacing) infilling. Water injection serves the dual purpose of pressure management and disposal of water produced. Water was initially injected into the oil column but was converted to deep injectors, injecting water into the aquifer below the 50% water saturation level in Shuaiba (Litsey *et al.*, 1986). Past studies had identified uneven vertical and lateral sweep due to uneven subsurface water distribution as a result of the complicated fracture and fault patterns as well as the subsurface hydrodynamics and flow mechanisms. As the field matured, production wells started experiencing co-production of oil and water. This rise in oil-water contact and process of water injection contributed to further increase of water-cut in producers. For example, in May 2000, monthly total oil production was about 20% of the total amount of liquid (water + oil) produced, whereas the rate dropped to about 5% in May 2006.
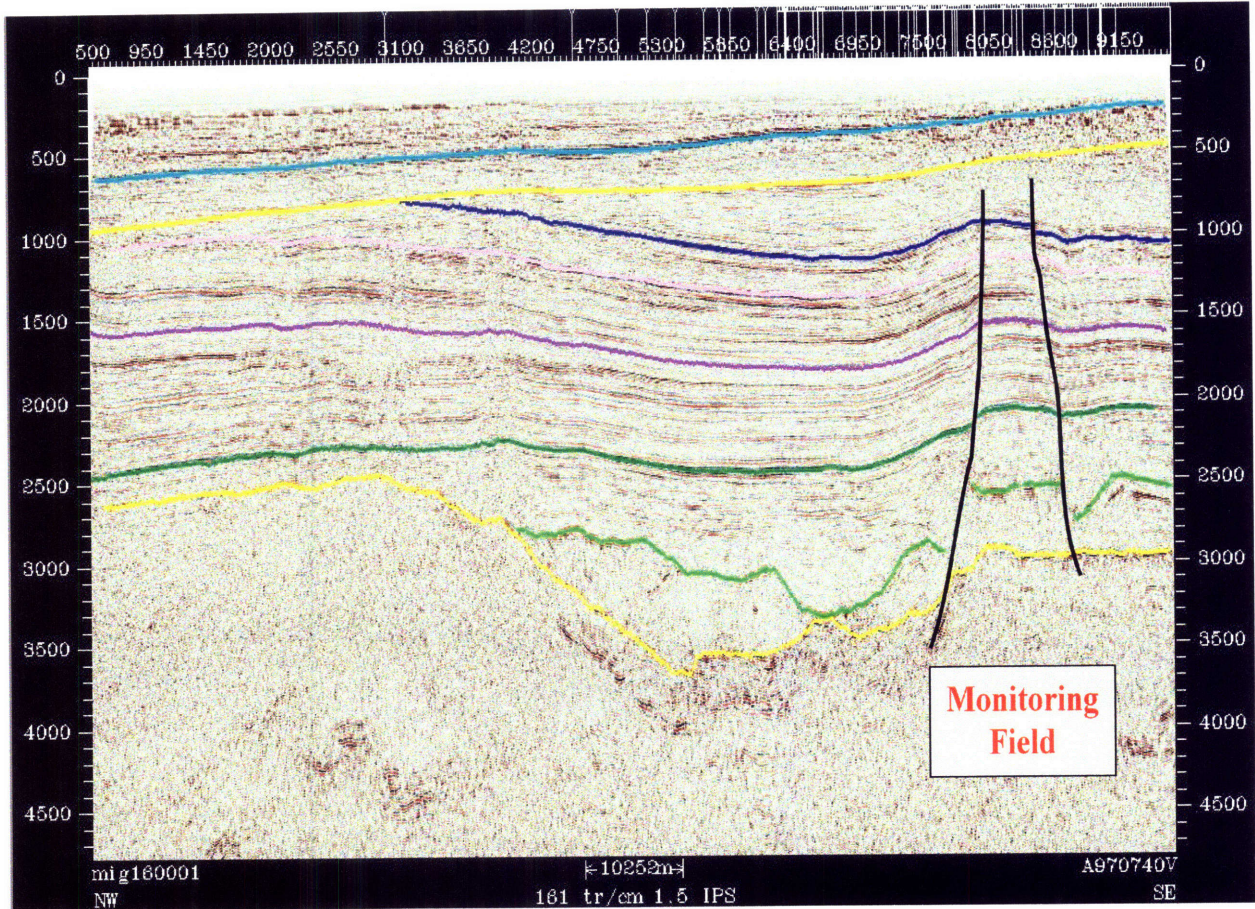
Figure 1.3: A regional NW-SE seismic line, showing the location and anticline structure of the field (bounded by two black lines) described in this study. The vertical axis of the plot is two-way travel times. (Figure source: PDO).
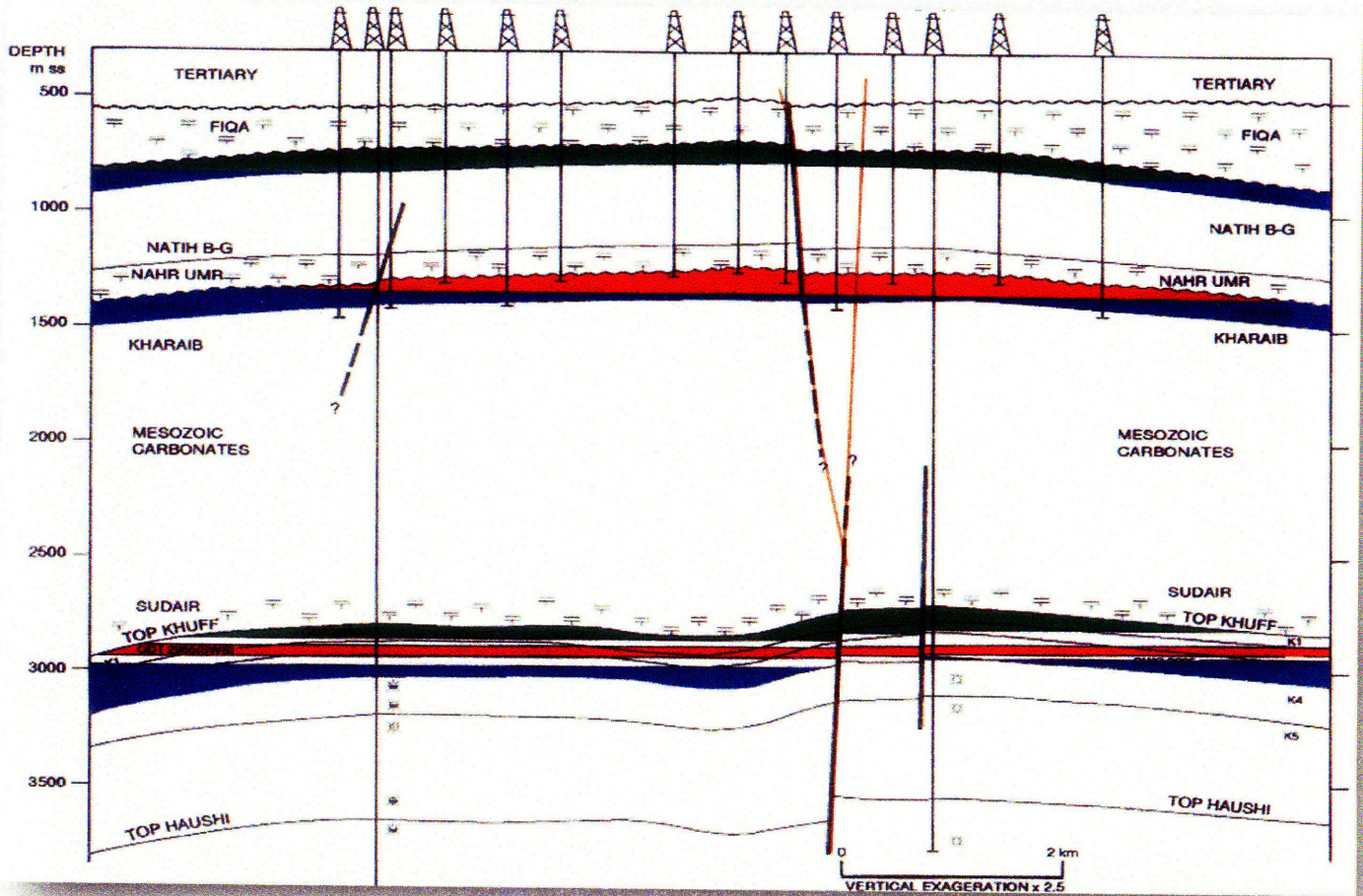
Figure 1.4: Structural cross-section of the field, with labels of various geologic units. Gas is produced from the uppermost green layer (Natih A) and underneath that is the oil producing layer Shuaiba shown in red. The fault lines in brown are suggested extension of the two major faults. Also shown on top with symbols are locations of some of the oil production and water injection wells that have completion depths into and below Shuaiba. The vertical axis shows depths in meters relative to the Mean Sea Level. (Figure courtesy: PDO)

AGE IN MA	CHRONO-START	GROUP	FORMATION	LITHOLOGY	REMARKS
	CENOZOIC / TERTIARY	FARS			MAIN UPLIFT OMAN MOUNTAINS
50			HADHRAMAUT		MARMUL
					OMAN MOUNTAINS EMPLACEMENT OF NAPPES (Tethyan obduction)
	MESOZOIC / CRETACEOUS	ARUMA	FIQA		
100		WASIA	NATIH		FAHUD SALT BASIN
		KAHMAH	SHUAIBA		GHABA/FAHUD SALT BASIN
			RAYDA		
150			TUWAIQ		LEKHWAIR HIGH
	MESOZOIC / JURASSIC	SAHTAN	DHRUMA		'TETHYS PLATFORM'
					GHABA SALT BASIN LEKHWAIR HIGH
200			MAFRAQ		
	TRIAS.		JILH		
250	PERMIAN	AKHDAR	KHUFF		FAHUD SALT BASIN 'NEOTETHYS OPENING'
			GHARIF		GHABA SALT BASIN EASTERN FLANK
		HAUSHI	AL KHLATA		GHABA SALT BASIN EASTERN FLANK
300					GONDWANA GLACIATION

Figure 1.5: Stratigraphic column of the field. (Figure source: PDO).

Natural seismicity in Oman has been historically low, and the region where the petroleum field is located is considered to be a *seismically quiet* area (Figure 1.1). However, starting in 1996, the staff working in the petroleum field reported seismic events. Those were essentially very small magnitude earthquakes that were felt, but not reported by any other local or regional network. It was therefore thought that the source of those events lay within the field itself. Figure 1.1 shows the distribution of naturally occurring earthquakes in the vicinity of Oman. Since the petroleum field (identified by white box on Figure 1.1) is located in an *aseismic*

area, it is quite likely that seismic events generated within the field are not of tectonic origin but are triggered by stress perturbations caused by various hydrodynamic processes and geomechanical changes within the reservoir.

To monitor the induced seismicity in the field and to assess its potential threat to existing wells and surface facilities, PDO deployed a monitoring network in 1999[2]. Initially the network consisted of 5 monitoring wells (VA1, VA2, VA3, VA4, and VA5) with borehole sensors buried at depths of about 150 m below the surface. Sometime in 2002, one of the stations (VA5) was removed and subsequently two new stations (VA6 and VA7) were installed. The locations of these stations are shown on a map by Figure 1.6. The data acquired by the network have been sent to MIT at regular intervals for processing and analysis. The data from the period November 1999 – June 2001 were preprocessed in Oman and only the selected event waveforms were sent to MIT, which were first located and published by Sze, 2005, and subsequently reanalyzed and published with modified results by Sarkar *et al.*, 2006. The next period of data coverage began in December 2002 and continues through 2008. The data from this period has been transferred to MIT as unprocessed, continuous recording of field data. Over the past two years, various tools were developed in-house in order to: i) preprocess the raw data, ii) identify events from the raw data, and iii) locate these events and carry out further analysis. For this thesis, about 1500 induced events were analyzed covering the period from November 1999 – February 2007.

---

[2] This network will be referred to as shallow/near-surface network throughout the thesis.

We had also received another set of microseismic data that was acquired by another independent network in the field for a Shell/PDO collaborative study (Jones *et al.*, 2004). Unlike the near-surface network, this network had deep-borehole installations of seismic sensors at multiple levels, roughly ranging from depths 750 m – 1250 m (below the surface). A schematic diagram of the wells and sensor positions is shown by Figure 1.7. The network consisted of 5 monitoring wells, spaced closely in the most seismically active part of the reservoir, and covered a much smaller area than the surface network. However, due to sensor positions at depths, their ability to acquire data at much higher frequencies, and their proximity to the two producing units (Natih gas and Shuaiba oil), the deep network recorded much smaller magnitude events than the shallow network, resulting in a greatly increased detectability of induced seismicity (roughly about 25 times more induced events per day) compared to the shallow network. The network was operational during February 2002 – August 2003, providing about 18 months of microseismic monitoring data from the field. From this project, we had received field data from October 2002 – August 2003. During this period, about 15,800 events had been identified with an average rate of ~ 47/day, out of which we analyzed and located about 5,400 events with our own tools and methods and present the results in this thesis. Attempts were made to select common events detected during this period by both (deep and shallow) networks for a joint location analysis, however due to clock synchronization problems and difference in sensor frequency bands between the two networks the common events could not be identified, and hence the task could not be accomplished.

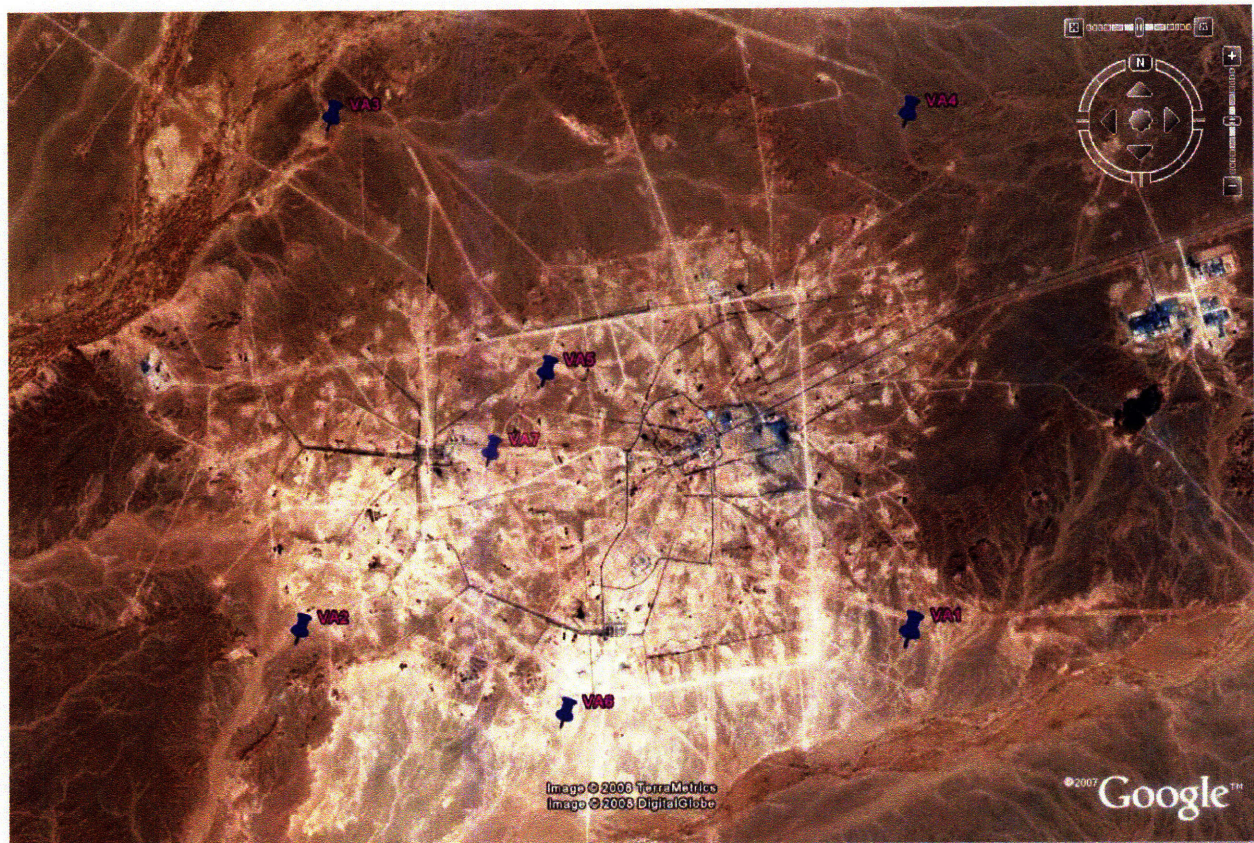Figure 1.6: Locations of PDO microseismic monitoring stations in the field, shown by blue pins (next to them are the station names in magenta). Station VA5 was only operational during 1999-2001. Stations VA7 was known to be installed, but no seismic data was received / processed from that station to date. In 2008, stations VA1, VA2, VA3, VA4, and VA6 are known to be active. (Figure courtesy: Google Earth).
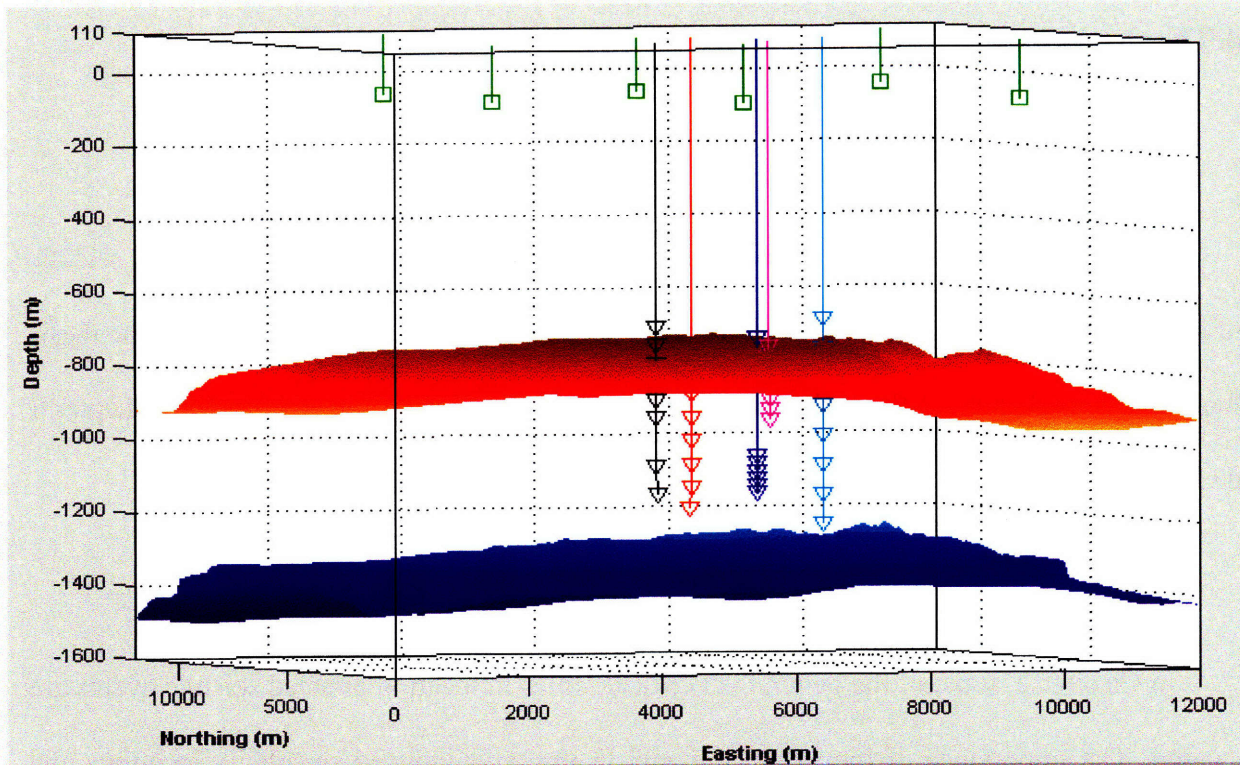
Figure 1.7: Combined plot of both deep and shallow networks used for passive seismic monitoring at the field. Well positions of the shallow network are shown in green (sensor positions are indicated by squares). Well positions and sensor orientation for the 5 monitoring wells of the deep network are shown by 5 different colors, with triangles denoting sensor positions in each well at different depth levels. Also plotted are two major horizons – Natih A in red, and Shuaiba in blue. Zero of the depth axis indicate mean sea level (MSL), which is roughly 110 m below the surface. Northing and Easting values correspond to a relative Cartesian coordinate system derived specifically for this study.

1.4 Thesis Outline

The thesis is organized to develop and apply the technology of using induced seismic data for reservoir monitoring and characterization purposes. The main four chapters of the thesis (Chapters 2 – 5) document the technical contribution of the dissertation work, while Chapter 1 and Chapter 6 provide introduction and conclusion to the work, respectively.

In Chapter 2, some of the general yet critical issues in locating induced seismic events are discussed. The importance of the velocity model in reservoir-induced seismicity locations and how it impacts the depth locations of the events are shown with an application on the 1999 – 2001 field data. During our research, it was found that most of the conventional earthquake location codes are not suitable for locating reservoir-induced seismic events, mainly because of the travel-time calculation methods that these codes normally use. We present an overview of the some of the conventional and more advanced location algorithms in this chapter. To address some of the challenges posed by the data used for this study, we developed a station-pair-differencing location algorithm, which we also present in this chapter – with theory and application. We show comparisons of location results between our method and another established method. Our method is simple, computationally efficient, and robust, and it can locate hypocenters of reservoir-induced seismic events with reasonable accuracy – at least for the field data concerned in this thesis.

In Chapter 3, we present analysis of induced seismic events, detected by the PDO shallow network for passive seismic monitoring of the petroleum field, covering the period from November 1999 – February 2007. We show spatial and temporal analyses of the seismicity based on the event locations. While spatial analysis of the seismicity reveals good correlation with preexisting fault maps in the reservoir and identification of possible new features, with the temporal analysis we interpret some of the structural changes that take place over time. Event locations also aide us in interpreting the likely cause of seismicity in the field, and their correlations with reservoir hydraulic data further strengthen our analysis and interpretation of seismicity.

In Chapter 4, we show locations of events detected by the deep network. Similar to the analysis with shallow network data in Chapter 3, we also show seismicity-fault correlations and spatial and temporal variations of seismicity during the 11-month period from October 2002 – August 2003. While the event locations from two independent datasets show much similarity in broader terms, in this chapter we show much finer scale analysis of fault correlation and new fault/fracture identification with this extensive event dataset.

In Chapter 5, we take advantage of repeating events occurring during the monitoring period and use the similarity of their waveforms to perform relative event location. We apply double-difference relocation to shallow-network events, and use double-difference tomography to image a certain part of the reservoir using the deep-network events. The results presented in

this chapter show promise in terms of using induced seismicity as a tool for reservoir imaging

and property estimation – both in three-dimensional and in a time-lapse sense.

1.5 References

Barkved, O., E. Gaucher, B. Hornby, T. Kristiansen, and C. Maison (2002), Analysis of seismic recordings during injection using in-well permanent sensors, *Expanded Abstracts*, 64th EAGE Annual Conference, Florence, Italy.

Baria, R., J. Baumgartner, A. Gerard, R. Jung, and J. Garnish (1999), European HDR research progamme at Soultz-sous-Forets (France) 1987-1996, *Geothermics*, 28, 655-669.

Blaskovich, F.T., S.S. Thurber, D.P. Echois, K.B.M. Al-Hinai (1985), Reservoir Management of the Yibal Field in North Oman: A Simulation Approach, Middle East Oil Technical Conference and Exhibition, Bahrain.

Boucher, G., A. Ryall, and A.E. Jones (1969), Earthquakes associated with underground nuclear explosion, *J. Geophys. Res.*, 74, 3808 – 3820.

Dasgupta, S.N., (2005), When 4D seismic is not applicable: Alternative monitoring scenarios for the Arab-D reservoir in the Ghawar Field, *Geophysical Prospecting*, Volume 53, Issue 2, pp. 215 – 227.

Deflandre, J.P., J. Laurent, D. Michon, and E. Blondin (1995), Microseismic surveying and repeated VSPs for monitoring an underground gas storage reservoir using permanent geophones. *First Break*, 13, pp. 129–138.

Dyer, B.C., R.H. Jones, J.F. Cowles, O. Barkved, and P.G. Folstad (1999), Microseismic survey of a North Sea Reservoir, *World Oil*, 220, 3.

Gibowicz, S. and S. Lasocki (2001), Seismicity induced by mining: Ten years later, *Adv. Geophys*, 44, 39–180.

Grasso, J., (1992), Mechanics of seismic instabilities induced by the recovery of hydrocarbons, *Pure and Appl. Geophys.*, 139(3/4), 507–534.

Gupta, H.K., (1992), Reservoir-Induced Earthquakes, Elsevier Science Publishers B.V., New York, NY.

Hitchings, V.H., and H. Potters (2000), Production and geologic implications of the Natih 9-C 3-D seismic survey, *The Leading Edge*, 19, 1117 – 1122.

Jones, R.H., D.G. Raymer, G. Mueller, G. Rynja, and K. Maron (2004), Microseismic Monitoring of the Yibal Oilfield, *Expanded Abstracts - 66th EAGE Annual Conference*, Paris, France.

Jones, R.H., and R. Stewart (1997), A method for determining significant structures in a cloud of earthquakes, *J. Geophys. Res.*, 102, 8245-8254.

Keck, R. G., and R. J. Withers (1994), A field demonstration of hydraulic fracturing for solids waste injection with real-time passive seismic monitoring, *Proceedings of the SPE 69th Annual Technical Conference and Exhibition*, SPE 28495, New Orleans, LA.

Kristansen, T.G., O. Barkved, and P.D. Pattilo (2000), The use of passive seismic monitoring in well and casing design in the compacting and subsiding Valhall Field, North. SPE Paper 65134.

Litsey, L.R., W.L. MacBride Jr., K.M. Al-Hinai, and N.B. Dismukes (1986), Shuaiba reservoir geological study, Yibal field, Oman, *J. Petroleum Geology*, 38, 651-661.

Maxwell, S.C., D.J. White, and H. Fabriol (2004), Passive Seismic Imaging of CO2 Sequestration at Weyburn, *Technical Abstracts*, 74th Annual International Mtg.: Soc. of Expl. Geophys.

Maxwell, S.C., Young, R.P., Bossu, R., Jupe, A. and J. Dangerfield, J. (1998), Microseismic logging of the Ekofisk reservoir, paper SPE 47276, *Proceedings of the 1998 SPE/ISRM Eurock '98*, Trondhiem, Norway.

McGillivray, P.R., (2004), Microseismic and Time-lapse Monitoring of a Heavy Oil Extraction Process at Peace River. Presented at 73rd SEG Annual Conference, Denver, CO.

Pollastro, R.M., (1999), Ghaba salt basin province and Fahud salt basin province, Oman – geological overview and total petroleum systems, *U.S.G.S. Open-File Report*, 99-50D.

Phillips, W.S., T.J. Rutledge, L.S. House, and M.C. Fehler (2002), Induced microearthquake patterns in hydrocarbon and geothermal reservoirs, six case studies, *Pure Appl. Geophys.*, 159, 345 – 369.

Raymer, D.G., J.Y. Behrens, and J. Rickett (2004), Genetic algorithm design of microseismic injection-monitoring networks in the Tengiz field. Presented at the 73rd SEG Annual Conference, Denver, CO.

Rutledge, J. T., and W.S. Phillips (2003), Hydraulic stimulation of natural fractures as revealed by induced microearthquakes, Carthage Cotton Valley gas field, East Texas, *Geophysics*, 68, no. 2, 441–452.

Rutledge, J.T., W.S. Phillips and B.K. Schuessler (1998), Reservoir characterization using oil-production-induced microseismicity, Clinton county, Kentucky. *Tectonophysics* 289, pp. 129–152.

Rutledge, J. T. and W. Phillips (1994), Subsurface fracture mapping using microearthquakes to detect during primary oil production, Clinton County, Kentucky, *Proceedings of 1994 SPE Annual Technical Conference and Exhibition*, SPE Paper 28384, New Orleans, LA.

Sarkar, S., E. Sze, and M.N. Toksoz (2006), Mircoseismic Monitoring of a Petroleum Field in Oman, presented during EAGE Workshop titled 'Passive Seismic: Exploration and Monitoring Applications', Dubai, U.A.E.

Sze, E. K-M., (2005), Induced seismicity analysis for reservoir characterization at a petroleum field in Oman, PhD Thesis, Massachusetts Institute of Technology, Cambridge, MA.

Tabeli, S., and F. Cornet, (1987). Analysis of Microseismicity Induced by a Fluid Injection in a Granitic Rock Mass, *Geophys. Res. Lett.*, 227.

Talebi, S., S. Nechtschein, and T.J. Boone (1998), Seismicity and Casing Failures Due to Steam Stimulation in Oil Sands, *Pure and Applied Geophysics.* 153 No.1, 219-233.

Teanby, N., J. M. Kendall, R.H. Jones, and O. Barkved (2004), Stress induced temporal variations in seismic anisotropy observed in microseismic data, *Geophys. J. Int.* 156, 3, 459-463.

van Driel, W.D., C. Hart, B. Lehr, and J. Coremans (2000), Reservoir compaction, surface subsidence and fault slip in the Yibal field, Oman, Netherlands Organisation for Applied Scientific Research.

Wilson, S., R. Jones, W. Wason, D. Raymer, and P. Jaques (2004), Passive seismic makes sense for 4D reservoir monitoring, *First Break*, 23, 59-65.

Zoback, M.D. and J.C. Zinke (2002), Production-induced Normal faulting in the Valhall and Ekofisk Oil fields. *Pure Applied Geophysics*, 159, 403-420.

Chapter 2

Induced Earthquake Location: Problems and Strategies

2.1 Introduction

The problem of locating earthquakes from arrival time data is one of the oldest challenges in seismology and continues to be an important topic of research. From the classical Geiger's method to the more advanced algorithms, we have seen a wide range of concepts and computational strategies implemented in order to solve the inherently non-linear problem of finding the hypocentral parameters and origin time of an earthquake from arrival time data. Accurate locations of earthquake epicenters require a good azimuthal coverage of stations. To find reliable hypocenter locations travel times must be calculated accurately. In this chapter we show how sensitive the location parameters, especially depths, can be to changes in the velocity model. For induced seismicity applications such as passive seismic monitoring of petroleum reservoirs, mislocation of depths could lead to misinterpretation of the cause of induced seismicity, thus bearing serious consequences in reservoir management decision making. Therefore, it is very important to use an accurate velocity model for locating earthquakes in reservoir-induced seismicity applications. In this paper we show locations of induced events from a reservoir monitoring application, where we use a 1-D layered velocity model derived from available Sonic logs to locate the events, and compare them with locations obtained using another 1-D layered model determined from a check-shot survey conducted in the field.

Although the physics of the location problem is essentially the same for both natural and induced earthquakes, yet most commonly used earthquake location algorithms do not work for induced earthquakes. Induced earthquakes in petroleum fields generally occur in sedimentary basins with alternating high and low velocity layers. Conventional earthquake location codes mostly use an average velocity model: they use either smooth velocity gradients or layers with increasing velocities, but cannot handle many thin layers with alternating high and low velocities as typically encountered in the sedimentary basins. Therefore, for a reservoir-induced seismicity application, it is very important to use a location code that can incorporate an accurate velocity model which consists of alternating high and low velocities. For accurate locations of induced earthquakes we propose a location algorithm that has three major components: i) Finite-Difference solver of the Eikonal equation (Vidale, 1988, 1990; Podvin and Lecomte, 1991) as the travel time calculator, ii) difference of arrival times at station pairs as the minimization function, and iii) a brute-force grid search as the search method – all of which play important roles in finding accurate hypocenter solutions for a reservoir-induced seismicity application as shown by this chapter. The finite difference scheme allows for accurate computation of first-arrivals of distinct phases in the presence of high-low alternating velocities, the station-differencing approach yields a simpler and more unique minimization function by eliminating the origin time, and finally the exhaustive grid search ensures that the global optimum hypocentral solutions be found. We show comparison of location results between our method and other existing methods.

2.2 Brief Overview of Earthquake Location Methods

2.2.1 Conventional methods

Among the travel-time based location methods, some of the most commonly used routines for locating earthquake hypocenters are HYPO71 (Lee and Lahr, 1975), HYPOLAYR (Eaton, 1969), HYPOELLIPSE (Lahr, 1980), BASIC-HYPO (Mendoza and Morgan, 1985), and HYPOINVERSE-2000 (Klein, 2000). These methods are based on Geiger's method (Geiger, 1912) or its variants, which essentially employ matrix inversion techniques to iteratively solve a set of linearized equations obtained from non-linear expressions of travel times to fulfill a certain minimization criterion. The basic methodology is essentially unchanged from the classic papers of Bolt (1960), Flinn (1965), and Engdahl and Gunst (1966). A general limitation of this class of methods is that depending on the initial guess the solutions may get "trapped" at local minima, thereby widening the uncertainty range of the solved parameters. While this is a significant cause of concern in using these methods to locate events in induced seismicity applications, the biggest hurdle in using these methods arises from the fact that most of them are not able to handle multiple alternations of high and low velocity layers in calculating the predicted travel times. Therefore, these routines or some of the commercial seismic analysis packages that use one of these routines in their back-end are not deemed suitable for the purpose of locating earthquakes in petroleum field-induced seismicity applications.

31

2.2.2 Advanced methods

Recent advances in computing power, developments in inversion and optimization techniques, and implementation of three-dimensional velocity models have pushed earthquake location beyond the traditional horizon. Today, earthquake location may involve cross-correlation time measurements, complex three-dimensional velocity models, determination of high-precision, relative earthquake locations, array processing and semblance techniques, and the definition of multi-dimensional uncertainty volumes using a variety of functional minimization approaches. Thurber and Rabinowitz (2000) provides a nice overview of the fundamental issues involved in seismic event location, and presents some of the more advanced location methods and their applications at a wide range of spatial scales (e.g. Sambridge and Kennett, 1986, 2001; Lomax *et al.*, 2000) After surveying the existing *advanced* methods, we found NonLinLoc (Lomax *et al.*, 2000) to be the most interesting and most suitable candidate for event location for our reservoir monitoring application. This is a probabilistic, non-linear, global search method that allows the use of 3D velocity models and produces comprehensive uncertainty and resolution information represented by a probability density function over the unknown hypocentral parameters. In absolute location studies, nonlinear global-search methods have several advantages over linearized approaches. Nonlinear global-search methods produce more stable solutions than linearized methods because they are not strongly dependent on starting locations and other inversion parameters.

NonLinLoc calculates the travel times between each station and all nodes of an x, y, z spatial grid, using a 3D version (Le Meur *et al.*, 1997) of the Eikonal finite-difference scheme of Podvin and Lecomte (1991), and then stores on disk as travel-time grids. This travel time calculation method relies on a systematic application of Huygen's principle in the finite difference approximation. Such an approximation explicitly takes into account the existence of different propagation modes such as transmitted and diffracted body waves, head waves. Local discontinuities of the time gradient in the first arrival time field are built as intersections of locally independent wavefronts. As a consequence, this method provides accurate first travel times in the presence of extremely severe, arbitrarily shaped velocity contrasts, which makes it quite suitable for our reservoir-induced seismic event location application. As for the inversion scheme, NonLinLoc follows the probabilistic formulation of inversion presented in Tarantola and Valette (1982) and Tarantola (1987). This formulation relies on the use of normalized and unnormalized probability density functions to express our knowledge about the values of parameters. If the probability density functions giving *a priori* information on the model parameters and on observations are independent, and the theoretical relationship relating a vector of observed data and unknown parameters can be expressed as a conditional density function, then a complete, probabilistic solution can be expressed as a posterior probability density function (PDF) (Tarantola and Valette, 1982). In an earthquake location problem, the unknown parameters are the hypocentral coordinates (x, y, and z) and the origin time t_o, the observed data are arrival times measured at seismic stations, and the theoretical relation gives predicted or theoretical travel times. In NonLinLoc, the posterior density function (PDF) can be determined in three different ways (Lomax *et al.*, 2000): (1) via a grid-search algorithm using successively finer, nested grids; (2) via a Metropolis-Gibbs sampling algorithm performing a directed random

walk within a spatial volume to obtain a set of samples that follow the posterior density function; and (3) via an Oct-Tree Importance sampling algorithm (Oct-Tree algorithm). The Oct-Tree algorithm gives accurate, efficient and complete mapping of the PDF of the earthquake location problem (Lomax and Curtis, 2001). It uses recursive subdivision and sampling of cells in three dimensions to generate a cascade of sampled cells, where the number of sampled cells follows the values of the PDF at the cell center, thus leading to higher density of cells in areas of higher PDF (lower misfit). Multiple minima in the PDF are reliably detected by the grid-search algorithm and the Oct-Tree algorithm but are missed by the Metropolis-Gibbs sampling algorithm. The NonLinLoc solution, in the form of a PDF, represents a complete, probabilistic solution to the location problem, including information on uncertainty and resolution (Lomax *et al.*, 2000). The solution is fully nonlinear, and, therefore, the resulting PDF may be irregular and multimodal. The solution includes estimation of location uncertainties due to the geometry of the network, measurement errors of the observed arrival times, and errors in the calculation of the theoretical travel times. The maximum likelihood (or minimum misfit) point of the complete, non-linear location PDF is selected as an "optimal" hypocenter. The significance and uncertainty of this maximum likelihood hypocenter cannot be assessed independently of the complete solution PDF.

2.3 Special Problems in Location of Induced Earthquakes

The problem of earthquake location is to find its hypocenter (x, y, z) and origin time (t_o). Assuming that the velocity model is known and fixed, these four parameters define the model vector, $\mathbf{m}$: $\mathbf{m} = (x, y, z, t_o)$. For a travel-time based earthquake location problem, the data are given by arrival times of distinct phases (usually first-arrivals) t_i picked from n observations/seismic stations $(i = 1, 2, 3, \ldots, n)$. In order to *invert* these times for the unknown parameters $\mathbf{m}$, one must first calculate the *forward model*, i.e. the predicted arrival times, t_i^p:

$t_i^p = F_i(\mathbf{m})$, where F is the operator that gives the predicted arrival time at each station for $\mathbf{m}$. F is a nonlinear function of the model parameters (with the exception of origin time, t_o). The difference between the observed and the predicted time is known as the travel time residual, r_i:

$r_i = t_i - t_i^p = t_i - F_i(\mathbf{m})$. The problem is to find the $\mathbf{m}$ that, in some sense, would give the *smallest residuals* between the observed and predicted travel times. Many different algorithms which solve the minimization of arrival time residuals can be found in the literature (e.g., Bolt, 1960; Flinn, 1960; Lee and Lahr, 1975; Sambridge and Kennett, 1986, 2001).

The nonlinear dependence of the travel times on the earthquake location parameters greatly complicates the task of inverting for the *best* earthquake model. While this is an inherent difficulty due to the physics of the problem itself, there are some extraneous factors that further complicate our goal of estimating the best location parameters. In induced earthquake applications such as passive monitoring of reservoirs, some of the major attributing factors to

earthquake location uncertainty are: a) sparse station distribution, b) lack of azimuthal and distance coverage by the receivers, c) an earth structure with alternating high and low velocities in sedimentary sections, and d) large uncertainty in S-picks due to near-simultaneous arrivals of converted and pure phases. These have been long-standing problems for locating earthquakes in general, and are widely discussed in the literature. In this paper, we discuss these issues in the context of reservoir-induced earthquake location problem, and try to find some practical solutions to these problems.

2.3.1 Velocity model

For an earthquake location scheme which uses a reference earth model to calculate the predicted travel times from assumed event locations to stations, the accuracy of the final location parameters is affected by the accuracy of the velocity model used. In petroleum fields, subsurface velocity models are known to change abruptly with depth due to layered sedimentary rocks. Alternating high and low velocity layers give rise to complex ray paths, thereby affecting travel time calculation. In the following, we present a case to illustrate the sensitivity of travel time calculations to velocity models.

We consider an actual seismic event from the monitoring field, located at a depth of about 2.5 km below the surface (Figure 2.1). P-wave travel times from this event to five monitoring stations located near the surface will be calculated for two different velocity models.
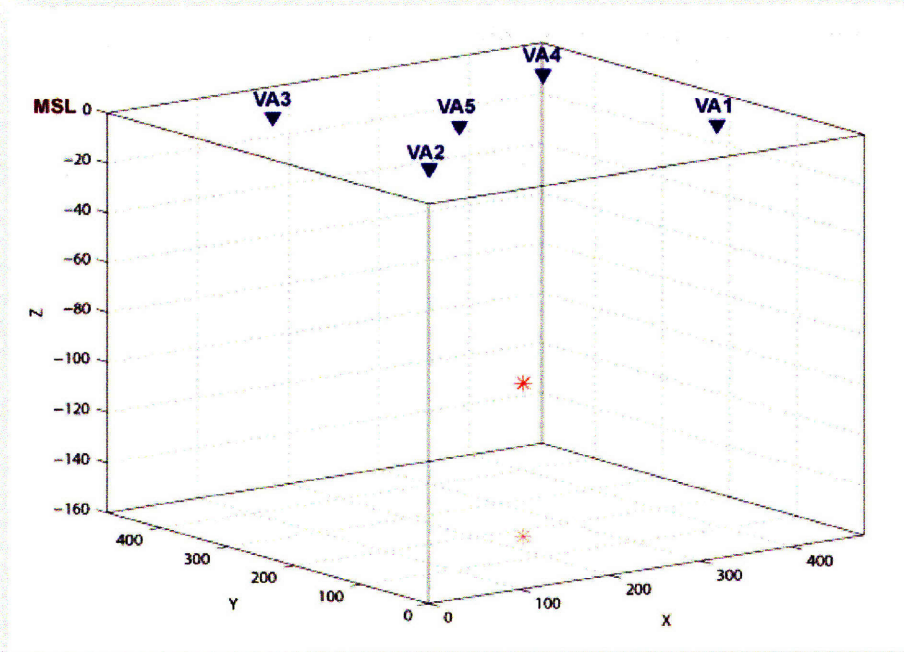
Figure 2.1: Positions of an event (red asterisk) and five receivers (blue inverted triangles) in a 3D grid. [The light colored asterisk on the base of the 3D box shows the projection of the 3D location of the event on a horizontal plane. The numbers on X, Y, and Z axes are expressions for grid locations, not the actual coordinates. X=236, Y=178, Z=99 in this example. MSL is the mean sea level, which is used as the depth datum for all calculations in this study].

The two P-wave velocity models obtained from two different methods are shown by Figure 2.2. The model shown by the upper panel is derived from a check-shot survey in the field, and the model shown by the lower panel is derived from well logs. Both models are 1-D layered representation of the velocity structure.
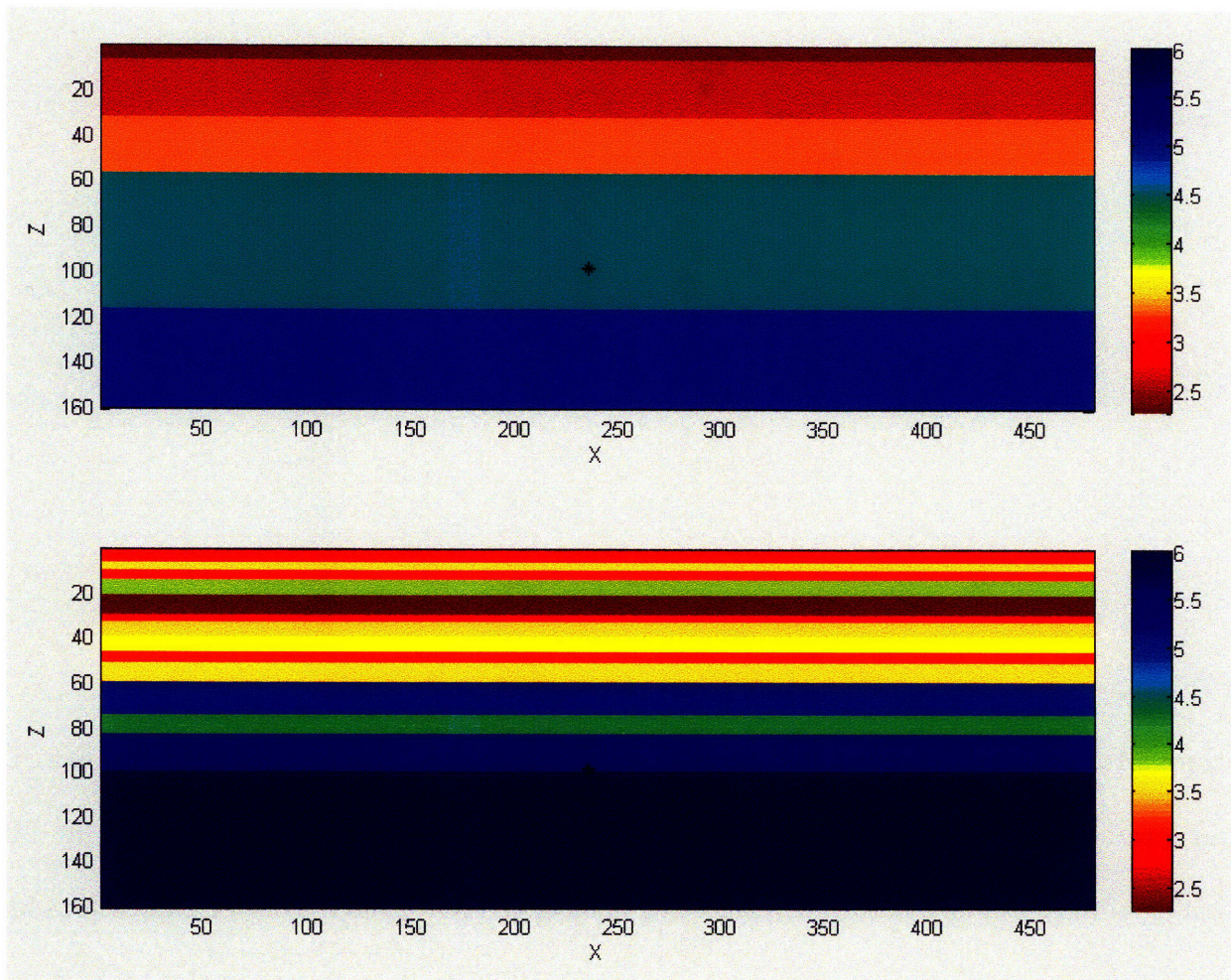
Figure 2.2: Vertical plane (X-Z) cross-sections of two velocity models: check-shot (upper) and well-log (lower). The black asterisk denotes the location of the event, for which travel times will be calculated through the two velocity models shown. The X and Z-axes show grid numbers (1 grid ≡ 25 meters), and the colorbar has units in km/s.

The check-shot velocity model, which monotonously increases with depth, is a good average representation of the reservoir properties; whereas the well-log derived velocity model is a more realistic and more accurate representation of the reservoir. It not only consists of more layers than the check-shot model, but also some of the layers have lower velocities than both

their bottom and top layers – which is often the case for sedimentary layers. The check-shot velocities, in some sense, are an average or "smoothed-out" version of the well-log model; however as we will show in the following that the difference in travel times between the "actual" and its "average" model is too significant to ignore. The algorithm which has been used to compute travel times in these velocity models is based on a finite difference approximation to the Eikonal equation proposed by Podvin and Lecomte (1991) and implemented by Lomax et al. (2000). The Podvin and Lecomte (PL) method is particularly well suited for applications to heterogeneous media, in that it can accurately estimate travel times in the presence of severe, arbitrarily shaped velocity contrasts. With this approach, the velocity model is discretized on an equally spaced grid comprised of constant velocity cells. (The grid spacing for the two velocity models used in our study is 25 meters.) Multiple arrivals (transmitted, diffracted, and head waves) are calculated at each grid node, and the first arrival is chosen.

Because of the accuracy requirements of hypocenter solutions (usually in kilometers) in conventional earthquake location, not much harm is done by using an "average" model, but the accuracy requirements in passive (induced) seismic monitoring applications are so high (usually in meters) that using an "average" model will not suffice for most applications. For the event-station pairs shown by Figure 2.1, the difference in travel times due to the difference in velocity models (Figure 2.2) are summarized by the following table:

Table 2.1: Comparison of P-wave travel times for two different velocity models

Station	Travel time of first arriving P-phase (sec)		
	Check-shot Velocity Model	Log-derived Velocity Model	~ Difference (%)
VA1	1.4505	1.2891	11 %
VA2	1.1636	1.0605	9 %
VA3	1.7849	1.5472	13 %
VA4	2.0011	1.7121	14 %
VA5	0.9703	0.8910	8 %

The magnitudes of percent difference between the two travel times indicate that they are significant enough to affect the location accuracy, and cannot be ignored. It is, therefore, very important to use a detailed velocity model for reservoir monitoring applications, particularly a model that captures the details of the sharp contrasts of velocities (high-low-high) in the layers. A sharp contrast in layer velocities often gives rise to head waves (refraction along the high velocity layer), which could easily be the first-arriving phases at the receivers. To illustrate the effect of velocity model on ray paths, we show the ray path from our discussed event to one of the stations in the network (e.g. VA1) for the two different velocity models. 3D raypaths are computed using an enhanced PL algorithm described by Reiter *et al.* (2005). In this method, first the sensitivities of travel times to cell velocities (i.e. derivatives) are computed. This is accomplished by back-propagation of node-to-node and node-to-cell dependencies from any

given receiver point toward the source. Consistent with the underlying ray theory, the resulting sensitivities are concentrated along a trajectory of cells connecting the source and receiver points, which define the PL version of a ray path. The following figures plot and compare ray paths in the two velocity models.
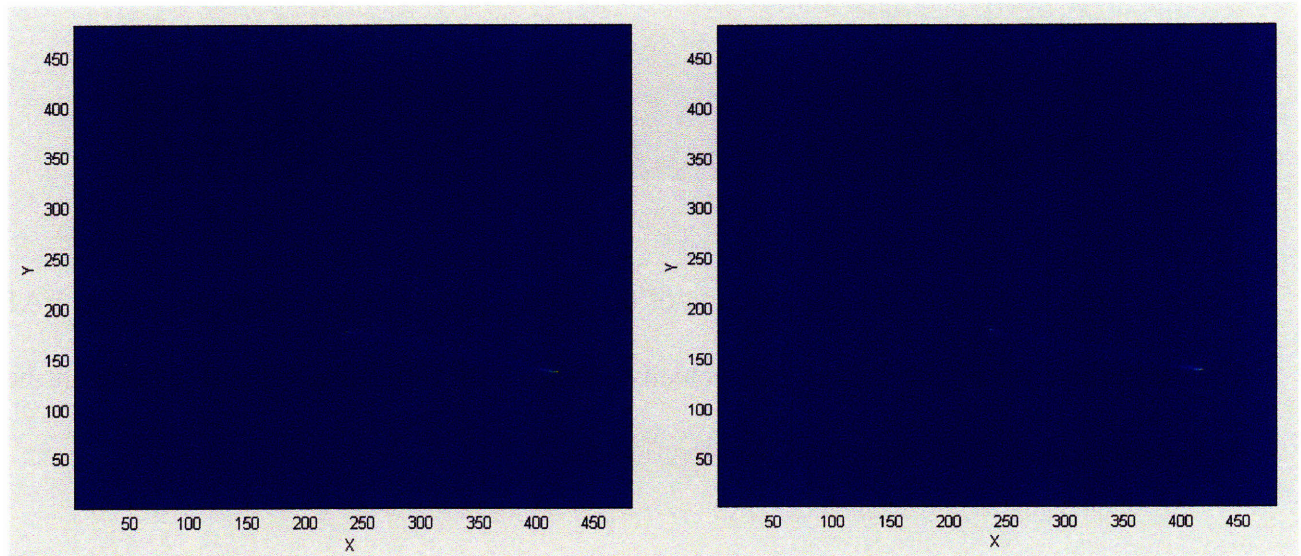

Figure 2.3 (a): Plan view (X-Y cross section) of the event-station ray path for the check-shot model (left) and the well-log model (right). Since the velocity model is 1-D layered and varies with Z only, the cross-sections of the two models along an X-Y plane are the same. The axes show grid locations.
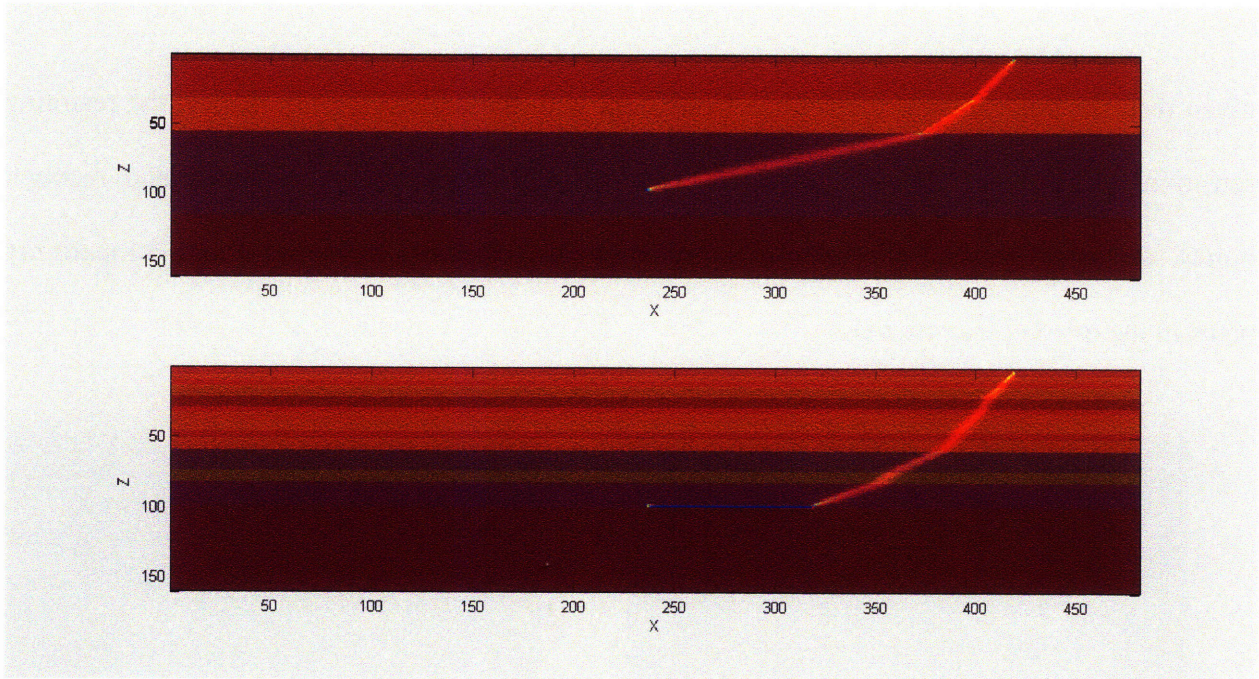
Figure 2.3 (b): Vertical (X-Z) cross-section of the 3D ray paths between event and station VA1 (for illustration see Figure 2.1) in two velocity models with respective velocity models in the background: check-shot (upper) and well-log (lower).
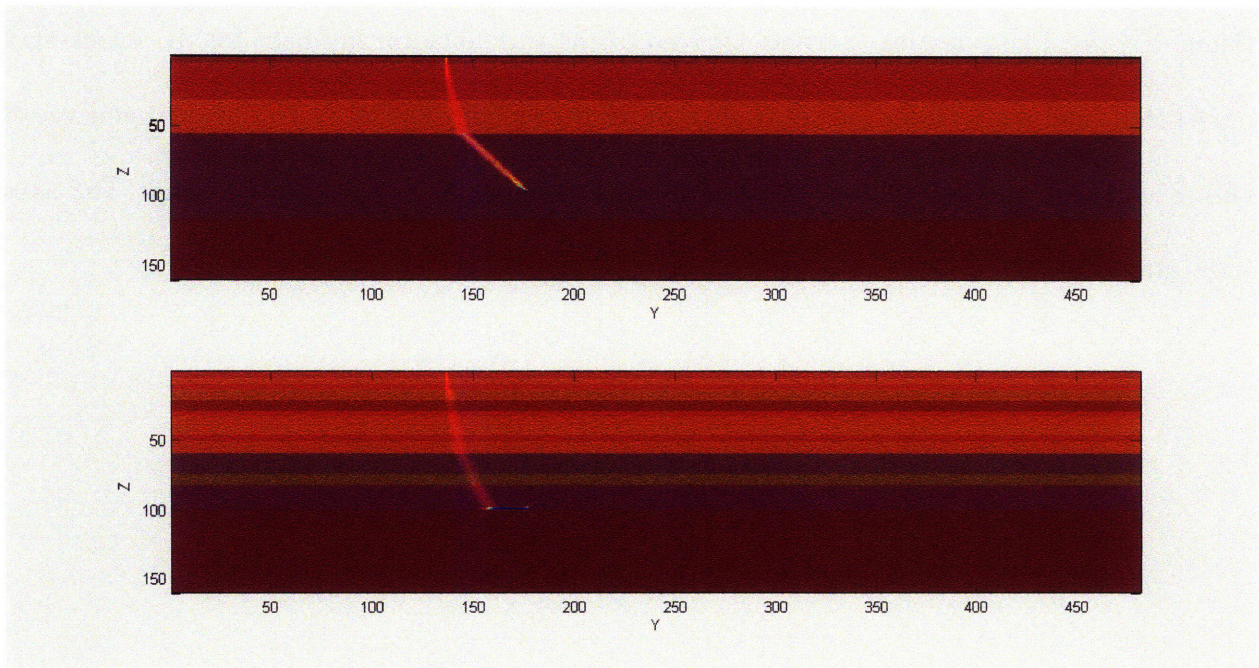
Figure 2.3 (c): Vertical (Y-Z) cross-section of the 3D ray paths between event and station VA1 (for illustration see Figure 2.1) in two velocity models with respective velocity models in the background: check-shot (upper) and well-log (lower).

The significant difference in the paths of the rays in these two velocity models as shown by these figures explains the *significant* anomaly in travel times of the first-arriving P-phases at the stations (Table 2.1). As we will show with more field data later in this chapter, an incorrect velocity model can lead to gross misinterpretation of reservoir dynamics due to mislocation of events. Therefore, for a reservoir monitoring study, much emphasis should be given in building an accurate velocity model which adequately captures the sharp velocity contrasts in the subsurface layers.

2.3.2 Uncertainty in S-picks

The quality of picks (data) dictates the accuracy level of solutions that can be achieved by a location method. Regardless of the location method used, it is invariably true that higher quality picks will guarantee more accurate earthquake locations. To obtain very high quality picks from observed seismograms is usually a challenging problem in earthquake seismology. Usually for natural and induced earthquakes, we have greater confidence in picking first arrivals of P-waves than S-waves. In induced seismicity applications such as those in petroleum reservoirs, it may sometimes be difficult to precisely identify first arrival of P-waves due to reasons such as: a) low signal to noise ratio due to ambient noise and b) emergent arrivals. However, with careful manual analysis, it is still possible to obtain reasonably good quality P-phase picks. The biggest difficulty arises in picking S-waves. While this difficulty is generally acknowledged in the analysis of earthquake records at all scales, the problem is much more severe for earthquakes occurring at shallow depths. Due to the complex nature of wave

propagation in sedimentary layers, induced earthquakes produce wave trains of intertwined arrivals of pure and converted phases at the seismograms. As shown by an example seismogram (Figure 2.4) of a petroleum-field induced earthquake recorded at a monitoring station near the surface, we found it very difficult to identify pure S-arrivals. Use of S-phase data has the potential to better constrain the depth determination in earthquake location, however using erroneous/highly uncertain S-picks would certainly have adverse effects in the quality of depth estimates. A conventional approach in earthquake location is to use S-P arrival times, which constrain the depth better than if only P (or S) arrival times are used (Gomberg *et al.*, 1990). However, this is only true when S-phase picks are "good", and the S-wave velocity is known with reasonable certainty. Gomberg *et al.* (1990) in a study show that even a single incorrectly timed S-phase can result in depth estimates and associated measures of uncertainty that are significantly incorrect.
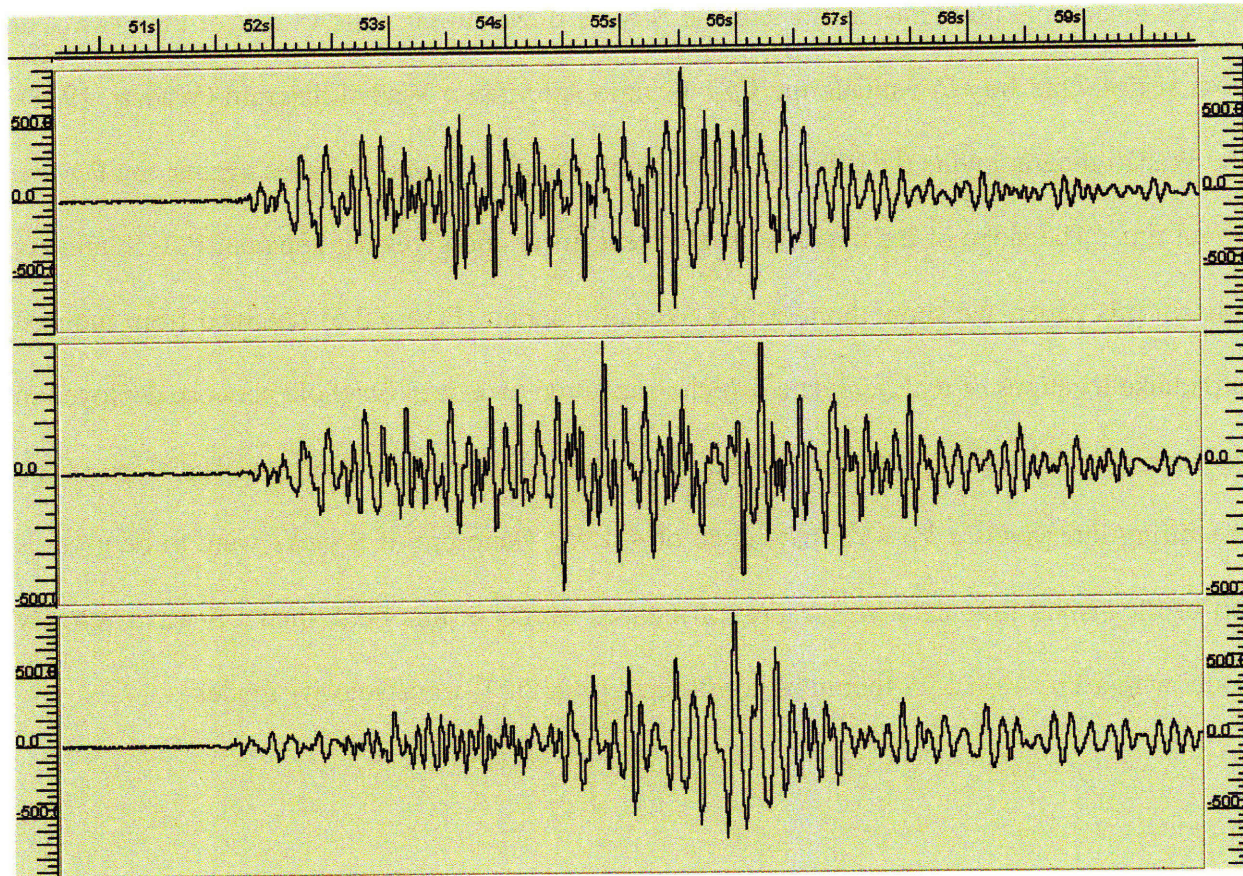
Figure 2.4: A 3-component seismogram due to an induced seismic event at a petroleum field in Oman. From top to bottom, one vertical (Z) and two horizontal components (H1 and H2) are shown.

2.3.3 Uncertainty in S-wave velocity model

While from the data side we need good S-picks, from the modeling side we also need a good S-wave velocity model to predict the travel times accurately. In earthquake location applications, it is a common practice to derive the S-wave velocity from Vp / Vs (ratio between P and S-wave velocity). This usually provides a fair estimate of S-wave velocity at global, regional

or even local scale problems, as the average S-wave trend closely follows that of the P-wave at those scales. One way to validate the Vp / Vs ratio is to plot a Wadati diagram (Wadati, 1933). The Wadati diagram plots the difference in time of arrival of S- and P-waves against the P-wave arrival time. The slope of the curve is usually near linear and gives the apparent P to S velocity ratio. In this paper, we show the plot of a Wadati diagram (Figure 2.5) obtained from induced earthquake locations of real field data, which is acquired by a deep borehole network deployed in the same petroleum field in Oman for the same passive monitoring purposes. The slope of the best fitting line yields a Vp / Vs magnitude of ~ 1.95. Therefore, if S-picks were to be used as part of the arrival time data for location of induced events in this field, then a S-wave velocity model with a $Vp / Vs = 1.95$ should be constructed from the P-wave velocity model.
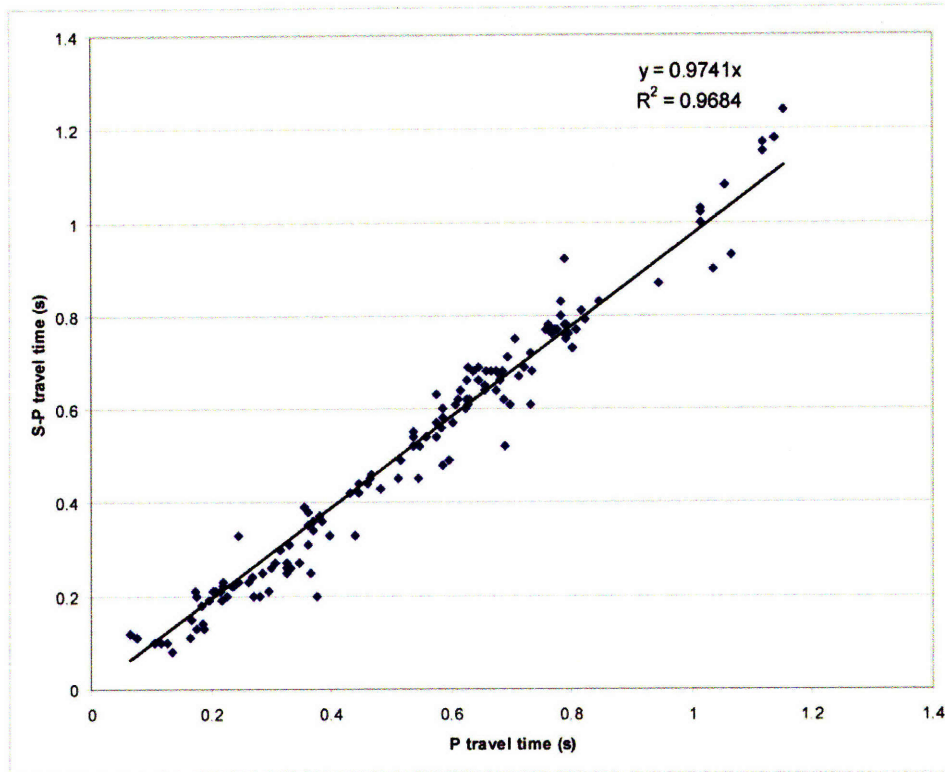
Figure 2.5: Plot of S minus P travel times vs. P travel times (Wadati diagram) for a set of observed induced seismic events. The slope of the best fitting straight line passing through the origin is related to the Vp/Vs ratio according to the relationship: *Slope = (Vp/Vs − 1)*.

For this field, we have additional means of validating the S-wave velocity model. Like the sonic logs measuring P-wave travel times, we also have some Sonic logs measuring shear wave travel times at some well locations. Based on available shear Sonic logs, it is possible to derive a S-wave velocity model for the reservoir independently of the P-wave model. To verify whether the *Vp / Vs* prescribed by the conventional Wadati diagram method agrees with the actual *Vp / Vs* measurements obtained from the field, we plot the *Vp / Vs* ratio at reservoir locations where both Sonic Vp and Sonic Vs logs were available (Figure 2.6). As seen from Figure 2.6, below a depth of ~ 1300 m, the *Vp / Vs* from logs conforms with the prescribed *Vp /*

$Vs = 1.95$ from the Wadati diagram method. However, in the shallower part of the reservoir, where a lot of seismicity is known to take place, the S-wave velocity does not necessarily follow the P-wave trend. The varying ratio of Vp / Vs in the shallower part of the reservoir indicates that S-wave travel time cannot be predicted by using a constant Vp / Vs in these layers. The common technique used by most of the earthquake location methods is to use a constant Vp / Vs; this may not be a good approximation for locating induced earthquakes in a reservoir monitoring application such as the one discussed in this thesis.
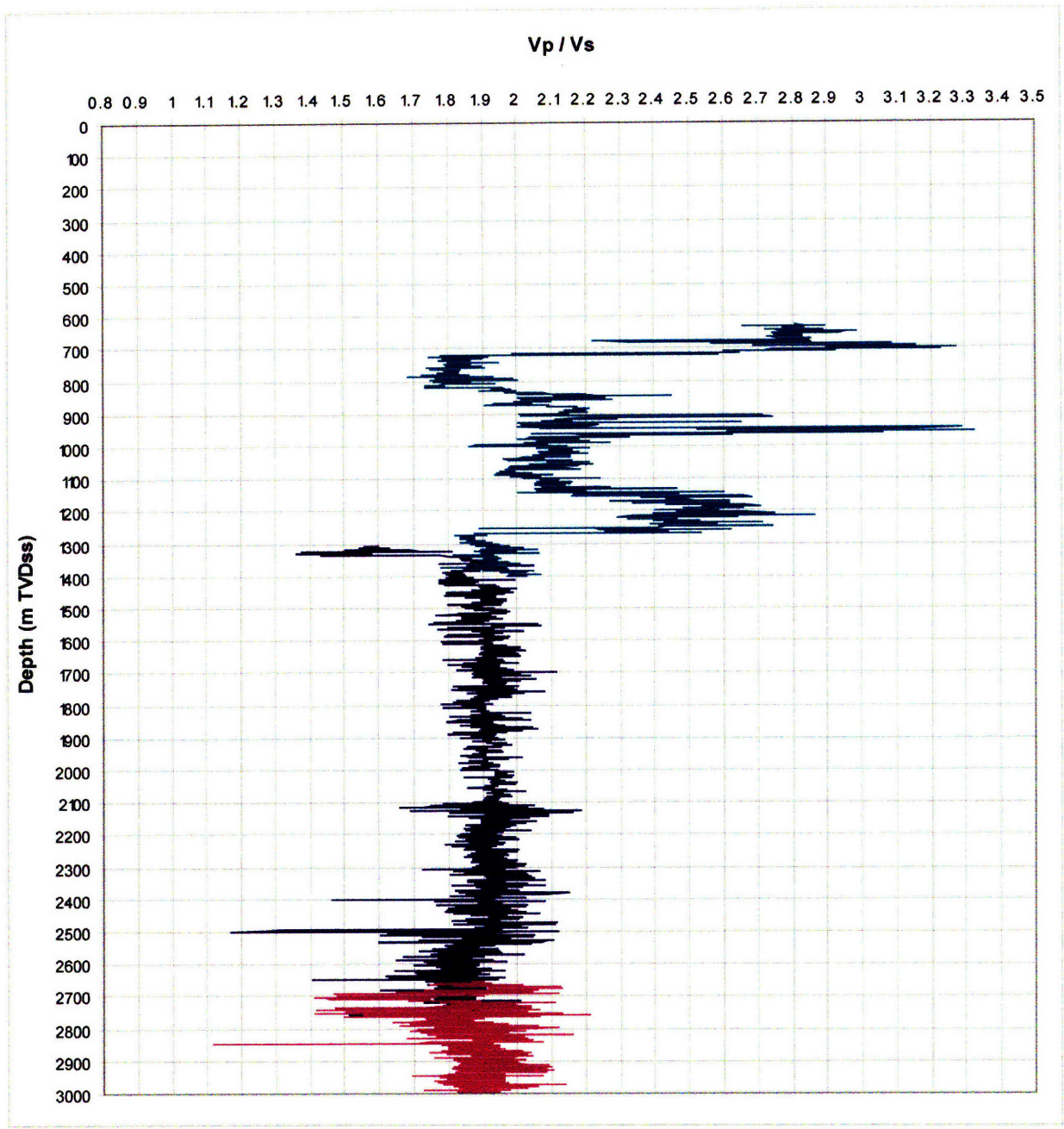
Figure 2.6: A Vp / Vs ratio plot from combining three well-logs with each color representing a separate log. Not all Sonic logs provided shear measurements at all depths, therefore to obtain the maximum coverage at depths three different logs were used. At similar depths, the values were consistent across different logs. The depth axis is shown as TVDss (total vertical depth subsea) in meters.

2.4 Location Methods for Induced Seismicity Application

Initially NonLinLoc (Lomax *et al.*, 2000) was used in our study to locate about 1500 events recorded during the years 1999 – 2007 for a passive seismic monitoring application at a petroleum field in Oman. However, NonLinLoc solutions were found to be sensitive to input *a priori* estimates of uncertainties, mainly pick uncertainties. This seemed to pose a problem for our particular application, because for various practical reasons (e.g. highly uncertain S-picks, low signal to noise ratio of the seismic signals) in many cases it was not possible to adequately assess the uncertainty of the travel time picks. In order to investigate this issue further, we did some synthetic tests with NonLinLoc: we used some fictitious events and generated synthetic travel times from those events to real stations as in the field using the actual velocity model, assigned various models (distributions) of errors to the travel time data (i.e. to simulate "picking errors"), located the events for those travel time data using NonLinLoc, and computed the absolute location errors (distance between the *true* hypocenter location and *inverted* hypocenter location) due to NonLinLoc inversion. To assess how critical the *a priori* uncertainty information (mainly the picking errors) is for obtaining "reliable" NonLinLoc inversion results, we supplied *false a priori* information by reporting an error for the data that is different than the *actual* error in the data within reasonable limits. Our tests revealed that misrepresentation of picking error in the data by a small amount could cause "significant" absolute errors in event locations computed by NonLinLoc. We simulated a few different scenarios with both "good" and "poor" station coverage, and found that in both cases the accuracies of the locations would suffer due to the discrepancy between *actual* and *reported* error in the data.

To further improve the accuracy of hypocenter locations (*X, Y, Z*) of induced seismic events, we devised a location method for the passive seismic monitoring application in Oman. We sought a location method that would address most of the practical issues as discussed in the preceding sections and find reasonably accurate absolute locations of the reservoir-induced seismic events. Our efforts culminated into a complete code that we were able to use for locating all the seismic events from the reservoir monitoring project in Oman. With more accurate velocity models, our method pre-computes the travel time grids using a 3D version of the Eikonal finite-difference scheme of Podvin and Lecomte (1991) and for each event uses *differences* of travel time formed from two stations – instead of individual event-station travel times – to construct the objective function. A natural advantage of using the travel time difference between station pairs is that it eliminates origin time from the equation, thus reducing the number of unknown parameters for which to solve (from four to three). To ensure that the global optimum hypocenter solutions are found, we use an *exhaustive grid-search* in our method. Use of an exhaustive grid-search also saves us from additional parameterization that might be required to formulate a directed or adaptive grid-search method. A more detailed description of the formulation of our location method is given in the following.

2.4.1 Data

Like all other travel-time based location methods, initial data for our method are obtained from arrival times/phase picks for a single event at different stations in the network, T_k^{obs}. The expression for observed travel time can be written as follows:

$$T_k^{obs} = t_o + tt_k^{obs} \pm e \dots\dots\dots\dots(1)$$

where, t_o is the origin time of the event, tt_k^{obs} is the observed travel time at station k from the event location $X,\ Y,\ Z$, and e is the (unknown) error present in the data. As discussed in the previous sections, we seek to eliminate the origin time from the formulation. We achieve this by taking the difference of observed arrival times between station pairs for the same phase pick:

$$T_i^{obs} - T_j^{obs} = tt_i^{obs} - tt_j^{obs} \pm \left(e_i - e_j\right) \dots\dots\dots\dots\dots\dots(2)$$

where, i = 1,2,…,k-1; and j = i+1,…..k. For our location method, instead of absolute arrival times, we use this form of differential arrival time data.

2.4.2 Model

We first calculate travel times tt_k^{cal} between each station and all nodes in the model space $(x,\ y,\ z)$ using the PL method (Podvin and Lecomte, 1991), and then store them on the disk as 3D travel-time grids. Similar to the data space, we take a step further and construct the differences of 3D travel-time grids between all station pairs, the expression for which can be written as follows:

$$T_i^{cal} - T_j^{cal} = tt_i^{cal} - tt_j^{cal} \dots\dots\dots\dots\dots (3)$$

The differences are also pre-computed and stored in the disk as 3D "difference" travel-time grids.

2.4.3 Objective function

For the *actual* event location, i.e. for the grid node X, Y, Z, the calculated and observed times are minimized:

$$T_i^{obs} - T_j^{obs} = T_i^{cal} - T_j^{cal}$$

$$\Rightarrow tt_i^{obs} - tt_j^{obs} \pm \underbrace{\left(e_i - e_j\right)}_{\delta} = tt_i^{cal} - tt_j^{cal}$$

$$\delta_n = \left(tt_i^{cal} - tt_j^{cal}\right) - \left(tt_i^{obs} - tt_j^{obs}\right) \quad \ldots\ldots\ldots\ldots\ldots (4)$$

where, n = 1, 2,.... # of pairs as constructed from available station data.

The goal is to minimize δ_n. The difference between calculated and observed times can be minimized in several ways - most common being L-2 norm and L-1 norm minimization. In simple words, the problem of finding the *actual* event location (X, Y, Z) is equivalent to searching for the node (X', Y', Z') in the 3D grid for which δ_n is minimum.

2.4.4 The Algorithm

To summarize our location method, the following is a step-by-step description of how we implement our algorithm in a personal computer:

Step 1. Pre-compute the difference travel time grids (*Equation 3*) for ALL station pairs and have them loaded into the computer memory. These are our MODEL grids.

Step 2. For a new event to be located, obtain the phase readings and construct the difference data (*Equation 2*) for all available station pairs.

Step 3. For every station pair, create a 3D grid of the same size as the model and populate the grid with the same observed difference data for that station pair. These are our DATA grids.

Step 4. For each node in the grid, compute the root-mean-square difference (this is equivalent to computing the L-2 norm, which could also be substituted with L-1 or other L-*p* norms) between the DATA grids and the MODEL grids.

Step 5. Sort the root-mean-square values from lowest to highest. The node index that corresponds to the lowest root-mean-square value gives the optimum location for the hypocenter.

The node location obtained from *Step 5* is the *most acceptable solution* because the errors in travel-time differences between observed and calculated travel times at all station pairs are

minimum at this node in the entire 3D grid. As a crude way of estimating the uncertainties of the hypocenter solutions from our location method, a list of grid nodes – in the order of descending root-mean-square magnitudes computed from *Step 4* – can be used to plot a "cloud" of solutions. The tighter the cloud, the more certain the hypocenter estimate will be. A more sophisticated analysis and development of uncertainty estimates for our location method can be accomplished following the methods and computational strategies given by Rodi (2008). Additional discussions on topics related to location uncertainty can be found in Appendix A of this thesis.

2.4.5 Validation

We test our location code by solving for the hypocenters of repeating seismic events (also known as *multiplets*) recorded during passive seismic monitoring at the field in Oman. Repeating events are identified by the similarity of their waveforms – events that have similar source mechanism and nearly identical locations (hypocenters) should yield very similar waveforms at the same station. Waveforms from an example set of seven repeating events are shown by Figure 2.7.
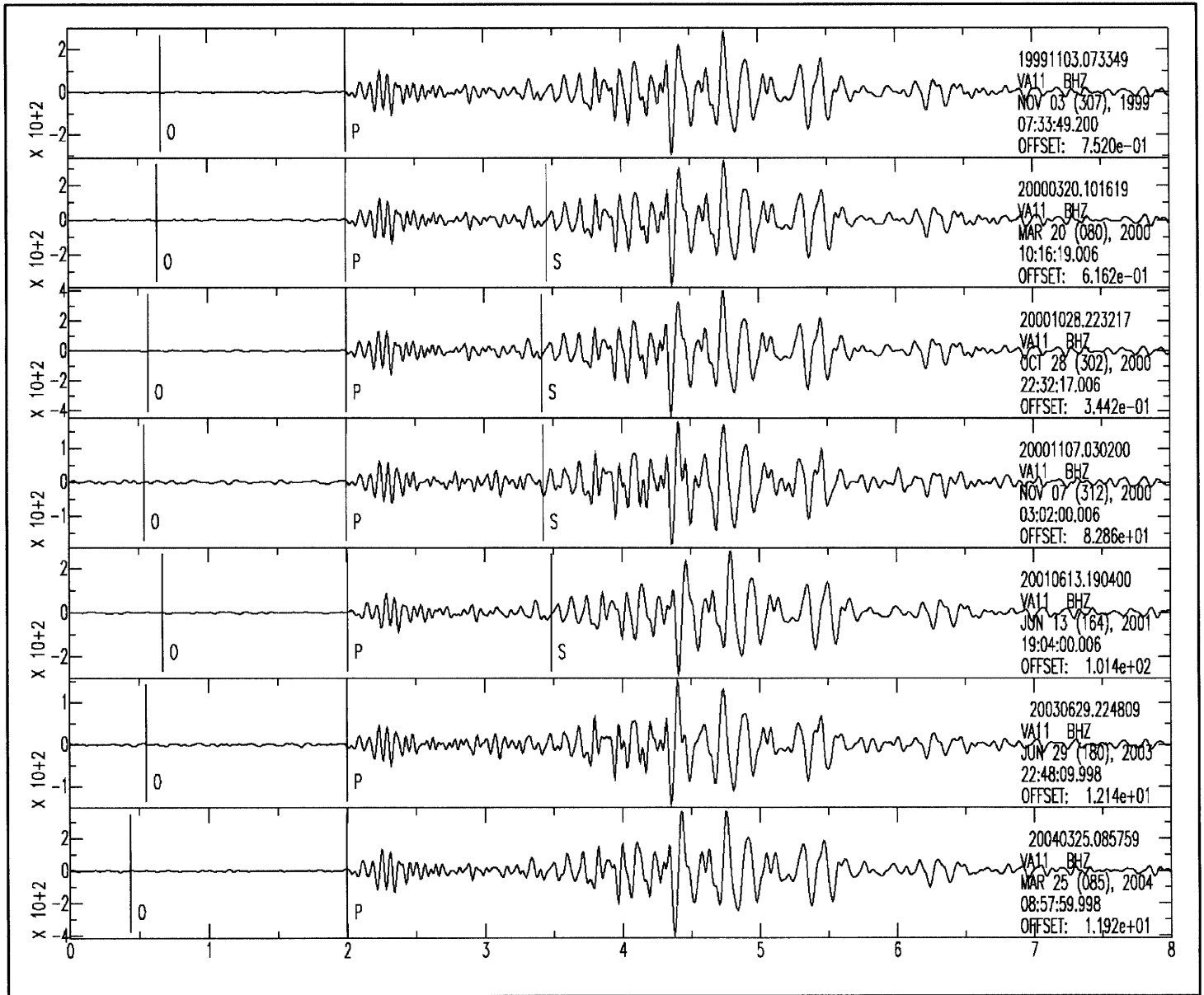
Figure 2.7: Similarity of waveforms among 7 different seismic events observed at station VA1. The seismograms are shown as aligned by their P-picks (letter 'P" on each window). Origin time and available S-picks are also identified on each seismogram, by "O" and "S" respectively.

We then located these events individually, using only their first-P arrival times to the stations, with our station-pair-differencing location code. The location results (X, Y, Z coordinates) are tabulated by Table 2.2 and also shown on a map by Figure 2.8.

Table 2.2: *X, Y, Z* coordinates and the number of stations/available P-picks for each event

Event #*	X (km)	Y (km)	Z (km)	# of P-picks used
1	6.08	3.88	1.05	5
2	5.98	4.08	0.95	5
3	6.05	4.10	0.90	5
4	6.08	3.93	0.93	4
5	6.08	3.80	0.93	5
6	5.95	3.43	1.00	4
7	6.05	3.50	1.00	5

*Events are numbered from 1-7 in accordance with the display order (top to bottom) of seismograms on Figure 2.7.
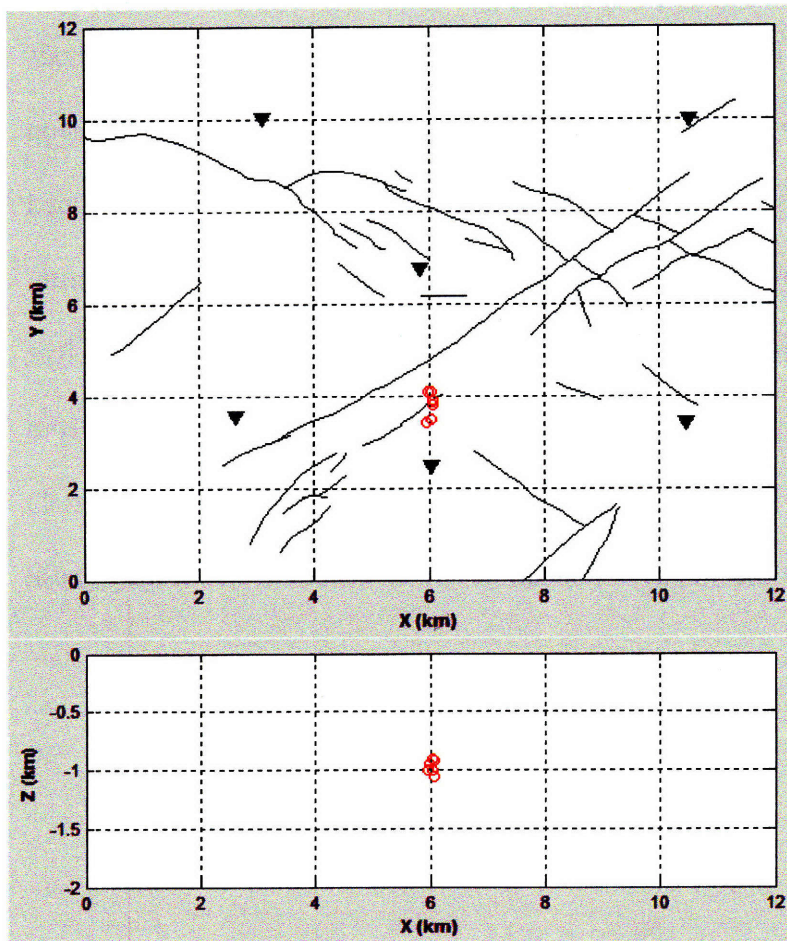
Figure 2.8: Locations of the 7 events (red dots) on an epicenter map and on a depth-cross section. Seismic stations and existing fault maps are denoted by green triangles and black lines respectively.

The station-pair-differencing method yields nearly identical hypocenter locations for these 7 events (Figure 2.8, Table 2.2), identified as *multiplets* by their actual waveform data. Therefore the method is validated for precision and robustness. We also compare hypocenter estimates using both L-2 norm and L-1 norm minimization with our code, which show almost identical results (Appendix A).

2.5 Application

In this chapter, we have discussed some of the problems that complicate the task of event location in reservoir-induced seismicity applications and proposed some strategy and methods for improving event location accuracy. In this section we show applications of our approaches on some induced seismicity field data. As mentioned earlier, the data used in this thesis are obtained from a passive seismic monitoring project at a petroleum field in Oman. Reservoir monitoring with passive seismic data started in this field in 1999 with a seismic network consisting of five near surface stations (as shown by Figure 2.1). In this section, we use induced event data from this field recorded during November 1999 – June 2001 by the monitoring network to assess: 1) the impact of velocity model and 2) the impact of location strategy/method in locating these events.

2.5.1 Velocity model

To locate the induced events we use a 1D layered velocity model with alternating high and low velocity layers that we had derived from sonic logs at some well-locations where the field is seismically active. This is our preferred velocity model for locating the events for this application, as this model provides detailed information about the subsurface layers. For comparison purposes, we use another velocity model available for this reservoir monitoring project, which is essentially an average model of the reservoir obtained from a check-shot survey in the field. These two velocity models have been described earlier in this chapter (Figure 2.2). The 3D reservoir model used for this application has dimensions of 480 x 480 x 160 grids (in x, y, and z respectively). This is essentially the discretized form of a 12 km by 12 km by 4 km region of the reservoir, using a uniform grid spacing of 25 meters in all three directions.

On Figure 2.9, we show a comparison of earthquake depth distributions obtained with these two velocity models – one is our sonic log-derived model plotted by the blue curve (right panel) and the other is the average check-shot model (plotted in red, left panel). It shows how sensitive depth locations of induced events are to change in velocity models. From a check-shot derived "coarse" model to a well-log derived "fine" model, the secondary cluster of events below 2 km (identified by black-dashed oval on Figure 2.9) is completely shifted to (shallower) depths less than 1.2 km.
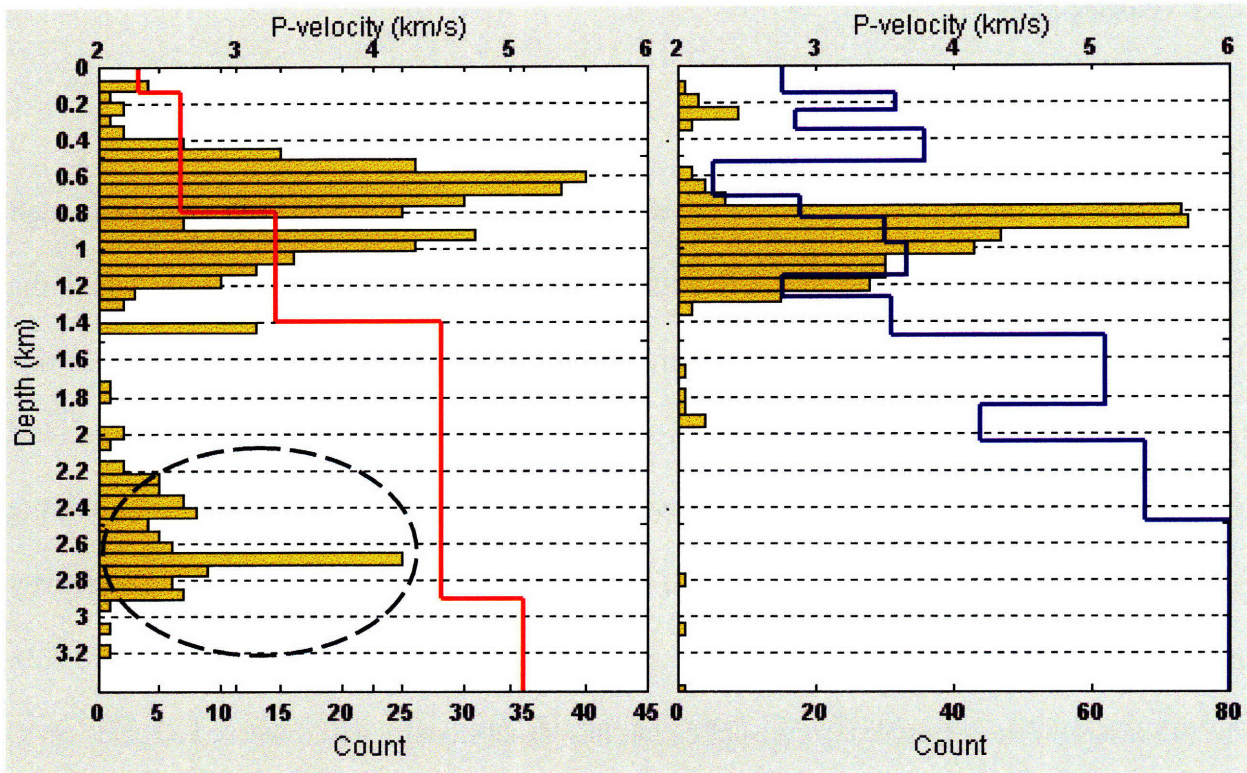
Figure 2.9: Comparison of depth locations (histogram plots) obtained using two velocity models. Red curve on the left panel is a check-shot derived average velocity, and the blue curve on the right panel is a well-log derived, more detailed velocity model. (Total # of events: left – 409, right – 380).

The shift is corroborated by comparing modeled and actual seismograms for some of these shifted events. By Figure 2.10 we show an example of depth validation for an event that was initially located at a depth of ~ 2.5 km by the check-shot velocity model, and subsequently got relocated (shifted) at a depth of ~ 0.8 km by the well-log derived velocity model. Synthetic seismograms for this event were generated using the discrete wavenumber approach (Bouchon, 1981; Muller, 1985) and compared with their actual/observed seismograms at a given station. It is seen from Figure 2.10 that for this event the modeled and actual seismograms are much more

60

similar for depth 0.8 km (Figure 2.10-b) than that for depth 2 km (Figure 2.10-a). Based on this seismogram comparison and other location studies in the same field, the presumption is that the depth distribution shown on the right panel of Figure 2.9 is more accurate than the one shown on the left. Using the red instead of the blue model would lead to mislocation of depths and wrong interpretation of the cause of induced seismicity in this field.
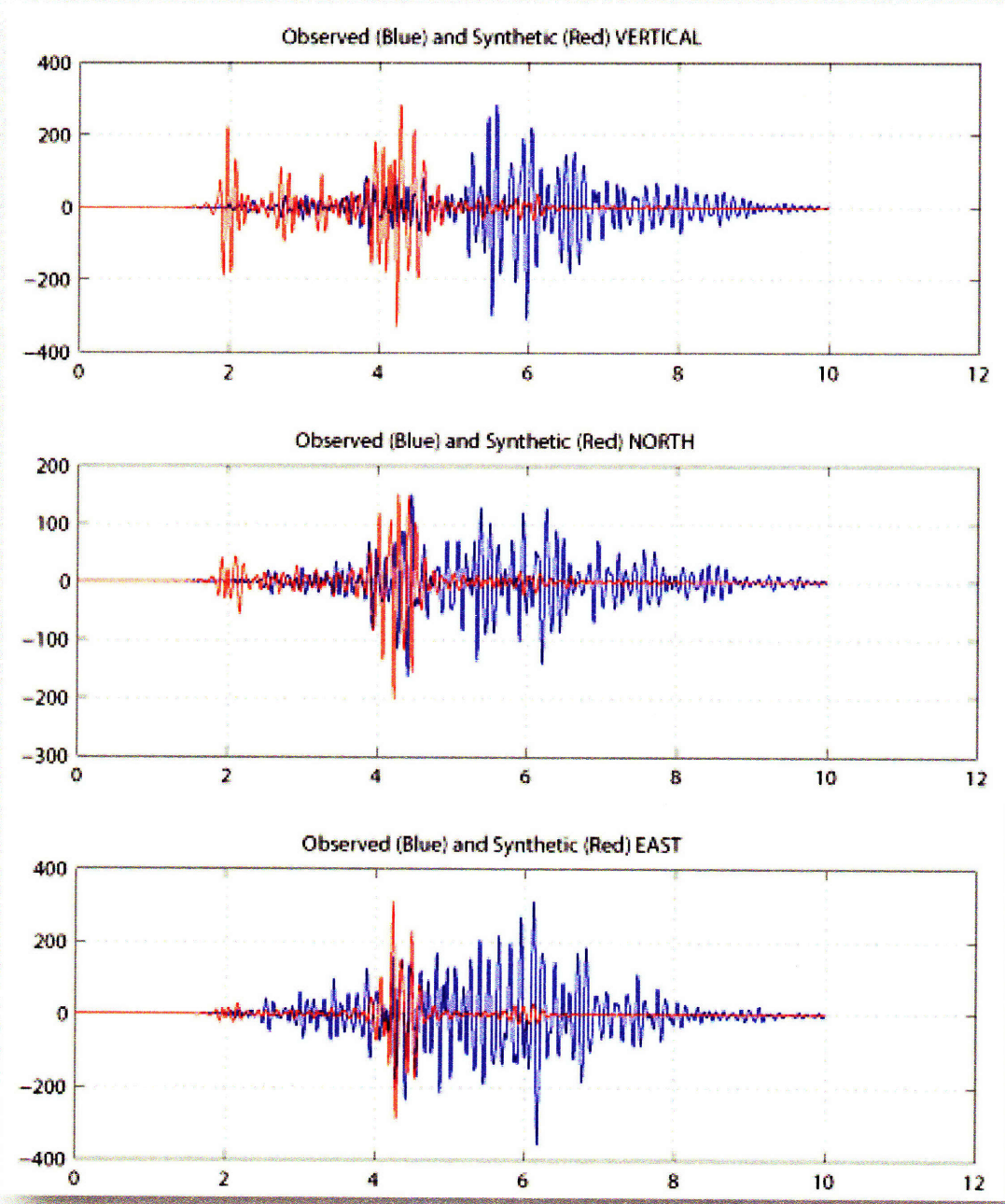
Figure 2.10-a: Comparison between the actual (observed) seismogram of an event observed at station VA1 and modeled (synthetic) seismogram of that event computed for the same station, filtered to the same bandwidth (6-16 Hz). The event was located at depth ~ 2.5 km. For synthetic seismogram modeling, the actual event location (hypocenter) and the check-shot derived velocity model is used. The observed and synthetic traces are plotted in blue and red respectively. The match between the two traces is very poor.
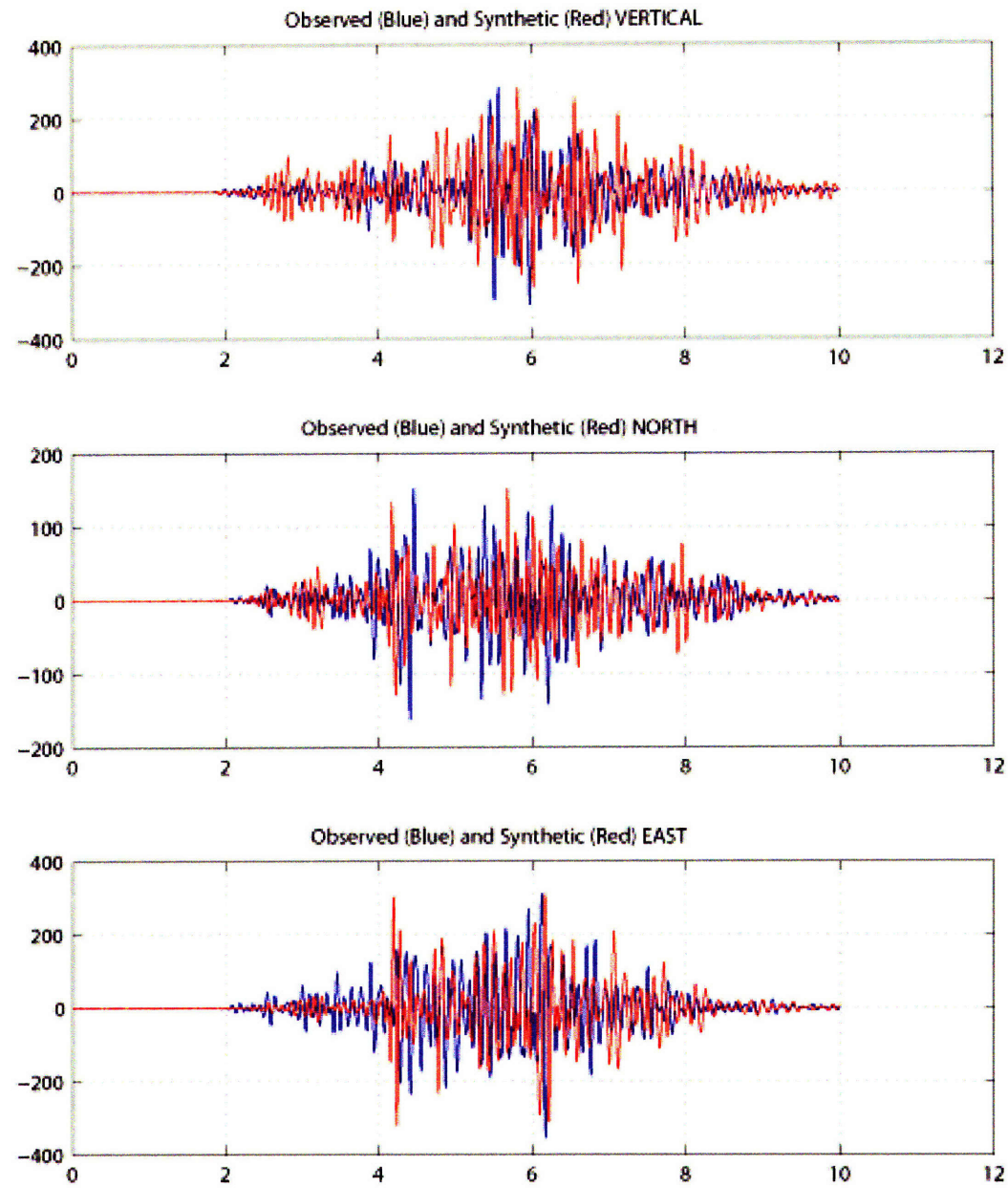
Figure 2.10-b: Comparison between synthetic and observed waveforms for the same event as in Figure 2.10-a, The synthetic calculation was performed for a new depth location (event depth = 0.8 km) using the log-derived velocity model. The match between sythetic and observed seismograms is quite good and certainly much better than that seen by Figure 2.10-a.

2.5.2 Location method

When the velocity model is more accurately known, our proposed location method, which minimizes the difference between observed and predicted differential travel times at station pairs through exhaustive grid search, yields reasonably accurate earthquake locations. We show results from application of our method to this field data and compare them with results obtained from NonLinLoc. Figure 2.11 shows a comparison between epicenters obtained by these two methods. Since the reliability of S-picks is highly questionable in this application, in our method we form the travel time differences at station pairs for first-arriving P-phases only. Predicted travel times are calculated using the same PL based routine for both methods. Therefore, the difference in solutions is mainly due to differences in formulation of the minimization function and the search method. For the minimization part, NonLinLoc offers two different choices for likelihood function: 1) the familiar least-squares L-2 norm likelihood function with Gaussian error assumption, and 2) the Equal Differential Time (EDT) likelihood function, which is based on a generalization by Font *et al.* (2004) of the Equal-Differential-Time (EDT) formulation of Zhou (1994). We compared solutions from our location method against solutions obtained by NonLinLoc, using each of these two choices in NonLinLoc, and found locations obtained by our method to be more accurate than those obtained by NonLinLoc. As seen from Figure 2.11, the epicenters obtained by our location method are more tightly clustered and well-correlated with preexisting faults than those obtained by EDT method of NonLinLoc.
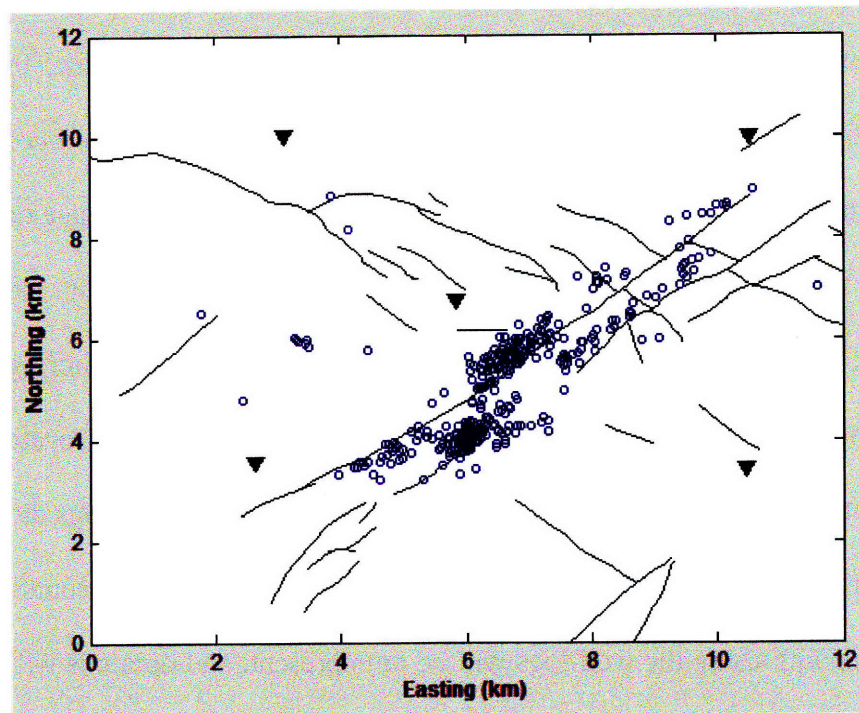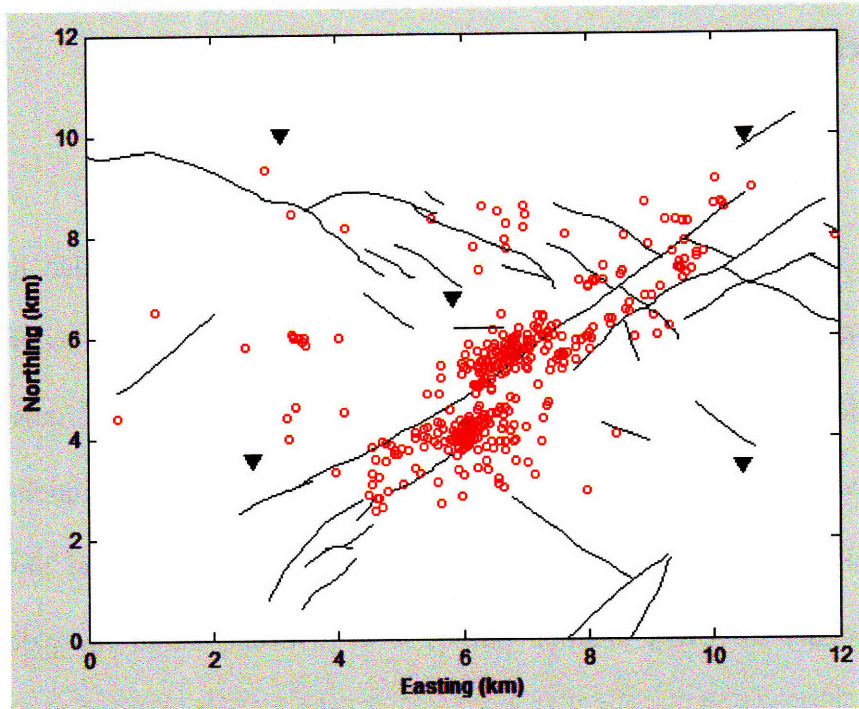
Figure 2.11: Map view of epicenters of the induced events computed using two different location methods: red circles (total #: 406) on the upper panel denote NonLinLoc solutions, whereas blue circles (total #: 393) on the lower panel are solutions from our new location method. Epicenter solutions obtained from our location code (blue circles) are less scattered than those obtained from NonLinLoc (red circles). The same velocity model (well-log derived: Figure 2.2) is used for both locations. (Green triangles denote seismic stations; black curves show the existing faults.)

65

2.6 Discussions and Conclusions

A major challenge in locating induced events in petroleum reservoirs arises due to usually complex velocity structure and seismic wave propagation in sedimentary rocks. Although alternating low and high velocities and heterogeneities are typical characteristics of most sedimentary layers, it is *atypical* for an earthquake seismologist to account for these aberrations in his/her location routine. In this chapter we showed the importance of retaining the low velocity layers in the earth model for event location purposes. With event-station ray path diagrams for two velocity models, we illustrated how head waves take precedence in arrival modes in the presence of low-velocity layers and how that impacts the net arrival time. In reservoir monitoring applications where accuracy requirements are very high, sometimes mislocation of event depths caused by miscalculation of arrival times due to using an average or smoothed velocity model of the actual reservoir can have significant consequences in the interpretation of seismicity, as we demonstrated with real field data from a passive monitoring study. It is therefore recommended that a velocity model as accurate as possible be used to locate reservoir-induced seismic events. Usually travel-time measurements obtained from well-logs are a much better choice for building a velocity model compared to check-shot surveys. Of course the paradoxical scaling-up issue with using the well-logs will be omnipresent, and opinions will be divided as to how many layers should be used, yet the most important thing to realize is that the low-velocity layers are the crucial ones that need to be properly accounted for in the final velocity model. In complex scenarios, integrating information about the sedimentary layers from several logs of the same type and of different types, and from other reservoir properties, can be very useful in building an optimum velocity model for location purposes. Sometimes the

abundance of very low-amplitude, emergent first-arrivals in the data itself will speak for the importance of low-velocity layers in the model – as we experienced during data analysis for this study. Manual picking is preferred over automated picking to ensure pick accuracy, however for large number of events this could become an issue. In earthquake location, first-arrivals of S-waves can provide powerful constraint on focal depth estimation, yet the uncertainty in S-picks can sometimes overwhelm the benefits – as we have seen in this study with induced earthquake data. Several converted phases generated along the travel path of seismic waves, from their relatively shallow sources in sedimentary layers to receivers at the surface, make the task of identifying pure S-waves from the seismograms very difficult. Therefore, caution must be exercised when using S-picks for locating induced events in shallow sedimentary layers.

To accurately model travel times through alternating high-low-high velocity layers, a finite-difference based method is recommended for forward calculations of travel times in reservoir-induced seismicity location applications. Most of the conventional earthquake location codes do not use finite difference travel time calculation, and therefore are not suitable for this type of application. Among the advanced location methods, NonLinLoc can be recommended. However, during our application, we have found NonLinLoc to be highly sensitive to *a-priori* uncertainty estimates. Much scatter and lack of correlation with faults in many places were seen in the induced seismicity data located by NonLinLoc.

To further improve the accuracy of our locations, we developed an algorithm that uses a minimization function made up of differences of arrival times between all station pairs for a

single event. Thus the origin times are not explicitly addressed by the minimization function, and the optimization is reduced to a three-parameter (hypocenter only) problem from the more conventional four-parameter (hypocenter and origin time) problem. By taking differences between all station pairs we increase the number of data points, some of which might be redundant – however, this redundancy in the data space may actually provide a basis for some sort of the regularization in the data space as well (pers. comm. Dale Morgan, MIT). Another big advantage of reducing the number of model/search parameters is that it greatly helps the grid search, which we use to find the optimum solution in our location method. In fact, we use an exhaustive grid-search to find the global minimum, which ensures greatest accuracy of our results within the limitations. However, exhaustive grid-search would be *impossible* – if not extremely time consuming – to conduct, if it were a regular four-parameter (hypocenter and origin time) grid-search problem. Therefore, by reducing the model parameters from 4 to 3, we are indeed making the exhaustive grid-search method quite tractable. Also, during practical applications, for a large grid size, forward calculations for each event can be very time consuming and costly. We handle this potential problem by pre-calculating the travel times for each grid-receiver pair and loading them into memory. Since the velocity model is known and fixed, travel times are calculated only once, and whenever a new event needs to be located only the minimization (search) is performed. Therefore, our station-pair-differencing location method is computationally very efficient and can easily be used for real-time induced seismicity location and monitoring. The simplicity and robustness offered by our station-pair-differencing location method motivates us to use it as the preferred method for locating induced events at the petroleum field in Oman. The method can also be used in similar applications.

2.7 References

Bolt, B. A., (1960), The revision of earthquake epicentres, focal depths and origin times using a high-speed computer, *Geophys. J. Roy. Astr. Soc.*, 3, 433–440.

Bouchon, M., (1981), A Simple Method to Calculate Green's Functions in Elastic Layered Media, *Bull. Seismol. Soc. Am.* 71, 959–971.

Eaton, J.P., (1969), HYPOLAYR, A computer program for determining hypocenters of local earthquakes in an earth consisting of uniform flat layers over a half space, *U.S.G.S. Open-File Report.*

Engdahl, E.R., and R.H. Gunst (1966), Use of a high-speed computer for the preliminary determination of earthquake hypocenters, *Bull. Seism. Soc. Am.*, 56, pp. 325–336.

Flinn, E. A., (1960), Local earthquake location with an electronic computer, *Bull. Seism. Soc. Am.*, 56, 467–470.

Flinn, E.A., (1965), Confidence regions and error determinations for seismic event location, *Rev. Geophys.*, 3, pp. 157–185.

Font, Y., H. Kao, S. Lallemand, S., C.-S. Liu, and L.-Y. Chiao (2004), Hypocentral determination offshore Eastern Taiwan using the Maximum Intersection method, *Geophys. J. Int.*, 158, 655-675.

Geiger, L., (1912), Probability method for the determination of earthquake epicenters from the arrival time only (translated from Geiger's 1910 German article): *Bull. of St. Louis University*, 8, 56-71.

Gomberg, J.S., K.M. Shedlock, and S.W. Roecker (1990), The effect of S-wave arrival times on the accuracy of hypocenter estimation, *Bull. Seism. Soc. Am.*, 80, pp. 1605–1628.

Klein, F.W., (2000), User's guide to Hypoinverse-2000, a Fortran program to solve for earthquake locations and magnitudes, *U.S.G.S. Open File Report*, 02-171.

Lahr, J.C., (1980), Hypoellipse/Multics, a computer program for determining local earthquake hypocentral parameters, magnitude, and first motion pattern, *U.S.G.S. Open-File Report*, OF 80-59.

Le Meur, H., J. Virieux, and P. Podvin (1997), Seismic tomography of the gulf of Corinth: a comparison of methods, *Ann. Geofis.*, 60, 1–24.

Lee, W.H.K., and J.C. Lahr (1975), HYPO71, A computer program for determining hypocenter, magnitude, and first motion pattern of local earthquakes, *U.S.G.S. Open-File Report*.

Lomax, A., J. Virieux, P. Volant, and C. Berge (2000), Probabilistic earthquake location in 3D and layered models: introduction of a Metropolis-Gibbs method and comparison with linear locations, in 'Advances in Seismic Event Location', Kluwer Academic Publishers, Amsterdam, The Netherlands, 101-134.

Lomax, A., and A. Curtis (2001), Fast, probabilistic earthquake location in 3D models using Oct-Tree importance sampling, *Geophys. Res. Abstr.* 3.

Mendoza, J., and D. Morgan (1985), BASIC-HYPO: A BASIC language hypocenter location program, *Bull. Seismol. Soc. Am.*, 75, 1211-1216.

Moser, T.J., T. van Eck, and G. Nolet (1992), Hypocenter determination in strongly heterogeneous earth models using the shortest path method, *J. Geophys. Res.*, 97, 6563-6572.

Muller, G., (1985), The Reflectivity Method: A Tutorial, *J. Geophys.* 58, 153–174.

Podvin, P., and I. Lecomte (1991), Finite difference computation of traveltimes in very contrasted velocity models: a massively parallel approach and associated tools, *Geophys. J. Int.*, 105, 271-284.

Reiter, D., W. Rodi, and M. Johnson (2005), Development of a tomographic upper-mantle velocity model beneath Pakistan and northern India for improved regional seismic event location, *Bull. Seismol. Soc. Am.*, 95, 926–940.

Rodi, W.L., (2008), Error analysis in the joint event location/seismic calibration inverse problem, *Air Force Research Laboratory Report*, AFRL-VS-HA-TR-2007-0000.

Sambridge, M.S., and B. Kennett (1986), A novel method of hypocentre location, *Geophysical Journal of the Royal Astronomical Society*, 87, 679–697.

Sambridge,M. S., and B. L. N. Kennett (2001), Seismic Event Location: Nonlinear Inversion Using a Neighbourhood Algorithm, *Pure and Applied Geophysics*, 158, 241–257.

Tarantola, A., (1987), Inverse Problem Theory: Methods for Data Fitting and Model Parameter Estimation, Elsevier, Amsterdam, The Netherlands.

Tarantola, A. and B. Valette (1982), Inverse problems = quest for information, *J. Geophys.*, 50, 159-170.

Thurber, H.C., and N. Rabinowitz (2000), Advances in Seismic Event Location, Kluwer Academic Publishers, Amsterdam, The Netherlands.

Vidale, J.E., (1988), Finite-difference travel time calculation, *Bull. Seism. Soc. Am.*, 78, 2062-2076.

Vidale, J.E., (1990), Finite-difference calculation of travel times in three dimensions, *Geophysics*, 55, 521-526.

Wadati, K., (1933), On travel time of earthquake waves, Part II. *Geophys. Mag.* 7, pp. 101–111.

Wittlinger, G., G. Herquel, and T. Nakache (1993), Earthquake location in strongly heterogeneous media, *Geophys. J. Int.*, 115, 759-777.

Zhou, H., (1994), Rapid 3-D hypocentral determination using a master station method, *J. Geophys., Res.*, 99, 15439-15455.

Chapter 3

Passive Seismic Monitoring using Data from Near-Surface Network

---

3.1 Introduction

The petroleum field in Oman undergoing passive seismic monitoring consists of two producing units – the Natih Gas reservoir and the underlying Shuaiba Oil reservoir (Figure 3.1). Gas extraction from Natih is being driven by compaction of the Natih formation in response to declining reservoir pressure. The Shuaiba oil reservoir was initially produced by natural depletion but water injection was introduced in 1972 to maintain reservoir pressure. Currently the Shuaiba oil reservoir is under water flood with production at water-cuts in excess of 95%. Structurally the field is a highly faulted, large anticline created by deep-seated salt movement. The structure is dominated by a major NE-SW trending central graben (Blaskovich *et al.*, 1985) and two major systems of extensive extensional faulting with two preferred directions (SE-NW and NE-SW) that affect the trapping mechanism in the oil reservoir. All faults are high-angle normal faults.

Staff working in the field have reported increasing seismic activity since 1996. Significant surface subsidence in the center of the field has been observed by InSAR, GPS and leveling surveys, and has been attributed to compaction of the Natih formation.
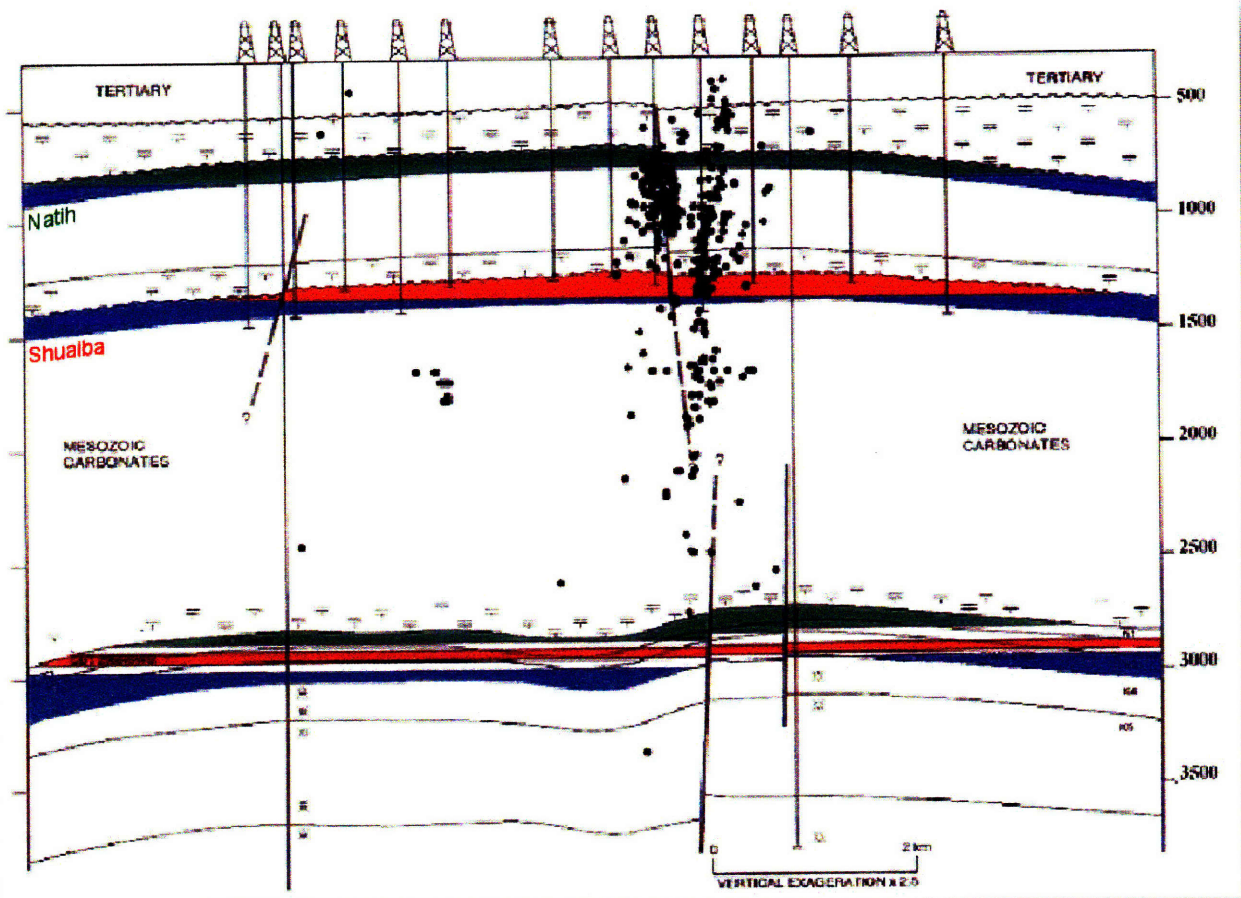
Figure 3.1: Schematic cross-section of the field showing producing Natih gas (upper green) and Shuaiba oil (upper red) formations. Black lines showing known/preexisting faults and black dots showing a set of induced seismic events. The geological interpretation is adopted from van Driel *et. al*, (2000).

Although beneficial as a recovery mechanism, continuing reservoir compaction in the gas layer poses a threat to the integrity of the some 500 Shuaiba and Natih wells that are exposed to deformation within and close to the reservoir. In highly compacting fields, shear stresses may cause slip and failure of wells. Preliminary modeling conducted at Petroleum Development

Oman (PDO) showed that the Natih gas reservoir is predicted to display significant compaction under depletion (van Driel *et al.*, 2000). In order to characterize the compaction of the Natih reservoir and to determine seismic risk to the surface facilities from the largest induced earthquake that may be triggered in the field, a seismicity and subsidence monitoring program was initiated for the field. Passive seismic data acquisition in this field started in 1999 with a seismic network consisting five *near-surface* seismic stations, each using three-component geophones installed in shallow boreholes at depths about 135 to 150 m below the surface. Enduring some changes over time, the network remains operational to date, recording more than 1500 induced earthquakes from the field since its deployment. As in any passive seismic monitoring application, the primary goal in this case is to accurately determine the location of these events and to relate them to reservoir structure and mechanism.

Some aspects that are critical to finding accurate locations of reservoir-induced seismic events are: i) accuracy of arrival time data/phase picks, ii) accuracy of the velocity model used for locating the events, and iii) robustness of the event location method in the face of scientific challenges posed by practical limitations with data (and sometimes with model). In this chapter, we show applications of various methods in passive seismic monitoring of the petroleum field in Oman with about seven years of induced seismicity data acquired by the near-surface (shallow) seismic network. We discuss various issues related to processing field data and obtaining reliable locations for the events, and then show the results and analyze the reservoir dynamics in light of the seismicity observed in the field.

3.2 Passive Seismic Data Acquisition and Processing

Petroleum Development Oman (PDO) started collecting passive seismic waveform data from its field in November 1999, with three-component (one vertical, two horizontal) downhole geophones installed in relatively shallow boreholes – at about 150 m below the surface. It was a good design consideration to place the seismic sensors downhole, as those are known to significantly reduce the ambient noise due to field operations to boost the microseismic signal and, in general, greatly improve the resolution of mapping active reservoir fractures or faults (Rutledge et al., 1998a, b; Phillips, 2000). The seismic network started data acquisition with five monitoring stations, labeled VA1, VA2, VA3, VA4 and VA5 (Figure 3.2). Station VA5 went out of operation in 2001, and in 2002 a new station VA6 was installed (Figure 3.2). Data is recorded continuously, with a sampling rate of 8 ms (125 samples per second), and stored in disk at the field acquisition module. The disk is retrieved periodically by field personnel and the "raw" *ringbuffer* data is copied and sent to MIT for processing and analysis.

Considerable time and effort is spent in pre-processing the raw data. State-of-Health (SOH) data pertaining to the sensors written on disk during acquisition by the field module are also analyzed to help identify actual seismic events from the raw streaming data. Reservoir-induced seismic events are identified based on trigger information generated during data acquisition. However, often there have been "false" triggers due to field operations, and sometimes due to regional or global earthquakes. It is, therefore, essential to visually analyze the waveform data pertaining to all "suspected" triggers in order to identify and eliminate those

76

events which are not related to induced-seismicity in the field. After identification of the actual induced seismic events, the *ringbuffer* data is converted to ASCII and SAC format for further analysis.
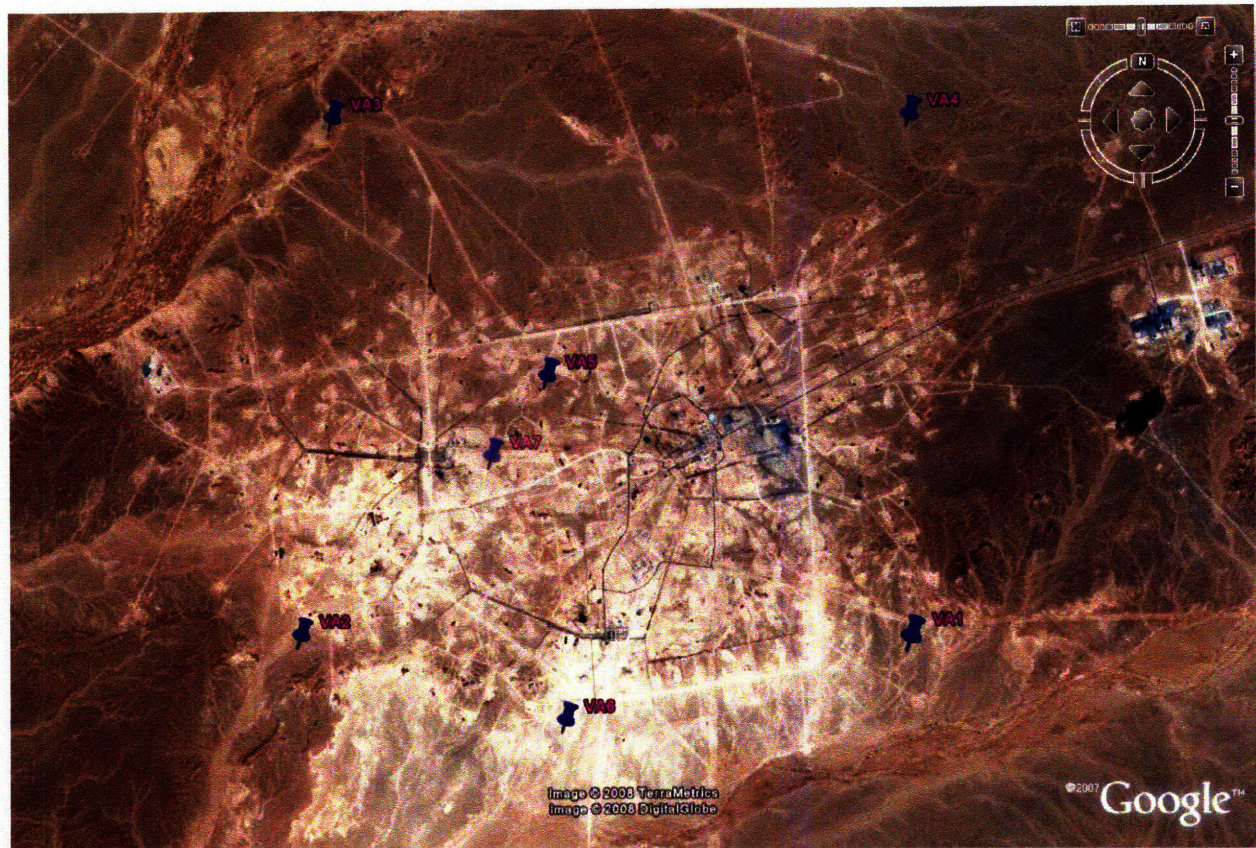
Figure 3.2: A field map showing location of the PDO passive seismic monitoring stations. VA5 was operational during 1999 – 2001, while VA6 was added to the network in 2002. The station VA7 seems to exist, but no data has ever been reported from it. (Figure courtesy: Google Earth).

The next step is to identify and read arrival times of first arriving P-and S-wave phases from seismograms of the induced events recorded at each station. This is considered the most

important part in data preparation as accuracy of locations is limited by the accuracy of arrival time picks. For this field data application, manual phase-picking is preferred over automatic picking. It is generally more accurate and often easy to detect and pick arrivals manually since the human eye can identify a change in amplitude or frequency in the signal even in the presence of significant noise. Several approaches have been proposed for the automatic P-wave arrival detection (e.g., Baer and Kradolfer, 1987; Earle and Shearer, 1994; Anant and Dowla, 1997; Bai and Kennett, 2000; Zhang *et al.*, 2003) using short-term-average and long-term-average (STA/LTA) ratios, energy analysis, frequency analysis, statistical analysis, polarization analysis, particle motion or a combination of these. The automatic picking of an S-wave arrival is more complicated since the S-phase, in most cases of induced earthquakes at shallow depths, is superimposed by a strong P-wave coda. Cichowicz (1993) presents an automatic S-phase picking algorithm using three-component data where the first arrival of the P-wave must be well defined. However, manual picking is still performed to increase the picking accuracy. Electrical and surface noise associated with drilling, production and other field operations taking place during the recording period limits the signal quality of seismograms to some extent. Therefore, during phase-picking from the seismograms, techniques such as filtering, particle-motion attributes such as polarization and three-component amplitude (Jurkevics, 1988) analysis are used as aide to visual inspection of seismograms for identification of P-and S-waves. The onset of P-waves observed at large numbers of the seismograms recorded by the stations over the years are low amplitude emergent arrivals; yet identification of the first arrivals of P-waves has been much easier than the first arrivals of S-waves. Visual identification of the first arrival of pure S-phases on the seismograms is very difficult because the separation of pure and converted phases is very hard to identify. The challenges faced with S-picks are discussed at greater length in the previous

chapter. Even the polarization method, which works quite well for P-wave identification, is hardly successful in identification of S-waves from this passive seismic data. Polarization of the S-wave is difficult to interpret because seismic records usually contain both the SH and SV components, as well as higher-mode Rayleigh and Love waves with similar arrival times (Ruud et al., 1988; Jepsen and Kennett, 1990). To improve our S-wave picks for an event, as a guide we often used an "expected" S-wave arrival time calculated from a hypocenter location estimated for that event using P-wave arrival times only.

3.3 Velocity Model for Location of Induced Seismicity

The importance of the velocity model in event locations and how it potentially impacts the depth locations of induced seismicity have been discussed in great detail in Chapter 2 and also in Sarkar and Toksöz (2008). Special care was given to obtain a good velocity model for this monitoring application. Using a sonic log obtained from a well in the field where most of the seismicity is known to occur, we derived a 1D layered velocity model to be used for locating seismic events in the field (Figure 3.3). Gamma Ray log at that well and lithology information were also taken into account in order to decide on the layer boundaries, especially for those strata having velocities lower than those above and below. By analyzing the logs, the layer boundaries were decided and the slowness measurements within each layer obtained from the sonic log were averaged to get an average slowness value for that layer. (Slownesses were converted to velocity to get the final layered velocity model). The high-low-high alternating velocities in the

79

sedimentary rocks give rise to complex ray paths, therefore to model the wave propagation and arrival times of various modes with reasonable accuracy it is important to use an accurate representation of the velocities of the stratified media in our location routine. A few more logs from a few different well locations became available later. We checked for lateral heterogeneities in the field to determine whether our layered velocity model would require any adjustments or corrections. To that end, we computed a moving average from all available Sonic logs and compared our 1D layered velocity model with that average (Figure 3.4). Our velocity model compared well with the average log, and no major changes in our model were deemed necessary. This, in one way, served as a validation for our velocity model.
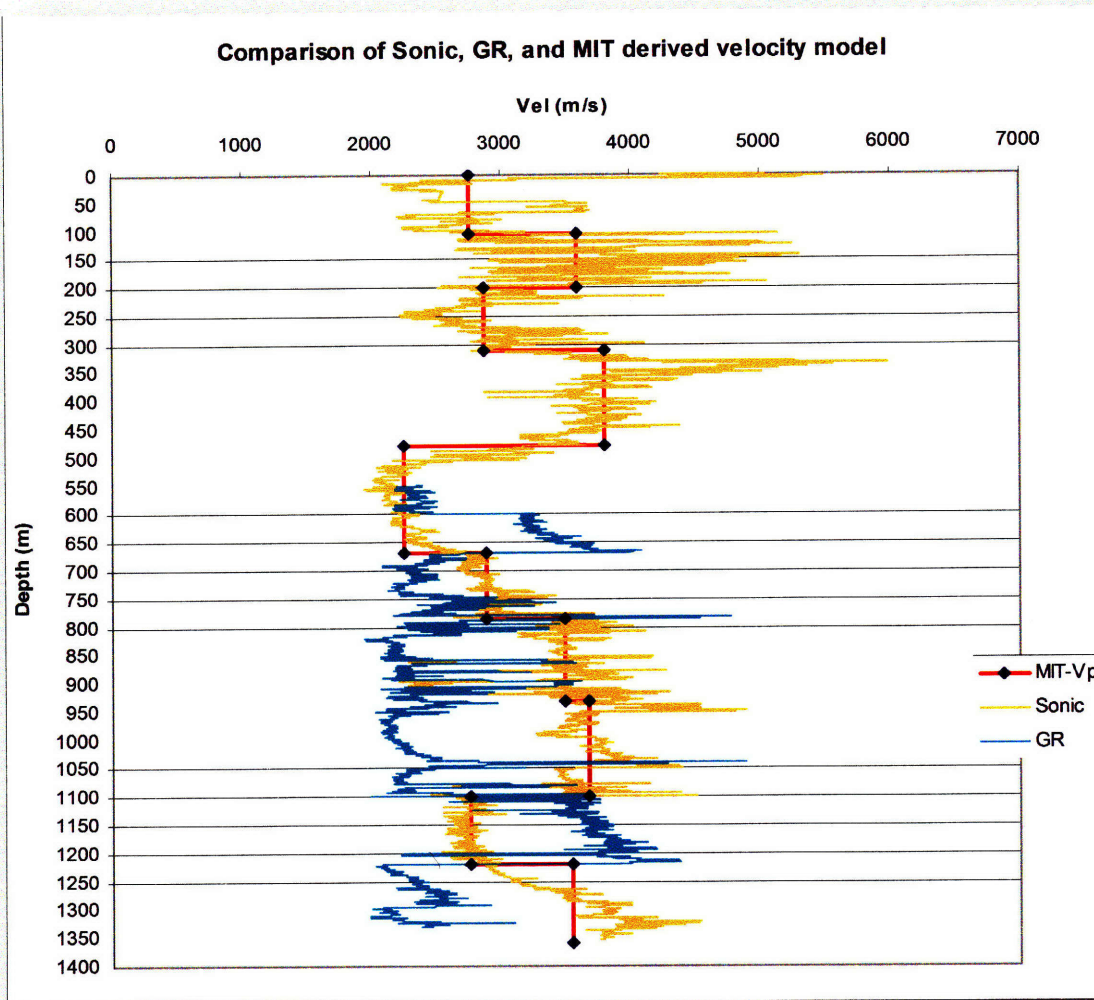
Figure 3.3: A sub-section of the logs (Gamma Ray and Sonic), and the layered velocity model derived from the Sonic log for induced seismicity location purposes.
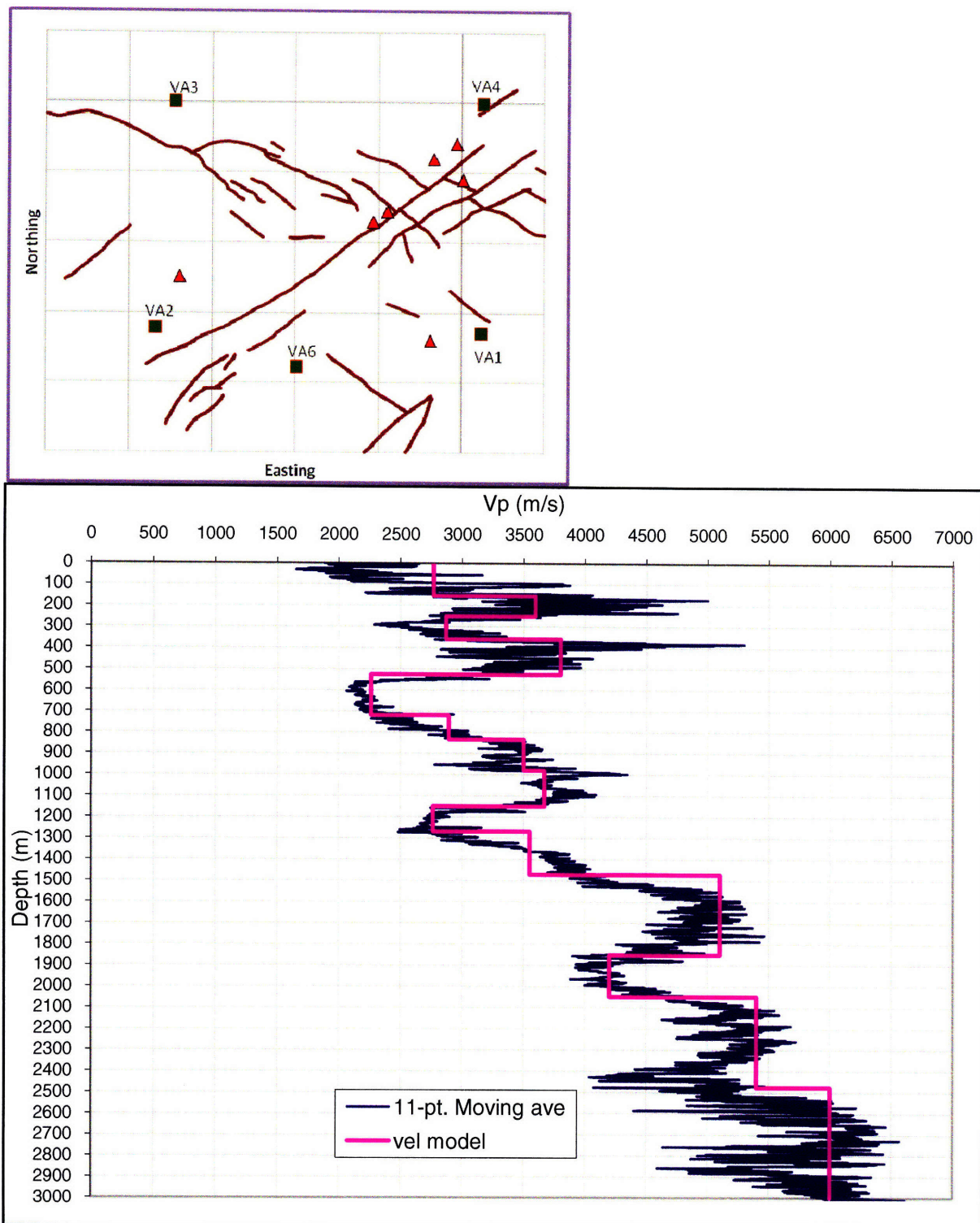
Figure 3.4: (Upper) – Position of wells in the field for which Sonic logs were available, shown by red triangles. The seismic monitoring stations and the fault lines are identified by green squares and brown lines respectively. (Lower) – A moving average of the available logs (blue curve), compared with the velocity model (pink curve) used to locate seismic events in the field.

3.4 Improved Accuracy of Focal Depths

Using a refined velocity model derived from well logs, significant improvements were made in the depth locations of previously located events. In a previous study conducted on the same petroleum field in Oman, Sze (2005) located about 400 induced seismic events that had occurred during November 1999 – June 2001. A check-shot derived velocity model was used in that study for event location. For this study, we located the same events again using our sonic log derived velocity model (Figure 3.4). In Figure 3.5 we show a comparison between the two depth distributions of events – one found by using an average (check-shot) velocity model from previous study (Sze, 2005) and another found by using a more detailed (sonic log) velocity model. The over-smoothed model seemed to have *mislocated* the deepest cluster of events centered at around 2.7 km in the previous study (Figure 3.5: left panel). The location accuracies of those events are improved in this study by using a more accurate velocity model (Figure 3.5: right panel). Most of the events that were previously thought to have depths below 2 km during 1999 – 2001, are found to be much shallower by this study. This changes the interpretation of induced seismicity for the period 1999 – 2001. If the prominent cluster between ~ 2.2 to 3 km (identified by black dashed oval on the left panel of Figure 3.5) were true, then water injection would have to be considered as a *very* significant mechanism for inducing seismicity in the field. However, the role of water injection in inducing seismicity in the field is dwarfed by the new results of event depth distribution from 1999 – 2001 (Figure 3.5: right panel). In fact, some other independent observations such as: i) event locations using data from a deep-borehole network in the same field, ii) geomechanical modeling studies on the cause of induced seismicity in the field, iii) evidences of well-buckling and pore collapse in shallower parts, and iv) synthetic

seismogram modeling for depth validation using Bouchon (1981) and Muller (1985) as shown in Chapter 2 of this thesis suggest that the majority of events recorded by the network during 1999 – 2001 are likely to be relatively shallow.
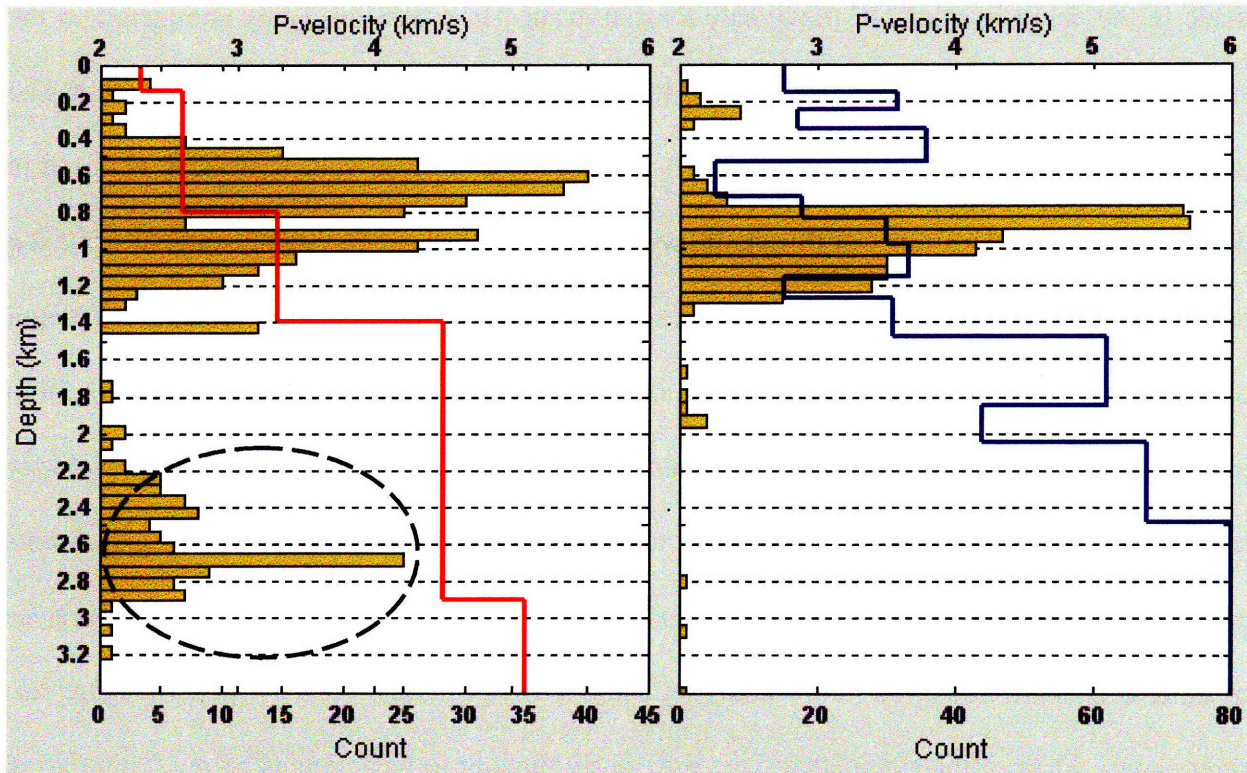
Figure 3.5: Comparison of depth locations (histogram plots) of the same set of events recorded during Nov 1999 – June 2001, obtained using two velocity models. Red curve on the left panel is a check-shot derived average velocity used to locate events in a previous study (Sze, 2005), and the blue curve on the right panel is a well-log derived, improved velocity model used in this study. The dashed oval in black on the left panel shows a significant artifact of the previous location study (Total # of events on this plot: left – 409, right – 380). Both results are obtained using the same location method.

3.5 Induced Seismicity Locations and Correlation with Reservoir Dynamics

In this paper, we present locations (X, Y, Z coordinates) of induced seismic events recorded by the PDO seismic monitoring network during November 1999 – February 2007. During this period, about 1300 seismic events of various magnitudes were recorded by 3 or more seismic stations of the network. The location uncertainty increases with decreasing number of observations/seismic stations. While the quality of arrival time picks (phase picks from seismograms) is most important in governing the accuracy of hypocenter estimate of an event, it is also quite important that the event be recorded by stations on all sides of it. However, due to various field conditions, a large number of events in the field, mostly during 2002 – 2007, failed to produce seismic signatures at all of the existing stations of the network. Due to factors such as network problems, sensor malfunction, low signal-to-noise ratio, event-station distances, we observed a significant portion of the recorded events (about 50%) to produce "readable" seismic data at only 3 stations. As discussed earlier, it was very difficult to obtain reliable S-picks from the observed seismograms; therefore in order not to introduce additional errors/uncertainty in the solution through erroneous S-picks, we decided to use only P-phase picks to locate the events. However, with 3 independent observations (P-phase picks from 3 stations) it is not possible to resolve the hypocentral parameters with reasonable certainty. Therefore, as final locations for the induced seismicity data acquired during 1999 – 2007, we show locations of only the events having at least 4 observations/P-phase picks from 4 different stations. As for the location method, we use a station-pair-differencing approach developed in-house (Sarkar and Toksöz, 2008), details of which are given by the previous Chapter. Depending on the clarity and quality of the phase picks, the uncertainty on these locations do vary as well; however, with our location

method, the events that have 4 or more P-arrival time observations can be located with a level of confidence that makes them suitable for monitoring and interpretation of induced seismicity in the field.

The epicenter map of Figure 3.6 reveals that, by and large, the seismicity in the reservoir is confined along the major NE-SW fault corridor. The depth map shows that events have mostly been occurring at relatively shallow depths, with a majority of the events being concentrated between 700 and 1200 m below the mean sea level (~ 800 – 1300 m below surface).
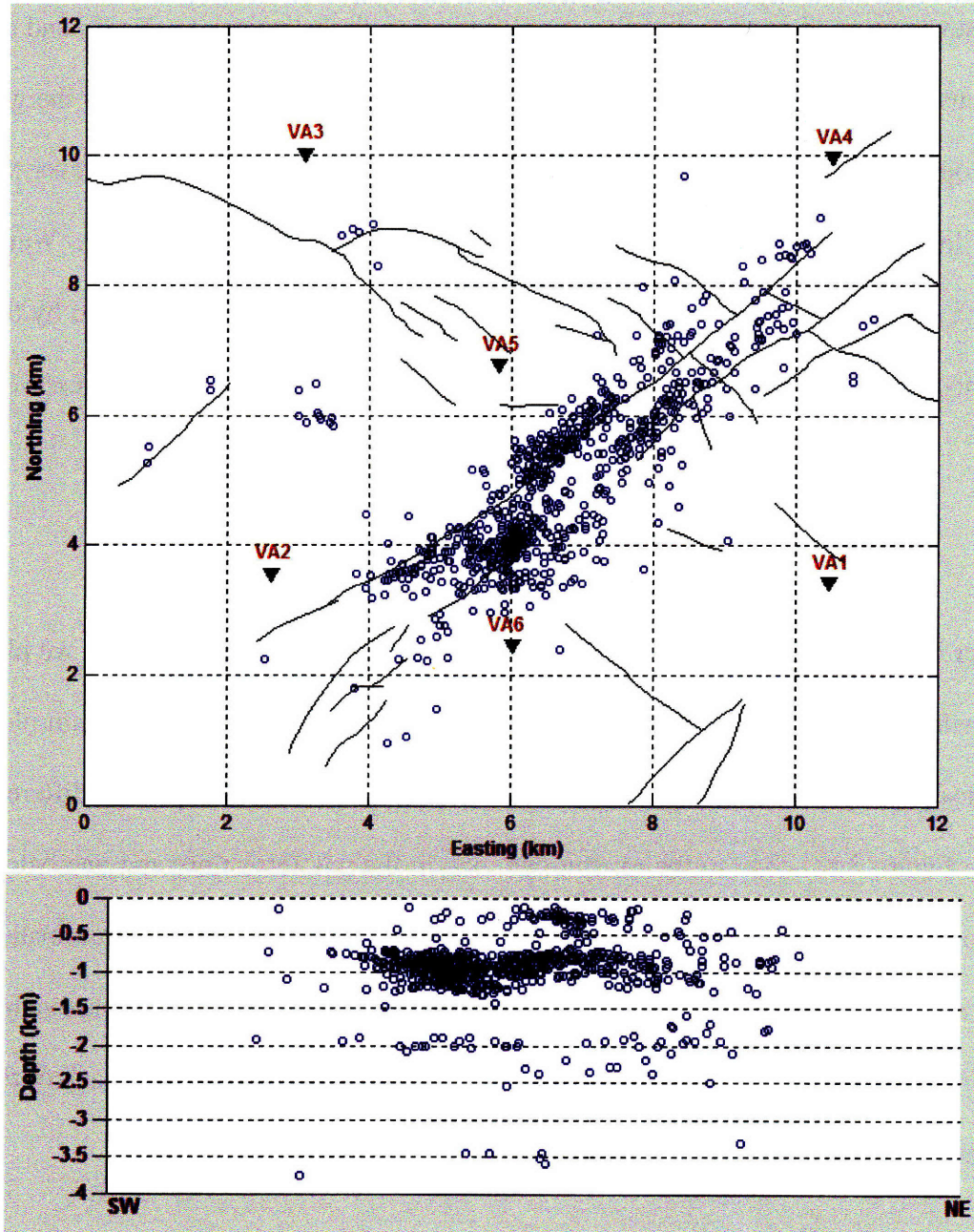
Figure 3.6: Locations of induced (passive) seismic events recorded during Nov 1999 – Feb 2007. The upper panel shows epicenter locations of the events, while the lower panel shows depth locations plotted along the major fault strike direction. Also plotted on the upper panel are: i) all seismic stations deployed by PDO during this period (green triangles) and ii) faults mapped from seismic on the Natih top horizon (black lines). Seismicity in the field is well-correlated with the two major NE-SW faults.

Plotting seven years of passive seismic event locations with the major gas (Natih) and oil (Shuaiba) horizons (Figure 3.7), it is seen that the events are more concentrated around the gas top than the oil top. This leads to a hypothesis that the bulk of the seismicity in the field over the years has been induced mainly due to continuous compaction of the gas reservoir. Water injection acts as a secondary mechanism for induced seismicity in the field, as evidenced by the diminishing number of events with depth as we trace the event locations from gas to oil reservoir (Figure 3.7).

To further illustrate the reservoir scenario in connection with induced seismicity, we plot a histogram showing the depth distribution of events (Figure 3.8). Based on the histogram plot, three distinct clusters of passive seismic events can be identified (identified by three different colored ovals on Figure 3.8) – one in the overburden, one in the gas formation, and one below the producing oil reservoir. The shallowest cluster in the overburden ranges approximately between 300 m and 600 m below the surface. Induced earthquakes are most likely reactivating existing faults or creating new faults both in the reservoir and above the reservoir. Breach of the seal above the reservoir could lead to gas leakage.
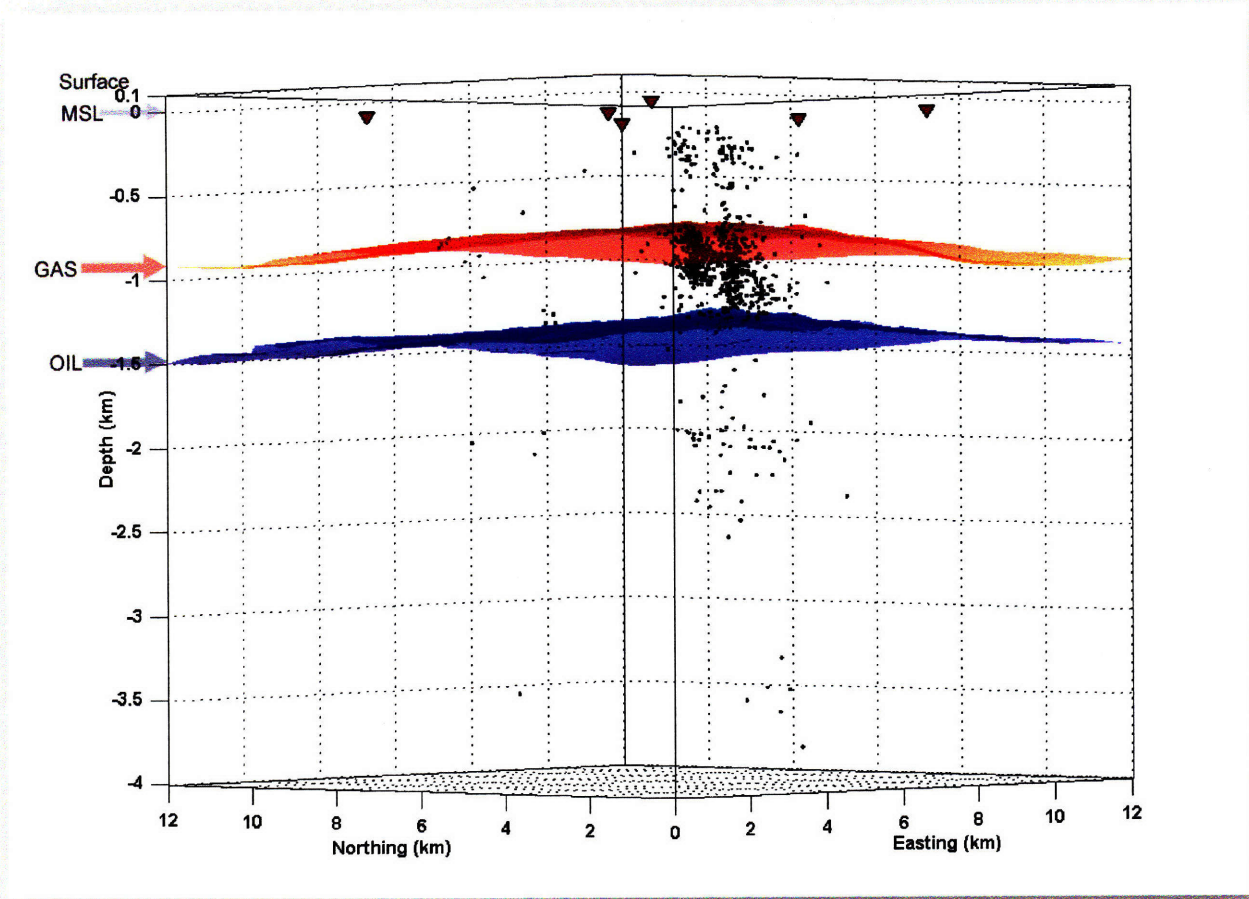
Figure 3.7: Three-dimensional perspective view of the passive seismic data (Nov 1999 – Feb 2007) plotted with black dots in 3D reservoir grid, with gas and oil tops superimposed as transparent surfaces. Dark red triangles denote station locations of the PDO seismic monitoring network. (Zero depth on this and on all other plots corresponds to the Mean Sea Level, MSL). Seismicity is caused mainly due to the compaction of the gas reservoir. Relatively few seismic events are seen in and below the oil reservoir.
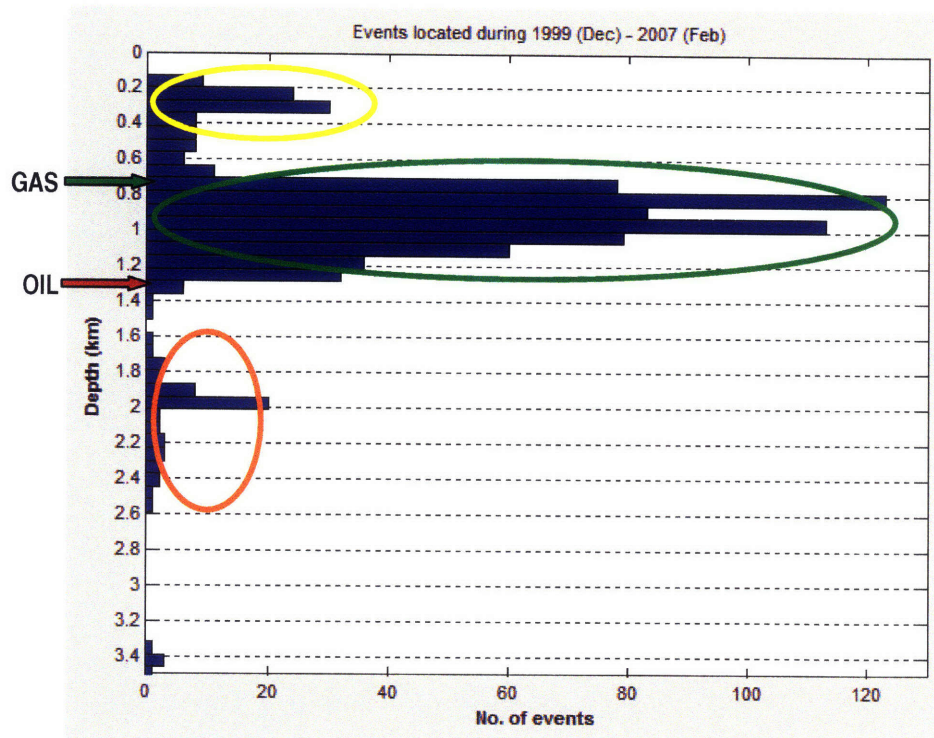
Figure 3.8: Depth distribution (histogram) of seismicity during 1999 – 2007 passive seismic monitoring. Based on their depths, events can be classified into three main clusters: i) overburden seismicity (yellow oval), ii) seismicity across the gas oil and reservoir (green oval), and iii) seismicity underneath the oil reservoir (orange oval).

The biggest and most significant cluster of induced seismicity spans from slightly above the Natih gas down to just above the underlying Shuaiba oil formation. The highest concentration of events during the 7 years of monitoring history is seen inside the Natih gas formation (named *Natih A*), near its boundary with the overburden, at about 800 m depth below the mean sea level height. The size of this cluster and the event distribution within this cluster strongly suggest that the majority of the seismicity in the field is caused by activities in the gas reservoir. Compaction of the Natih formation in response to declining reservoir pressure due to

90

extraction of gas is responsible for generating most of the tremors in the field during all these years. Quite a bit of seismicity is also seen in between the Natih and Shuaiba formation, and the trigger mechanism is most likely due to the changes in the Shuaiba. Collapse of the overburden and continuous water injection into and below Shuaiba may cause slight bulging of the oil top, thereby inducing tremors in the zone above and inside Shuaiba.

Another tiny cluster of deeper events appears on the 1999 – 2007 event depth distribution map (Figure 3.8) – below the Shuaiba oil reservoir and in between Shuaiba and another oil and gas bearing formation (at around 2800 m depth, as shown by Figure 3.1) – that is not currently in production. The most likely cause of seismicity in this region is again reactivation of faults due to percolation of water that is being injected into the Shuaiba formation. If that part continues to generate seismicity, it needs to be considered in the plans for penetrating into the formation underneath Shuaiba for future petroleum production. Therefore, it is important to continue monitoring that part of the reservoir for recurrence or any changes in induced seismicity.

3.6 Temporal Analysis of Induced Seismicity

To better understand the pattern of seismicity and to identify changes in that pattern over time, we analyze the seismicity map of the field in short time intervals. In this paper, we subdivide the seismicity data from November 1999 – February 2007 into three, approximately equal intervals (~ 1.5 – 2 years) and plot and compare their epicenter and depth distributions (Figures 3.9, 3.10 and 3.11).

It is observed from Figure 3.9 that the distribution of the epicenters (X, Y locations) during these three epochs is very similar – they remain confined in the main NE-SW fault corridor, with some clustering prominent in certain areas. We also note from the plots that the epicenters during the first epoch (1999 – 2001) are much more tightly clustered than those during the latter two epochs (2002 – 2004, and 2005 – 2007). There is indeed a bit of scattering in the field as seismicity is thought to be spreading in the region between the two major faults, perhaps activating smaller faults and fractures. However, some of the scatter in the seismicity locations may also be artificial, due to the change in station distribution from the first epoch to the rest. VA5 was removed and a new station VA6 was added to the network sometime in 2002. The "five-spot pattern" station distribution during 1999 – 2001 was actually better-suited to locate the events occurring along the NE-SW faults, compared to the station distribution during 2002 – 2007. Azimuthal coverage for the events provided by the stations, which is a very important factor for accurate event locations, was better during 1999 – 2001 with the station VA5 in the center of the network.
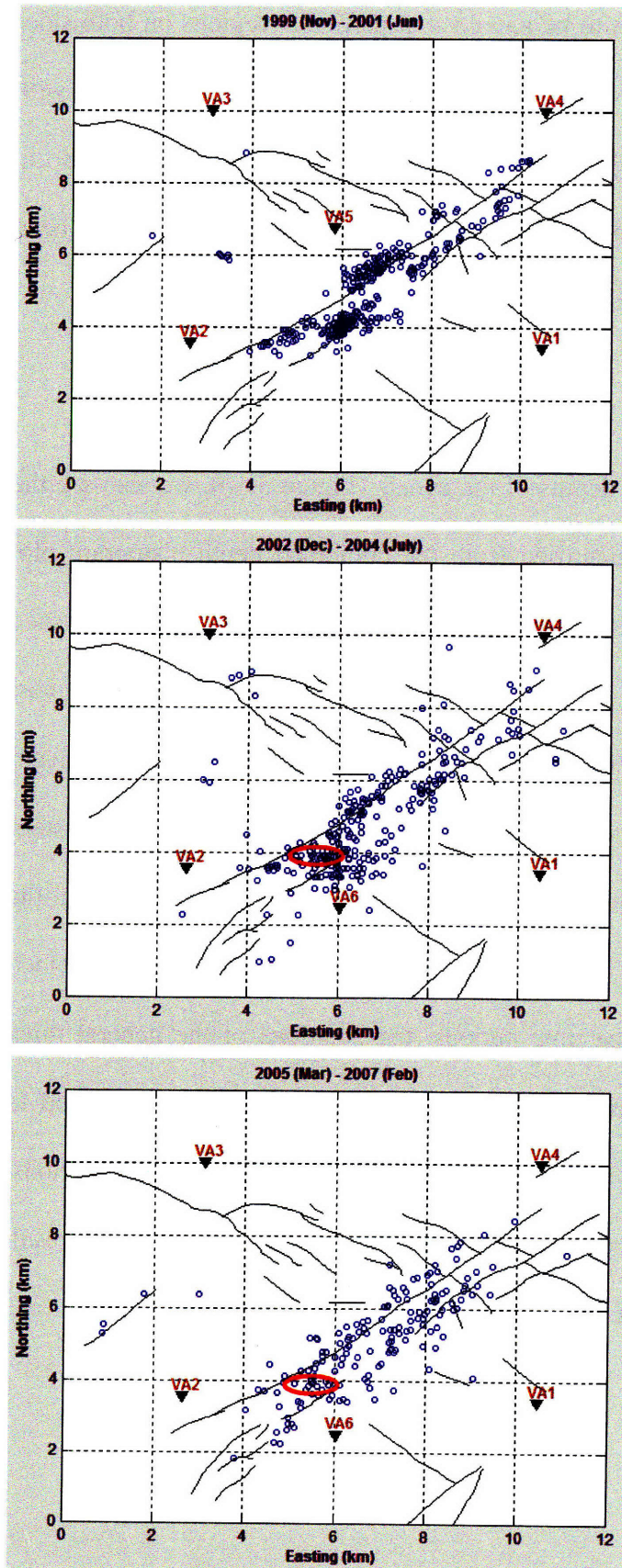
Figure 3.9: Epicenter distribution of seismicity (blue circles) during three time periods, plotted against faults (black lines) mapped by reflection seismic on Natih horizon. Events are correlated with the major faults (NE-SW) at all time periods; and they are seen to be spreading more along the fault in recent years. Also, more events are seen in between the two faults in recent years, indicating increasing faulting and fracturing in the reservoir with time. A prominent zone where seismicity seems to be bridging the gap between two faults is identified by red oval on the two plots.

93

During 1999 – 2001, seismicity seems to be localized at particular regions on both sides of the faults (Figure 3.9). The clusters, however, seem to become progressively diffused with time, as more and more events start occurring almost everywhere on the two faults and also in the space between them. This is an indication that the areal extent of fault reactivation has been gradually increasing with time in the reservoir.

As for the temporal analysis of focal depths of the events (Figure 3.10), we also see the three main depth clusters – as previously identified from the combined depth histogram plot (Figure 3.8) – persist through each time period. An interesting feature, identified by the dashed oval on Figure 3.10, appears during 2002 – 2004, and is seen to retain its position almost identically through 2005 -2007. This slightly dipping plane emerges as events continue to trigger between the northern and southern fault to connect the two fault systems on the south-western side of the fault corridor (Figure 3.9). The depth histogram plots on Figure 3.11 also reveal the presence of the three main clusters in each time period, previously noted from the combined histogram plot (Figure 3.8). Across the three time periods, the positions of the general three clusters remain same, while the peaks in each of them vary slightly from one time period to another. Also, the deepest cluster is observed to grow in size during the latter time periods, indicating persistent fault reactivation in the deeper parts of the reservoir, most likely as a result of continued water injection into the Shuaiba.
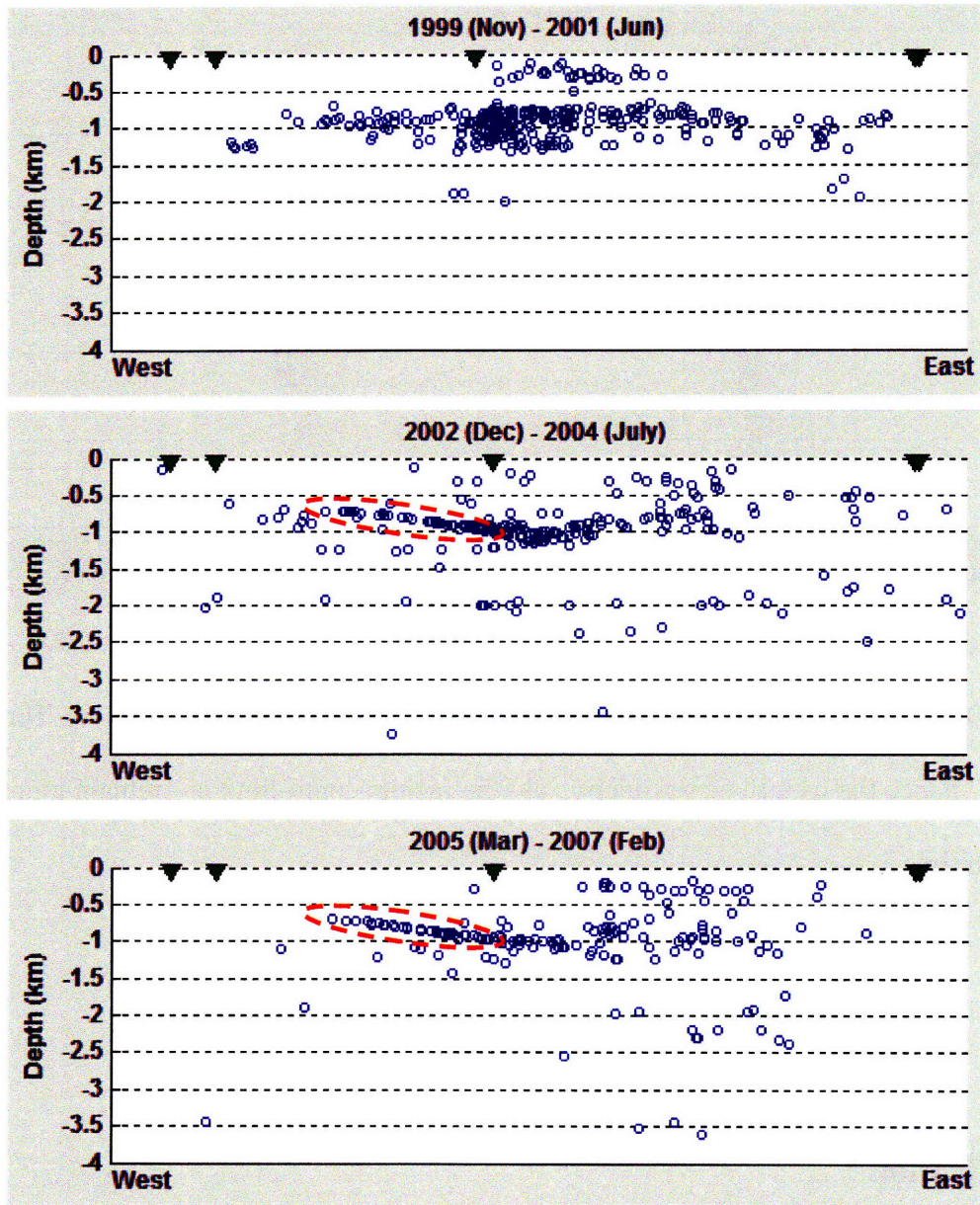
Figure 3.10: Depth locations of seismicity (blue circles), shown along an east-west vertical plane through the reservoir, in three different time periods. The West to East axes shown here are 9 km in length (from 2 to 11 km of the "Easting" axis of the actual grid). A dipping feature consistently appearing during 2002 – 2004 and during 2005 – 2007 is identified by red dashed oval.
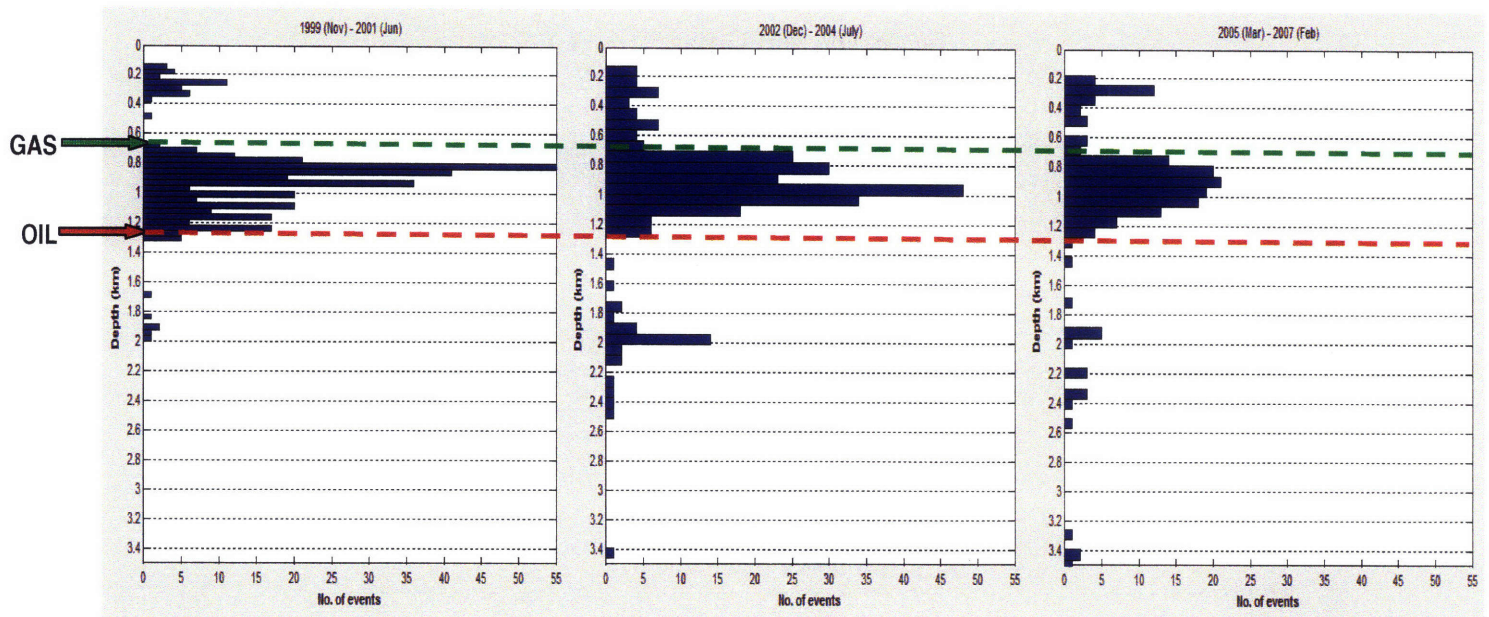
Figure 3.11: Depth distribution of seismicity with time (from left to right: 1999 – 2001, 2002 – 2004, and 2005 – 2007), shown in relation to gas and oil tops (green and red dashed lines). The main three clusters – hence the pattern of seismicity, and the factors controlling it – remain more or less the same with time.

3.7 Fault Identification

Passive seismic data can serve as a valuable tool to map faults and fractures in reservoirs. In this chapter, we use ~ 6 years of passive seismic data from the producing petroleum field to correlate with existing fault maps and also to identify previously unidentified faults. Figure 3.12 shows two cross-section plots taken from two sides of the known fault region to demonstrate how passive seismic data can be used to trace faults at depth. Events from two sides of the fault

corridor – identified by dashed ovals and labeled as *ne* and *sw* – are plotted against a vertical

plane along the line A-B (Figure 3.12). The set of events identified by the red dashed oval, *ne*, on

the north-eastern side of the dividing line A-B, shows clear separation of the two faults with

depth, and the fault can be traced all the way from near the surface/overburden to below the

Shuaiba formation. The south-western side of the divide, set *sw*, shows the 'infill' seismicity

between the two major faults, and how that connects the two faults and at which depths.
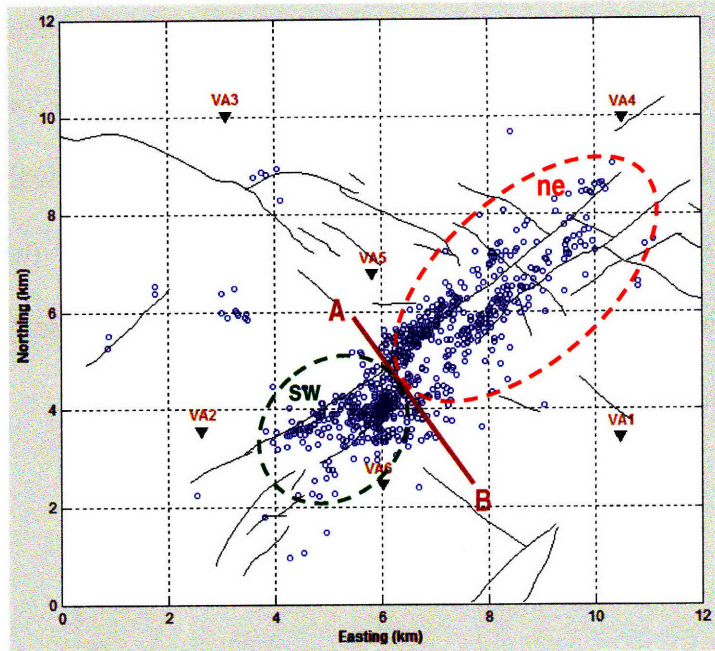
Figure 3.12: Left – A line A-B, which is nearly perpendicular to the major strike direction of the faults. Events on two sides of this line A-B are grouped as *ne* and *sw*.
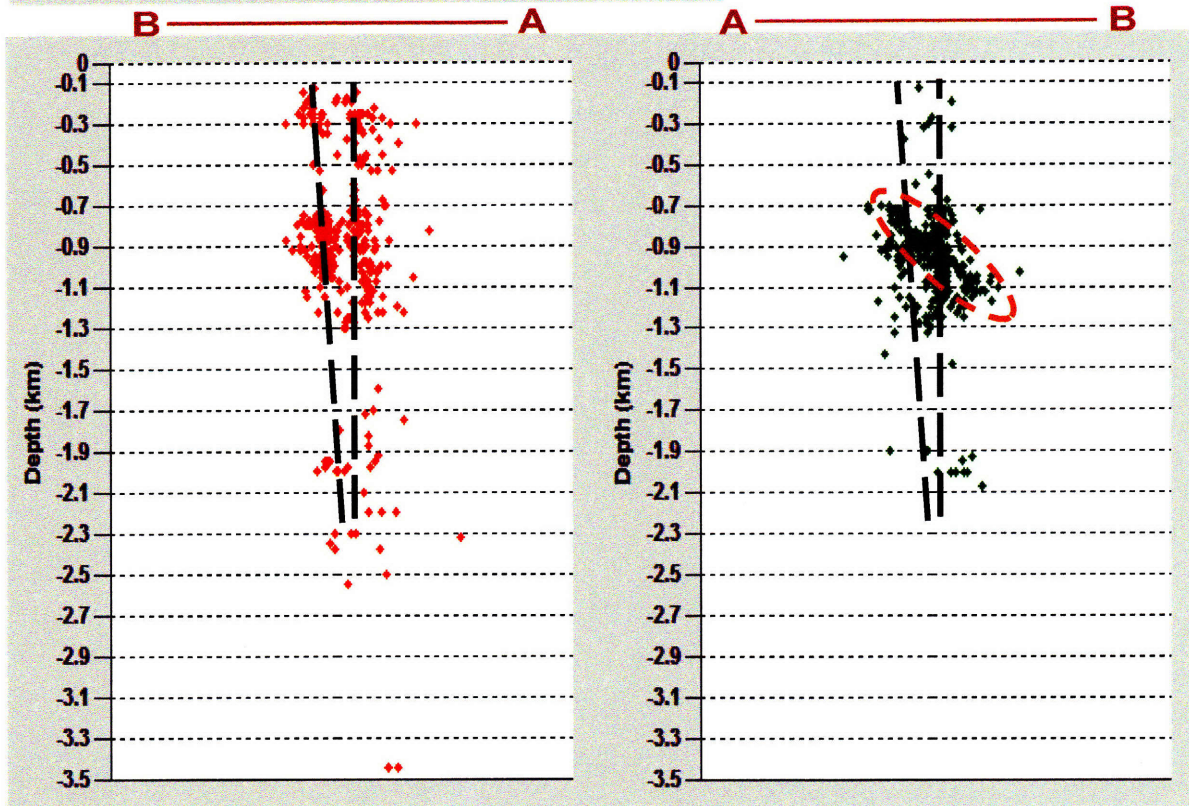
Figure 3.12 (cont'd): Depth sections shown for event groups *ne* (red) and *sw* (green). Black lines indicate trends of the events in depth along the two major faults. Orange dashed oval shows a dipping feature that connects the two major faults in the *sw* group.

3.8 Production/Injection and Correlation with Induced Seismicity

The petroleum field in discussion is a major gas producer. It produces gas from Natih, where compaction of the *Natih A* formation is a significant recovery mechanism for gas. Oil is produced from the Shuaiba reservoir below Natih, and a large amount of water is injected into the Shuaiba formation to maintain the reservoir pressure in Shuaiba. Roughly about 15-20% of the water that is injected is lost into the formation. Therefore the dominant hydraulic processes in the field are: i) gas production, ii) water injection, iii) total liquid (water + oil) production and iv) liquid (water) volume loss[3] into the formation. Seismic events occurring in the field during the last eight years have been consistently located mostly in and around the Natih (gas) formation, with a relatively small number of events falling around and below the Shuaiba (oil) formation. This observation has led to a hypothesis that seismicity in the field is mostly induced by gas production and associated compaction of the Natih reservoir. A secondary mechanism for inducing earthquakes in this field is thought to be related to water injection, as a large amount of water that is *lost* into the formation may very well be reactivating preexisting faults or zone of weaknesses and even inducing new fractures through localized pressure buildup. To test these hypotheses and to further understand what might be causing the seismicity in the field, we analyzed the available field data related to production and injection. In this section, we show comparisons between the monthly rate of seismicity (no. of events per month) and monthly totals for: i) gas production, ii) water injection, iii) total liquid (water + oil) production and iv) liquid (water) loss obtained for the whole field. First we compare the overall seismicity data with these

---

[3] liquid loss = water production + oil production − water injection

field hydraulic data, and then we compare the located event data classified by depth with relevant

hydraulic data[4].

3.8.1 Comparison of production/injection data with event data/triggers

Due to various problems during data acquisition and retrieval process, there were large

gaps in available seismic data over the entire monitoring period. Therefore, although we had

monthly field hydraulic (production/injection) data continuously from 1999 – 2006, comparisons

between rate of seismicity and hydraulic parameters were only possible for some very limited

time windows. Even during some time intervals when seismic data were available, several

days/weeks of data were found missing, making the comparisons even more difficult. In such

situations, in order to complete the monthly event tally and broaden the window of comparison,

we used "trigger" information as proxy for actual event counts. During data acquisition, trigger

data would be written on a separate part of the disk than the seismic *ringbuffer* data, and in most

cases were found to be less discontinuous than the seismic data upon retrieval. Regardless,

during pre-processing of the raw data it was seen that the triggering mechanism was not

foolproof - many triggers were found that had not been generated by actual induced seismic

events, whereas several events failed to register any trigger. During time intervals when both

seismic data and trigger information were continuous and complete, triggers could be verified

and validated by actual seismic events. During intervals when seismic data was missing or

---

[4] Only field-wide total hydraulic data were made available to us. The comparison would be more meaningful and accurate if production/injection data from different wells were available, which could then be correlated with events occurring at similar locations.

incomplete, we used trigger counts to supplement the number of missing event counts. On Figure 3.13, we show monthly event and trigger counts from 1999 – 2006. For periods where both trigger and data information were complete (continuous), we see that the number of *validated* triggers and the number of events are in good agreement with each other (Figure 3.13: blue diamond markers on the blue curve for triggers, and black square markers on the black curve for events). Figure 3.13 also depicts missing event data in three categories: a) data completely missing in a given month (shown by discontinuity of the black curve), b) data missing for at least 2 weeks in a given month (shown by red squares on the black curve) and c) data missing for about 1 – 2 weeks in a given month (shown by green circles on the black curve). For comparison with reservoir hydraulics, during the months which had incomplete seismic waveform data we used trigger[5] information (points on the blue curve, Figure 3.13) as a proxy for event count; and for the months which had complete seismic data we used the actual event count (points on the black curve, marked by black squares, Figure 3.13).

---

[5] Instances of triggers generated by at least three stations of the network were regarded as "events". In the process, however, we also made an effort to identify and exclude triggers that were not likely associated with an actual event: triggers that seemed to be have a different pattern than those validated by actual event data (waveform), triggers that had been caused by some field operations – e.g. a workover operation – generated very frequently at large numbers and/or generated during the same time of the day for several days. Therefore, the trigger information that we have used (Figure 3.13) is our best guess for the number of seismic events during periods when actual seismic data was unavailable, and must be interpreted with caution.
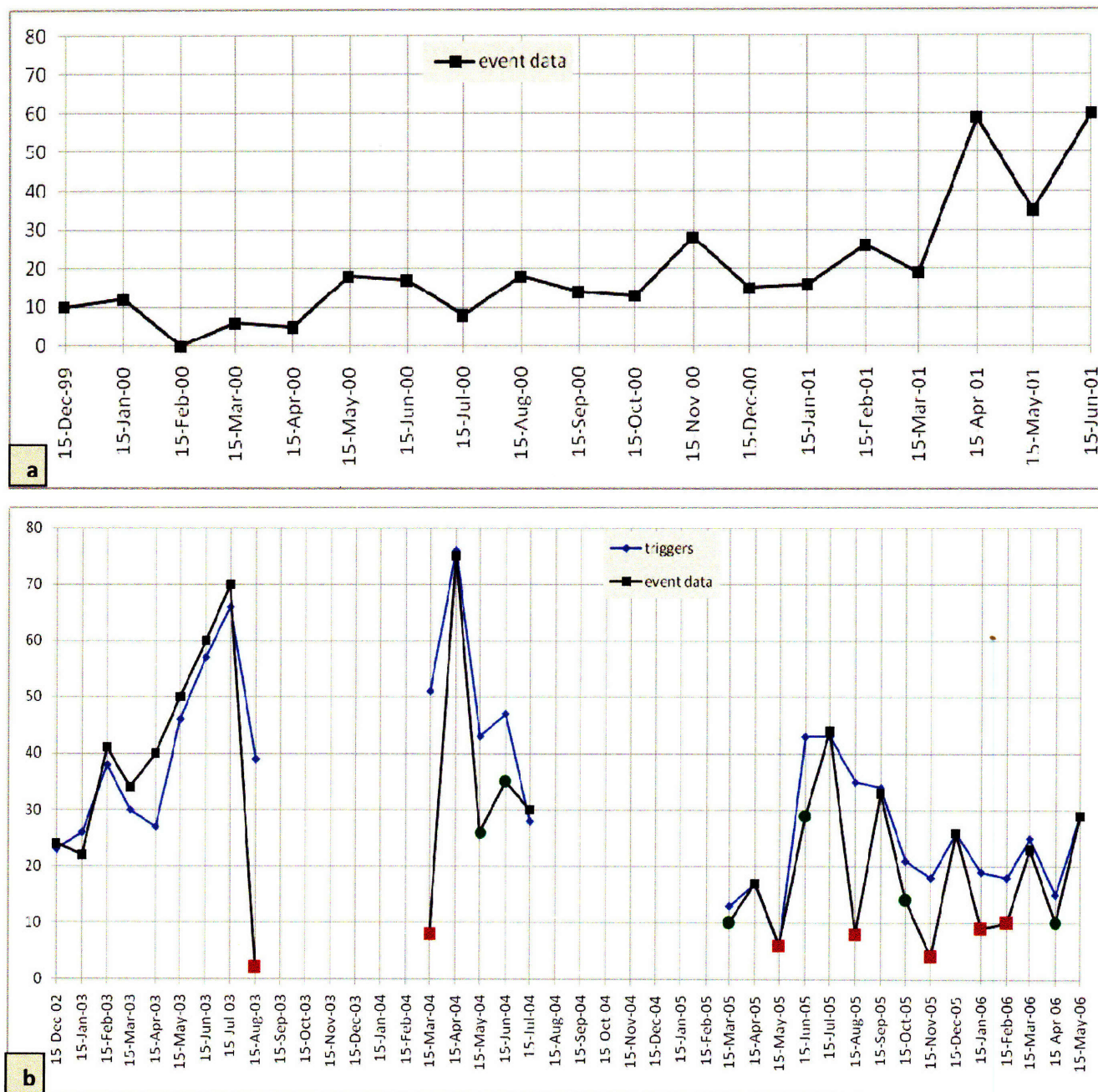
Figure 3.13: (a) - Monthly number of induced events in the field (black curve) during Dec 1999 –

June 2001. (Raw data was not processed for this period; therefore no trigger information was

available. The event counts in this period are just the number of events sent to us by PDO for

analysis.) (b) - Monthly counts for triggers (blue curve) and actual seismic events (black curve)

during Dec 2002 – May 2006. The discontinuity in black or blue curves indicates periods

(months) of missing data. On the black curve: black squares denote almost complete event data

information, green circles denote 1-2 weeks of seismic data gap, and red squares denote significant data gap, ~ greater than 2 weeks, within a month. To construct "complete" time series data within each of the three "continuous" time intervals for which data were available (Dec 02 – Aug 03, Mar 04 – Jul 04, and Mar 05 – May 06), points on the black curve with red and green markers are substituted by the blue curve for that same point.

We compare monthly gas and liquid production, water injection, and liquid loss data with the number of seismic events per month (number for events substituted/supplemented by number of triggers during periods of incomplete seismic data). We show comparisons between variables in three different time intervals by various charts on Figure 3.14[6]. It is seen from the charts that, for all three time periods, the trends between seismicity and gas production (blue and green curves) have the highest similarity. The remaining parameters – water injection, total liquid production, and water loss into the formation – seem to show some similarity with seismicity in their trends at certain months; however those similarities can at best be described as "patchy". Unlike the monthly gas production, which shows an overall good correlation with the monthly event rate during all three intervals, these injection and liquid production related reservoir mechanisms exhibit only sporadic similarity with trends in induced seismicity in the field, suggesting that there is very little overall correlation between these and induced seismicity. Since

---

[6]On each chart, the scale on the right side of the vertical axis pertains to actual numbers of events. Values for the hydraulic data (prod/inj/loss) data axes are not shown – on each chart they have to be interpreted in a relative sense, with values increasing from bottom to top along the vertical axis.

The horizontal axis shows months: data reported at the 15th of a month covers one month of data starting from the 15th of the preceding month. Therefore, for example, monthly data that is shown for May 2000 is actually data that pertains to the period from April 15, 2000 – May 15, 2000.

103

more than one hydraulic activity is most likely working in tandem to induce seismic events in the field, seismicity at certain times and at certain depths may be more related to one activity than another; hence some of the local variations, aberrations and anomalies in the seismicity time series pattern can be better explained by one type of hydraulic data than the others.
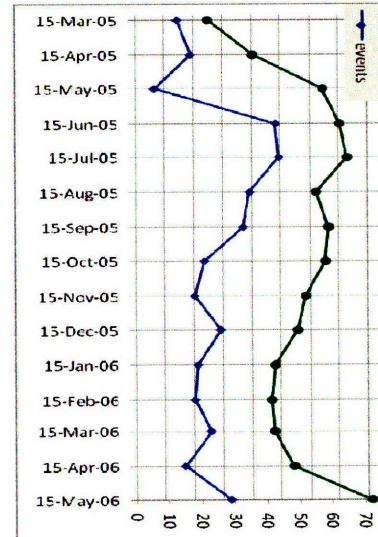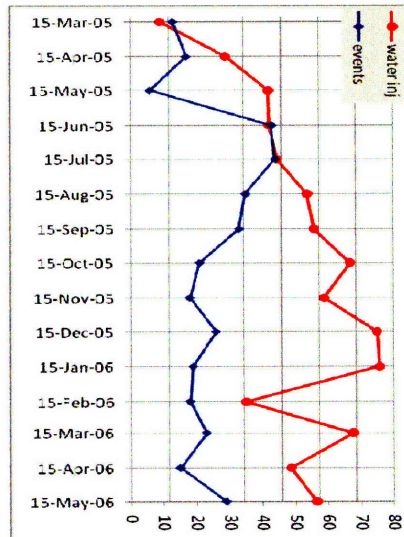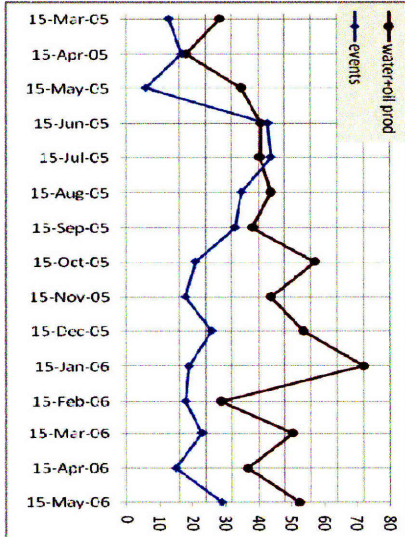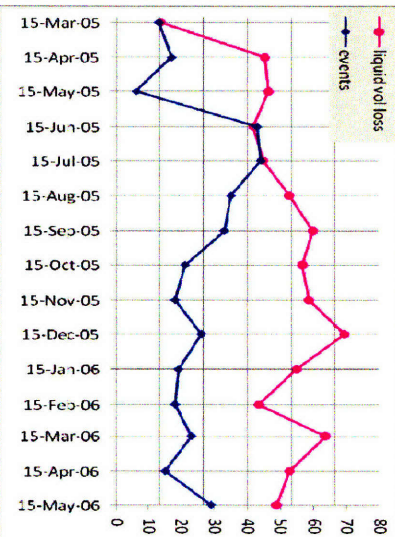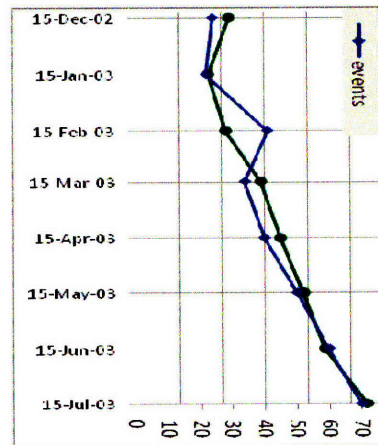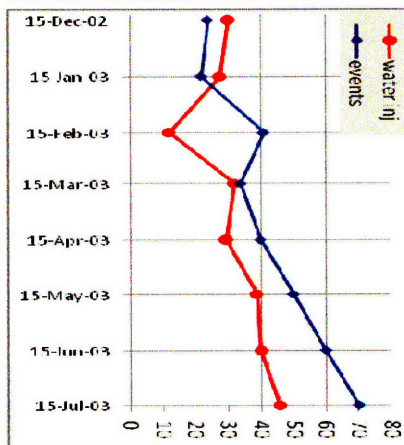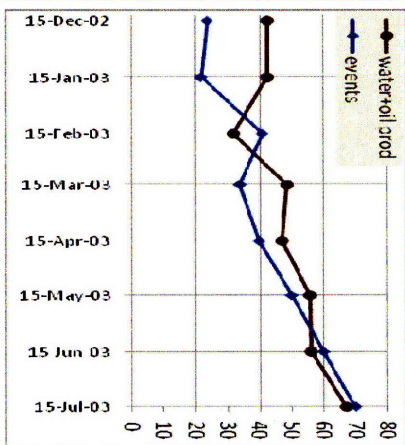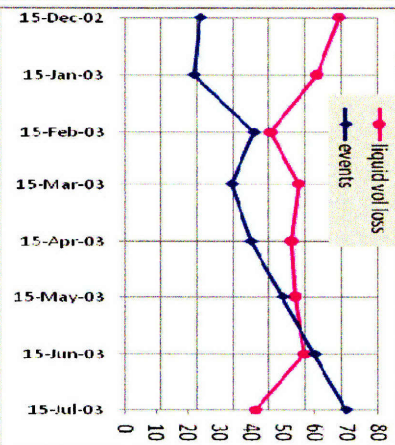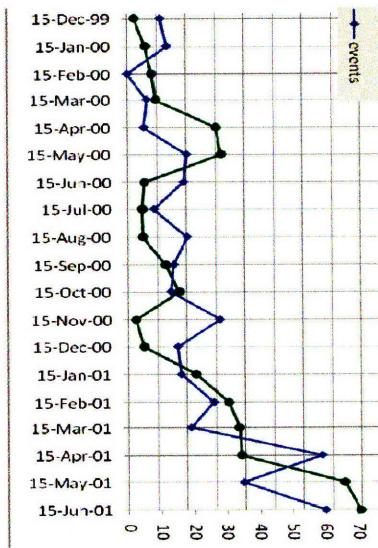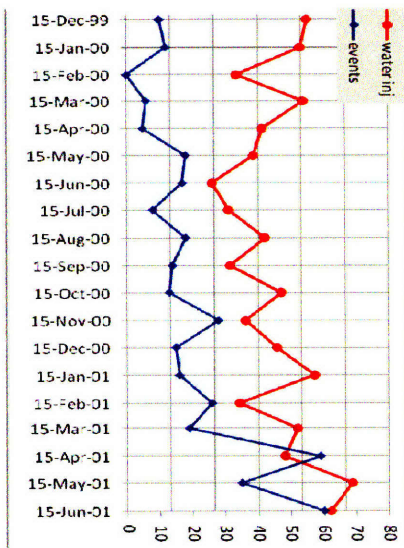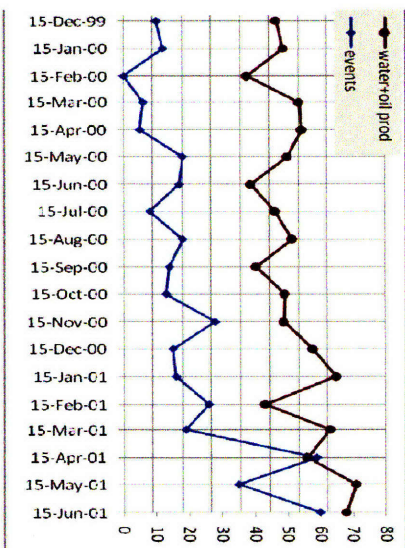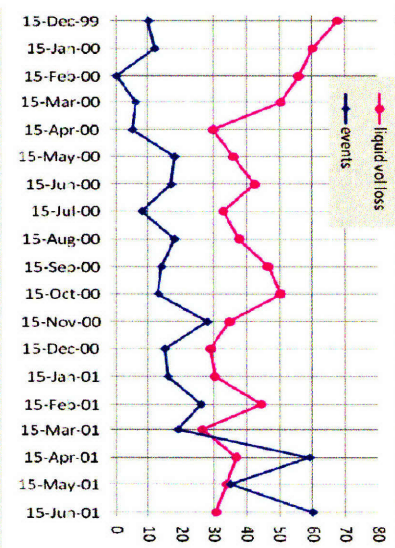
(green curve), water injection (red curve), cumulative liquid production (brown curve) and water loss (magenta curve), in three different time intervals. Each chart shows comparison between number of induced seismic events and one of the four major reservoir hydraulic parameters. Comparison charts for the same pairs of variables, but for different time intervals, are plotted along rows, whereas comparison charts between different pairs during the same time interval are shown in columns. Horizontal axes show time in months (Dec '99 – Jun '01 for the figures in the left, Dec '02 – Jul '03 for the figures in the middle, and Mar '05 – May '06 for the figures in the right). Labels on the right side of the vertical axis in each chart show event counts[7].

For a more quantitative analysis of the correlation between induced seismicity and each of the production/injection quantities shown by Figure 3.14, we resorted to q simple cross-correlation technique. We computed correlation-coefficients of monthly seismicity data and monthly data of: a) gas production, b) water injection, c) liquid production and d) liquid volume loss at different lags. These variables were cross-correlated during two different time periods: Dec 99 – Jun 01, and Mar 05 – May 06. (The other period, Dec 02 – Jul 03, for which

---

[7] During 2005 – 2006, we see a significant drop in the number of events, compared to previous years' levels. This drop may not be real, as we have also observed a gradual degradation in network performances and data acquisition during that period. The performance of the seismic monitoring network during that period was aggravated due to various factors such as sensor malfunction, changes in detection threshold, human negligence, etc. All these network/instrument issues *may* have led to poor recovery of the actual trigger and seismic data from the acquisition module, therefore the apparent drop in seismicity that we see during that time period could be *spurious*. It is therefore, important to process and analyze seismic data thereafter – for an extended period of time – to have a better understanding of that apparent "drop" in monthly seismicity rate.

106

comparison charts are shown by Figure 3.14, is too short to produce any meaningful cross-correlation results). The cross-correlation results (correlation coefficients at different lags) are shown by Figures 3.15a and 3.15b. It is seen from Figures 3.15a and 3.15b that during each time interval the correlation coefficient between gas production and seismicity at zero lag is the highest compared to that between other pairs. The cross-correlation results show strongest correlation between gas production and seismicity (green curves, Figure 3.15a), and very little to almost no meaningful correlation between seismicity and water injection (red curves, Figure 3.15a), seismicity and cumulative liquid (water + oil) production (brown curves, Figure 3.15b) and seismicity and water loss into the formation (magenta curves, Figure 3.15b). During December 1999 – June 2001, the correlation between gas production and seismicity is clearly distinguishable from other correlations in the same period by its sharp correlation peak at zero lag. The seismicity time series data constructed for March 2005 – May 2006 is supplemented with large amounts of trigger data (due to frequent data gaps, as seen by red squares and green circles on Figure 3.13), and hence is noisy. This may have contributed to the diminished correlation coefficient for gas production and seismicity (green curve at the bottom-left, Figure 3.15a) during that period. Nevertheless, in a relative sense, indeed, among all hydraulic parameters, gas production yields the highest correlation with seismicity during that period. Therefore, analyses of the trends and patterns (Figure 3.14) and a more quantitative cross-correlation analysis (Figures 3.15a and 3.15b) reveal that in each of these two intervals – nearly 4 years apart - gas production is strongly correlated with induced seismicity and is likely to be the predominant mechanism in inducing seismicity in the reservoir.

107
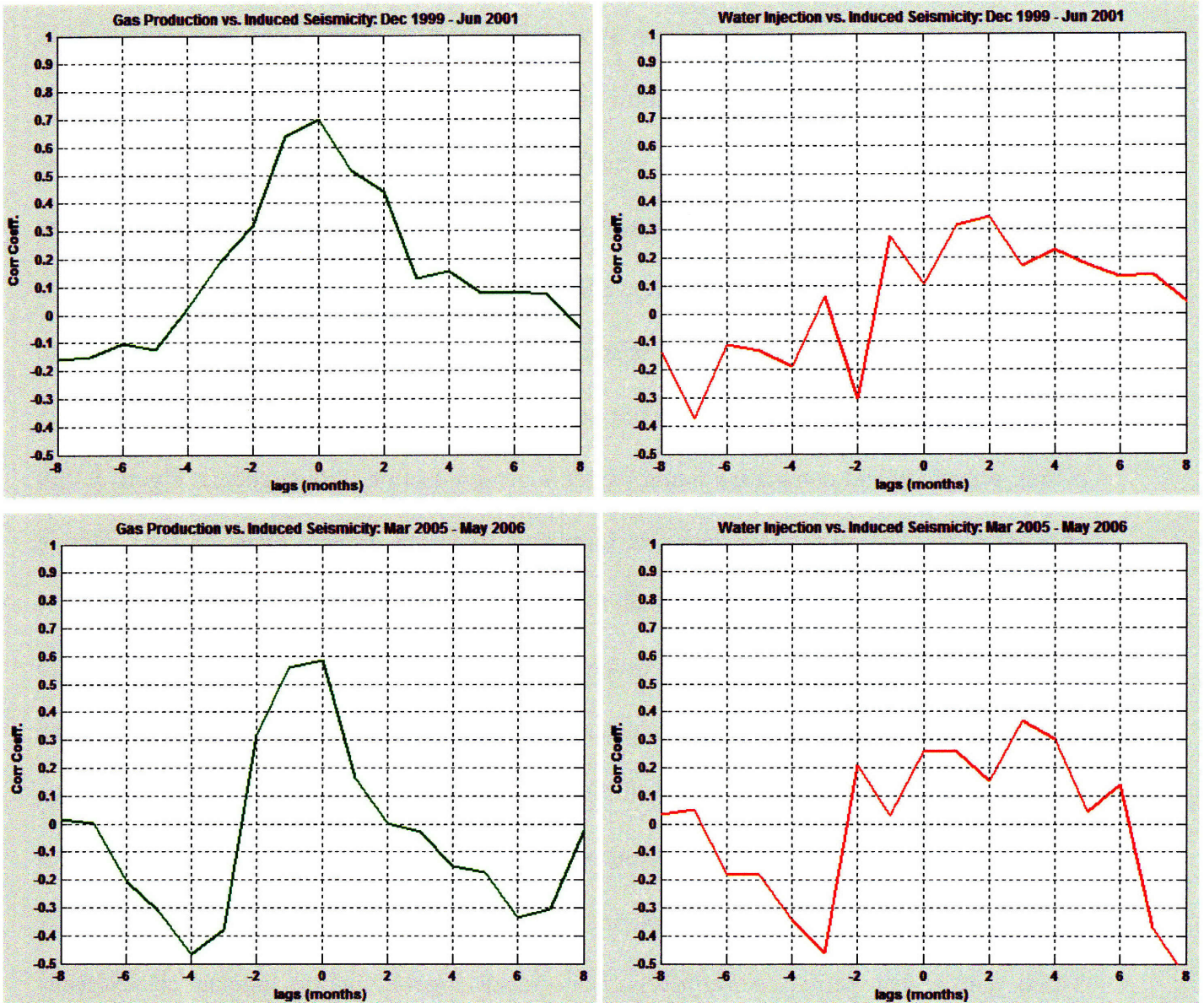
Figure 3.15a: Cross-correlation results (correlation coefficient vs. lag) for seismicity and gas production (left), and for seismicity and water injection (right), computed for two different time intervals: Dec '99 – June '01 (top row), and Mar '05 – May '06 (bottom row).
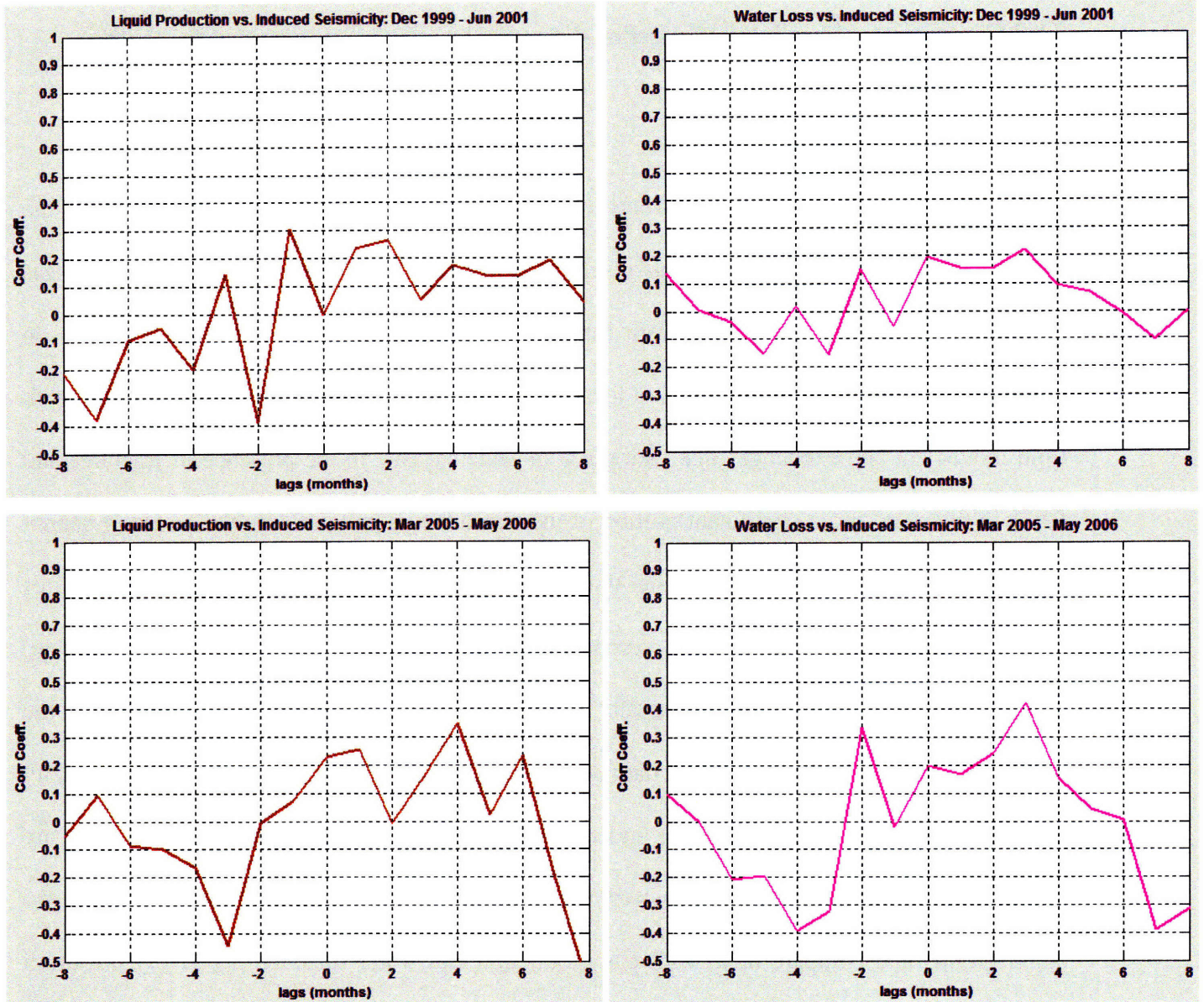
Figure 3.15b: Cross-correlation results (correlation coefficient vs. lag) for seismicity and cumulative oil and water production (left), and for seismicity and water loss (right), computed for two different time intervals: Dec '99 – June '01 (top row), and Mar '05 – May '06 (bottom row).

3.8.2 Comparison of production/injection data with located events grouped by depths

Among the induced seismic events located during the last eight years, the majority of the events have been located near the gas reservoir, and cross-correlation with all data shows gas production as the dominant mechanism for inducing seismicity in the field (green curves on Figure 3.15a). However, events that are located in and around Shuaiba could be correlated with fluid movement and exchanges that take place in Shuaiba. Due to the presence of fractures and faults in the reservoir, a significant portion of the water that is pumped into the reservoir cannot be recovered. The large volume of water thus *lost* into the formation, is likely to induce fractures and hence seismicity in the reservoir – especially in the Nahr-Umr formation (shaly overburden) above Shuaiba, and also in the Kharaib formation below Shuaiba. Therefore, some of the similarity observed in the time series data between water loss or injection pattern and seismicity may be meaningful. In order to better understand how events within different depth sections are related with the reservoir hydraulic activity at or near that depth, we divide the events into two depth groups and compare them with gas production and water injection separately. From all located events, we construct two groups of seismicity time series data: a) events located shallower than 1 km and b) events located deeper than 1 km. Events that are shallower than 1 km are compared with gas production data; and events that are deeper than 1 km are compared with water injection data. We show charts of the time series data[8] by charts on Figures 3.16. From these rate comparison charts, located events seem to be well correlated with gas production for most time periods, whereas their correlation with water injection seems to be limited to selected

---

[8] Time series of located events consists of monthly (from 15th to 15th) event data. This series does not contain the same number of events as in the previously used event/trigger series (Figures 3.13), because only a fraction of the events, for which trigger information had been recorded and/or actual seismic data was available, could be located. Therefore, the data presented in this section are a small subset of actual events that had occurred in the field.

short intervals only, e.g. similar trends during January – March 2000, July – September 2000, October – December 2005, etc. To analyze their relationship in a more quantitative manner, we perform cross-correlations between the curves shown by Figures 3.16, except for the two time series of January – July, 2003 and March – July, 2004, as these intervals are too short to produce any meaningful cross-correlation results. The results of cross-correlations for the longer two time intervals (Dec 1999 – June 2001, and March 2005 – May 2006) are given by Figure 3.17.
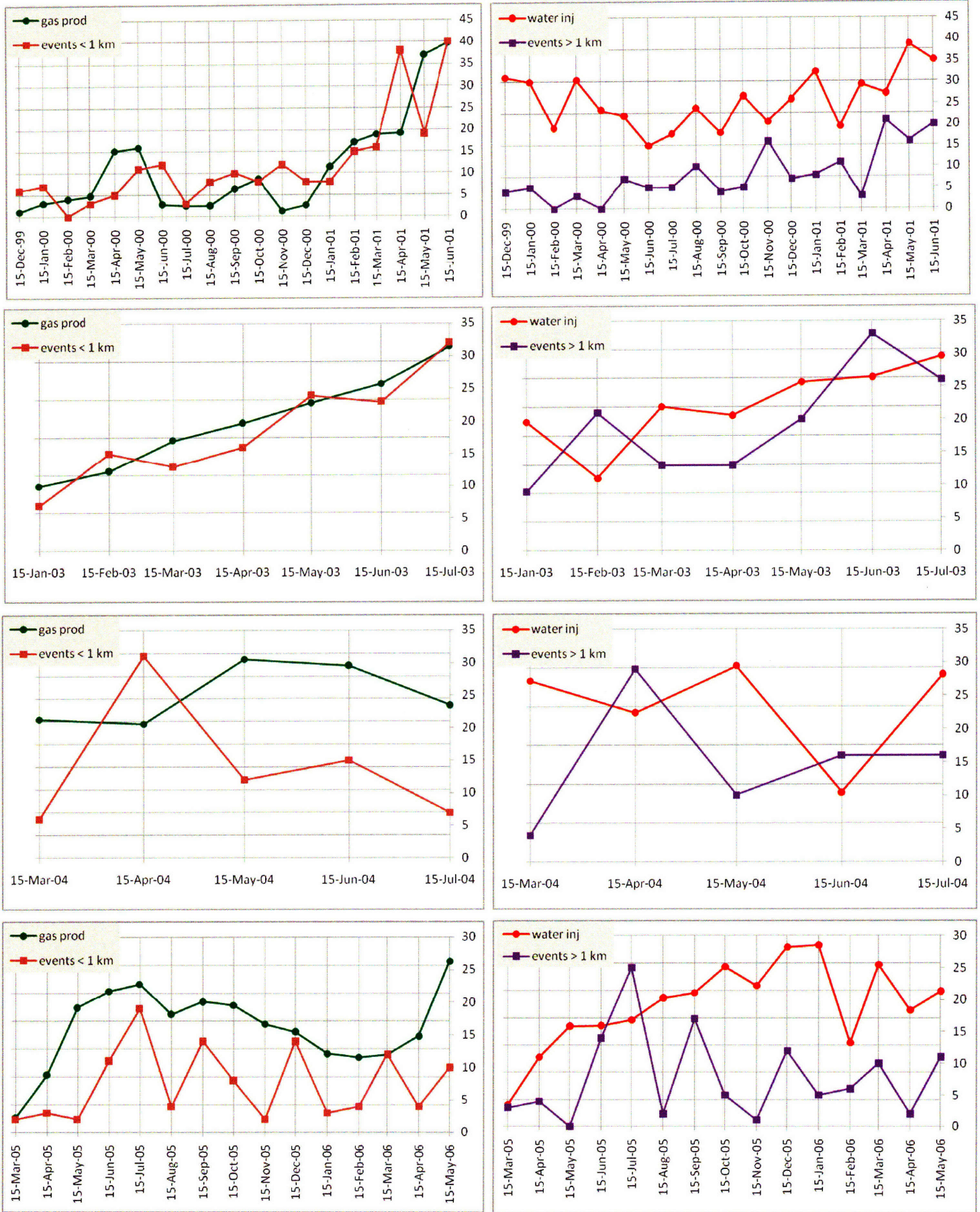
Figure 3.16: Time series charts for located seismic events separated into two depth groups (<1

km on the left, >1 km on the right), compared with gas production (green curve) and water injection (red curve), shown for different time intervals (in rows).
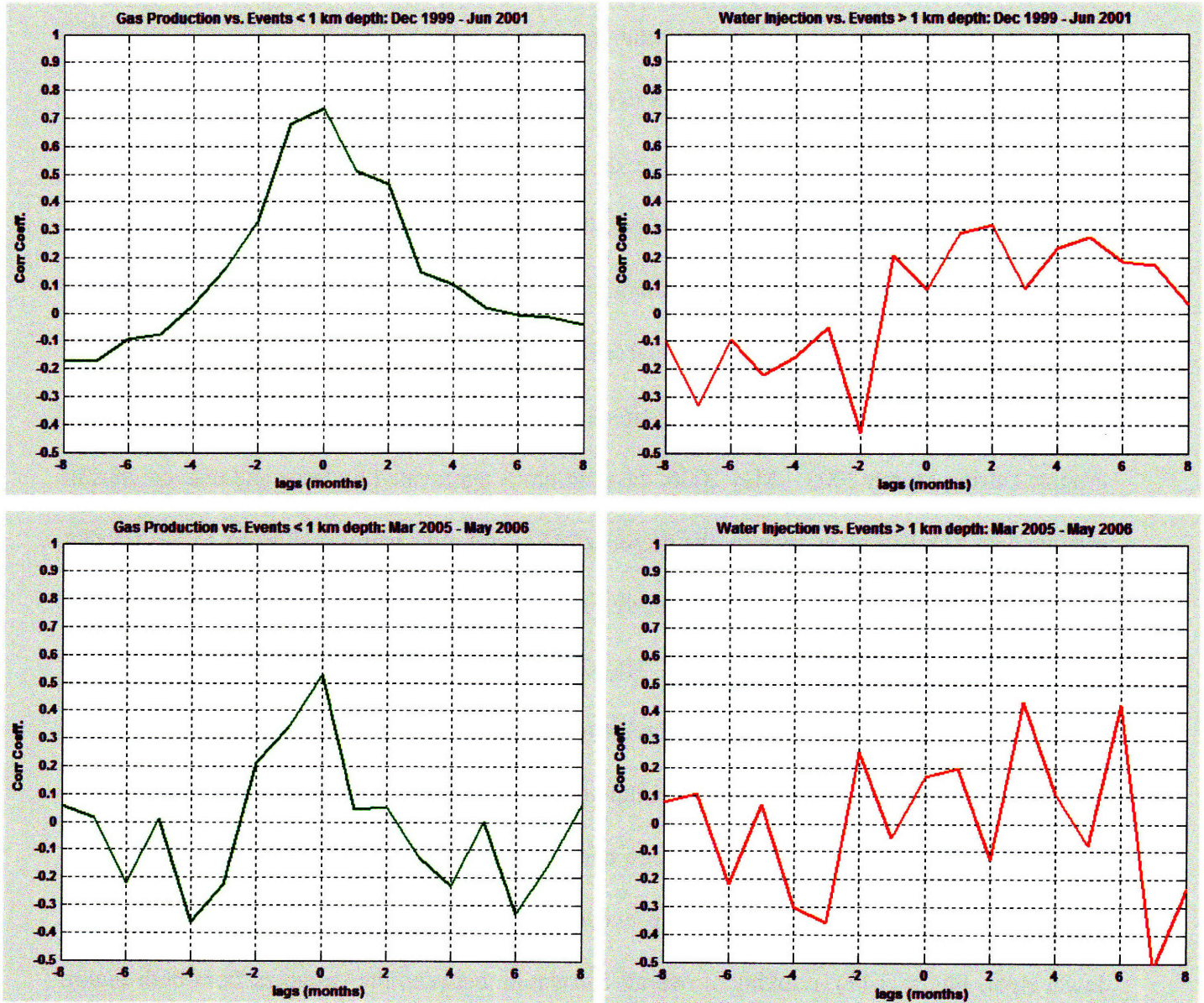
Figure 3.17: Cross-correlation results (correlation coefficient vs. lag) for no. of events shallower than 1 km and gas production (left), and for no. of events deeper than 1 km and water injection (right), computed for two different time intervals: Dec '99 – June '01 (top row), and Mar '05 – May '06 (bottom row).

As seen from Figure 3.17, during both time periods, gas production is well correlated with events at depths above 1 km (green curves, top and bottom). It is also observed that water injection is *not* well correlated with events at depths below 1 km (red curves, top and bottom, Figure 3.17). Even though some correlations can be observed between water injection and seismicity at depths below 1 km from the time series plots of Figure 3.16, they are quite localized and the correlations between the two do not seem to hold for the entire period of data compared. The cross-correlations, therefore, do not yield a high correlation coefficient for water injection for the overall period. It is also possible that some of the events have uncertainty in their depth locations, hence the poor correlation with water injection. Moreover, due to difficulty in phase data picks only a subset of events from the retrieved events were locatable, which might have contributed to the uncertainty of estimated number of "actual" events in the two depth groups. During March 2005 – May 2006, the problem is aggravated by large and uneven gaps in seismic data acquisition, as seen by the presence of several red squares and green circles for that period on Figure 3.13. The lower magnitude of correlation-coefficient between gas production and shallow events during March 2005 – May 2006 than that obtained during Dec 1999 – June 2001 is possibly due to uncertainty in the estimation of actual number of events in that depth group occurring during that period. In a relative sense, however, correlation-coefficient for gas vs. shallow events during that period (green curve, lower left, Figure 3.17) is much higher than correlation-coefficient for water vs. deep events obtained during the same period (red curve, lower right, Figure 3.17). Looking at overall correlation between the variables from both Figure 3.16 and Figure 3.17, it can be concluded that seismicity in the field is more correlated with gas production than water injection.

From all of the above time series comparisons and cross-correlations, for both overall seismicity and seismicity grouped by event depths, two major conclusions can be drawn:

a) Seismicity is strongly correlated with gas production over the passive seismic monitoring history of the field.

b) Seismicity, at best, is correlated with water injection in local patches during certain times; however longer term correlations between seismicity and water injection (or liquid production, or liquid loss for that matter) are likely to be absent.

3.9 Subsidence and Correlation with Induced Seismicity

In 1999, total surface subsidence detected over the center of the field since the start of oil

and gas production was reported to be 50 cm (van Driel *et al.*, 2000). Since then, surface

subsidence in the field has been monitored by annual precise leveling surveys. Maximum

subsiding rates of up to 6 cm/year have been observed and the results are confirmed by analysis

of Interferometric Synthetic Aperture Radar (InSAR) data (Bosman *et al.*, 2001). GPS

measurements of the deformation in the field have been conducted since 2003. The results from

leveling, InSAR, and GPS data have been consistent during the overlapping time periods, and are

being used for monitoring subsidence in the field. Surface subsidence in the field is primarily

caused by the compaction of Natih. Compaction of Shuaiba, resulting from oil production,

should be very small because the reservoir pressure has been maintained by water injection.

Horizontal displacements associated with vertical subsidence have been known to cause damage

to well casings in the producing fields (Maury *et al.*, 1992). If the reservoir (Natih) continues to

compact at this rate, it will lead to many problems such as leakage of the connectors of well

casings or loss of well access due to buckling and bending. The objective of the surface

subsidence monitoring in the field is to acquire information about the magnitude and spatial

variations of the compaction of Natih. In this chapter, we show seven years (1999 – 2006) of

leveling data and compare them with passive seismic data acquired during that time period.

From yearly leveling data we derived differential vertical displacement of the ground

between 1999 and 2006, which we show by Figure 3.18. The induced seismicity in the top ~1 km

116

of the reservoir is superimposed on Figure 3.18. The prominent feature on the vertical subsidence map is the subsidence bowl in the center of the field – bounded by the graben fault on one side, subsiding at a greater rate than the surrounding, with maximum vertical displacement measured ~35 cm in 7 years (from 1999 to 2006). The fault-bounding graben acts as a barrier with more gas extracted from the reservoir to the northwest of this structure than to the southeast. This explains the shape of the subsidence bowl. The gas column height is known to change abruptly across the fault, where we also see an abrupt change in the amount of subsidence. Vertical displacement in the field is known to be directly correlated with the compaction of Natih in response to gas production; therefore, a subsidence map such as the one shown by Figure 3.18 is a good way to monitor and characterize the magnitude and spatial variation of Natih compaction between two time periods. Seismic events are also seen to occur along subsidence discontinuities, providing evidence to explain the fault reactivation mechanism; the uniform depletion of the Natih gas reservoir in the presence of discontinuous changes in reservoir thickness across pre-existing fault structures is primarily inducing fault reactivation (and seismicity) in the field.
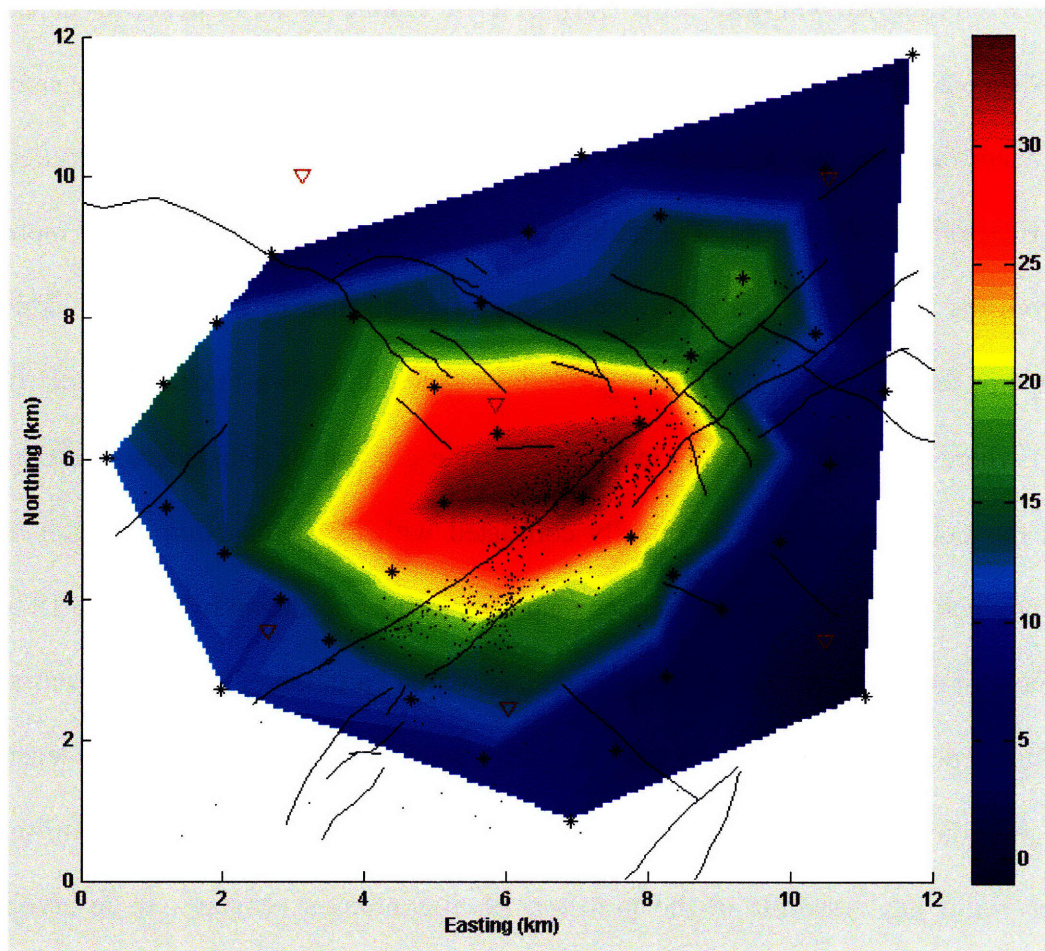
Figure 3.18: Total vertical displacement of the surface between years 1999 – 2006, estimated from leveling measurements. The colorbar shows magnitude of vertical displacement in cm. The colors shown on the map are derived by interpolation from leveling data obtained at station locations marked by black asterisks. Black dots show seismicity in the field in the top 1 km of the reservoir during 1999 - 2006. Black lines show preexisting faults mapped at Natih. Triangles in dark red denote near-surface stations for monitoring seismicity.

3.10 Discussions and Conclusions

The major goals of this chapter were to analyze the passive seismic data obtained from a petroleum field in Oman and to interpret that seismicity in relation to the reservoir structure and dynamics over an extended period of time. We used the methods and location algorithms described in Chapter 2 to locate the induced seismic events from the field. Improvements were made in the velocity model used by a previous study on induced seismicity location at this field. With our more accurate velocity model, relocation of ~ 400 events from the previous study yielded better depth estimates for those events. We preprocessed raw field data for 2002 – 2007 for the ongoing monitoring study, used semi-automated techniques to identify induced seismic events from continuously recorded seismic data, manually picked the arrival times, and completed locations of ~ 900 events from this period. Reservoir monitoring during this period suffered significantly due to degradation of network performance leading to a gradual drop in event detectability and locatability. Some of the network performance issues are highlighted by Appendix B.

The locations of ~1300 events spanning approximately 6 years revealed interesting details about the field. Some of the major conclusions from interpretation of induced seismicity data are as follows:

- The general pattern of induced seismicity has not changed much over the years – it remains concentrated in the same general area, along the two major faults.

- The biggest concentration of seismicity has been observed in and around the gas formation (Natih A), leading to a hypothesis that compaction of Natih due to gas production is the leading cause of induced seismicity in the field. Comparison of monthly event rate with gas production data from the field also supports this hypothesis, as it shows strong correlation between the two processes.

- Some of the seismicity in the field may also be induced by water injection in and around the oil formation (Shuaiba), but the effect is less significant than gas production as suggested by relatively fewer numbers of events around Shuaiba. Comparison and cross-correlation between seismicity and water injection data shows very weak correlation between the two processes.

- Large scale reactivation of faults has been observed in the field throughout the monitoring period. The reactivation is thought to have spread in the overburden – to depths as shallow as ~ 400 meters below the surface.

- In recent years, there have been indications of increasing seismicity in the Kharaib formation below Shuaiba. These are not only important because through reactivation of faults and/or creating new fractures, these might be providing fluid migration pathways between Shuaiba and the deeper Khuff formation, but also this seismicity could be a threat to well integrity if in the future Khuff is penetrated for production.

- In the south-western side of the major fault system, there has been an increase in seismicity in between the two faults in the recent years, and the distribution of seismicity data show strong evidences of new features developing in that zone.

3.11 References

Anant, K. S. and F. U. Dowla (1997). "Wavelet transform methods for phase identification in three-component seismograms", *Bull. Seism. Soc. Am.*, 87, 1598 – 1612.

Baer, M., and U. Kradolfer (1987). "An automatic phase picker for local and teleseismic events", *Bulletin of the Seismological Society of America*, 77, no. 4, 1437–1445.

Bai, C.-Y., and B. L. N. Kennett (2000). "Automatic phase-detection and identification by full use of a single three-component broadband seismogram", *Bulletin of the Seismological Society of America*, 90, no. 1, 187–198.

Blaskovich, F. T., S .S. Thurber, D. P. Echois, and K. B. M. Al-Hinai, (1985). "Reservoir Management of the Yibal Field in North Oman: A Simulation Approach", *Middle East Oil Technical Conference and Exhibition*, 11-14 March, Bahrain.

Bosman, G., R. Hanssen, and M. Tuttle, (2001). "Advances in deformation measurements from spaceborne radar interferometry", *Shell EPNL*, 7025, 34 – 36.

Bouchon, M., (1981), A Simple Method to Calculate Green's Functions in Elastic Layered Media, *Bull. Seismol. Soc. Am.* 71, 959–971.

Cichowicz, A., (1993). "An automatic S-phase picker", *Bulletin of the Seismological Society of America*, 83, no. 1, 180–189.

Earle, P. S., and P. M. Shearer (1994). "Characterization of global seismograms using an automatic-picking algorithm", *Bulletin of the Seismological Society of America*, 84, no. 2, 366 – 376.

Jepsen, D. C. and B. L. N. Kennett, (1990). "Three-component analysis of regional seismograms", *Bull. Seismol. Soc. Am.*, 80, 2032 – 2052.

Jurkevics, A., (1988). "Polarization analysis of three-component array data", *Bull. Seismol. Soc. Am.*, 78, 1725 – 1743.

Maury, V. M. R., J. R. Grasso, and G. Wittlinger, (1992). "Monitoring of subsidence and induced seismicity in the Larq gas field: The consequences on gas production and field operation", *Engineering Geology*, 32, 123.

Muller, G., (1985), The Reflectivity Method: A Tutorial, *J. Geophys.* 58, 153–174.

Phillips, W. S., (2000). "Precise microearthquake locations and fluid flow in the geothermal reservoir at Soultz-ous-Forets, France", *Bull. Seismol. Soc. Am.*, 90, 212-228.

Ruud, B. O., E. S. Husebye, S. F. Ingate, and A. Christoffersson, (1988). "Event location at any distance using seismic data from a single, three-component station", *Bull. Seismol. Soc. Am.*, 78, 308 – 325.

Rutledge, J. T., W. S. Phillips, and B. K. Schuessler, (1998a). "Reservoir characterization using oil-production induced microseismicity, Clinton County, Kentucky", *Tectonophysics*, 289, 129-152.

Sarkar, S. and M. N. Toksoz, (2008). "Location of and Monitoring with Induced Earthquakes in Oil and Gas Fields", 70th EAGE Conference & Exhibition incorporating SPE EUROPEC 2008.

Sze, E. K-M., (2005). "Induced seismicity analysis for reservoir characterization at a petroleum field in Oman", *PhD Thesis*, Massachusetts Institute of Technology.

van Driel, W. D., C. Hart, B. Lehr, and J. Coremans, (2000). "Reservoir compaction, surface subsidence and fault slip in the Yibal field, Oman", *Netherlands Organisation for Applied Scientific Research*.

Zhang, H., C. Thurber, and C. Rowe, (2003). "Automatic p-wave arrival detection and picking with multiscale wavelet analysis for single-component recordings", *Bulletin of the Seismological Society of America*, 93, no. 5, 1904 – 1912.

Chapter 4

Passive Seismic Monitoring with Deep-Borehole Network Data

4.1 Introduction

This chapter shows a study of induced seismicity in reservoir monitoring and structure identification using a data set obtained from a deep-borehole network in the petroleum field in Oman. The network was installed for a passive seismic monitoring trial in the field undertaken by PDO in collaboration with ABB Offshore Systems and Shell E&P Technology and Research. The overall project objective was to acquire a large data set of production induced microseismic activity and investigate how this data could be used to monitor the movement of fluids, map changes in reservoir stresses due to pressure fluctuations and thus assist in the reservoir management decision making process (Jones et al., 2004). Several thousands of microseismic events had been detected during the lifecycle of the network (February 2002 – August 2003). We had received microseismic event data from Phase 2 of this project (October 2002 – August 2003). In this chapter we show locations of about 35% of that data and their use in identification of faults and fractures. A detailed analysis of locations of these events and their correlation with existing faults were performed, demonstrating the value of this technology and promises that it holds for reservoir monitoring and characterization.

4.2 Data Acquisition and Processing

A deep-borehole seismic network to monitor induced seismicity in the field was installed on February 2002. The network consisted of five monitoring wells, with each well containing a down-hole geophone array, consisting of 8 sensors, distributed across ~ 650 – 1200 m depth (relative to the Mean Sea Level datum) interval spanning the overburden (Fiqa) shale, the gas reservoir zone (Natih), and the oil-overburden shale (Nahr-Umr), almost touching the top of the oil reservoir (Shuaiba) (Figure 4.1). Each sensor level is comprised of four identical sensors (geophones or MEMS accelerometers) arranged in a patented *tetrahedral* configuration (Jones and Asanuma, 2004), instead of the more conventional orthogonal three geophone arrangement. The tetrahedral geophone arrangement provided data redundancy and allowed for performance checking of the system during its operational life (Jones *et al.*, 2004). The network was operational during February 2002 – August 2003, providing about 18 months of microseismic monitoring data from the field.
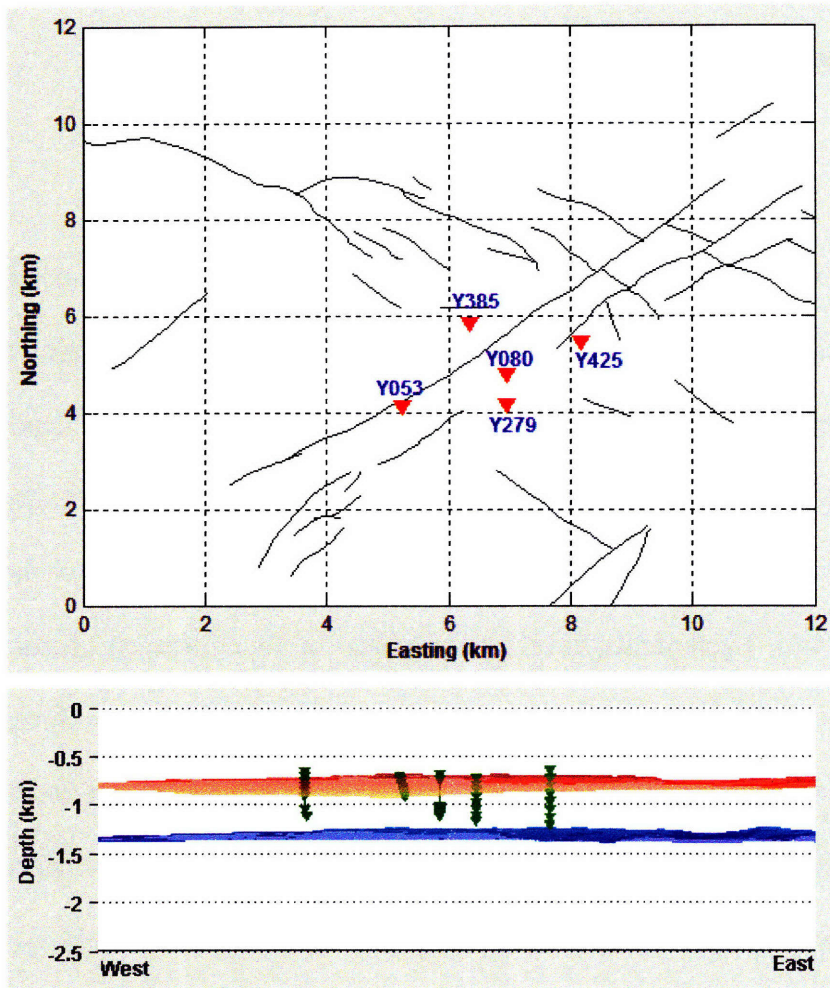
Figure 4.1: Borehole array for monitoring induced seismicity in the field. (Top) - Surface locations (red triangles) and labels of the monitoring wells shown on a 12 by 12 km reservoir grid. Also shown are faults (black lines) mapped from surface seismic at Natih horizon. (Bottom) - Depth cross-section on a vertical (East-West) plane showing how the borehole sensors are distributed at depths. Red and blue surfaces denote Natih (gas) and Shuaiba (oil) tops respectively.

The deep borehole microseismic acquisition system was a triggered system – i.e. preliminary event detection was made in the field using software based trigger algorithms. The data streams containing microseismic events were extracted and written to disk. Data were recorded with a sampling rate of 0.5 ms (2000 samples per second). The first stage of processing was to detect when an "event" had occurred. A simple threshold trigger was used (coupled with a choice of various signal pre-filtering/conditioning if required) for this purpose: the data acquisition software in the field monitored a number of channels, and if the specified amplitude was exceeded on any one of those channels, the unfiltered data for all channels would be recorded. One second of data from before the trigger and three seconds after were recorded to give a total of four seconds of data for each trigger. The system was allowed to trigger again 2 seconds after the first trigger.

For the deep-borehole microseismic monitoring project, we received field data from October 2002 – August 2003. During this period, about 15,800 events had been identified with an average rate of ~ 47/day. However, we analyzed and located events from alternate days only. The typical frequency content for events close to the monitoring wells was in the range 100 to 300 Hz, while the more distant large events typically had peak frequency between 20 and 40 Hz. We identified and read arrival times of first arriving P-and S-wave phases from seismograms of the induced events recorded at each station. This was considered the most important part in data preparation, as accuracy of locations is limited by the accuracy of arrival time picks. To pick arrival times, manual phase-picking was used. Given the noise levels and signal characteristics, automatic picking techniques to identify P and S-wave arrivals were not deemed suitable. An example seismogram for an event and its phase picks are shown by Figure 4.2.
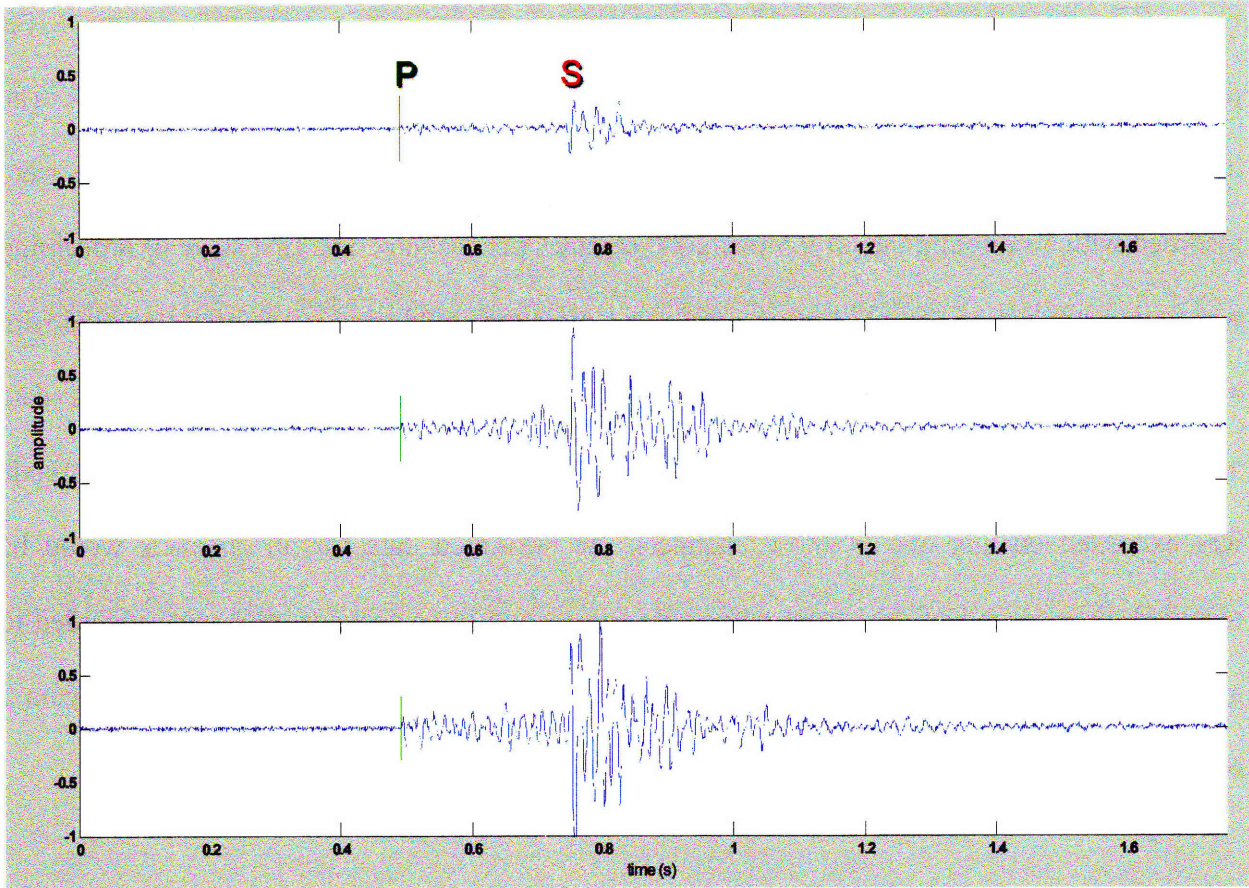
Figure 4.2: Three components of seismic data for an induced event detected by the deep-borehole network, along with the P and S-phase picks.

4.3 Location of Microseismic Events

The importance of the velocity model in event locations and how it could potentially impact the depth locations of induced seismicity has been discussed in great detail by Chapter 2 and also by Sarkar and Toksöz, 2008. To locate the events detected by the deep-borehole network, a velocity model derived from Sonic well-logs (Figure 4.3), identical to that used to locate events detected by the near-surface PDO network, was used.
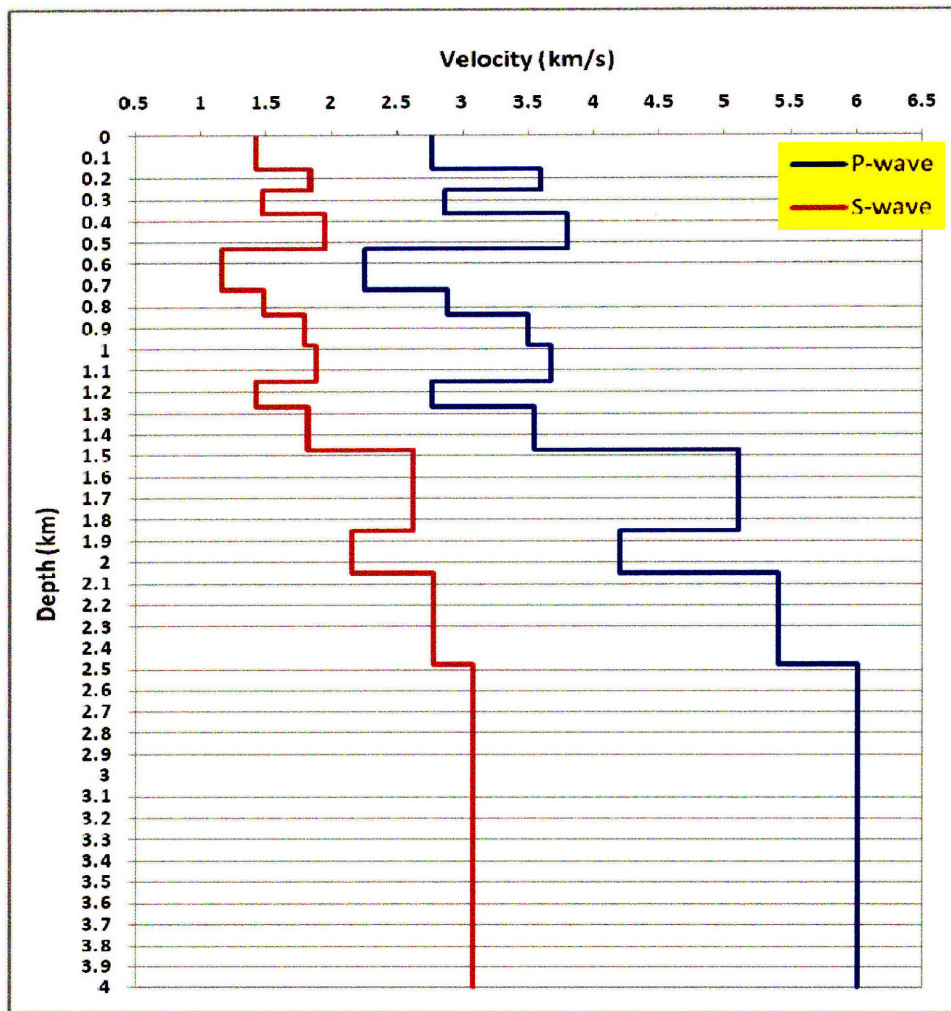
Figure 4.3: Layered model for seismic wave propagation in the reservoir, derived from Sonic logs.

Arrival time picks for first-arriving P-and S-wave phases were manually obtained from events occurring every other day during 11 months of microseismic data acquisition by the deep-borehole network, during October 2002 – August 2003. About 5,400 events were thus processed and located using two different location methods – NonLinLoc (Lomax *et al.*, 2000) and the Station-Pair-Differencing approach (Sarkar and Toksöz, 2008). Two methods produced very similar hypocenter solutions for the events. The epicenter and depth distribution of all (located) events in the field are shown by Figure 4.4. Within the range of microseismic detectability (i.e. 1-2 km from the monitoring wells) of the network, the epicenters of the events lie along the two major NE-SW faults in the field. Seismicity is more continuous along the northern fault than along the southern fault. We see some distinct clusters associated with both of the faults on the event epicenter map (Figure 4.4). From the depth map shown by Figure 4.4, we see how the events are distributed in depth: during the 11 month interval events are spread between 500 and 1500 m depth (relative to the Mean Sea Level).
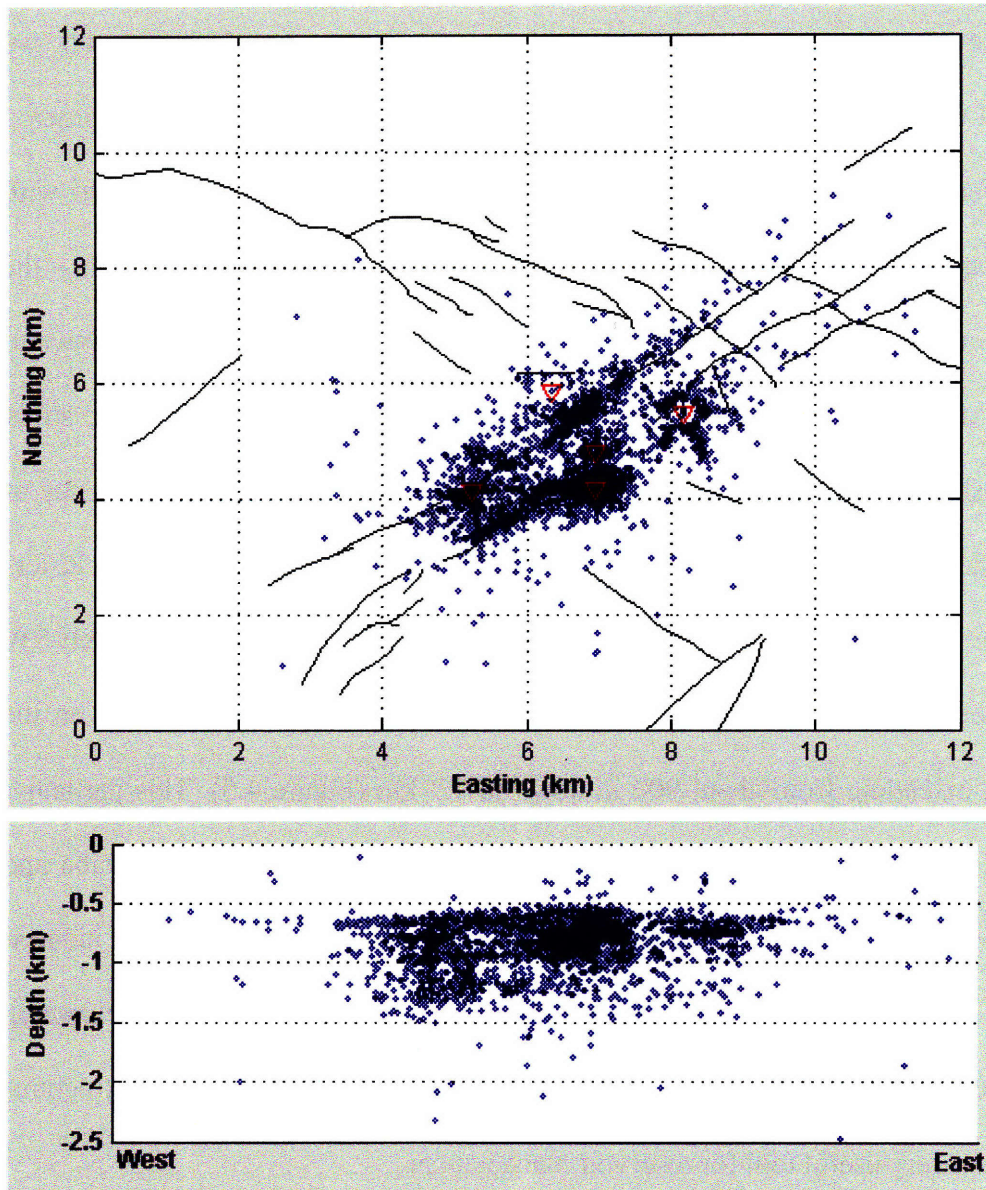
Figure 4.4: Location of induced seismic events occurring every other day during the period Oct 2002 – Aug 2003. Top: Showing event epicenters (blue dots), with fault maps derived from surface seismic at Natih horizon (black lines) and surface coordinates of the monitoring wells (red triangles). Bottom: Showing depth distribution of the events along a vertical plane (East-West section). The length of the West to East axis shown on this plot is 9 km (corresponding to a profile line extending from 2 to 11 km along the Easting axis of the top plot).

The located events show good correlation with existing fault maps. In Figure 4.5, we show events that fall on the two major faults in the field (two different colors - red and green – are used for two different faults). Location of these events can be used for tracing the faults with depth. Depth locations of these selected sets of events help delineate the faults at depth – the seismicity is continuous along 1 km depth of the two faults, extending from about 500 m down to 1.5 km, as seen by depth cross-sections on Figure 4.5. Depth profiles taken along the strike direction (SW-NE) show clustering of the events on the fault plane, thus revealing zones of reactivation along the faults due to production and injection activities. Some of the clusters appear to form some linear features along the dipping plane of the two faults. On the NE-SW cross-section plot, for events shown in green, a continuous structure can be identified on the south-western flank, extending from about 900 m down to 1.3 km (Figure 4.5). This particular structure was likely formed by *water* moving from the (water) injection wells in Shuaiba and inducing earthquakes in the formation between Natih and Shuaiba. Thus locations of induced events can be quite useful for identifying faults and fractures in the reservoir and for mapping them in detail. Additionally, when the cause of the induced events associated with the structures is known, it becomes a very useful tool for reservoir management.
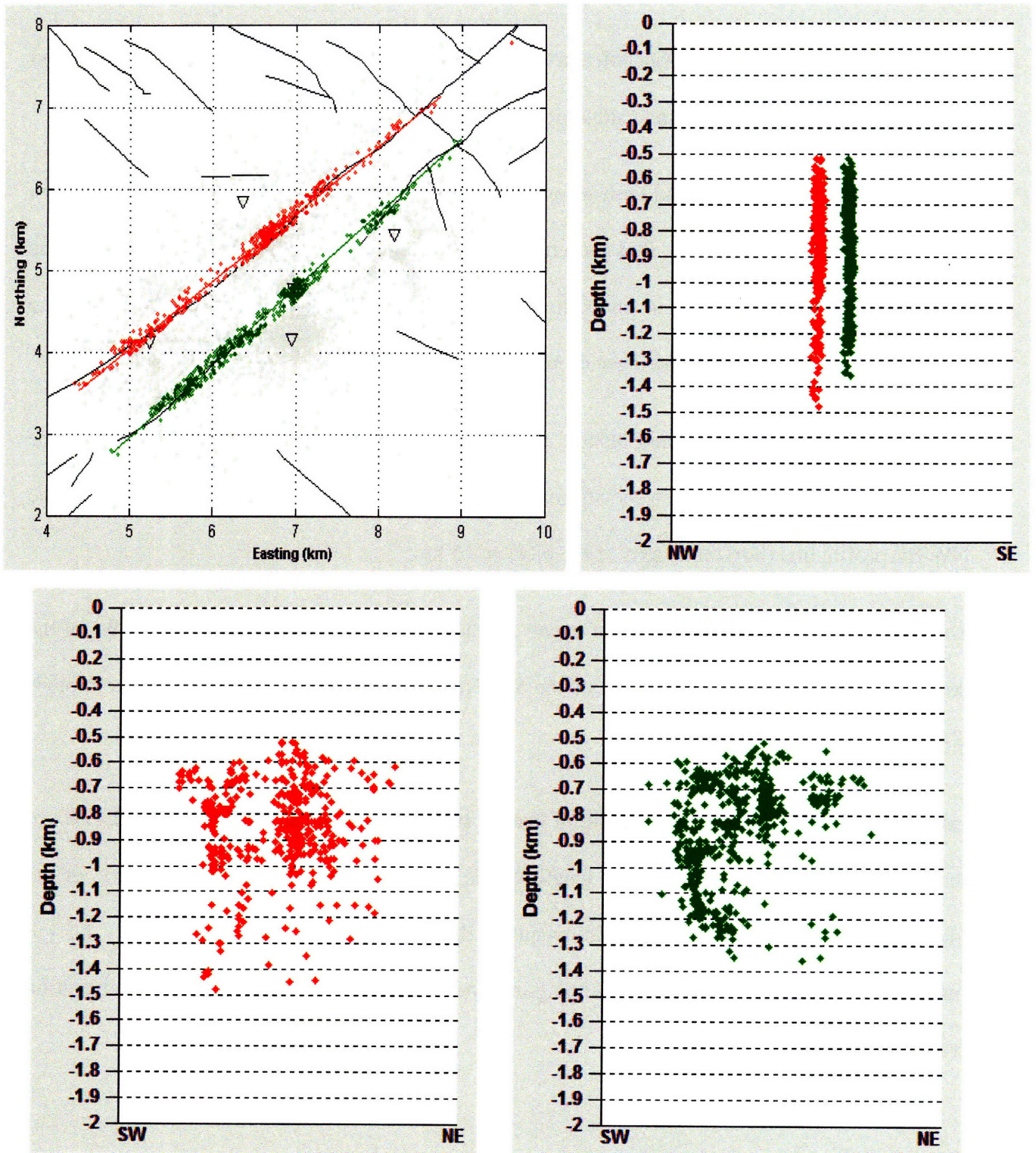
Figure 4.5: Events associated with two main faults and detail mapping of the two structures for

depth analysis. For each fault, events falling within a distance of 100 meters on both sides of the

fault are selected for display (in red and green colors) and analysis. Events are selected and analyzed in 3D, but for better understanding their 2D projections are presented.

Upper left: Event epicenters and fault maps. The overall seismicity (all located events) is shown by grey dots in the background. Red and green dots denote events that fall on or very close to the two major faults (within 100 m on both sides of each fault). Black triangles denote surface locations of the borehole monitoring stations.

Upper right: View of the two fault planes, mapped by induced seismic events associated with the two faults (red and green), from the strike-perpendicular (NW-SE) direction. The length of the NW-SE profile line (horizontal axis of the plot) is 8.5 km.

Lower left: Depth section of red set of events, plotted along the strike direction (NE-SW) of the corresponding (red) fault. The length of the SW-NE profile line (horizontal axis of the plot) is 8.5 km.

Lower right: Depth section of green set of events, plotted along the strike direction (NE-SW) of the corresponding (green) fault. The length of the SW-NE profile line (horizontal axis of the plot) is 8.5 km. The coalesced seismic events on the south-western side between ~ 9 – 1.3 km most likely denote a path for water escaping into the formation above Shuaiba from the injection wells.

The histogram plot of event depth distribution (Figure 4.6) shows that the microseismic events can be divided into two main depth groups. The more populous group is centered around the upper boundary of Natih formation at ~750 m depth (producing gas unit Natih A), extending upwards by about 250 m into the overburden Fiqa formation and downwards by about 250 m to the base of Natih formation. The smaller and deeper group of events is centered at about 1150 m depth in the Nahr-Umr formation, halfway between the base of Natih and top of Shuaiba formation. The boundary between these two depth groups occur at a depth of about 1050 m (below the Mean Sea Level datum).
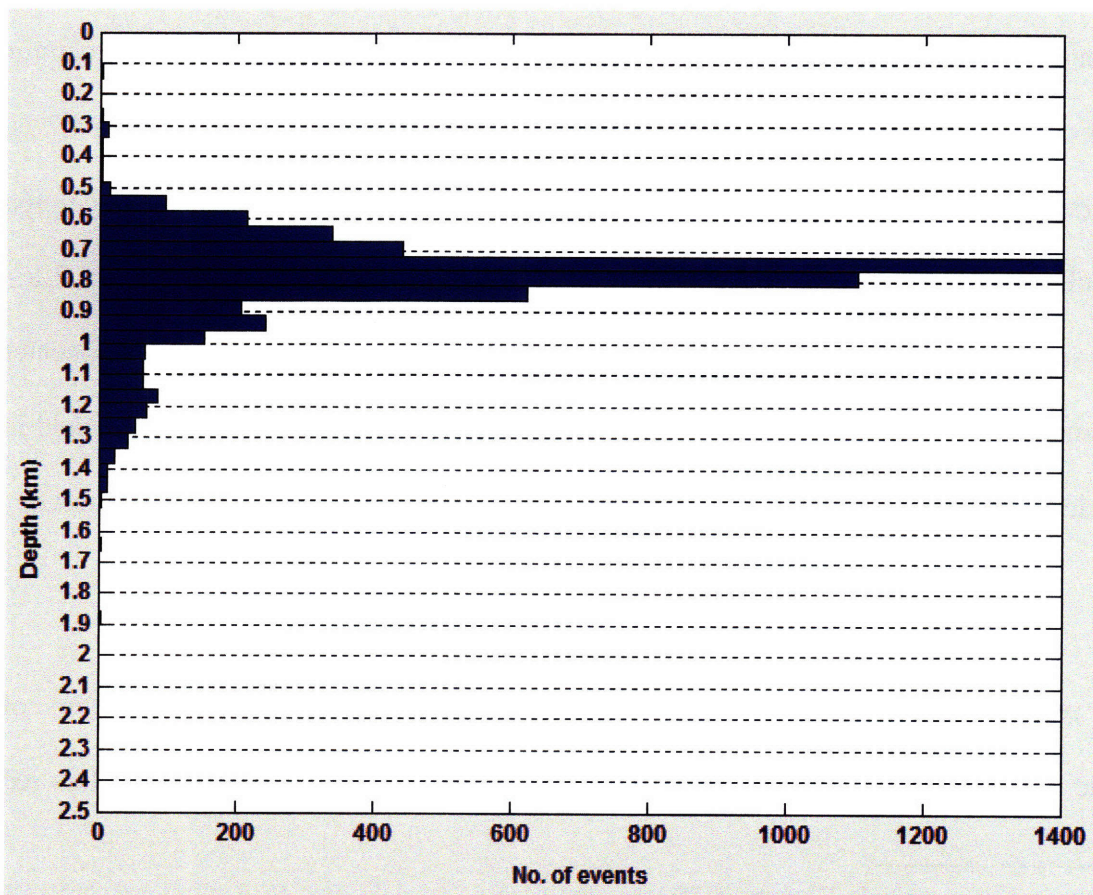
Figure 4.6: Histogram plot showing depth distribution vs. occurrence of events

4.4 Mapping faults and fractures using Induced Seismicity Locations

Both depth-groups (discussed in the preceding section and shown by Figure 4.6) contain events within clusters predominately located on a specific subset of pre-existing faults parallel and often co-planar to large faults already mapped as bounding the central Graben fault system that strikes north-east south-west and crosses close to the crest of the field (Figure 4.5). In this section, we show plots of some of the localized clusters of events (Figures 4.7.1 – 4.7.5[9]), which can be used for detailed mapping of the structures associated with the seismicity. Many of these clusters extend continuously from above the Natih down to the Shuaiba along single structures (e.g. clusters colored red and blue on Figure 4.7.1, and cluster colored magenta on Figure 4.7.2). Other clusters remain localized within one or the other of the depth groups (e.g. clusters colored green and yellow on Figure 4.7.3, and cluster colored brown on Figure 4.7.5). Figures 4.7.1 – 4.7.5 depict some of the major clusters of events in the field – grouped by their 3D hypocenter locations – and show the microseismic evidence for large-scale fault re-activation in the field in response to depletion of the Natih gas reservoir and water injection into the Shuaiba oil reservoir.

The two faults can be traced in their dip directions by the two local clusters of microseismic events on the south-western flank of the Graben system, shown by the colors red

---

[9] By these figures, we show multiple 2D views of the three-dimensional spatial distribution of events and clusters in the reservoir. Each cluster is represented by a different color. For every cluster map, we usually show one epicenter map (X-Y cross section) and two depth-sections taken in orthogonal directions. For clusters falling on the two main faults, we show one depth-section for the cluster along the general strike direction of the fault (approximately NE-SW) and another depth-section along the perpendicular direction of the strike (approximately NW-SE) of the fault. On the figures, the A-B profiles indicate a strike-normal direction, whereas the C-D profiles indicate a strike-parallel direction, unless otherwise specified. For some other clusters, we use an east-west and a north-south profile to show the depth distribution – they are labeled as E-W and N-S, respectively, on the figures.

and blue on Figure 4.7.1. The red cluster of events, on the southern fault, delineates a structure that extends about 1 km in the strike direction and about 800 m in the dip direction. Across the Graben system, on the northern fault, the blue cluster of events identifies a similar structure. In between the two faults, there lies another structure – as identified by the black cluster of events (Figure 4.7.1) – that had not been mapped previously by surface seismic. This black cluster of microseismic events has its peak around 750 m (below the Mean Sea Level), at the boundary between the Natih gas formation (Natih A1 unit) and its overburden shale, Fiqa. This cluster may be due to reactivation of a fault not mapped before or to a newly created fault or fractures. As seen from the map view (Figure 4.7.1, upper left panel) and as seen by the sharp delineation in the fault parallel direction (Figure 4.7.1, lower panel – middle window), this black cluster seems like a structure oblique to the main faults, which could possibly provide connectivity between the two major faults. Therefore, this black cluster may be very important in terms of reservoir fluid movement. Presence of a conjugate fault system has been shown by maps derived from surface seismic, but at deeper levels (Shuaiba). However, this black cluster is an indication of the possible existence of another fault/fracture system at the shallower levels (Natih and overburden) as well, in the south-western flank of the major Graben system. From the overall epicenter distribution map (Figure 4.4), dense clouds of events can be seen on this side of the field. Evidence of new (or previously unidentified) faults and/or fractures in between the two major known faults on this side of the field was also seen from the analysis of passive seismic data recorded by the near-surface PDO network (Chapter 3).
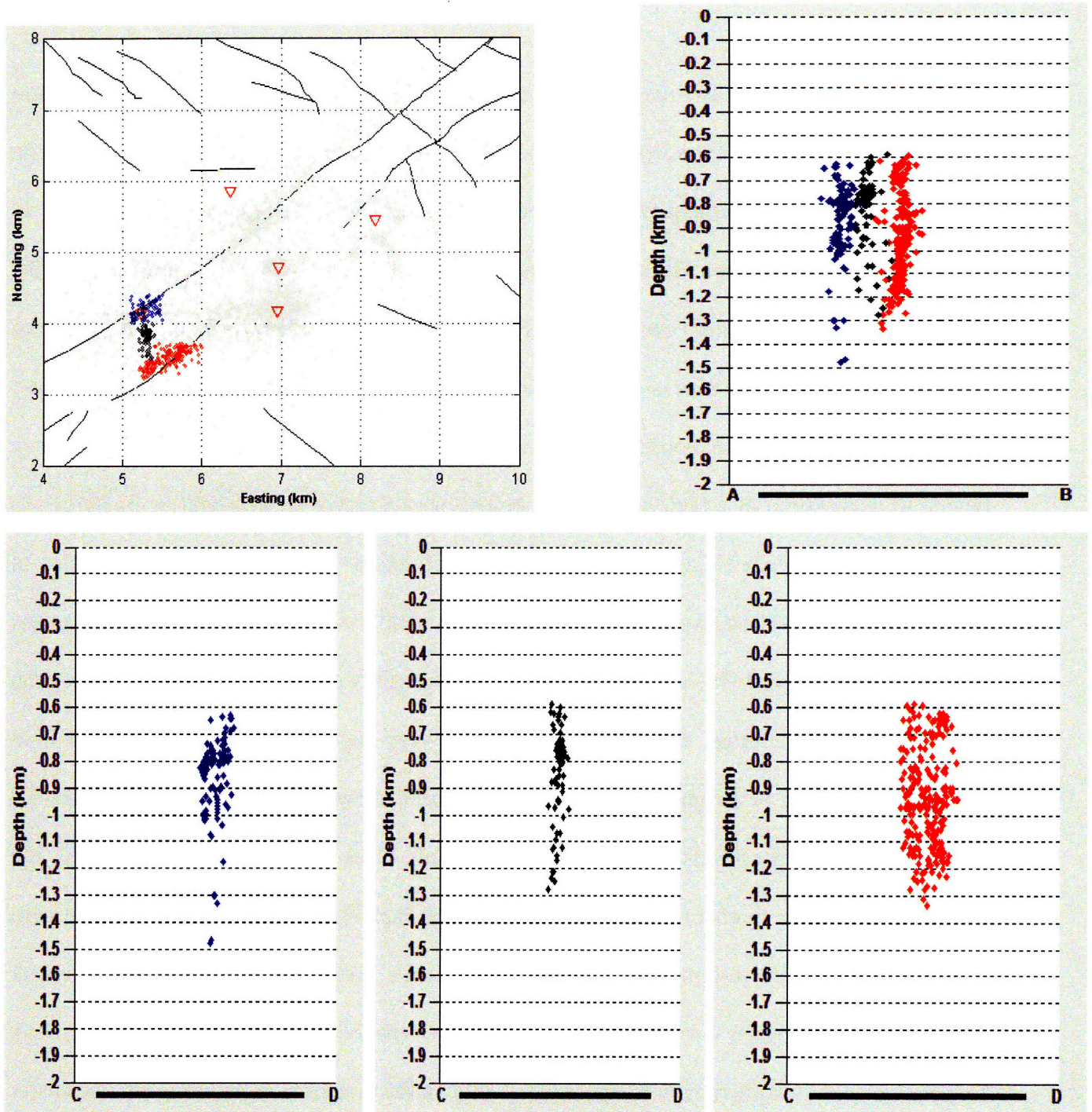
Figure 4.7.1: Events forming three separate clusters on the south-western side of the field shown by red, black and blue dots. Upper Left: Plan view of the events, and pre-mapped faults (black lines) and seismic stations (red triangle). Upper Right: Depth distribution of the three clusters along a plane (A-B) perpendicular to the strike. Lower: Depth distribution of the three clusters along a strike-parallel (C-D) plane shown separately by three separate panels. [*The lengths of both A-B and C-D profile lines are 4.2 km*].

Another sharp fault structure, previously unmapped by surface seismic, becomes visible from location of microseismic events recorded by the deep-borehole network. The magenta colored cluster plotted in Figure 4.7.2 has a strike length of about 1 km in the east-west direction, and has a dip length of about 1 km ranging from the overburden Fiqa all the way down to the base of Shuaiba. The dip direction is near-vertical (as seen from the upper right panel of Figure 4.7.2). The depth section derived for the strike direction of this feature (E-W) shows the extent of the dipping plane with events distributed at different depths along it. This is probably the longest continuous structure in the dip direction identified from locations of passive seismic events analyzed during the period of Oct 2002 – Aug 2003. This magenta cluster is another indication that, during that period, seismicity in the field had not only occurred along the known major faults, but also the field had experienced some significant amount of "in-fill" faulting/fracturing in the south-western side of the reservoir. This observation is quite consistent with the analysis of induced seismic data recorded by the surface network in the field (ref. Chapter 3).
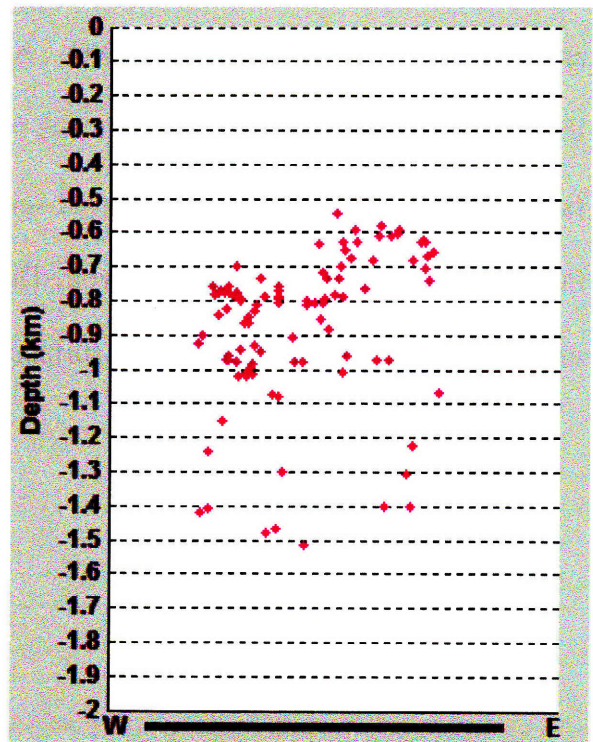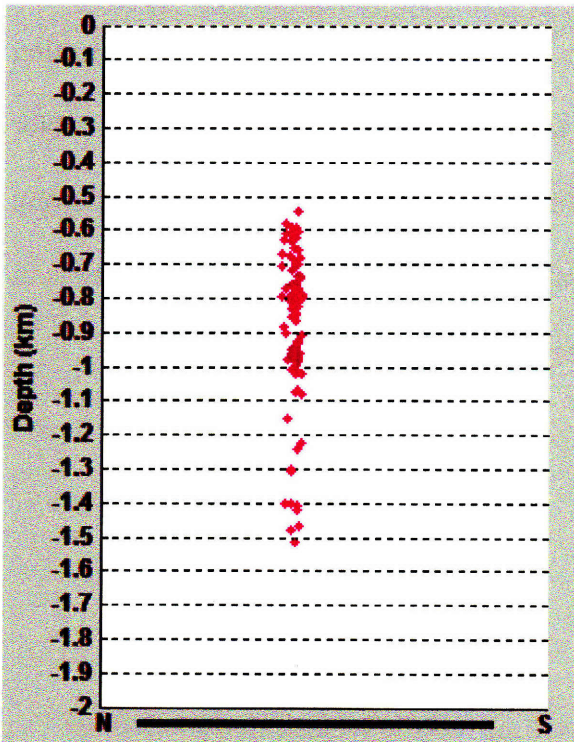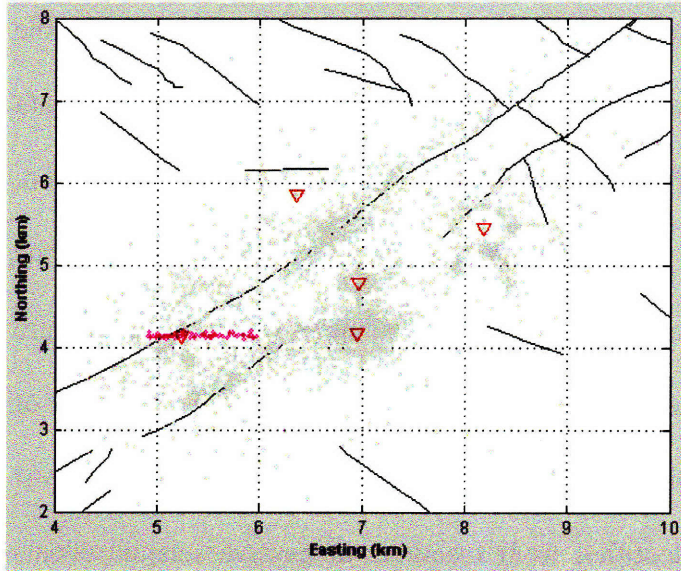
Figure 4.7.2: An east-west striking structure previously unmapped, identified by a cluster of induced events shown in magenta. Upper: Plan view of the events, pre-mapped faults (black lines) and seismic stations (red triangle). Lower Left: Depth section of the cluster along a North-South (N-S) plane. Lower Right: Depth section of the cluster along a West-East (W-E) plane. [*The lengths of the N-S and W-E profile lines shown on this plot are 2.8 km*].

Two dense "circular halo" clusters around two monitoring wells and a third planar cluster joining the two are shown together on Figure 4.7.3. A large cloud of microseismic events (colored cyan in Figure 4.7.3) appears near the eastern edge of the fault break of the southern major fault. As seen from the depth cross-section map of Figure 4.7.3, the cyan events are centered on the Natih A reservoir. From verbal communications with the reservoir team it was learned that a gas producing well exists where the cyan cluster was located. The events in this cluster may be correlated with gas production from that producing well. A monitoring well is located in the middle of the cluster. Many very small magnitude events were recorded only by that monitoring well. Another smaller but very similar cluster, shown by green dots in Figure 4.7.3, was identified to the north of the large cyan cluster. The depth plots of the green cluster show that the highest concentration of events in this cluster is between the Fiqa formation and upper Natih, suggesting strong correlation of this cluster with production of gas. The two clusters (green and cyan) seem to be connected by another cluster shown by yellow in Figure 4.7.3. The yellow cluster of events identifies a fault, as seen by the sharp linear feature on the E-W cross-section of Figure 4.7.3 (lower panel, middle window). The depth cross-section of this (yellow) cluster of events shows that the events follow the distribution of the events of the cyan cluster to the south and of the green cluster to the north, and in the space between the clusters the events are distributed in the Natih gas layer (N-S profile on Figure 4.7.3). Many of the small events falling in these three clusters (especially green and cyan) were recorded by only one monitoring well (in each cluster as shown by the map in Figure 4.7.3); therefore these clusters appear as *clouds* of microseismicity. A question arose as to whether the large microseismic cluster (i.e. the blue *cloud*) was due to some specific reservoir conditions around the gas producer (that is known to lie within the cluster), or whether it was simply due to the high sensitivity of the network, due

141

to the proximity of that cloud to a monitoring well. To understand this issue better, we randomly sampled some events and analyzed their relative magnitudes based on the waveform amplitude ratio. It seemed that the cluster had events in different magnitude ranges, suggesting that it would be a significant feature even without the proximity of the monitoring well to the cluster. The proximity of the monitoring well explained the high proportion of small events that would less likely be detected using only the wells that were more distant. A greater understanding of this feature could be obtained by a more detailed investigation of the microseismic data and reservoir conditions in the area of this cluster. Determination and interpretation of discrete structures could be improved by using some of the advanced mapping techniques, such as - the collapsing technique (Jones and Stewart, 1997), the re-picking method (Rowe et al., 2002; Fehler et al., 2000; Philips, 2000), and the double-difference relative location method (Waldhauser and Ellsworth, 2000).
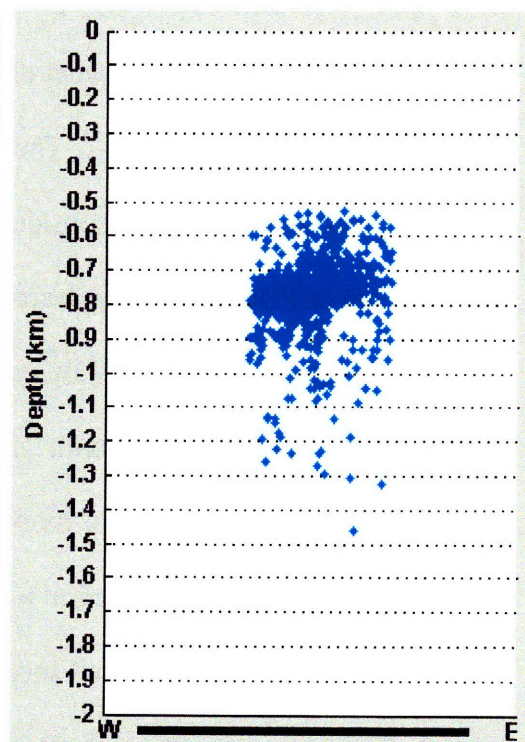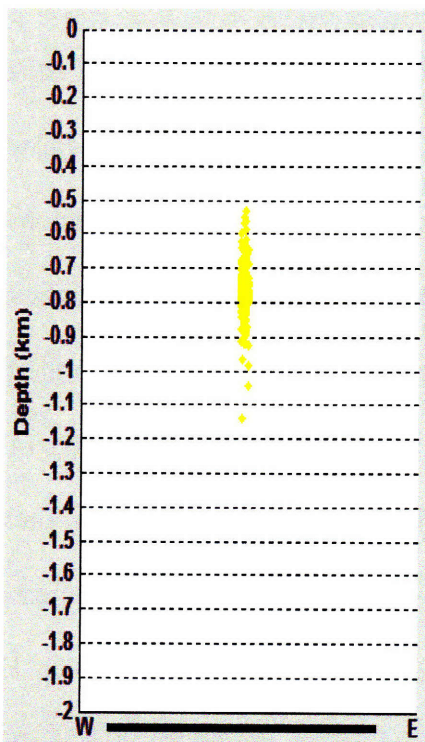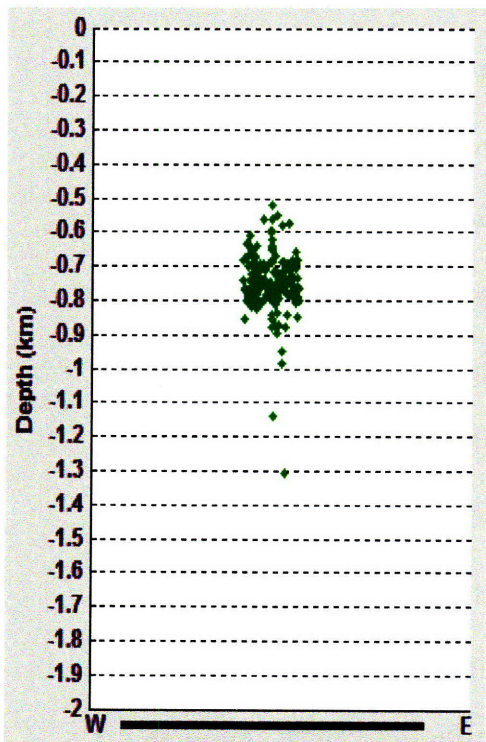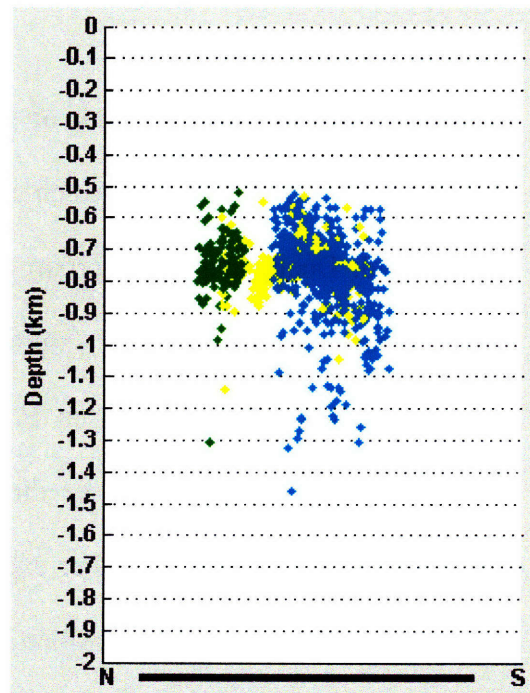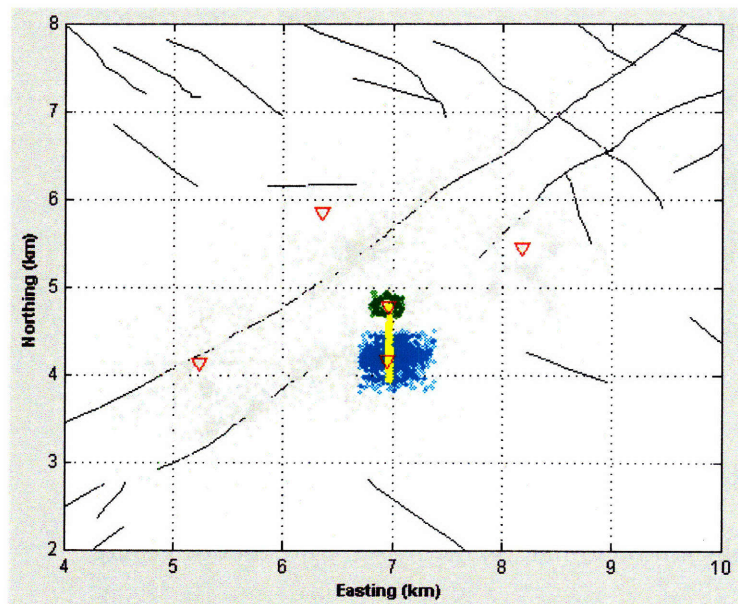
Figure 4.7.3: Maps of three clusters near the middle and south of the field formed by events shown in green, yellow and cyan. Upper Left: Plan view of the events, and pre-mapped faults (black lines) and seismic stations (red triangle). Upper Right: North-south (N-S) sections of the three clusters shown together. Lower: West-East (W-E) sections of the three clusters shown separately. [*Both N-S and W-E profile lines were chosen to be 3.2 km long*].

The longest streak of continuous events is observed along the NE-SW strike of the northern major fault, between near the middle of the reservoir grid and the north-east side of the field. Detail maps of a group of events selected from that zone in the middle, shown in dark green, are presented by Figure 4.7.4. The dipping plane of this cluster is shown from two perpendicular directions in Figure 4.7.4: one along the strike (section C-D) and the other perpendicular to the strike direction (section A-B). Both sections highlight some interesting features of that cluster. For example, the section A-B shows some horizontal lineations on the fault plane. One such lineation, identified by black dashed line on the lower left panel of Figure 4.7.4, coincides with the upper boundary of Natih A. The image shown by section C-D normal to the strike (lower right panel of Figure 4.7.4) shows hints of existence of very closely spaced two or more rupture planes[10]. The location of this dark green cluster coincides with the region that shows highest surface subsidence in the field. From discussions with the reservoir management team at PDO it was also learned that the well having the highest gas production rate in the field lies near to and south of this cluster. All these facts lead to the hypothesis that the events in this cluster are correlated with gas production and compaction of the Natih reservoir. However, during the microseismic monitoring period with the deep-borehole network, periodic bursts in seismicity were observed in the weeks/months following increase in water injection into Shuaiba through an injection well located to the south of that cluster. During those periods of bursting microseismic activity, events were seen on the fault across both Natih and Shuaiba reservoirs. A tentative interpretation for both faults being seismically active following a heavy water injection would be that water from the injection might have entered the fault in the Shuaiba and then moved both laterally and upward from Shuaiba to Natih.

---

[10] Hint of two distinct lines can actually be seen from very close observation of the events on the epicenter map. Some advanced mapping techniques will be required to identify if there is more than one fault.
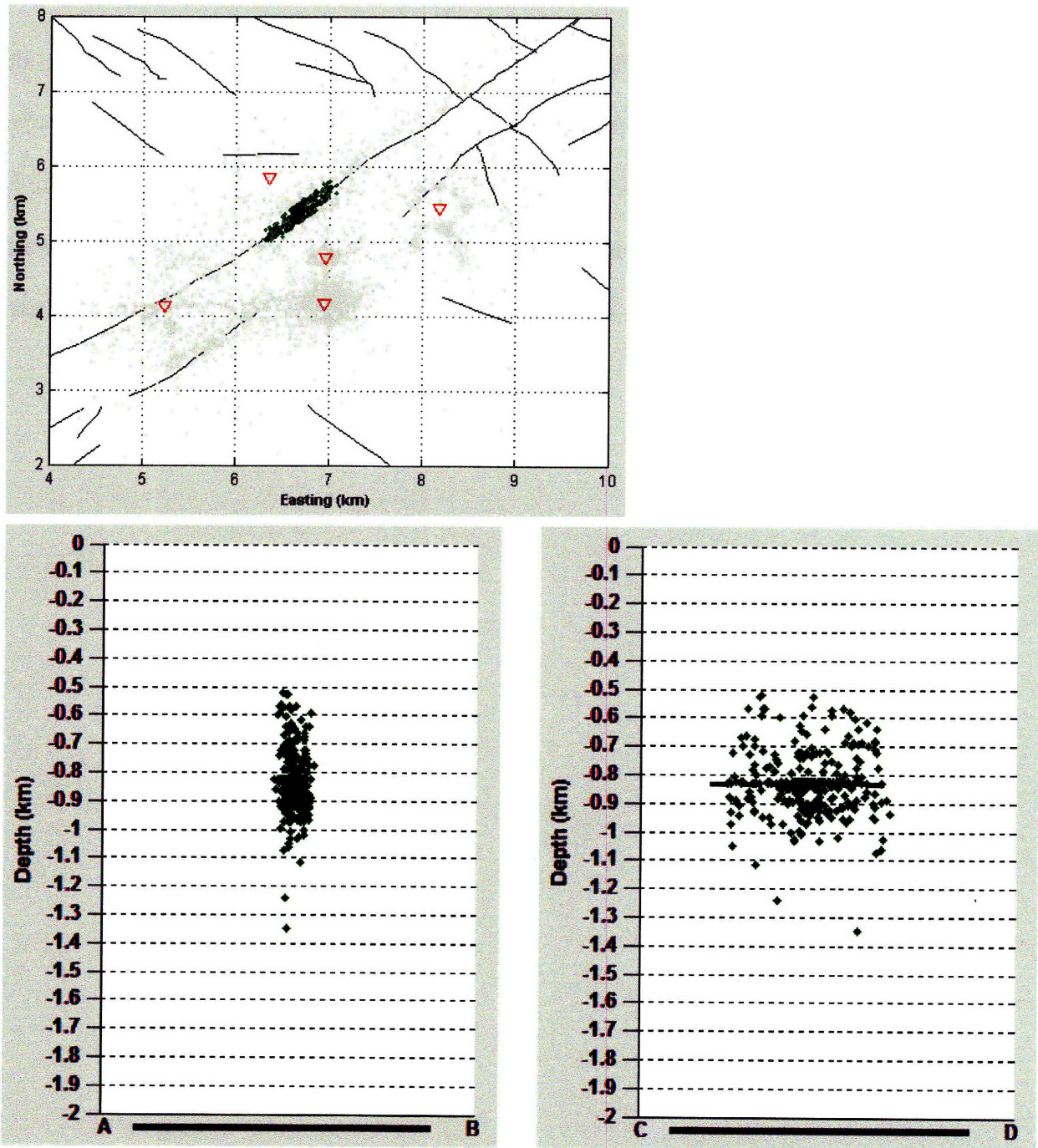
Figure 4.7.4: Upper: X-Y (horizontal) section of the events, pre-mapped faults (black lines), along with seismic station coordinates (red triangle). Lower left: Event distribution along A-B section, normal to the general strike direction of the northern fault. Lower right: Event distribution along C-D section, parallel to the general strike direction of the northern fault. Black dashed line marks a strong lineation observed within the cluster. [*The lengths of the A-B and C-D profile lines are 2.5 km*].

145

Another prominent feature during the monitoring period was seen in the northeastern side of the field, surrounding the seismic monitoring well located to the south of the southern major fault (Figure 4.7.5). The cluster shown in brown by Figure 4.7.5 with a unique "halo" feature is confined mostly in the (upper) Natih gas reservoir with some of the seismicity extending upward to the lower half of the overlying Fiqa shale. This cluster of events is also thought to have been induced by gas production.
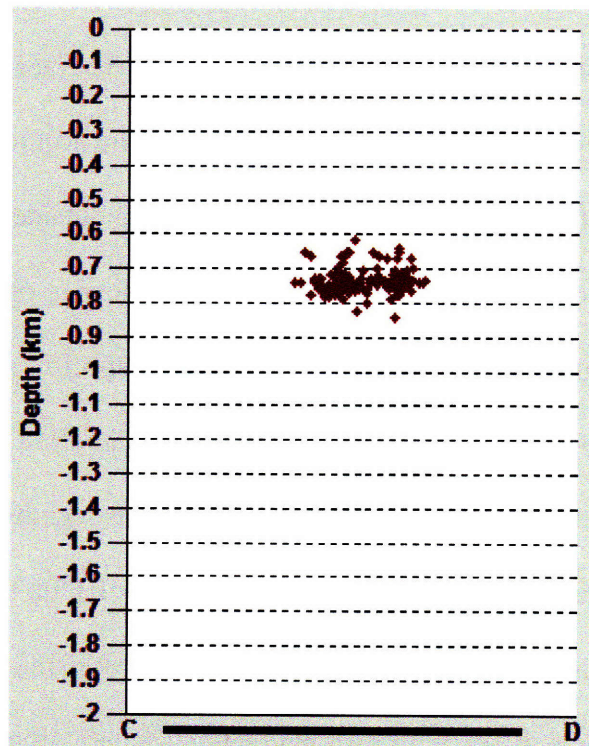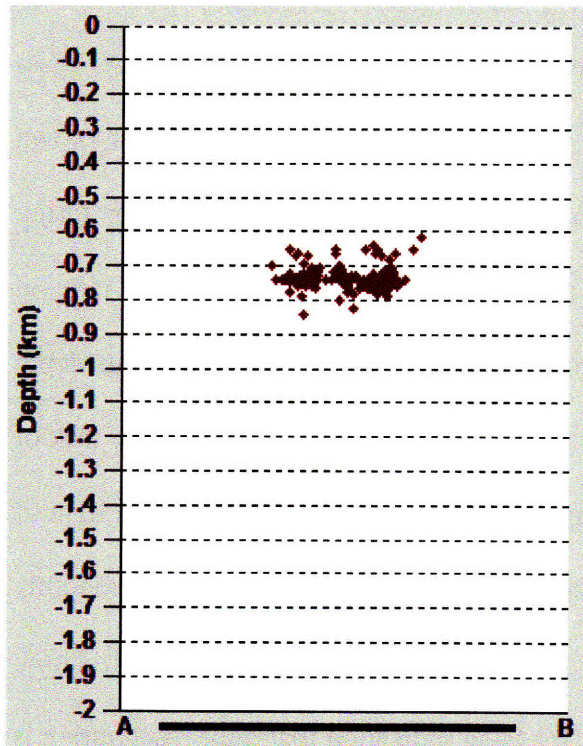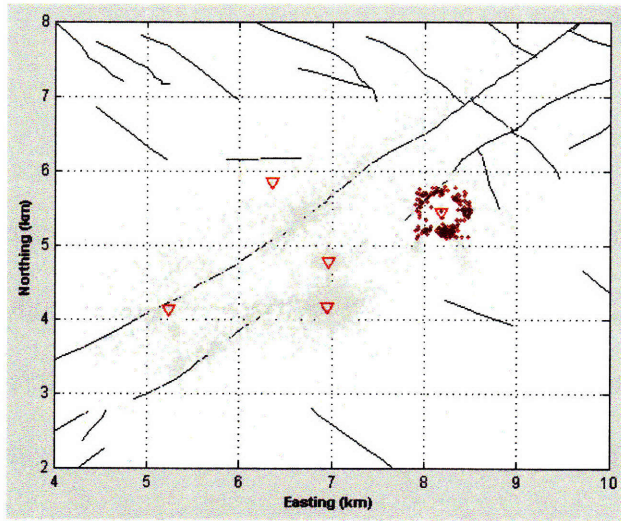
Figure 4.7.5: A "circular halo" on the north-eastern side of the field. Upper: Epicenter of the events forming this "halo", surface coordinates of the monitoring wells (red triangles), and pre-mapped faults (black lines). Lower left: Depth section perpendicular to the general strike direction of the southern fault. Lower right: Depth section parallel to the general strike direction of the southern fault. [*The lengths of A-B and C-D profile lines are 2.8 km*].

4.5 Analysis of Event Locations by Depth

Analysis of microseismic event locations by depth intervals can be useful to better understand the clustering and fault structure with depth. We divide the events into four depth intervals: a) 500 – 700 meters, b) 700 – 800 meters, c) 800 – 1100 meters, and d) 1100 meters and greater, and plot them by Figures 4.8(a) – 4.8(d), respectively. On Figure 4.8(a), we plot all events located between 500 – 700 m depth, and compare them with: i) the structural contour of the Fiqa horizon (the overlying Shale above Natih) and ii) the fault map at the top Natih A1 (gas) horizon derived from surface seismic. The accuracy of event locations in this interval is known to suffer due to some of the events falling outside (above) the borehole sensors of the monitoring network. Also the fault map that we show is only approximately valid for this depth interval because the fault map was derived at a specific seismic horizon, slightly deeper than this depth interval of the selected seismic events. Therefore the scattering of event locations and the lack of correlation with faults at certain places, as seen by Figure 4.8(a), should be interpreted in light of these two limiting factors. The pattern of Fiqa contours (Figure 4.8(a)) indicates its smoothly varying shape above Natih, and the microseismic events that occur inside Fiqa show correlation at some places with its topographic discontinuities. This is an indication that fault reactivation is taking place in the field across the overburden shale, namely Fiqa formation. Figure 4.8(b) shows a much better correlation of seismicity with faults and topographic contours, as these all belong to roughly the same depth levels (microseismic events between 700 – 800 m, faults from Natih A1 horizon, and topographic contours of the Natih A1 horizon). In this depth interval, the most dominant features are the two "circular halo" clusters (previously shown by Figure 4.7.5, colored green and cyan). The event concentration of the larger cluster is highest in this depth interval,

148

and the smaller cluster is mostly contained in this depth interval. A "horse-shoe" type structure appearing at the north-east side of the field is fully developed in the 700-800 m depth interval. Events between 800 – 1100 meters show good correlations with the existing fault maps (Figure 4.8(c)). The events are plotted with fault maps derived at Natih A and the contours of Natih B, a fine-grained limestone below Natih A. Some major clusters are seen in this depth interval, e.g. i) in the south-western side of the field – on both faults and the zone in between, and ii) on the northern fault in the middle of the field. The last plot (Figure 4.8(d)) in the depth series shows events located below 1100 meters, plotted together with fault maps derived at top Shuaiba horizon and the topographic contours of Shuaiba. We see relatively few events below 1100 meters, as compared to other depth intervals.
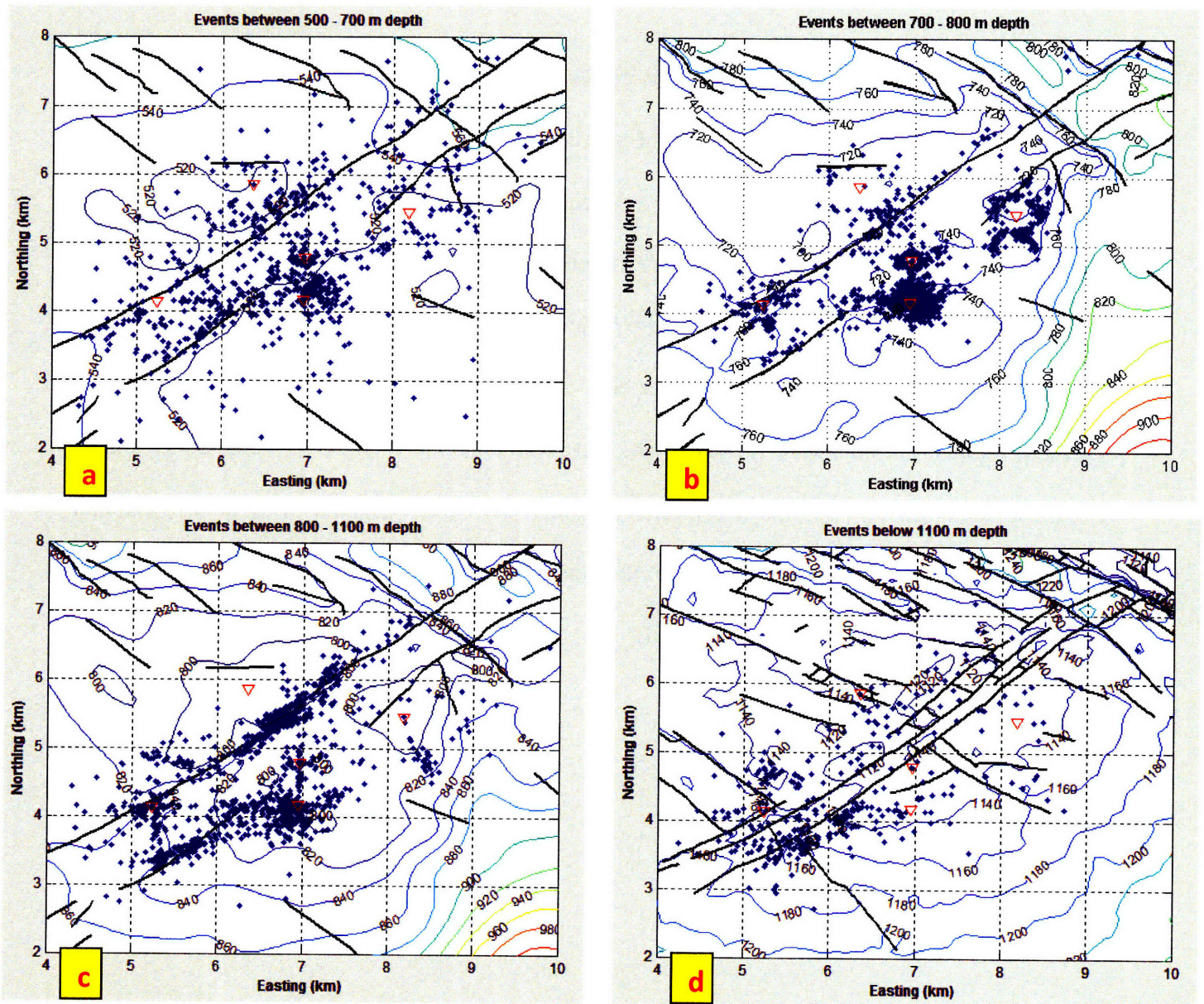
Figure 4.8: (a) – Events (blue dots) between 500-700 m depth, fault maps (thick black lines) derived from surface seismic at Natih A1 horizon, and topographic contours of the Fiqa horizon; (b) - Events (blue dots) between 700-800 m depth, fault maps (thick black lines) derived from surface seismic at Natih A1 horizon, and topographic contours of the Natih A1 horizon; (c) - Events (blue dots) between 800-1100 m depth, fault maps (thick black lines) derived from surface seismic at Natih A1 horizon, and topographic contours of the Natih B horizon; (d) - Events (blue dots) between 1100 m depth, fault maps (thick black lines) derived from surface seismic at Shuaiba horizon, and topographic contours of the Shuaiba horizon.

150

Around some of the clusters shown by Figures 4.8, some "spoke" like features are observed (e.g. lines protruding outward from the "halo" in the NE of the field: Figure 4.8-b). One possible explanation to this radial pattern of seismicity could be that they are formed due to local compaction around gas production wells. The mechanism is explained by a schematic diagram (Figure 4.9).
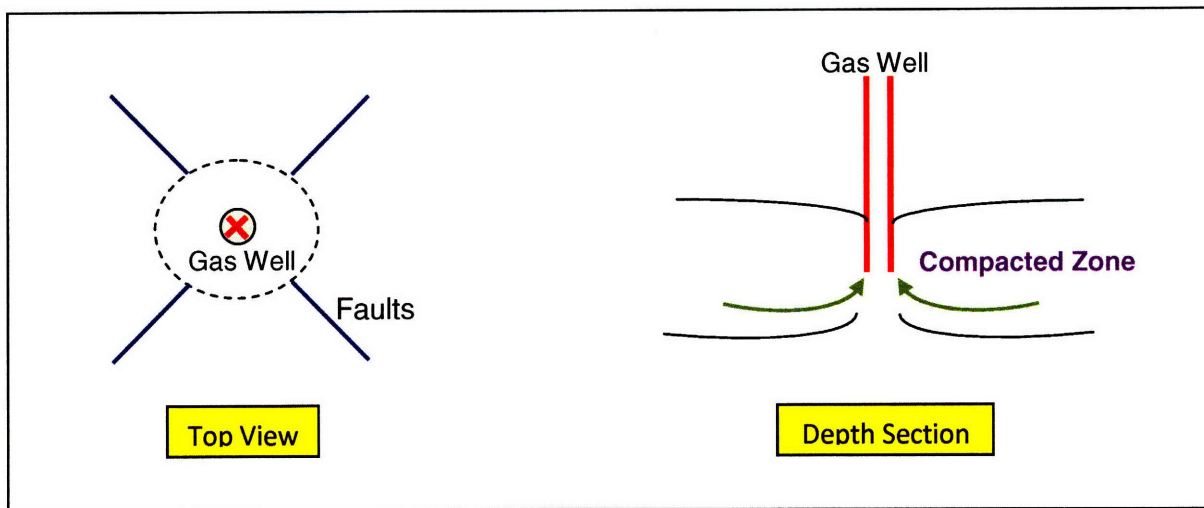
Figure 4.9: Faulting mechanism due to compaction around a gas producing well, used for explaining some of the induced seismicity data in the field.

4.6 Analysis of the Time History of Microseismicity

Analyzing event locations with time, and comparing rate of seismicity with production/injection history provide additional insights into the cause of seismicity in the field. The discussed field of this study undergoes three major reservoir operations: 1) gas production from Natih, 2) oil production from Shuaiba, and 3) water injection into Shuaiba. Long term monthly cumulative production/injection data were available for this study, however the available seismicity data spanned only 11 months and that, too, was incomplete. For monthly seismicity time series data, this was considered short period and noisy. Therefore, correlation analysis between monthly production/injection rate and rate of seismicity would not lead to any definitive conclusion about their temporal relationship. In this section, we only show a comparison chart for induced seismicity detected by the deep network vs. gas production (Figure 4.10), which is known to be the primary cause of inducing earthquakes in the field.
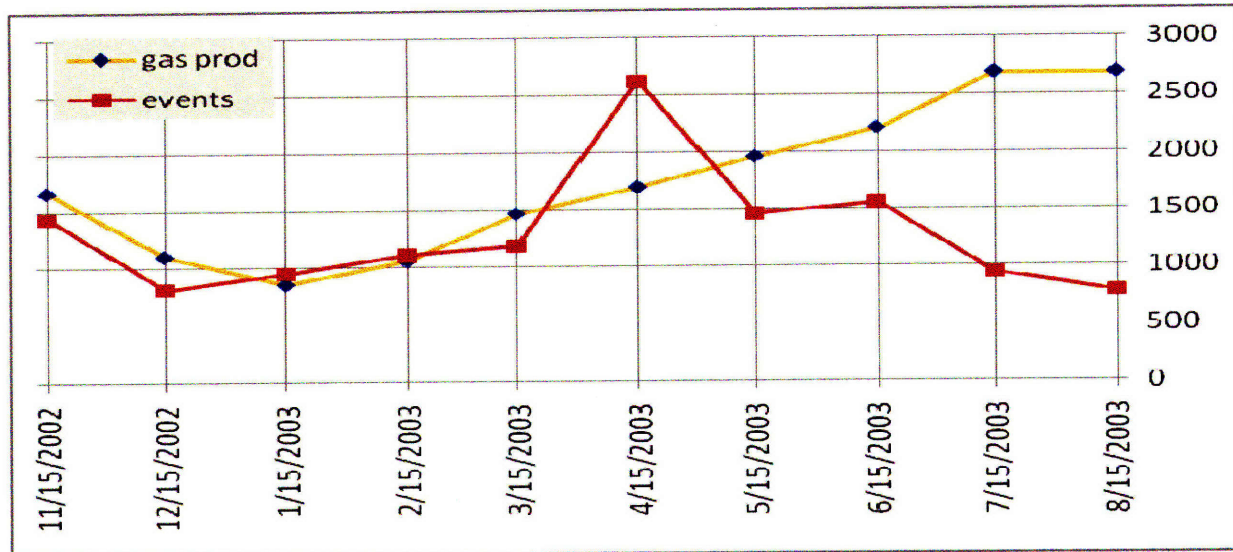
Figure 4.10: Comparison of monthly number of events (brown) with gas production (yellow). Horizontal axes have units in months, and the right side of the vertical axes shows vent counts. (Not shown are the actual numbers for gas production. The gas production increases vertically from low to high). Some similarity between the two trends is observed during the first half of the plot; however, due to a very short window of analysis and large uncertainty in the seismicity event counts data, a conclusion cannot be drawn from this comparison.

If access to all field data was provided, it would be possible to relate the temporal pattern of microseismicity to patterns of production/injection activities during a passive seismic monitoring study. Such an analysis would be very useful for reservoir monitoring and characterization, as time history of induced seismicity and its spatio-temporal variation with reservoir production/injection activities would help in understanding the flow behavior in faults and fractures – e.g. to identify sealing faults or permeable flow paths. However, to properly investigate the temporal correlation of induced seismicity with reservoir production/injection

153

mechanisms, detailed production/injection data from different wells in the field are required so that the seismicity clusters and their temporal changes can be correlated with local production/injection mechanisms. In this study, we only had monthly cumulative data for production/injection from the entire field; therefore, the temporal changes in seismicity at various locations in the reservoir could not be explained by the reservoir hydraulics. Nevertheless, in this section we show month-by-month plots of seismicity from the entire field (Figures 4.11) for the period of data analyzed (October 2002 – August 2003). The plots indicate that microseismic events occur more or less simultaneously across the whole extent of an active zone. There are also episodic bursts of seismicity, which are likely to be caused by local changes in production and/or injection. At petroleum fields where fluid injection is a major process, pore fluid diffusion has been used to explain some of the propagation of microseismic event fronts (Shapiro *et al.*, 2002). However, from Figures 4.11, we do not see any clear evidence for any coherent diffusion of the envelope of microseismic activity away from sources.

Events during Oct. 2002

Events during Nov. 2002

Events during Dec. 2002

Events during Jan. 2003

155
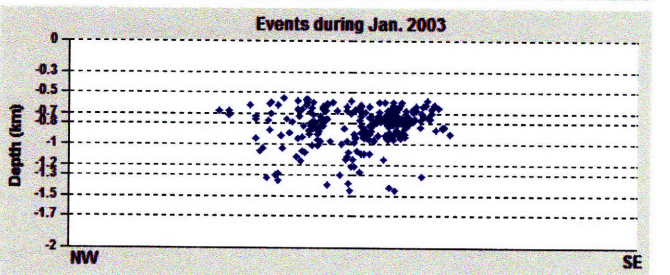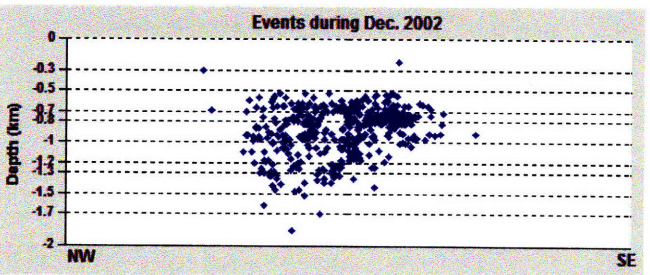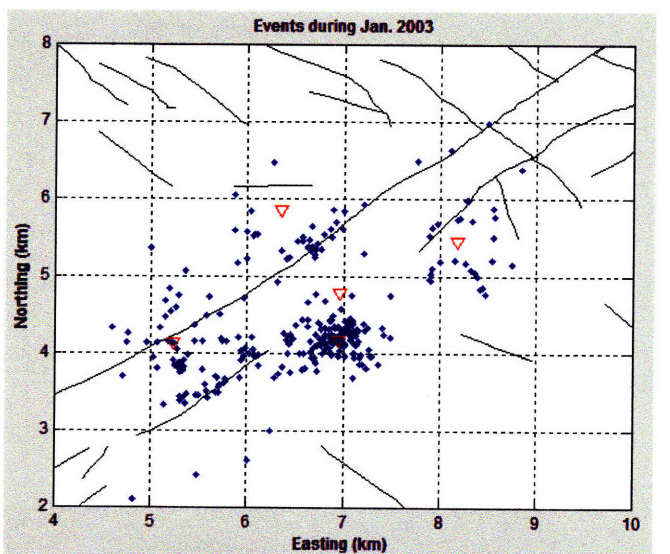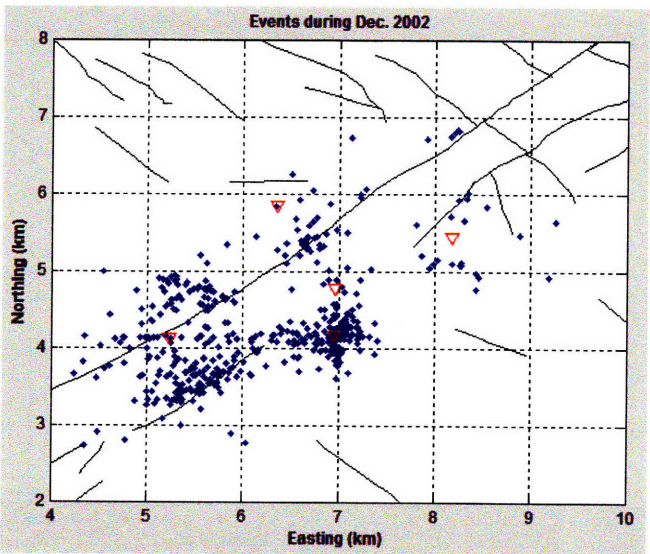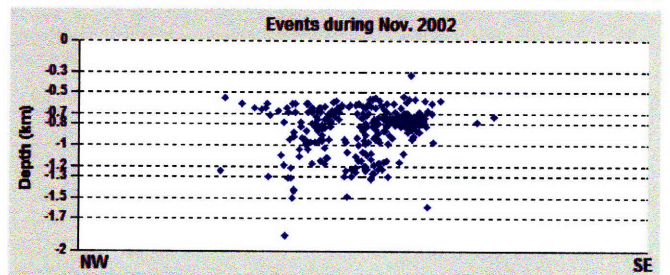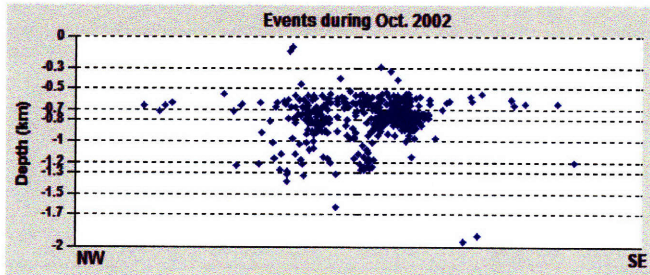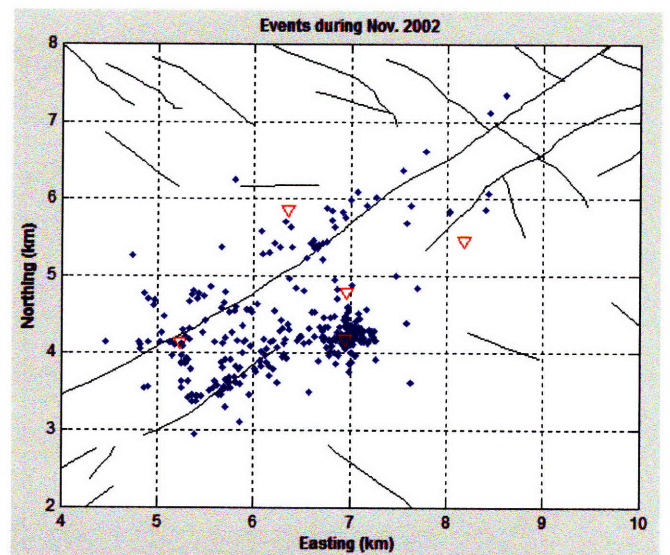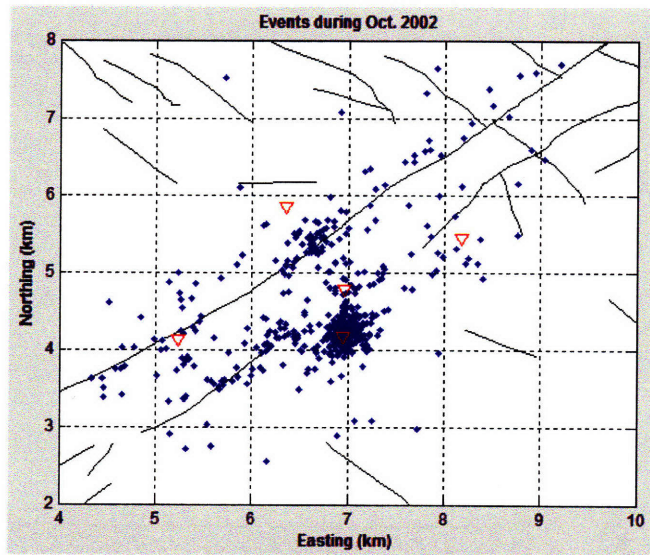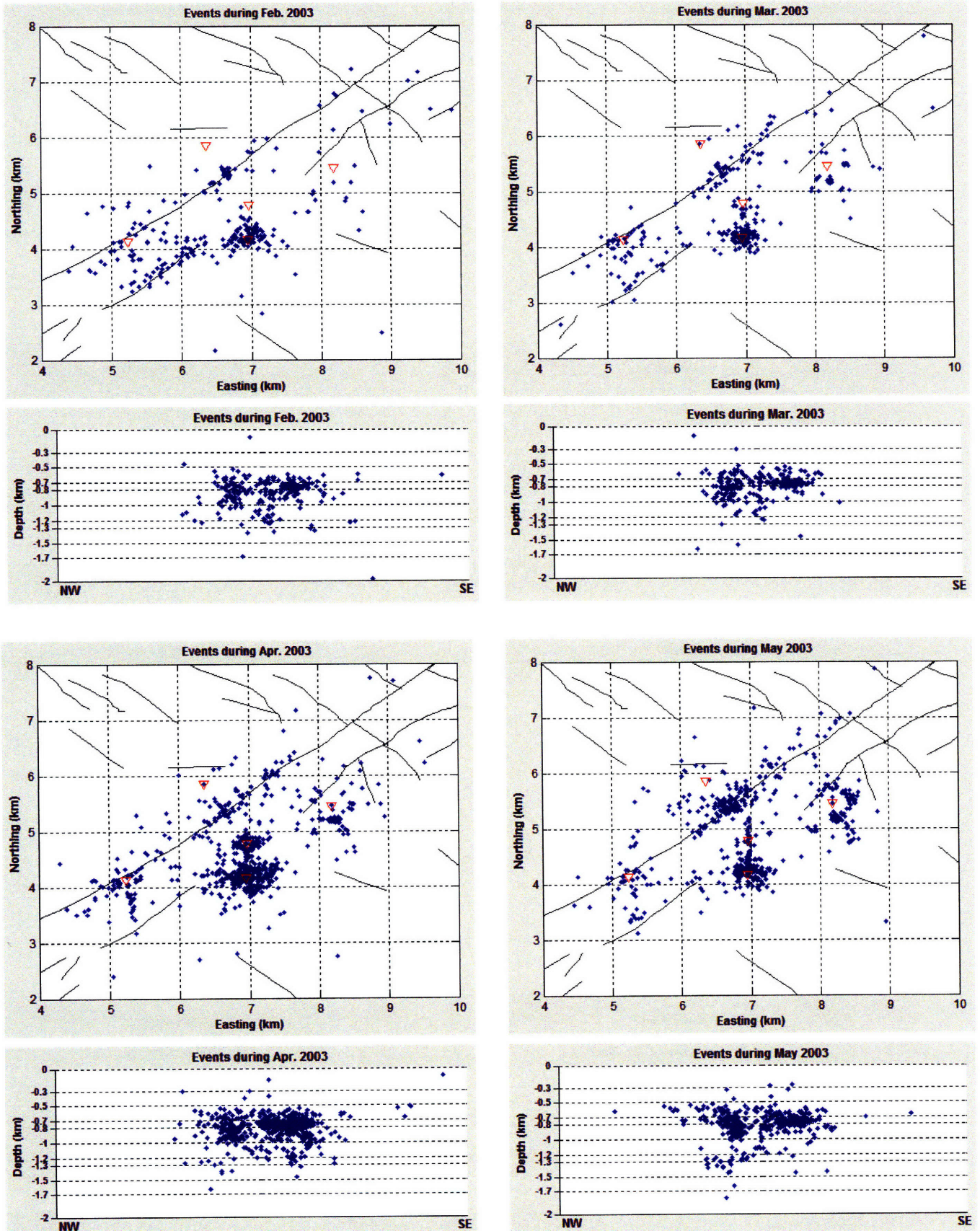
Figure 4.11: Monthly plot of seismicity locations (upper – epicenters, lower – depths)
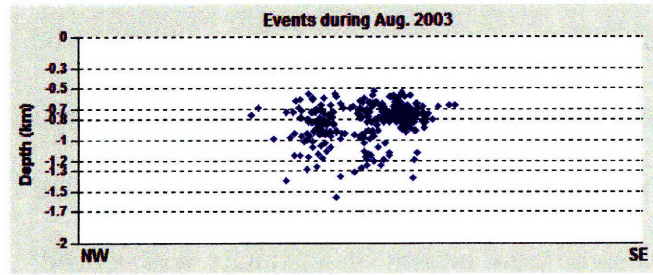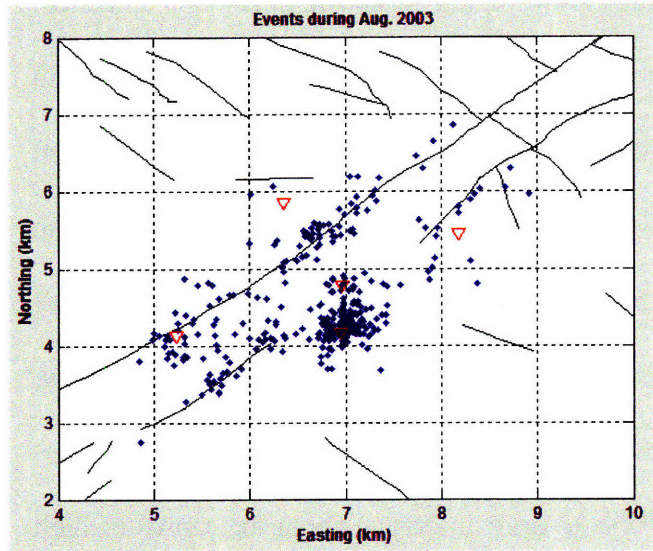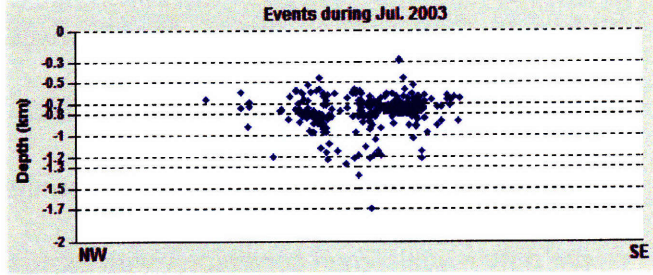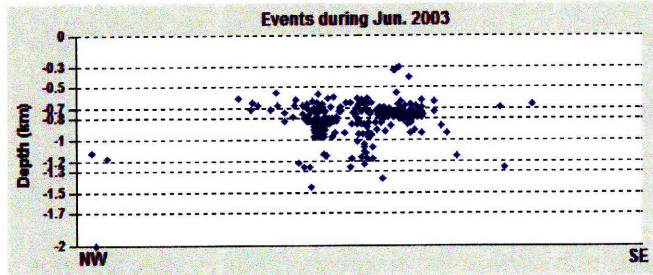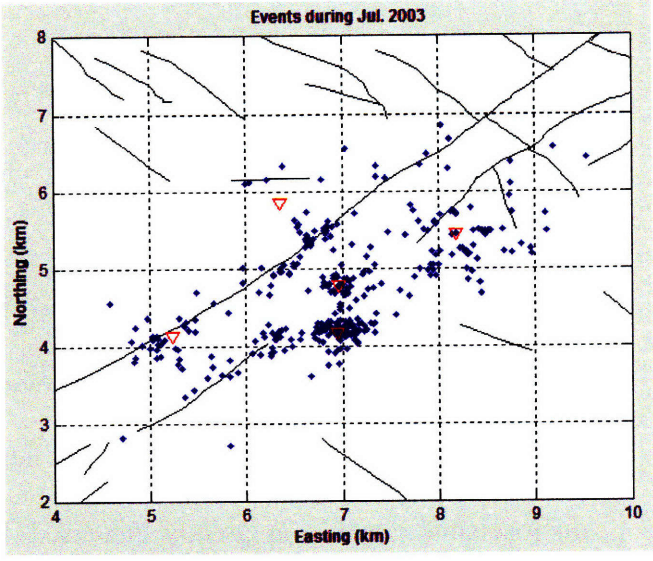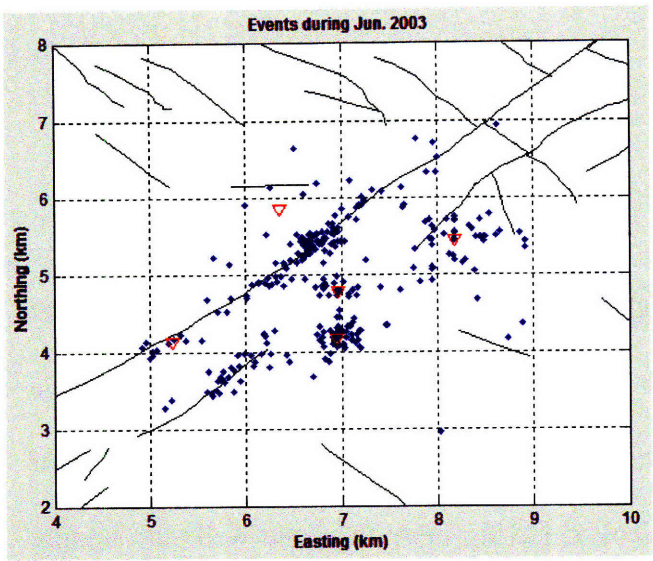
Figure 4.11 (cont'd): Monthly plot of seismicity locations (upper – epicenters, lower – depths).

4.7 Discussions and Conclusions

The deep-borehole seismic network installed in this field provided an excellent dataset for reservoir monitoring and characterization using induced seismicity. By placing the acquisition sensors in boreholes and in or near the (oil and gas) producing units, detectability of microseismic events was greatly increased. Moreover, having more than one well surrounding the seismically active zone greatly improved the location accuracy. For this study we located a subset of events from this extensive dataset, and used those locations to identify discrete spatial structures in the reservoir. As shown throughout the chapter, analysis of event locations in 3D not only reveals good correlation with existing fault maps, but also suggests features that had not been mapped before. The data also show that during the period when the data were collected, major fault systems crossing the field were being reactivated, causing fault slip across both Natih and Shuaiba reservoirs and through the overburden. As we did not have access to the detailed reservoir production and injection schedule and reservoir simulation results during the monitoring period, we were not able to make the most use of the seismicity data in terms of correlating the seismicity with processes such as water front movement, fracture dominated flow, compartmentalization due to faulting, etc. However, by analyzing the event locations – especially their depths – in great detail, we were able to draw inference about the causes of fault reactivation. For example, the majority of the fault slip or seismicity in the field was likely to be induced primarily by depletion of the Natih gas reservoir. Water injection into the Shuaiba reservoir assisted and extended the range of fault reactivation below Natih. In the south-western side of the field, between the two major faults a significant amount of seismicity was noticed. This might have created small-scale faults and/or dense fractures in that region. The general

pattern of seismicity and its correlation with structures from the deep-network data are consistent

with the interpretation from the shallow-network data (Chapter 3).

4.8 References

Fehler, M., W. S. Phillips, R. Jones, L. House, R. Aster, and C. Rowe (2000), A method for improving relative earthquake locations, *Bull. Seism. Soc. Am.*, 90, 775 – 780.

Jones, R. H. and H. Asanuma (2004), Optimal Four Geophone Configuration, Vector Fidelity and Long-Term Monitoring, *Proceedings of EAGE 2004*, Paris, June 2004.

Jones, R.H., and R. Stewart (1997), A method for determining significant structures in a cloud of earthquakes, *J. Geophys. Res.*, 102, 8245-8254.

Jones, R.H., D.G. Raymer, G. Mueller, G. Rynja, and K. Maron (2004), Microseismic Monitoring of the Yibal Oilfield, *Expanded Abstracts - 66th EAGE Annual Conference*, Paris, France.

Lomax, A., J. Virieux, P. Volant, and C. Berge (2000), Probabilistic earthquake location in 3D and layered models: introduction of a Metropolis-Gibbs method and comparison with linear locations, in 'Advances in Seismic Event Location', Kluwer Academic Publishers, Amsterdam, The Netherlands, 101-134.

Phillips, W. S. (2000), Precise microearthquake locations and fluid flow in the geothermal reservoir at Soultz-ous-Forets, France, *Bull. Seismol. Soc. Am.*, 90, 212-228.

Rowe, C., R. Aster, R. Jones, B. Borchers, and M. Fehler (2002), Using automated high-precision repicking to improve delineation of microseismic structures at the Soultz geothermal reservoir, *Pure. Appl. Geophys.*, 159, 563 – 596.

Sarkar, S. and M. N. Toksoz (2008), Location of and Monitoring with Induced Earthquakes in Oil and Gas Fields, *70th EAGE Conference & Exhibition incorporating SPE EUROPEC 2008*, Rome, Italy.

Shapiro, S.A., E. Rothert, V. Rath, and J. Rindschwentner (2002), Characterization of fluid transport properties of reservoirs using induced microseismicity, *Geophysics*, 67 (1), 212-220.

Waldhauser, Felix, and W. L. Ellsworth (2000), A double-difference earthquake location algorithm: Method and application to the northern Hayward fault, *Bulletin of the Seismological Society of America*, 90, 1353-1368.

Chapter 5

Reservoir Imaging Using Induced Seismicity Data

5.1 Introduction

This chapter focuses on using double-difference relocation and tomography methods to relocate events and to obtain velocity and structural images of the reservoir. Data from both networks – discussed in Chapters 3 and 4 of this thesis – are used in this chapter. For the surface-network data, a waveform cross-correlation technique is used to identify events that belong to the same cluster. Waveforms of similar events are cross-correlated to get accurate differential travel times, which help improve event locations by the double-difference relocation technique. Better correlation of relocated events with faults is observed from application of this method to the surface-network events, and detailed velocity and structure images for the reservoir are obtained from application of tomography with the deep-network events.

5.2 Seismic Tomography Method

In this study, we use a double-difference (DD) seismic tomography method based of Zhang and Thurber (2003), which makes use of both absolute and more accurate relative arrival time data to jointly invert for both locations and velocity models. DD tomography is a generalization of double-difference (DD) location method of Waldhauser and Ellsworth (2000): it simultaneously solves for the three-dimensional (3-D) velocity structure and seismic event locations. DD tomography uses an evolving weighting scheme for the absolute and differential arrival times in order to determine the velocity structure progressively from larger scale to smaller scale. This method yields more accurate event locations and velocity structure near the source region than standard tomography, which uses only absolute arrival times (Thurber, 1983; Eberhart-Phillps, 1993; Thurber, 1993) It has the unique ability to sharpen the velocity image near the source region because of the combination of the higher accuracy of the differential time data and the concentration of the corresponding model derivatives in the source region (Wolfe, 2002). The latter results from the cancelation of model derivative terms where the ray paths from nearby earthquakes overlap away from the source region.

The DD tomography algorithm described by Zhang and Thurber (2003) uses P and S wave data to jointly invert for Vp, Vs, and event locations. Knowing 3D Vp/Vs variations is helpful for having a more complete characterization of the mechanical properties and geological strata. Vp/Vs variations could be determined directly from the Vp and Vs models if they have essentially identical quality. In cases where S-wave arrival data are less numerous and of poorer

quality than P-wave data, however, Vs would not be as well resolved as Vp, making the interpretation of Vp/Vs variations difficult (Eberhart-Phillips, 1990). For this study, we use a modified version of the DD tomography method, which solves for event locations, Vp, Vs, and Vp/Vs based on S-P travel times. A detail discussion of this particular method can be found in Zhang and Thurber (2008). We provide a summary of the method by the following paragraphs.

Vp/Vs variations can be determined by the inversion of S-P time differences (Walck, 1988; Thurber, 1993). By assuming the ray paths of P and S waves are identical, which is true when Vp/Vs is constant, Vp/Vs can be determined from S-P arrival times $Ts-Tp$, as follows (Thurber, 1993) -

$$T_s - T_p = \int_{path} \left(\frac{V_p}{V_s} - 1 \right) \frac{ds}{V_p} \tag{1}$$

where Ts and Tp are S and P wave arrival times at one station, respectively. Since P and S waves from the same event share the same origin time, the unknown origin times are removed from this equation. During the inversion, the Vs values can be updated using Vp values and Vp/Vs ratios to calculate S wave ray paths for the next iteration, however, this results in an approximation in equation (1) due to the differing paths for the P and S waves (Thurber and Eberhart-Phillips, 1999).

However, in case of a complicated geological area, the P and S ray paths may differ significantly and thus the results may be biased when equation (1) is applied to them. To reduce

the effect of the assumption of similar ray paths for P and S waves, two strategies are implemented in our inversion algorithm: 1) at each iteration, ray paths for P and S waves are checked and subsequently removed from the Vp/Vs inversion if they are considerably different and 2) differential S-P times from event pairs at common stations are used in the same way as DD tomography to determine Vp/Vs ratios. For strategy (1), the ray paths are calculated based on the velocity models determined directly using P- and S-wave data. We do not obtain the Vs model using Vp values and Vp/Vs ratios since this method may result in biased Vs values (Wagner *et al.*, 2005). For strategy (2), by using the differential S-P times, we can remove the effect of different ray paths of P and S waves outside the source region. Near the source region, P- and S-wave ray paths are generally closer to each other.

Based on equation (1), the differential S-P arrival time residuals from event i to station k can be linearly related to the perturbations of event locations and Vp/Vs ratios, as follows (Zhang and Thurber, 2008):

$$dr_{kSP}^i = (T_{kS}^i - T_{kP}^i)^{obs} - (T_{kS}^i - T_{kP}^i)^{cal} = \sum_{l=1}^{3} \frac{\partial T_{kS}^i}{\partial x_l^i} \Delta x_l^i - \sum_{l=1}^{3} \frac{\partial T_{kP}^i}{\partial x_l^i} \Delta x_l^i + \int_i^k \delta(Vp/Vs) \, ds \Big/ Vp \qquad (2)$$

where $(Ts-Tp)^{cal}$ is the calculated differential time between the S and P wave arrival time at a given station, $(Ts-Tp)^{obs}$ is the observed differential time, $\delta(Vp/Vs)$ is the perturbation to Vp/Vs, and ds is an element of path length. Similar to the equations of DD tomography, we subtract a similar equation for event j observed at station k from equation (2), as follows,

$$dr_k^{i,j}{}_{SP} = dr_{kSP}^i - dr_{kSP}^j = \sum_{l=1}^{3}\left(\frac{\partial T_{kS}^i}{\partial x_l} - \frac{\partial T_{kP}^i}{\partial x_l}\right)\Delta x_l^i - \sum_{l=1}^{3}\left(\frac{\partial T_{kS}^j}{\partial x_l} - \frac{\partial T_{kP}^j}{\partial x_l}\right)\Delta x_l^j$$
$$+ \int_i^k \delta(Vp/Vs)\frac{ds}{Vp} - \int_j^k \delta(Vp/Vs)\frac{ds}{Vp} \tag{3}$$

where

$$dr_k^{i,j}{}_{SP} = (T_{kS}^i - T_{kP}^i)^{obs} - (T_{kS}^i - T_{kP}^i)^{cal} - (T_{kS}^j - T_{kP}^j)^{obs} + (T_{kS}^j - T_{kP}^j)^{cal}$$
$$= (T_{kS}^i - T_{kS}^j)^{obs} - (T_{kP}^i - T_{kP}^j)^{obs} - (T_{kS}^i - T_{kS}^j)^{cal} + (T_{kP}^i - T_{kP}^j)^{cal} \tag{4}$$

Equation (3) shows that the Vp/Vs structure can be directly imaged by using the differential P and S arrival times. More accurate differential times can be calculated from waveform cross-correlation techniques for similar waveforms.

5.3 On the Relocation and Tomography using Data from the Shallow Network

Locations of induced seismic events recorded by the near-surface (shallow) PDO network were derived using travel-time based single-event location techniques of Sarkar and Toksöz (2008), and Lomax *et al.* (2000). The arrival times for first P and S-phases had been manually picked. In cases where the signal to noise ratio is low, we expect there to be noise in both P and S picks. As a result, the locations may not be accurately determined. In this section, we show use of the cross-correlation techniques to measure the delay times between event pairs based on their waveform similarity. By using cross-correlation delay times, we can calculate accurate

differential arrival times between event pairs observed at the same stations and then use the double-difference location and tomography methods to determine better seismic locations and velocity model.

5.3.1 Multiplet Analysis using Full-Waveform Cross-Correlation

Seismic multiplets are a group of events that have very similar waveforms and thus very similar source mechanisms and nearly identical locations. In passive seismic monitoring, identification of multiplets serves mainly two purposes: 1) they help us with validation of our locations and 2) they help us with temporal characterization of induced seismicity. To identify microseismic multiplets, we performed full waveform cross-correlation between traces of all pairs of events observed at the same station. The traces were filtered to the same bandwidth before cross-correlation. A very high threshold for the correlation-coefficient (greater than 0.95) was chosen to identify multiplets. Figure 3 shows some waveforms from a set of multiplets. The events in this multiplet set spanned from 1999 to 2004, indicating certain locations of the faults have continued to trigger earthquakes at various time intervals.
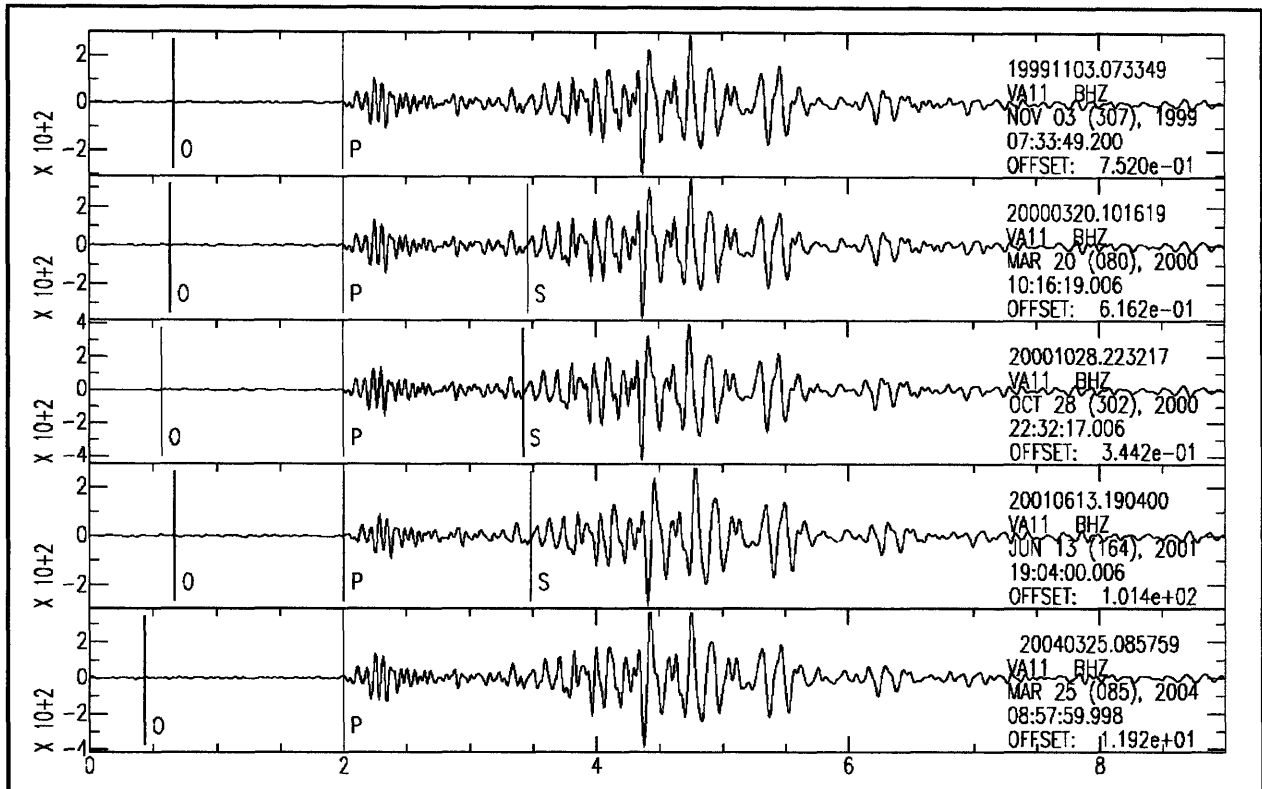
Figure 3: Seismograms of microseismic multiplets, all filtered to the same bandwidth, are shown for the same station. These events were triggered at different times, from 1999 – 2004.

5.3.2 Waveform cross-correlation using the bispectrum (BS) method, BCSEIS

Researchers using cross-correlation (CC) to align waveforms often choose those time-delay estimates with CC coefficients above a specified threshold. For example, Schaff et al., (2002) only select those time delays with CC values larger than 0.70 and mean coherences above 0.70. The selection of an optimum threshold value for waveform cross-correlation is important but difficult. If it is set too high, then only a limited number of very accurate differential time data are available for further analysis. If the threshold value is set too low, then many unreliable

differential time estimates are found which will negatively affect the relocation and tomography results.

The BCSEIS algorithm that we adopted for measuring waveform CC times works in the third-order spectral domain and can suppress correlated Gaussian or low-skewness noise sources (Nikias and Raghuveer, 1987; Nikias and Pan, 1988). BCSEIS employs a third-order spectral method to calculate two additional time delay estimates with both the raw (unfiltered) and band-pass filtered waveforms, and uses them to verify (select or reject) the one computed with the CC technique using the filtered waveforms (Du et al., 2004). Thus this BS verification process can reject unreliable CC time delay estimates and also can accept additional CC time delays even if their associated CC coefficients are smaller than a nominal threshold value if they pass the BCSEIS verification procedure (Du et al., 2004).

Using the BCSEIS, we cross-correlated a set of ~ 1300 events recorded by the PDO shallow network during November 1999 – February 2007. We measured 112910 differential P and S times from 71856 event pairs. Among them 26% are S times and 74% are P times. A subset of these cross-correlated differential travel times (P and S) are used in the double-difference (DD) relocation of shallow-network events.

169

5.3.3 Double-difference Relocation and Tomography using Cross-correlation Times

Before attempting to do seismic tomography using induced seismic event data recorded by the near-surface network, we investigated the source-receiver ray paths for the 1D velocity model derived from sonic logs. It is observed that most ray paths do not cross, making it difficult to use a seismic tomography approach to determine a reliable velocity model using the surface network (Figure 4).
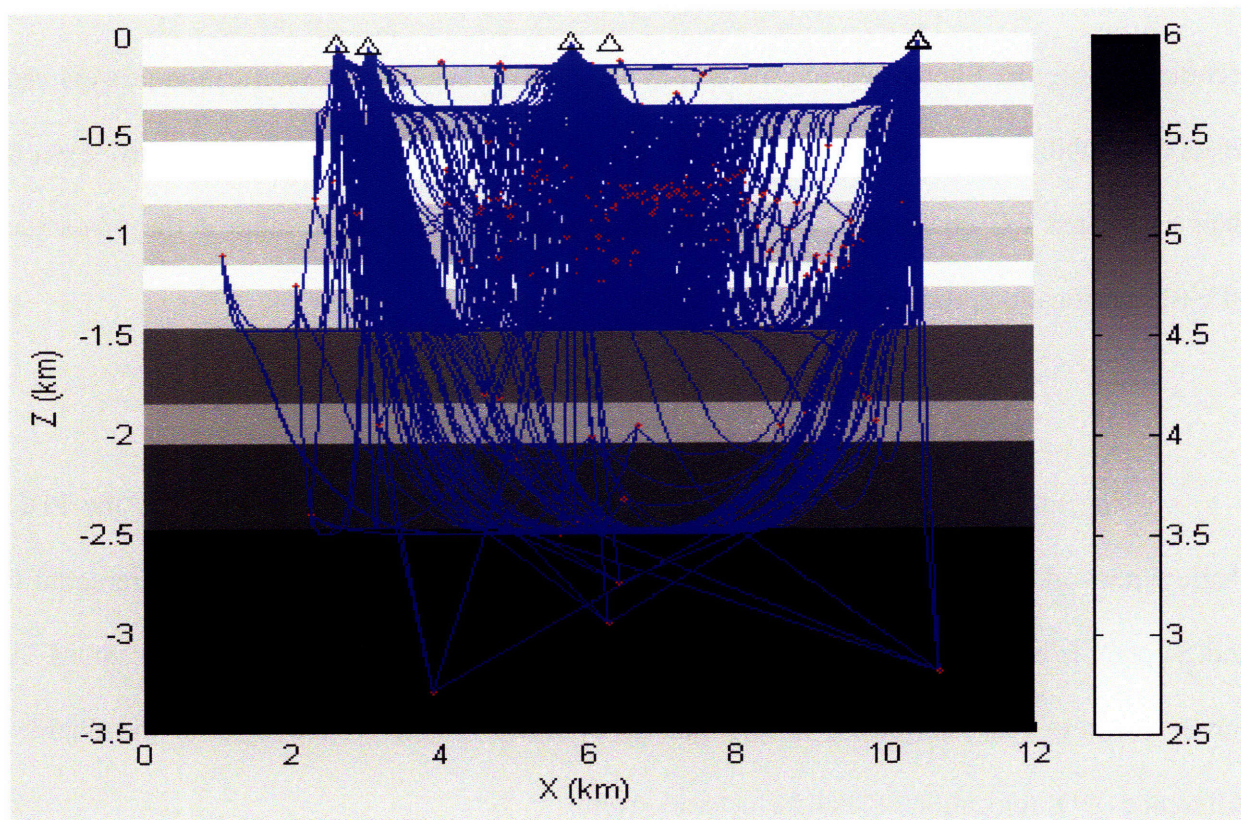
Figure 4: Source-receiver ray paths (blue curves) for events recorded by the near-surface network, projected on a vertical (X-Z) plane. Red dots denote locations of events, and black triangles are seismic stations. Plotted in grayscale on the background is the layered velocity

model derived from Sonic log for induced seismicity analysis in this reservoir. The colorbar to the right shows magnitudes of the velocity.

For the current distribution of stations and events, obtaining reliable estimates of velocity perturbations using the DD tomography method would not be possible. However, it may still be meaningful to relocate the events using the DD relocation method. It is generally true that a multiple event location method such as double-difference (DD) improves the relative accuracy of event location within a cluster. Locations obtained by single event location methods such as Station-pair-differencing (Sarkar and Toksöz, 2008) or NonLinLoc (Lomax et al., 2000) are good for overall and primary analysis of induced seismicity in the field, however by using cross-correlation times and a relative event location method such as DD it is possible to further collapse the events within a cluster and thus improve the fault images. Single event location methods such as the ones used in this study use absolute arrival time data, whereas the multiple/relative event location method can use both absolute and differential time data – obtained from catalogue (initial picks) and also from cross-correlated waveforms. In this section, we show applications of double-difference location technique to the induced seismicity data and compare the results with two single event location techniques that were discussed in the previous chapters.

We selected a subset of 673 events having at least four P-arrivals from the November 1999 – February 2007 shallow network dataset and located them using four different methods – NonLinLoc, Station-pair-differencing, double-difference, and double-difference for joint

velocity-location inversion (tomography). For NonLinLoc location both P- and S-picks were used, while for the station-pair-differencing method only P-picks were used. The double-difference locations used NonLinLoc results as the initial locations, however S-wave travel times were further down-weighted during the double-difference relocation. The NonLinLoc location results are shown in blue dots by Figures 5.a, 5.b, and 5.c. The event epicenters obtained using NonLinLoc are in good agreement with the existing fault maps (Figure 5.a) in general, however quite a bit of scatter in their locations is observed in some areas – especially towards the south/south-west side of the field. By using the Station-pair-differencing approach, we were able to reduce much of the scatter in both epicenter and depth locations of the same events. These location results are shown by red dots on Figures 5.a, 5.b, and 5.c. As seen from these figures (comparison of red and blue dots), the event clustering and their correlation with faults are much improved by the Station-pair-differencing location technique as compared to the NonLinLoc location method.

Next, we relocate the same events using the double-difference tomography method developed by Zhang and Thurber (2003). In the double-difference method, we apply both non-tomographic (location only) and tomographic (joint velocity-location) inversions. In both cases, we use NonLinLoc derived solutions as the initial locations, and the same Sonic log-derived 1D layered velocity model used for single-event locations as the initial model for the velocity. First, we use double-difference method to determine the seismic event locations only, without inverting for the velocity model. The location results from this method are plotted by green dots on Figures 5.a, 5.b and 5.c, which show quite a bit of improvement over the initial NonLinLoc locations (blue dots on the same Figures) – double difference event locations are seen to be much

less scattered and more concentrated along the faults. On the epicenter plot (Figure 5.a), for example, the event locations are more precise than the initial NonLinLoc (and also the Station-pair-differencing) locations as they show better correlation with existing faults. To the north-east of the divide on the southern fault, event alignment with the fault traces is improved due to the double-difference relocation. The relocated event epicenters also show better alignment with the fault map to the north (green dots, Figure 5.a) than the initial epicenters (blue and red dots, Figure 5.a). In fact, in the middle of the reservoir grid and on the northern fault there appear two very closely spaced yet distinct lineations – features that remain undistinguished by both the single event location methods. Another improvement by the DD relocation is seen on the fault-strike-perpendicular depth-section view, where the two known major faults can be more clearly traced by the event locations (green dots, Figure 5.c) as compared to the depth-section view obtained along the same plane resulting from the single-event location methods (blue/red dots, Figure 5.c).

The event locations are arguably further improved by performing a joint inversion for velocity and hypocentral parameters using both absolute and differential times. Although the surface network cannot be used to reliably determine the velocity model due to inadequate ray coverage (Figure 4), yet the advantage of including the velocity inversion in the double-difference location method is that it allows some sort of compensation for the path anomaly caused by the inaccuracy in the velocity model. In other words, the velocity tomography acts to create a set of "station corrections" that can absorb bulk shifts that are due to path heterogeneities. Therefore, by using a joint hypocenter-velocity inversion, the absolute locations of seismic events are likely to be improved. Locations determined using this method are shown

by magenta dots on Figures 5.a, 5.b and 5.c. Among the two double-difference location methods, the tomographic method yields sharper features than the non-tomographic method. On the epicenter map (Figure 5.a), the magenta dots appear to be less scattered and have better correlation with existing fault maps than the green dots within the clusters, thereby suggesting improvement in relative accuracy of the events.

Moreover, among the two double-difference solutions (magenta and green), the epicenter locations shown by magenta are more similar to the epicenter locations shown by red (which is more accurate among the two single-event location methods). For example, a NW-SE trending feature cutting across the two main faults in the middle of the reservoir grid can be identified in both red and magenta epicenter maps, whereas it is not distinguishable by either the blue (initial locations) or green (non-tomographic double-difference relocation) epicenter maps. Similarities between the two epicenter maps in magenta and blue (Figure 5.a) suggest that by adopting a joint velocity-location inversion approach (double-difference tomography in this study) for event relocation, we were able to improve the event locations – in both relative and absolute sense.
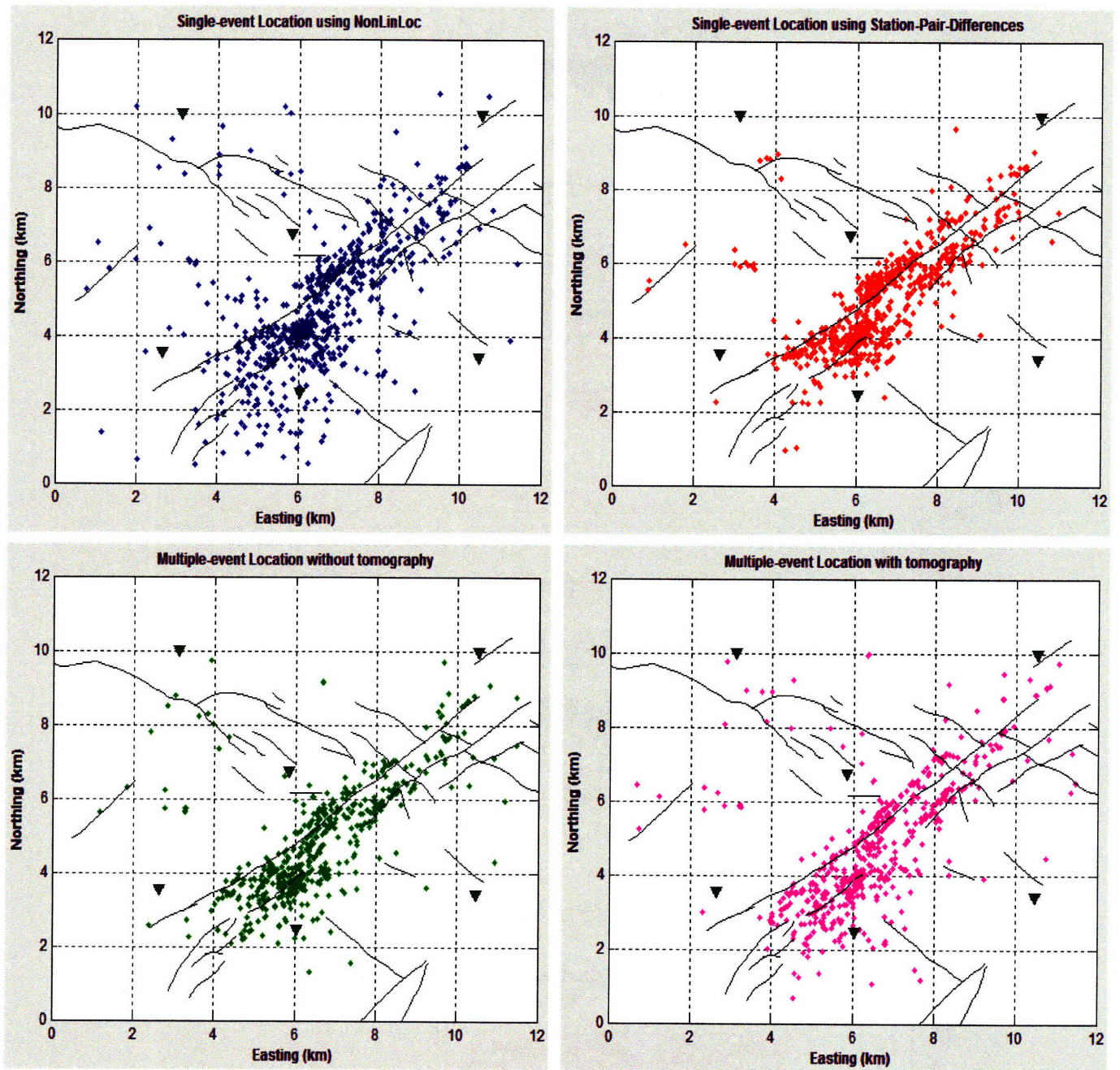
Figure 5.a: Comparison of event epicenter locations between 4 different methods: Upper left – NonLinLoc (blue, # of events plotted: 663); Upper right – Station-pair-differencing (red, # of events plotted: 671); Lower left – DD without tomography (green, # of events plotted: 618); Lower right – DD with tomography (magenta, # of events plotted: 642).
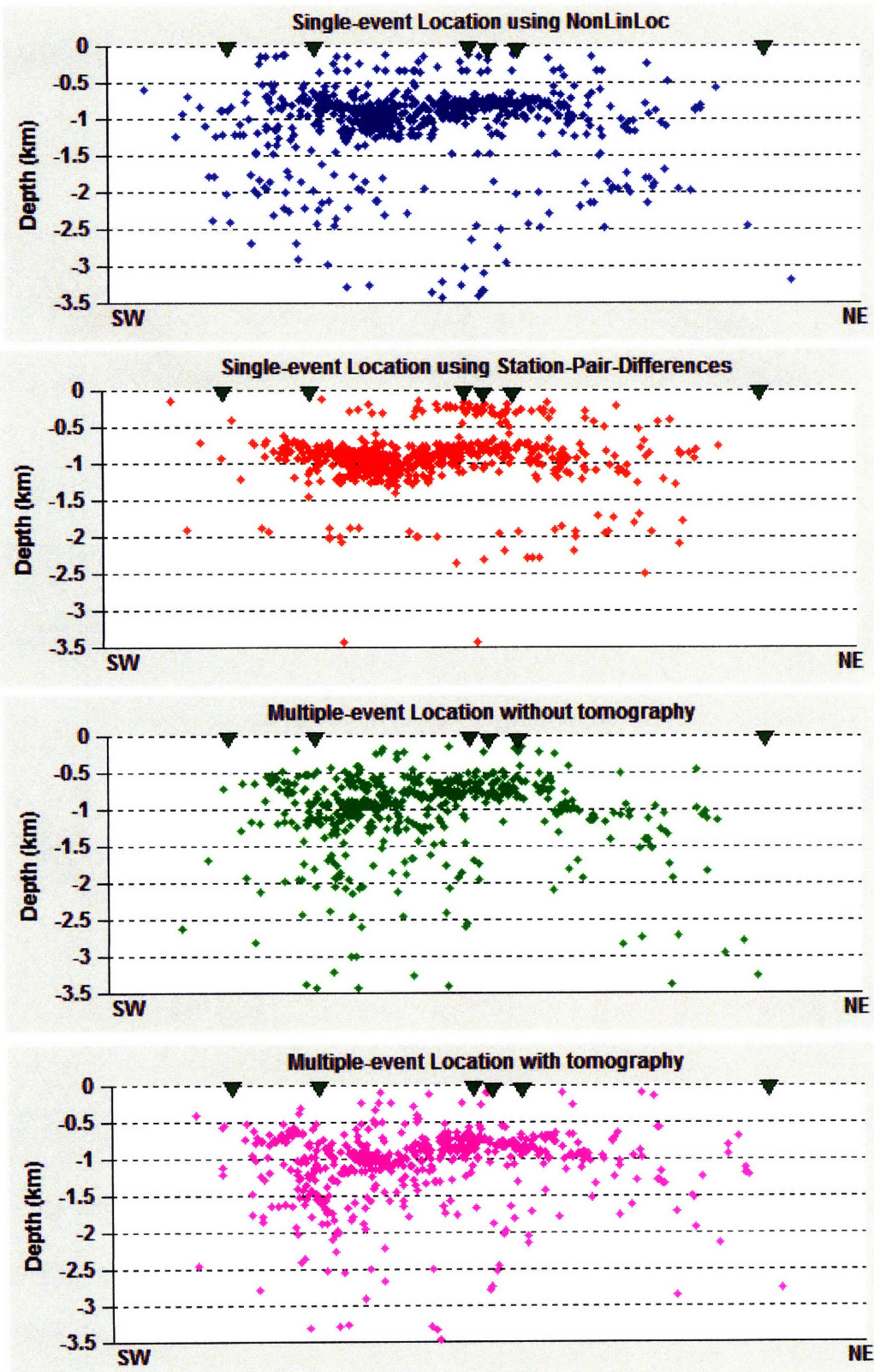
Figure 5.b: Comparison of event depths, plotted along a plane parallel to the major strike direction (NE-SW) of the main faults, obtained by 4 different methods: from Top to Bottom – NonLinLoc (blue), Station-pair-differencing (red), DD without tomography (green), and DD with tomography (magenta).

176
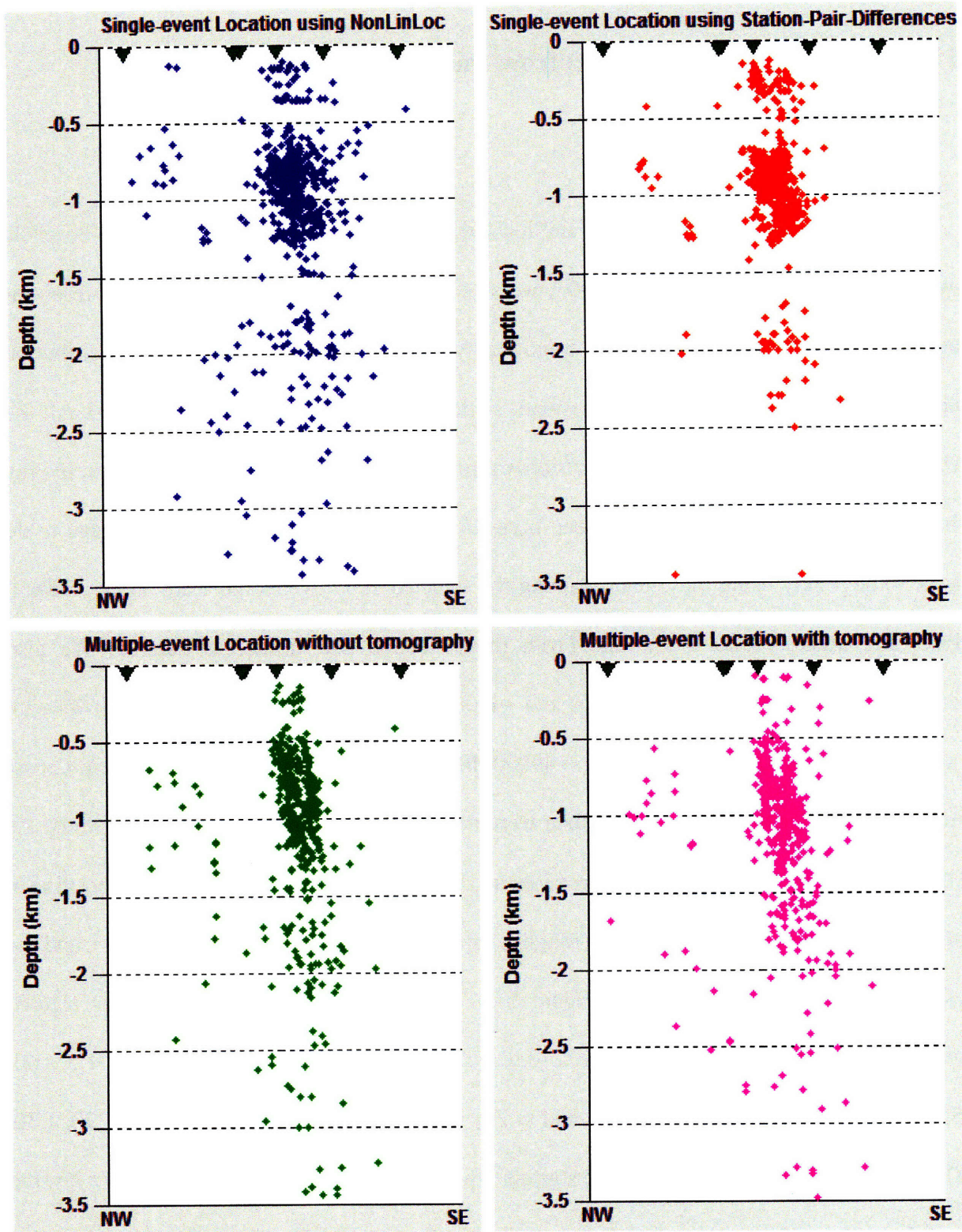
Figure 5.c: Comparison of event depths, plotted along a plane perpendicular (NW-SE) to the major strike direction of the main faults, obtained by 4 different methods. Ordering and color scheme of the plots are the same as Figure 5.a.

177

5.4 Reservoir imaging using Data from the Deep Network

Out of ~ 5,400 events analyzed and located for reservoir monitoring with deep-borehole network during Oct 2002 – August 2003, we selected 1999 microseismic events for reservoir imaging using the double-difference tomography method. The selected event distribution (epicenters and depths), and the deep-network stations are shown by Figures 6 (*a* & *b*). All the selected events have at least 12 P and/or S arrival time picks. Unlike the surface network, the ray paths from the induced events to the deep network stations provide good, even coverage to do seismic tomography using these data. Among the selected 1999 events there are about 25000 P arrivals and about 11800 S arrivals. From them ~11800 S-P times are derived. We also constructed ~143000 differential P times and ~49000 differential S times from event pairs with an average offset of 180 m. From them, ~49000 differential S-P times were constructed. Cross-correlation times for the deep network data were not available during the time of this study. As for the coordinate system used in the inversion, a Cartesian system was set up with the positive Y axis oriented 50° clockwise from north (roughly parallel to the strike of the major faults), and the X axis oriented positive southeast (Figure 6-a). The inversion grid nodes (in this *rotated* coordinate system) are located at X = -1.1, -0.6, -0.3, 0, 0.3, 0.6 and 1.0 km, Y = -2.5, -1.5, -1.0, -0.5, 0, 0.8, 1.5, and 2.5 km (Figure 6), and at Z = 0.50, 0.60, 0.70, 0.80, 0.90, 1.10, 1.20, 1.30, 1.60, 1.80, 1.90, 2.00, and 2.20 km. The starting Vp model for tomography inversion is a layered model derived by on averaging 5 well-logs (Sonic) at 5 nearby wells (Figure 7). For the starting Vp/Vs ratio a constant of 1.92 is used.
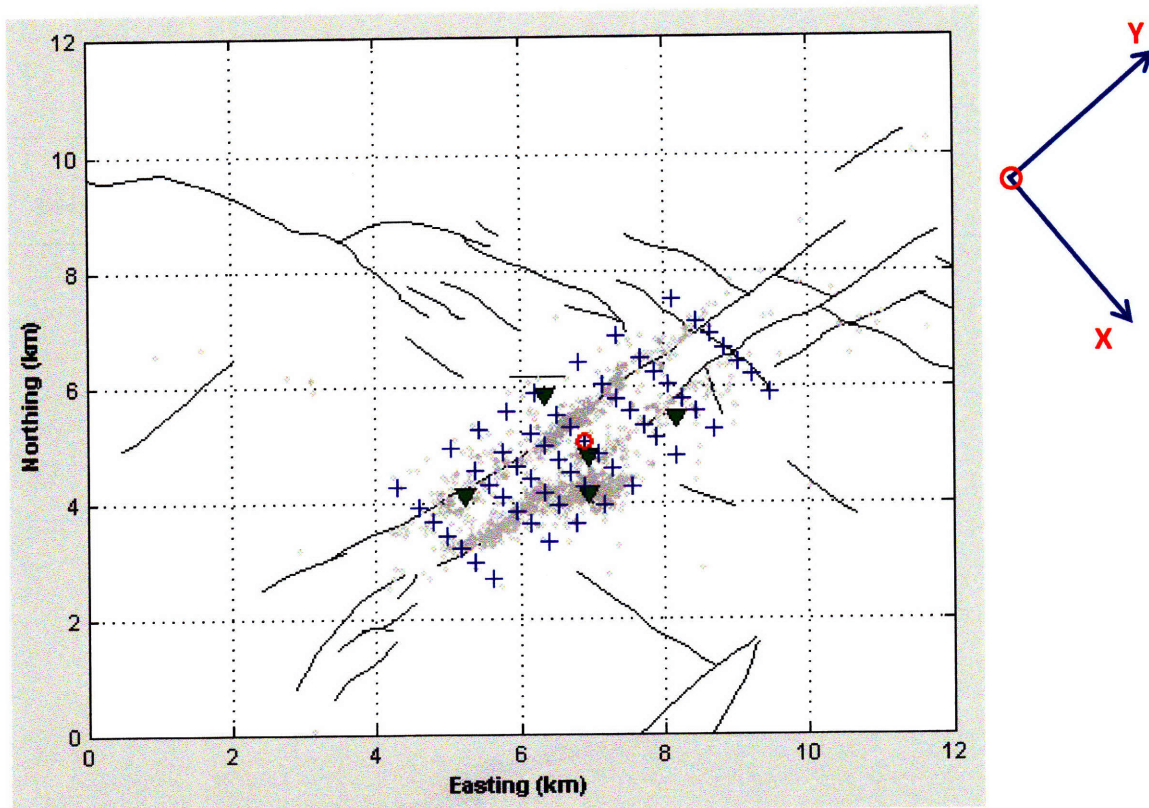
Figure 6 (a): Setup for double-difference tomography using deep-network data: events (grey dots), stations (green triangles), inversion grids (blue "+" symbols), and the center of the rotated coordinate system (red circle) – all shown in map view. Also shown are faults mapped from surface seismic in black lines, and a schematic diagram of the rotated coordinated system on the right.
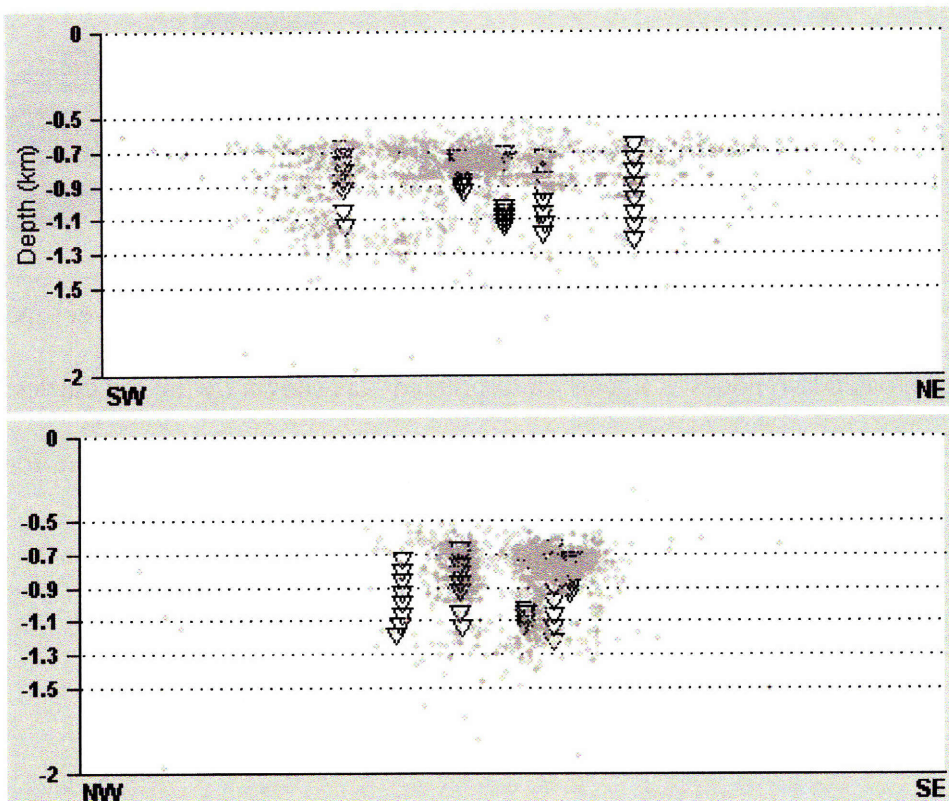
Figure 6 (b): Depths of events (grey dots) shown along strike (NE-SW) and normal to strike (NW-SE) direction. Stations shown in black triangles.
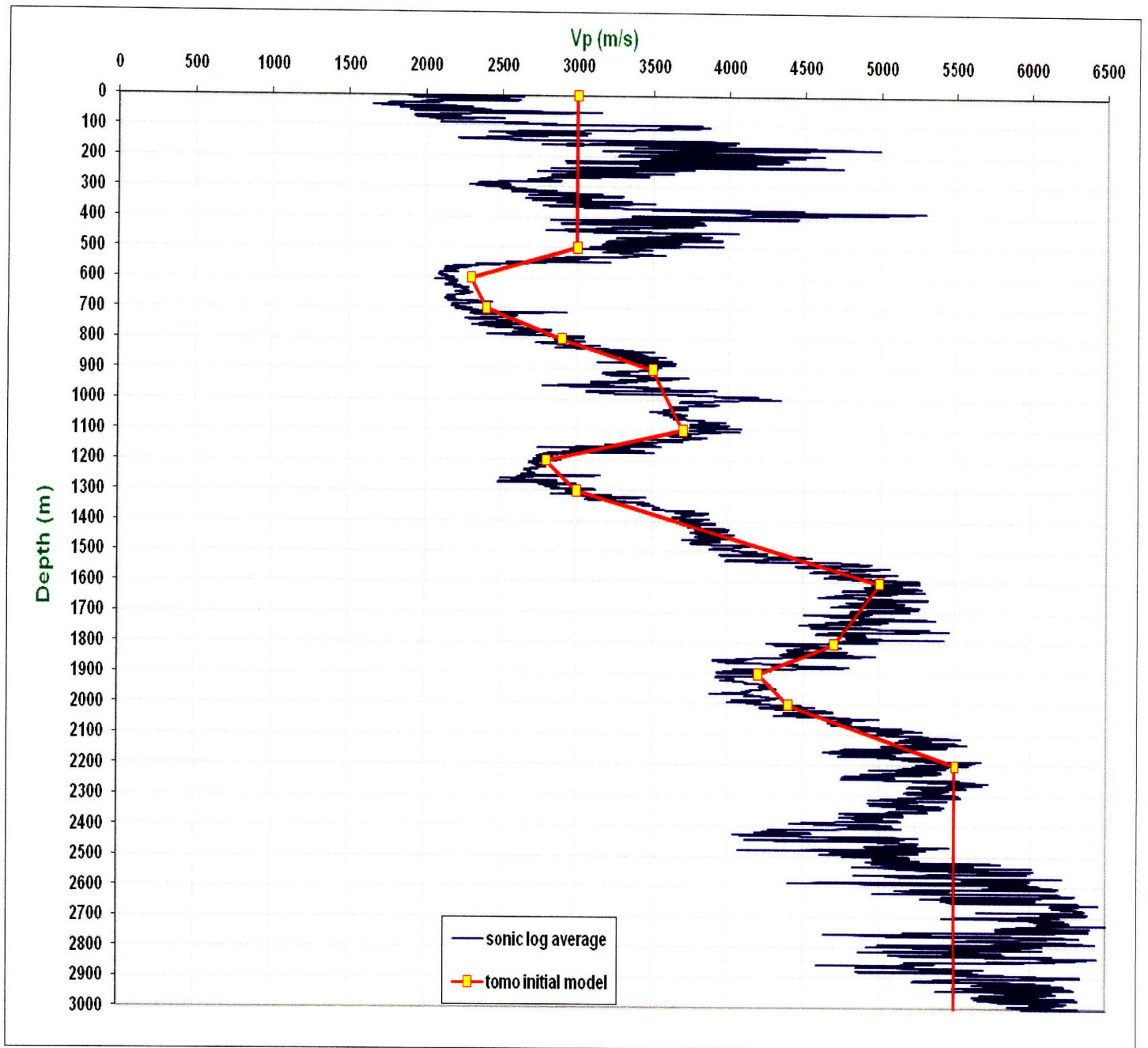
Figure 7: Initial P-wave velocity model for depth nodes shown by yellow squares. For travel time calculation, the velocity between two nodes is linearly interpolated – as shown by the red curves. Blue curve shows an average Vp derived from five Sonic logs, which serves as a guideline for selecting the depth nodes for inversion and the corresponding starting velocities.

5.4.1 Model Resolution Analysis

To check the model resolution, we used both the conventional checkerboard test (Humphreys and Clayton, 1988) and the strict resolution test based on the resolution matrix (Aki et al., 1977; Berryman, 2000; Zhang and McMechan, 1995; Minkoff 1996; Yao *et al,*. 1999; Vasco *et al.,* 2003). The X and Y coordinates of the plots used to show the model resolution test results (and also the tomoDD results) are of the rotated coordinate system as shown by Figure 6 (a).

5.4.1.1 Checkerboard Test

To create a checkerboard model, we added ±5% velocity anomalies to every other grid node in X and Y direction and to every other two grid nodes in Z-direction. Synthetic travel time data (absolute and differential) are generated for this checkerboard velocity model, which are subsequently inverted using the double-difference tomography method. As for the starting model for this "synthetic" inversion, we use the same initial model (shown by Figure 7) to be used for "real" inversion. By Figures 8 (panels *a – l*) we plot results from the checkerboard test, where on each panel we show comparison between the actual (checkerboard) and inverted model perturbations at different depths for P-wave velocity. On the inverted models, we also superimpose the DWS contours (plotted in blue and labeled in red). The DWS (derivative weight sum: Toomey and Foulger, 1989) is a statistical parameter that helps the assessment of parameter

resolution; it gives a measure of density of rays that pass near a grid point that is weighted according to how close each ray passes to the node. It is, therefore, superior to the more commonly quoted "hit" matrix, which is merely a count of the number of rays that pass close to the grid point. A large DWS indicates that the velocity at the grid point is based on a large body of data. The checkerboard test results help us examine where in the reservoir and how well the double-difference tomography method is likely to resolve the *actual* model. As seen by the plots of Figure 8, the best resolution is obtained between depths of $0.7 - 1.1$ km (panels $c - f$). On each plane, the DWS contour distributions indicate that the central part (high DWS) is much better resolved than the edges (low DWS) of the model. At or below $Z = 1.2$ km (panels $g - l$), and at or above $Z = 0.6$ km (panels $a - b$), the checkerboard recovery is very poor; therefore the actual inversion results at those depths should not be depended upon. The model parameters by the actual inversion, more or less, should be well resolved in the central part of the selected tomography region and between depths $\sim 0.6 - 1.1$ km, according to the checkerboard test.
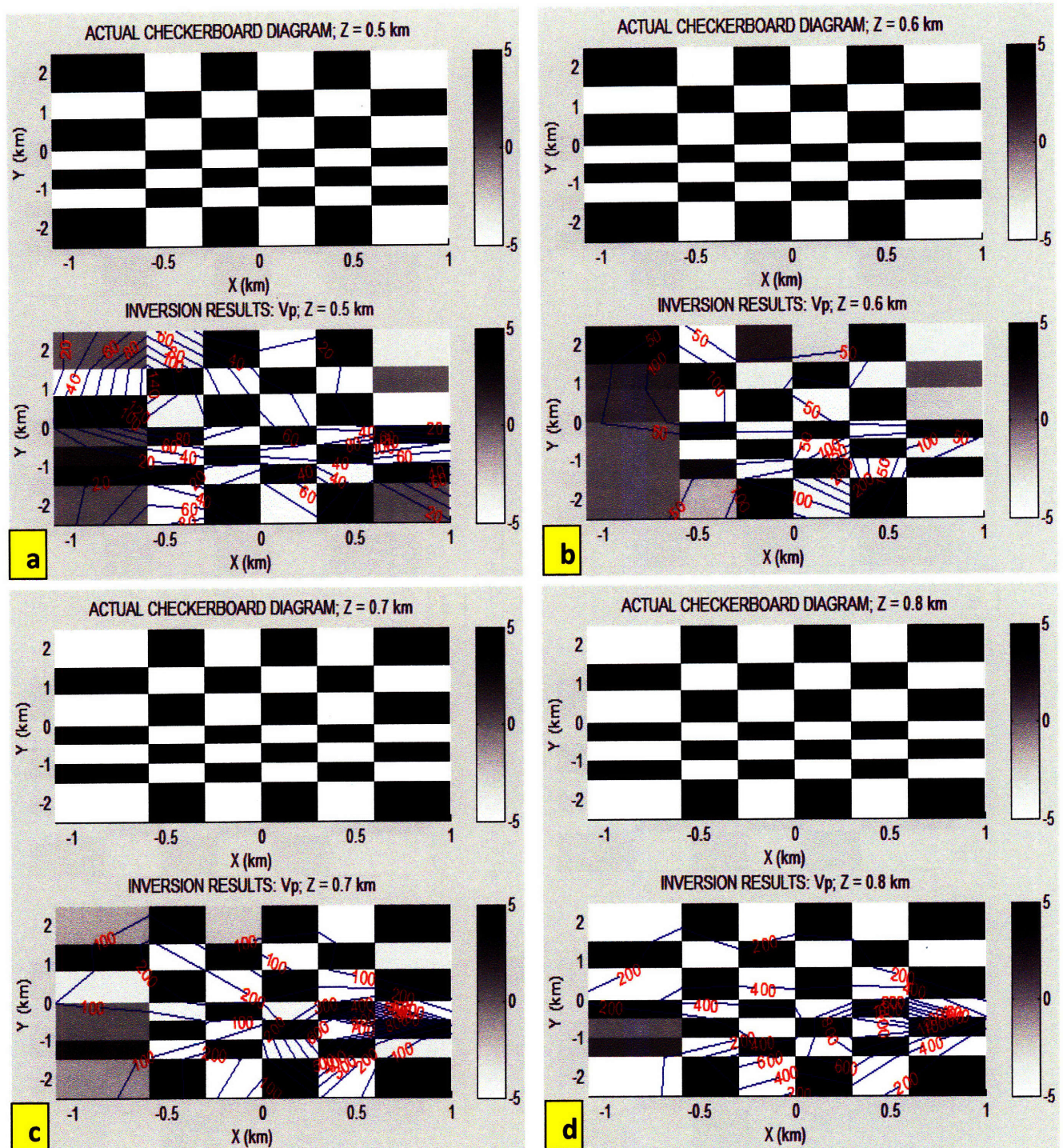
Figure 8 (a-d): Comparison between actual and inverted model perturbations at depths 0.5, 0.6, 0.7 and 0.8 km. DWS contours from inversion are plotted in blue and labeled in red. *c* and *d* show good match between inverted and actual results in most parts, whereas *a* and *b* show moderate recovery.

183
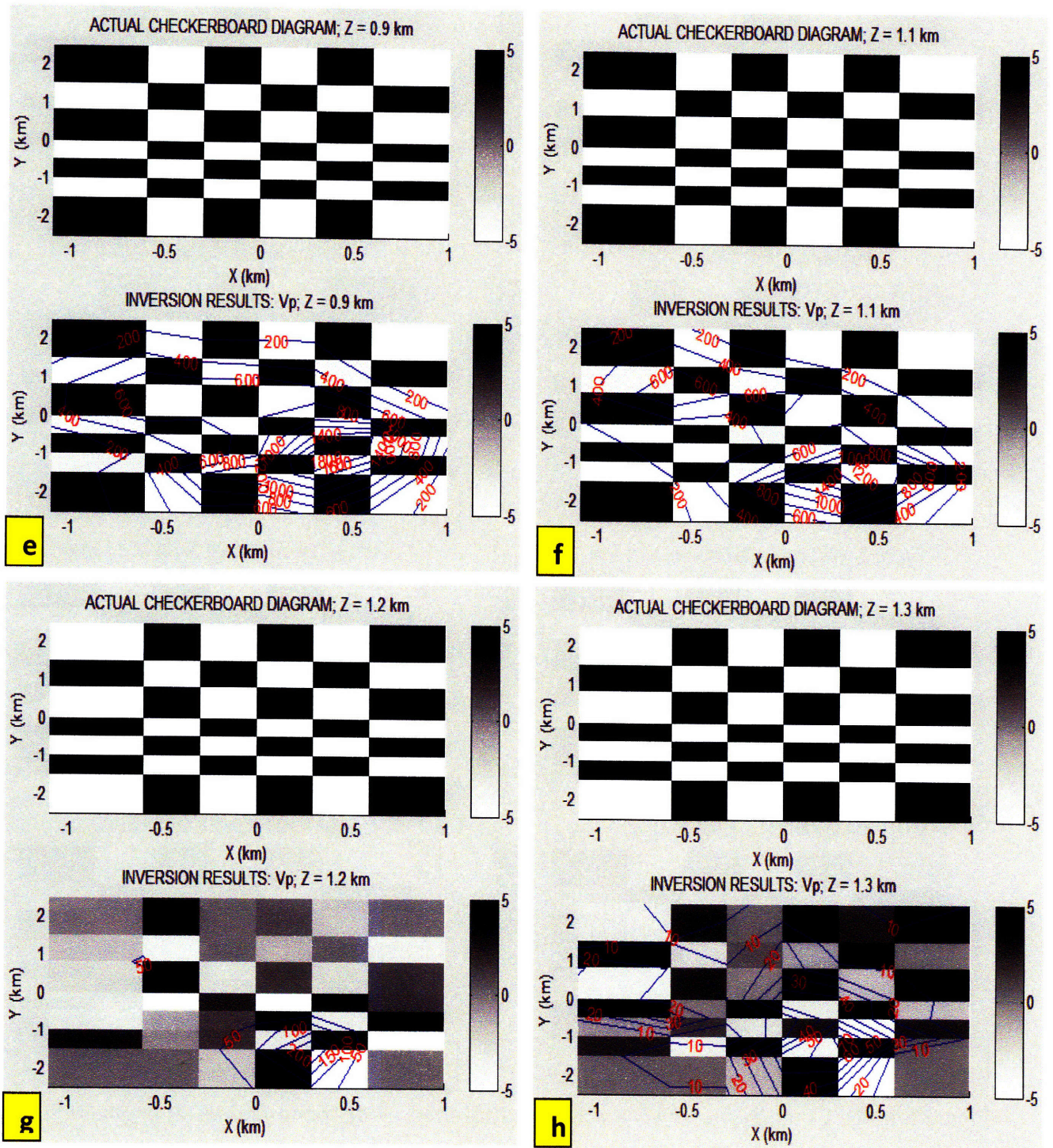
Figure 8 (e – h): Comparison between actual and inverted model perturbations at depths 0.9, 1.1, 1.2 and 1.3 km. DWS contours from inversion are plotted in blue and labeled in red. *e* and *f* show good match between inverted and actual results in most parts, whereas *g* and *h* show poor recovery.
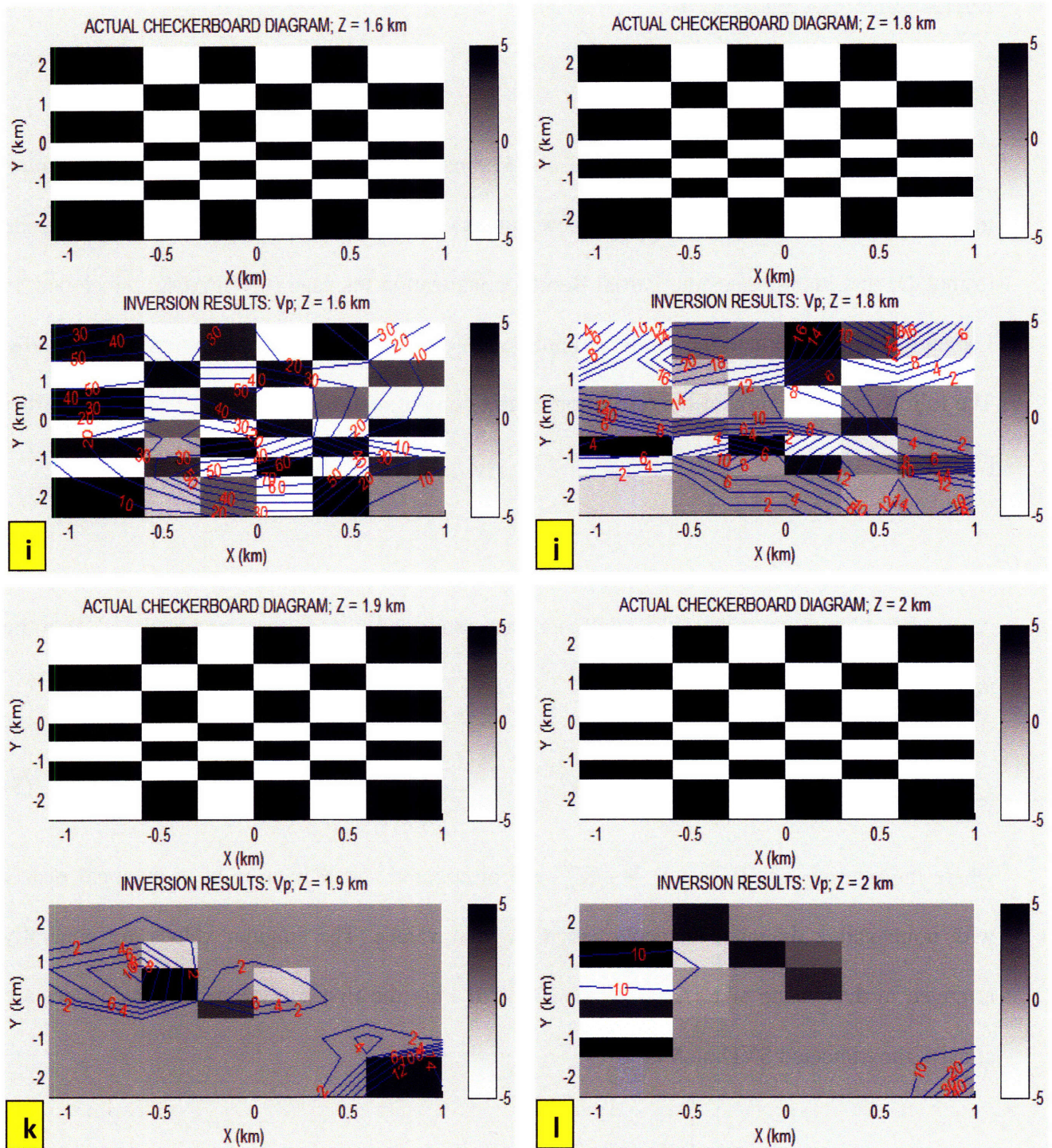
Figure 8 (i – l) : Comparison between actual and inverted model perturbations at depths 1.6, 1.8, 1.9 and 2.0 km. DWS contours from inversion are plotted in blue and labeled in red. *i* and *j* show moderate to poor match between inverted and actual results, whereas *k* and *l* show very poor recovery.

185

5.4.1.2 Resolution Matrix Test

In addition to doing the routine checkerboard test, we also computed the resolution matrix of the inverse problem using a new version of the double-difference tomography code (tomoDD) that incorporates the Partial Reorthogonalization Package (PROPACK) developed by Larsen (1998) to estimate the model resolution matrix for large seismic tomography problems. The following is a review of the resolution matrix computation method from Zhang and Thurber (2007).

For a linear inverse problem with m observations and n model parameters, the SVD of the m by n sensitivity matrix $\mathbf{A}$ is

$$\mathbf{A} = \mathbf{USV}^{\mathrm{T}} = \sum_{i=1}^{n} s_i \mathbf{u}_i \mathbf{v}_i^{\mathrm{T}} , \tag{5}$$

where the matrices $\mathbf{U} \in \mathbf{R}^{m \times m}$ and $\mathbf{V} \in \mathbf{R}^{n \times n}$ are orthogonal and $\mathbf{S}$ is an m by n diagonal matrix with nonnegative diagonal elements called singular values. The singular values are generally arranged in decreasing size (Aster $et\ al.$, 2005). If only the first p nonzero singular values are chosen, the truncated SVD of $\mathbf{A}$ is

$$\mathbf{A} = \mathbf{U}_p \mathbf{S}_p \mathbf{V}_p^{\mathrm{T}} = \sum_{i=1}^{p} s_i \mathbf{u}_i \mathbf{v}_i^{\mathrm{T}} . \tag{6}$$

The pseudoinverse of $\mathbf{A}$ is then given by

$$\mathbf{A}^{-1} = \mathbf{V}_p \mathbf{S}_p^{-1} \mathbf{U}_p^{\mathrm{T}} . \tag{7}$$

186

The resolution matrix **R** is represented as

$$\mathbf{R} = \mathbf{A}^{-1}\mathbf{A} = (\mathbf{A}^{\mathrm{T}}\mathbf{A})^{-1}\mathbf{A}^{\mathrm{T}}\mathbf{A} = \mathbf{V}_{\mathrm{p}}\mathbf{V}_{\mathrm{p}}^{\mathrm{T}}, \tag{8}$$

which acts as a filter between the true and inverted model parameters. Equation (8) actually gives two ways to compute the resolution matrix **R**: one uses the inverse of **A** and the other uses the inverse of $\mathbf{A}^{\mathrm{T}}\mathbf{A}$. When **A** is ill-conditioned, the rounding errors that occur when $\mathbf{A}^{\mathrm{T}}\mathbf{A}$ is formed make it impossible to recover the smallest singular values with high accuracy, as any information about the smallest singular values becomes drowned in the rounding errors (Larsen, 1998). Since the singular values of $\mathbf{A}^{\mathrm{T}}\mathbf{A}$ are squares of those from **A**, the system of $\mathbf{A}^{\mathrm{T}}\mathbf{A}$ is more ill-conditioned.

Because of the noise in the data and ill-conditioning of the system, it is typically necessary to use some regularization methods to stabilize the inverse system. Suppose the regularization operator is **L**, then the pseudoinverse of **A** is

$$\mathbf{A}^{-} = (\mathbf{A}^{\mathrm{T}}\mathbf{A} + \alpha^{2}\mathbf{L}^{\mathrm{T}}\mathbf{L})^{-1}\mathbf{A}^{\mathrm{T}}. \tag{9}$$

The most common regularization tool is damping, or zeroth-order Tikhonov regularization (Aster *et al.*, 2005). Assuming the damping factor is λ, the pseudoinverse of **A** in this case is defined as

$$\mathbf{A}^{-} = \mathbf{V}\mathbf{S}^{-1}\mathbf{D}\mathbf{U}^{\mathrm{T}}, \tag{10}$$

where **D** is a diagonal matrix defined as

$$D = \frac{S^2}{S^2 + \lambda^2 I}.$$ (11)

In the case of using other non-diagonal regularization methods such as first-order or second-order smoothing constraints (Pratt and Chapman, 1992), there is no simple equivalent to Equation (10) to represent the pseudoinverse of the matrix A, although generalized SVD can be used to develop a similar representation (Aster *et al.*, 2005).

Suppose the SVD of the augmented matrix $B = \begin{bmatrix} A \\ \alpha L \end{bmatrix}$ is defined as $B = P \Lambda Q^T$. The resolution matrix R in this case is equal to

$$R = Q \Sigma Q^T,$$ (12)

where Σ is given by $\Sigma = I - \Lambda^{-1}(P_2)^T(P_2)\Lambda$ and P_2 is the submatrix of P corresponding to the Nr rows of the smoothing constraints (Vasco *et al.*, 2003). In many cases, one also includes damping in addition to the smoothing constraints. In this case Σ is given by

$$\Sigma = D \Lambda^{-1}\left(I - (P_2)^T(P_2) \right)\Lambda$$ (13)

Larsen (1998) uses several "tricks" to efficiently estimate the approximate SVD of any matrix. For more detailed description about the numerical methods used in PROPACK and examples and validity of its application on large-scale tomography problems, interested readers should refer to Larsen (1998), and Zhang and Thurber (2007).

In this section we show the diagonal resolution values computed for this tomography problem, at different inversion grids. Figures 9 (a – g) show contours of the diagonal values of the resolution matrix for Vp and Vs in across fault (X-Z) cross-sections, obtained at different Y-locations; Figures 10 (a – h) show contours of the same in horizontal (X-Y) cross-sections, obtained at different depth (Z) nodes used for inversion. We consider a region to be adequately resolved where diagonal elements of the resolution matrix are greater than 0.25 (Thurber *et al.*, 2003). The higher the diagonal values, the greater the likelihood of resolvability from the actual inversion. The resolution contours seen on the constant-Y slices suggest that Vp would be best resolved between depths 0.6 and 1.1 km and in the central part of the model (Figures 9). As expected the resolution is poor near the edges of the model. We see almost no resolution between 1.2 km and 1.3 km, as identified by a sharp break of the resolution contour above and below those depths (Figures 9). This is due to the presence of a low velocity layer at that depth. As seen from the initial velocity model (Figure 7), a large velocity contrast between adjacent nodes (e.g. from Z=1.3 to Z=1.6 km, Vp changes from 3 km/s to 5 km/s, which is a 67% change), forces the ray paths from events at that depth to travel along the layer boundary of the adjacent layer (above or below, depending on where the event is in that layer and its position relative to the station), thereby yielding very poor ray coverage in that layer. Such large contrasts are "problems" for tomographic imaging; however such is the reality in sedimentary layers (as seen by the well-log on Figure 7) – which makes detailed imaging of petroleum reservoirs using induced events a very challenging problem. The patterns of resolution contours for Vs are very similar to those for Vp, except that at the same regions Vs is less well resolved than Vp. This is also expected because S-picks are much fewer in number and assigned lower weights than P-picks.
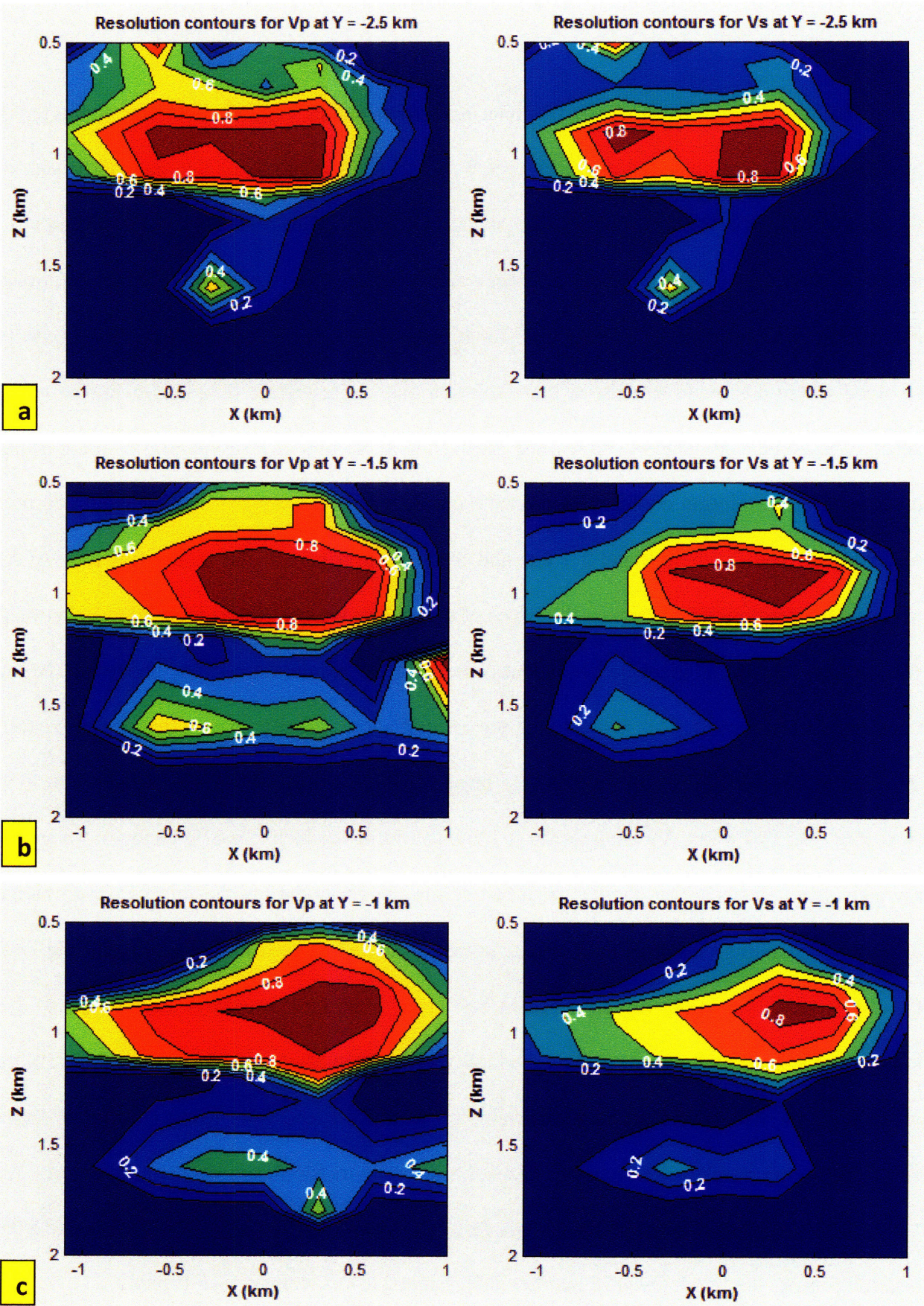
Figure 9: Resolution contours. The actual inversion is likely to be well resolved in places where contour magnitude > 0.25
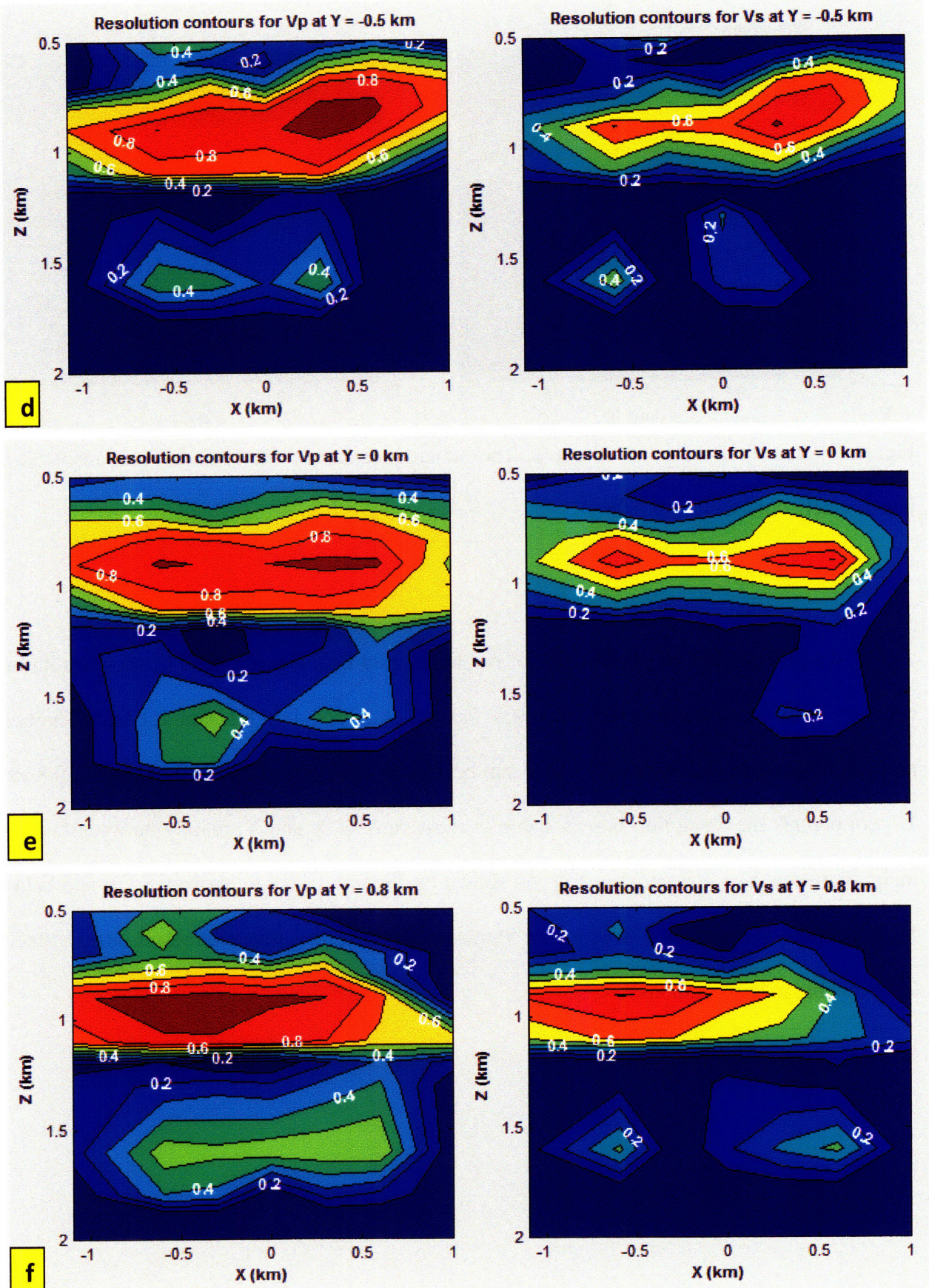
Figure 9 (cont'd): Resolution contours.
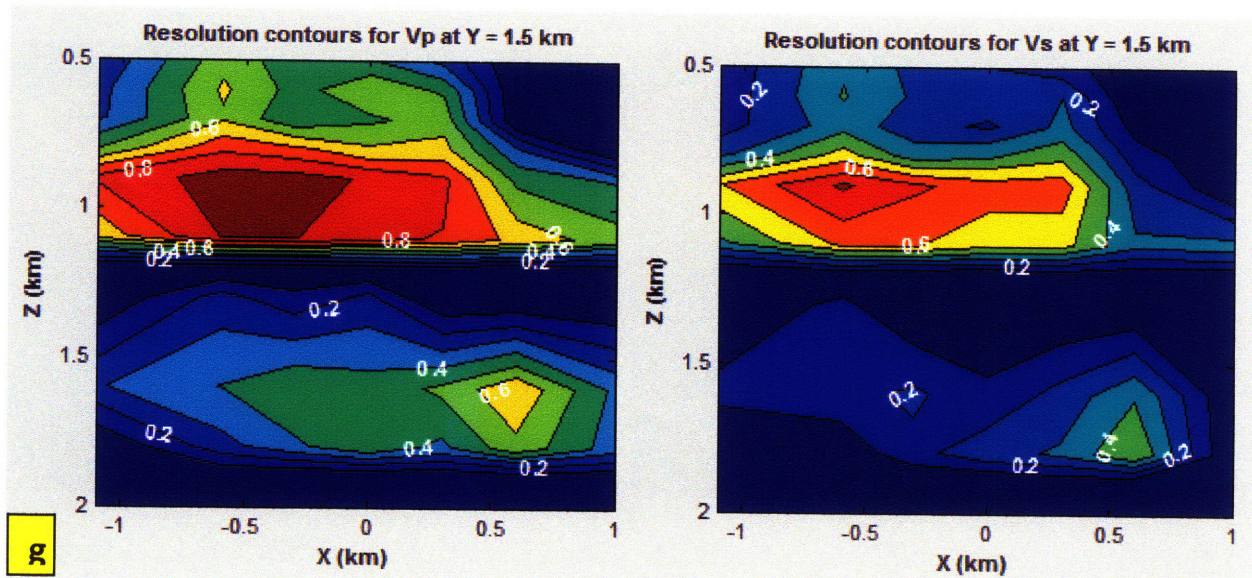
Figure 9 (cont'd): Resolution contours. The actual inversion is likely to be well resolved at places where contours are > 0.25

We plot another set of 2D slices of resolution contours. Figures 10 (a-h) show resolution contours at different depth planes (Z = 0.5, 0.6, 0.7, 0.8, 0.9, 1.1, 1.2, and 1.3 km). The best resolution for almost all parts of X and Y can be seen at Z=0.9 km (Figure 10-e). At 0.7, 0.8 and 1.1 km depths, the resolution is reasonable in most parts of X and Y, mainly between the two faults (between X = -0.5 and X =0.5). As shown by Figures 10-a,g,h, above 0.5 km and below 1.1 km depths, the resolution is very poor in most parts; therefore, inversion results are not likely to be reliable in those regions.
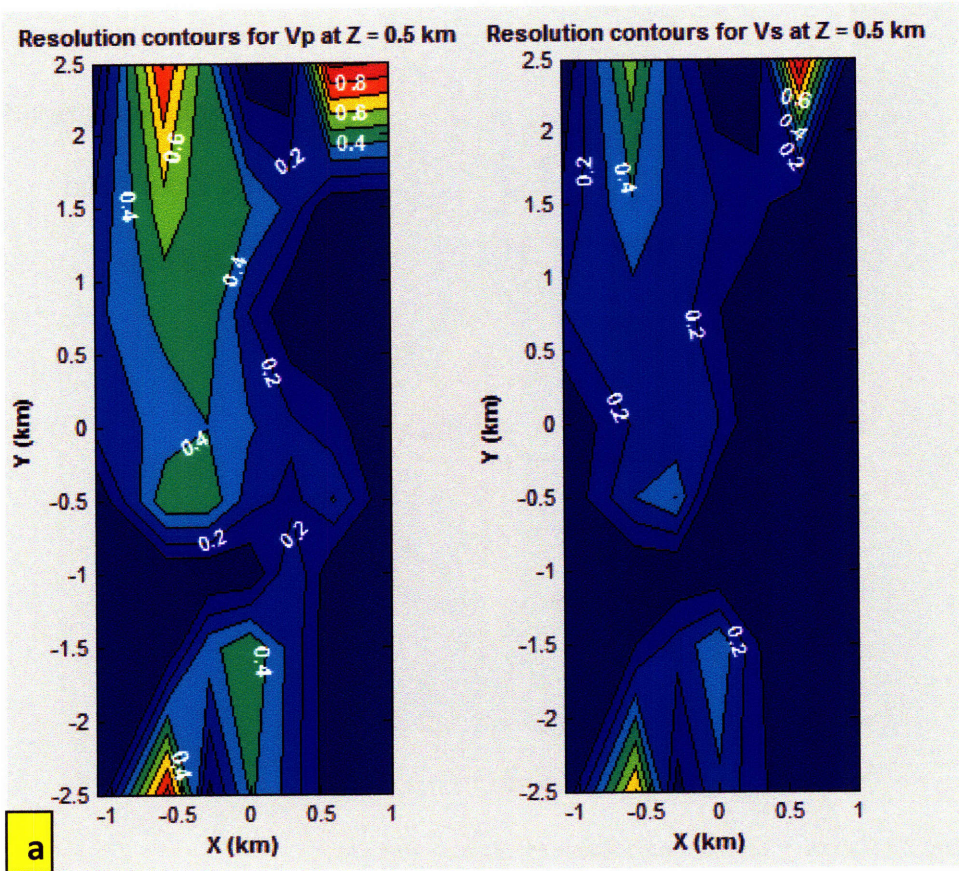
Figure 10 (a-b): Resolution contours for Z = 0.5 and Z=0.6 km.
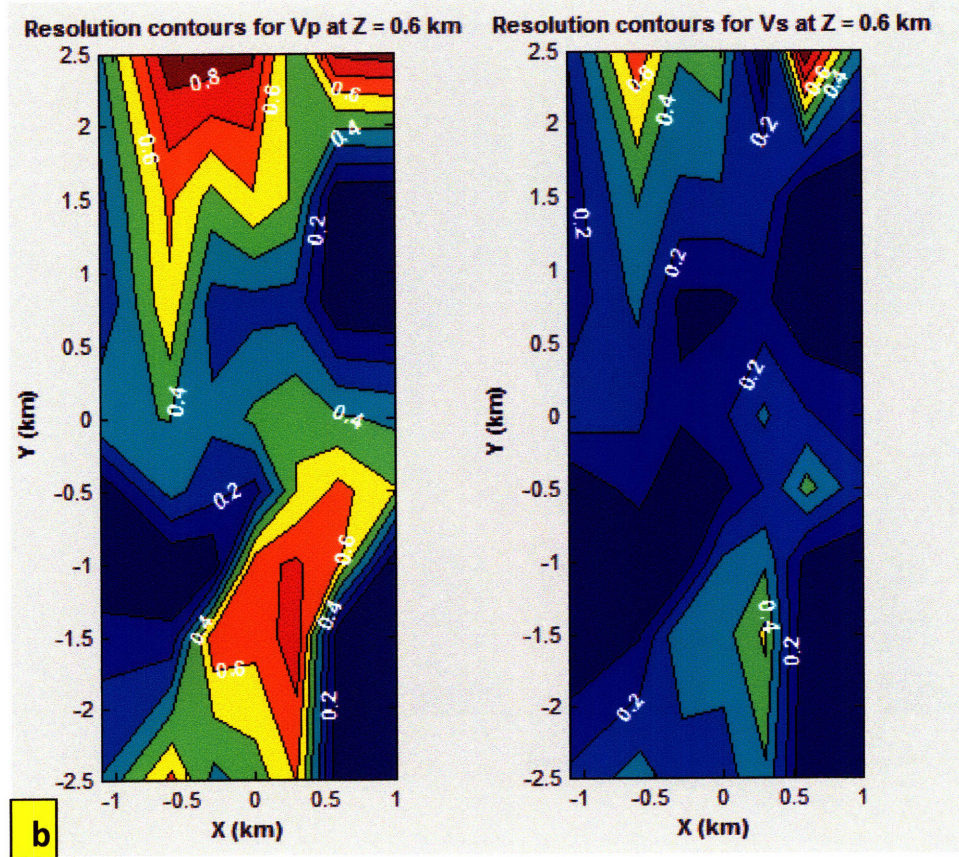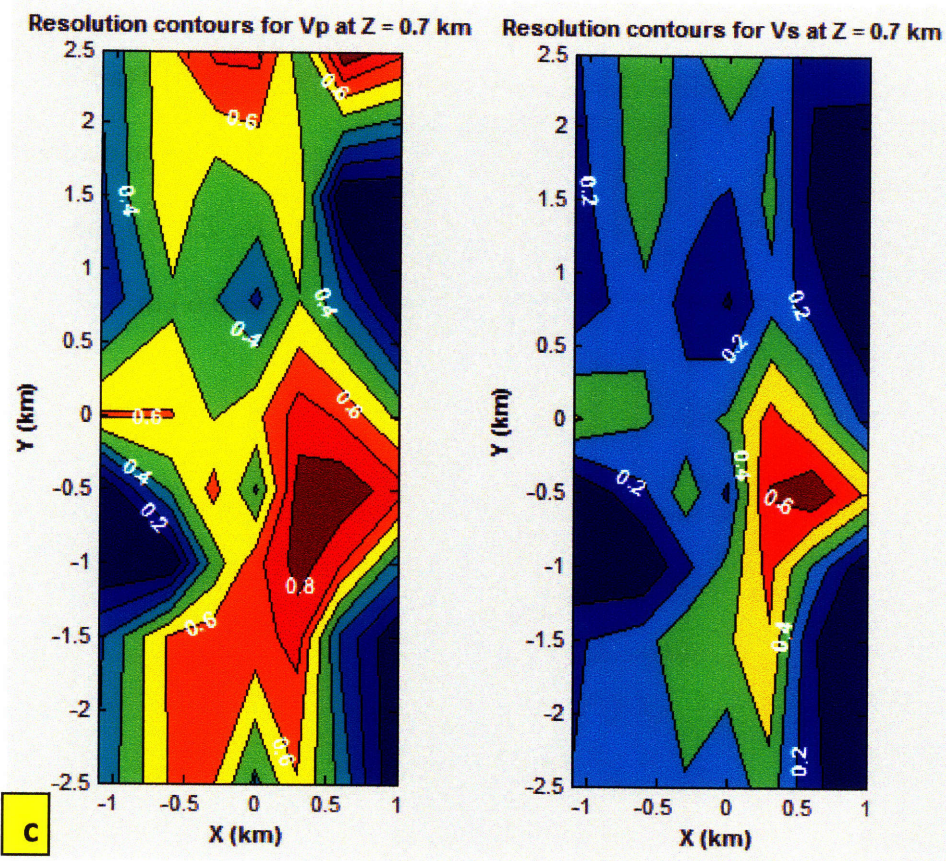
Figure 10 (c-d): Resolution contours for Z = 0.7 and Z=0.8 km.
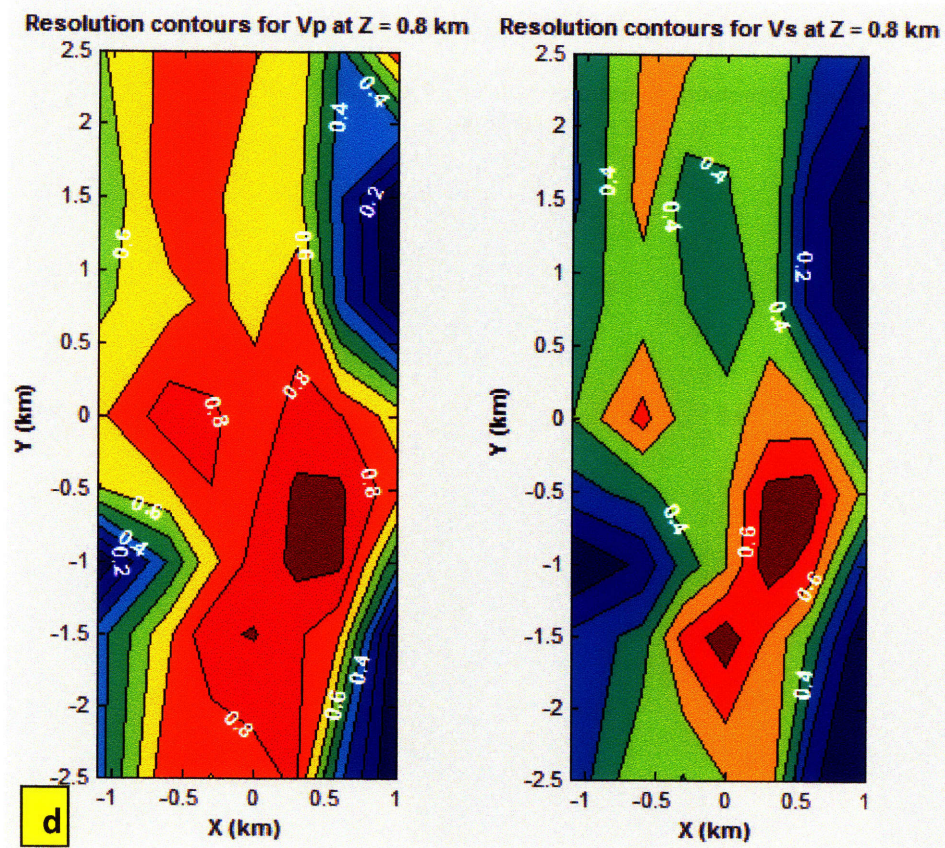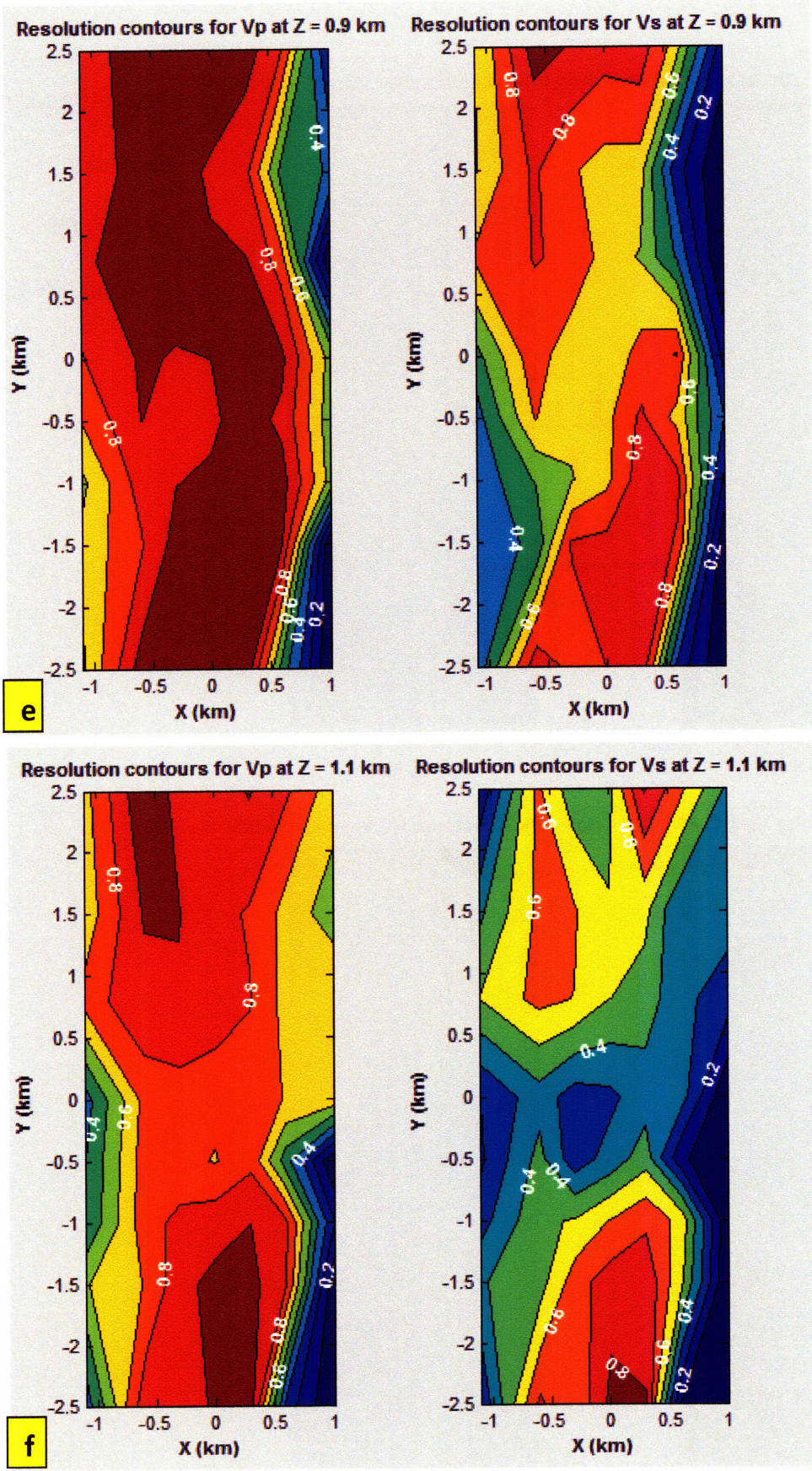
Figure 10 (e-f): Resolution contours for Z=0.9 and Z = 1.1 km.
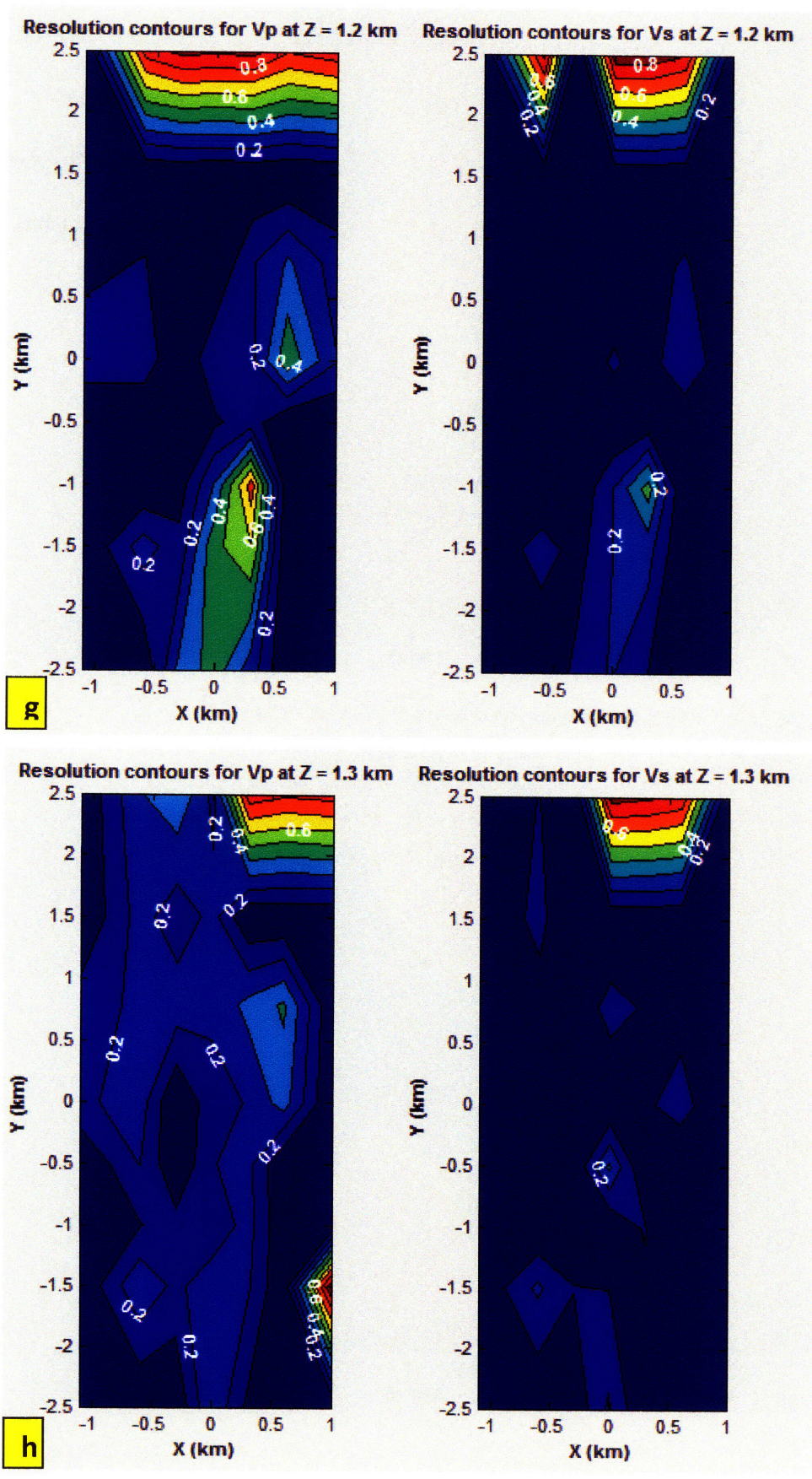
Figure 10 (g-h): Resolution contours for Z=1.2 and Z=1.3 km.

Therefore, it may be observed that the checkerboard test results (Figures 8) and the resolution test results (Figures 9 and 10) are consistent. To summarize both test results: for the given event and station distribution (for the deep network), and the background velocity model, reservoir images that are obtained by using the double-difference tomography method would be most reliable between 0.6 and 1.1 km depths, and in the region between the two faults and bounded by the stations.

5.4.2 Double-difference Relocation

The double-difference tomography method (tomoDD) used in this study jointly inverts for locations and velocity perturbations. As a result, in addition to producing reservoir images, relative accuracies of the events are likely to be "improved" by this method. By Figures 11, we show comparison between the initial event locations used for this study and their relocations obtained from the tomoDD method. Some improvements can be seen in their depth relocations (Figure 11), for example – tighter clustering of the events along the northern fault (the left fault on Figure 11) at depths, and sharper delineation and better identification of the feature on the south-western side of the southern fault (the right fault on Figure 11) that is most likely caused by water injection (ref. interpretations in Chapter 4 of this thesis). Nevertheless, as seen by Figure 11, in general the improvements in event locations are at best "moderate" in this study using deep-network data. One of the reasons for not observing much change in the final locations is that our initial (starting) locations are already quite good. Another reason is that due to some difficulties with data format, the waveforms from the deep-network data had not been cross-

correlated for this study. Since we know that the biggest improvement in double-difference relocation is obtained by incorporating cross-correlation differential times, the lack of cross-correlation times in this study might have reduced the possibilities of improvements in relative location accuracies.
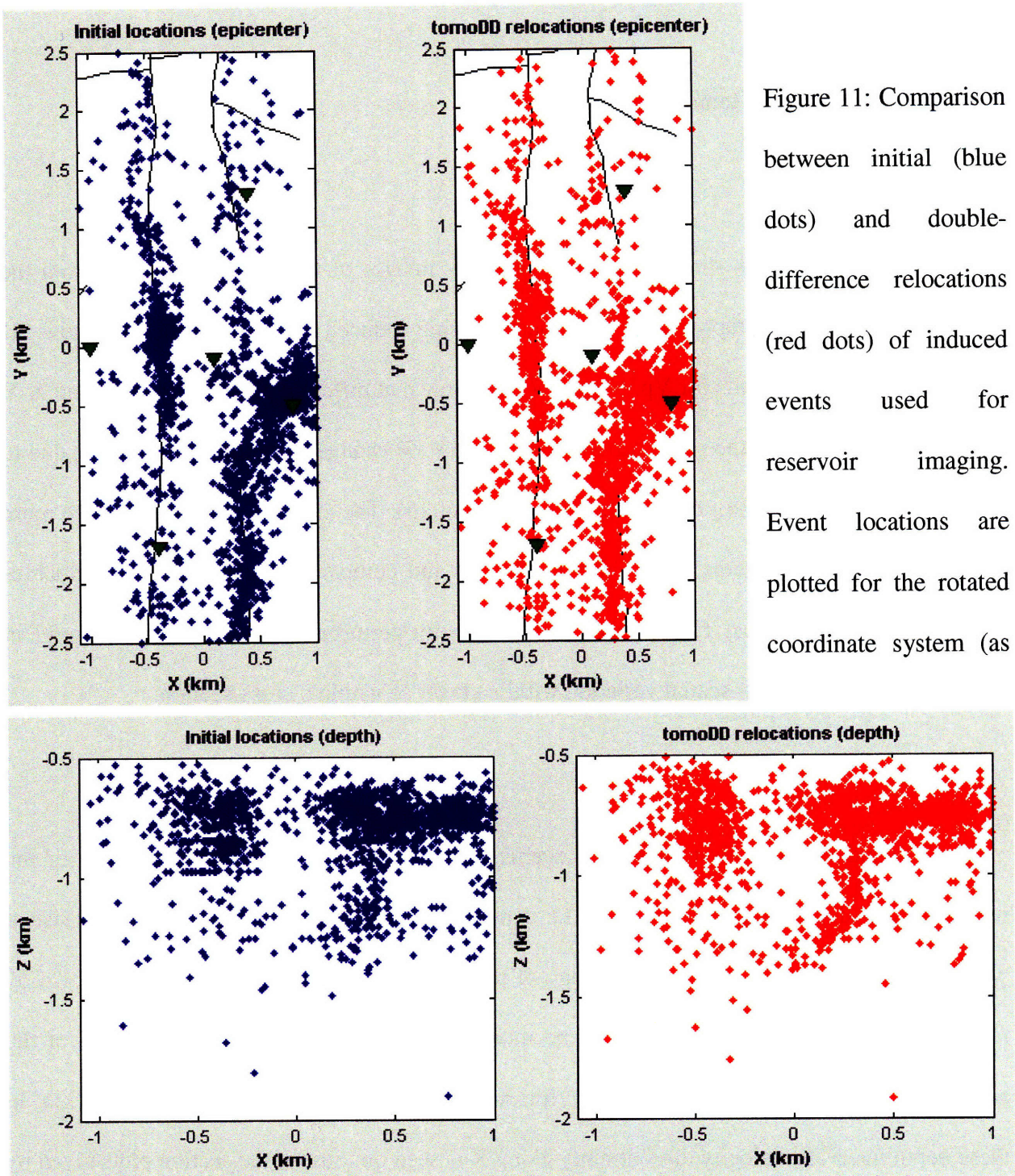
Figure 11: Comparison between initial (blue dots) and double-difference relocations (red dots) of induced events used for reservoir imaging. Event locations are plotted for the rotated coordinate system (as shown by Figure 6). On the epicenter map, black lines and green triangles show existing faults and locations of monitoring wells (boreholes), respectively. The depth locations of events are shown on a vertical plane along the Y-axis of the rotated coordinate system (X-Z cross-section), which makes the section almost perpendicular to the strike direction of the major faults (NW-SE section of the original grid).

5.4.3 Double-difference tomography

In this section we show and discuss velocity images of the reservoir derived from the double-difference tomography (tomoDD) method using induced seismicity data. We show 2D sections of inversion results for Vp, Vs and Vp/Vs, drawn at different X-Z (Figures 12) and X-Y planes (Figures 14), and the perturbation of Vp and Vs (% change from the initial model) due to inversion plotted along the same planes (Figures 13 & 15). The absolute velocity plots are more useful in identifying various layers in the reservoir and comparing the variation of velocities between layers and across faults, whereas the velocity perturbation plots are more useful in gaining information about spatial variation within a layer or within a cross-section.

The induced seismic tomography seems to recover a layered velocity structure of the reservoir with depth (Figures 12: a-g). The depth layers seen from tomography are consistent with the log-derived model and the geology of the field. For the different Y-sections shown by Figures 12, the depth layering seems to be more or less continuous along X (NW-SE of the actual geographic orientation in the field) for all depths, except between ~ 0.8 and 1.1 km. In these depth intervals, velocity discontinuity along X is seen on most of the section plots given by Figure 12. On some of the sections for Vp (e.g. at Y= - 0.5 km and Y = 0 km, Figures 12-d & 12-e respectively), these discontinuities are seen to align with the fault positions, indicating that these velocity anomalies may have been caused by fault displacements. These two Y-slices are at or near the center of the rotated coordinate system and of the field, and according to the resolution tests are likely to have good resolutions. The bowl shaped velocity contours at depths

200

between 0.8 and 1 km seen on these two slices near the center of the field may be related to the displacement of Natih formation. Other independent studies on subsidence monitoring using GPS and InSAR in the field indicate the highest rate of surface subsidence in that region, which is thought to have been caused by a faster rate of compaction of Natih in that area. The height of Natih gas column is known to change discontinuously across the major faults; hence the amount of reservoir compaction on either side of the faults is expected to differ. Therefore, the concavity of the velocity contours and the bowl-shaped velocity model observed at the depth of Natih on some of the X-Z sections may be linked to the differential compaction of Natih. Moreover, the well-logs in this depth interval also show frequent fluctuations and big jumps in Vp (Figure 7: blue curve). Therefore, the relatively "strong" anomalies compared to the other layers, seen in this depth interval from the tomographic images, are likely to resemble the true structure of the Natih reservoir.

The layered structure of Vs with depth, in most places, is similar to that of Vp, as seen by the panels on the second column of the plots on Figure 12 (a-g). As in Vp, we can also identify traces of the faults from some of the Vs images (e.g. Figures 12-d & 12-e: second column). As for Vp/Vs, a starting value of 1.92 for the entire model was used. While for most parts of the reservoir the initial estimate seems to hold in the final image of Vp/Vs, at the depth of upper Natih (gas producing reservoir: Natih A formation) we mostly see lower Vp/Vs ($\approx 1.7 - 1.8$) than the initial estimate (Figures 12(a-g): 3rd column). This is also realistic; and, indeed very similar estimates for Vp/Vs had been obtained from sonic-Vp and Vs measurements from well-logs.
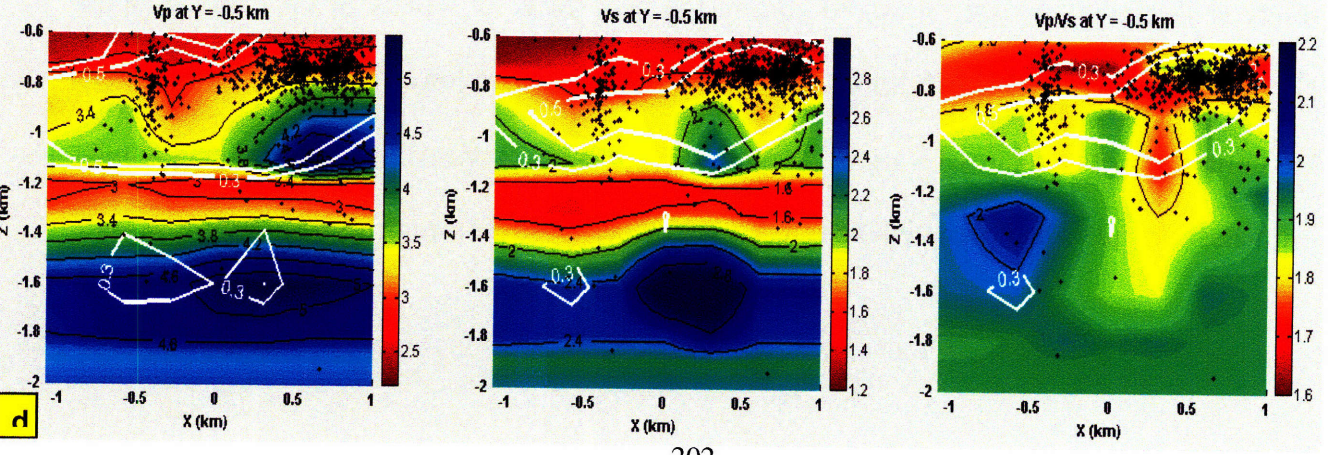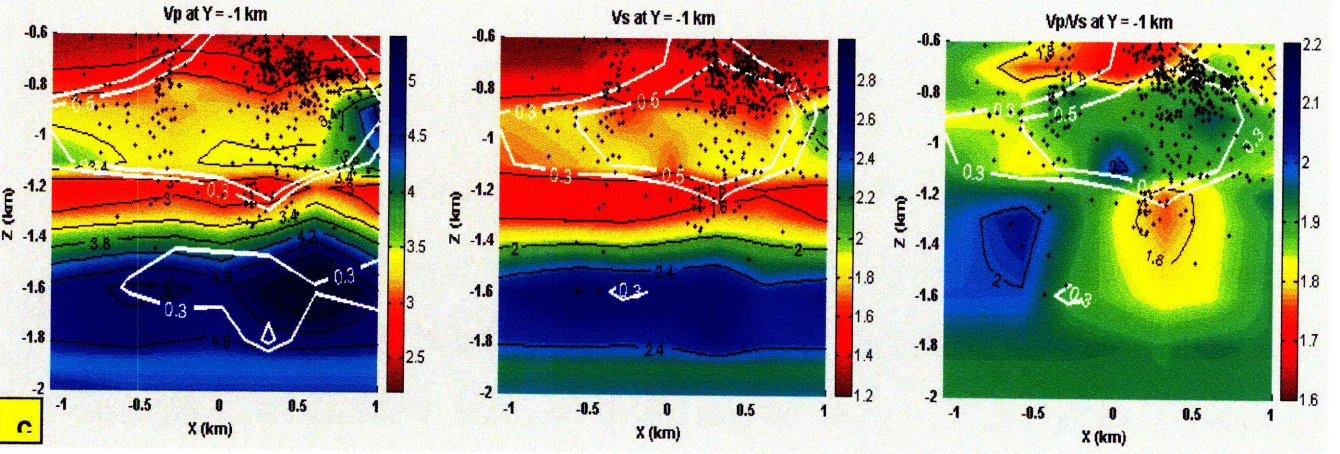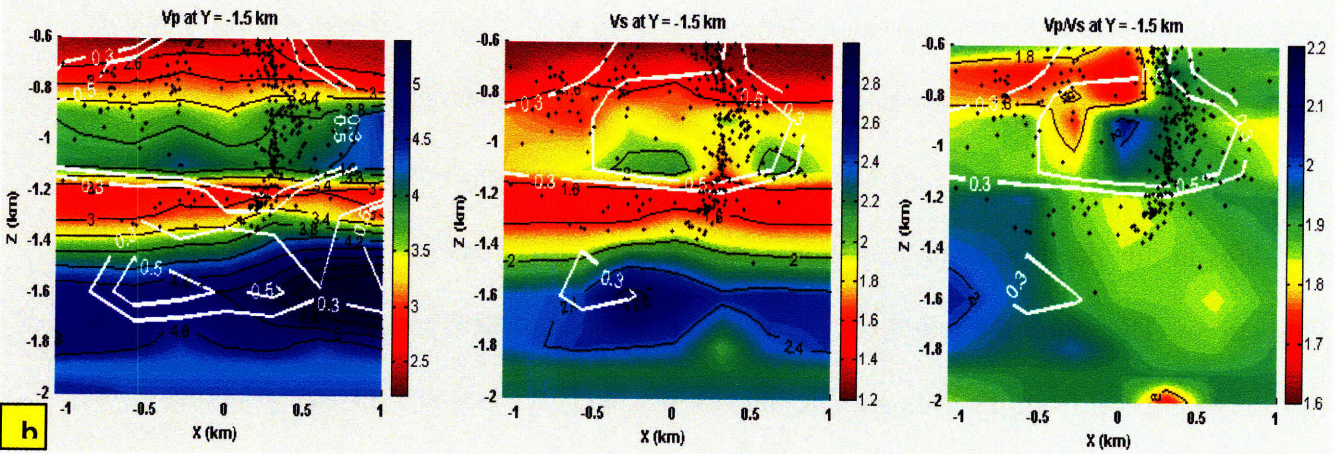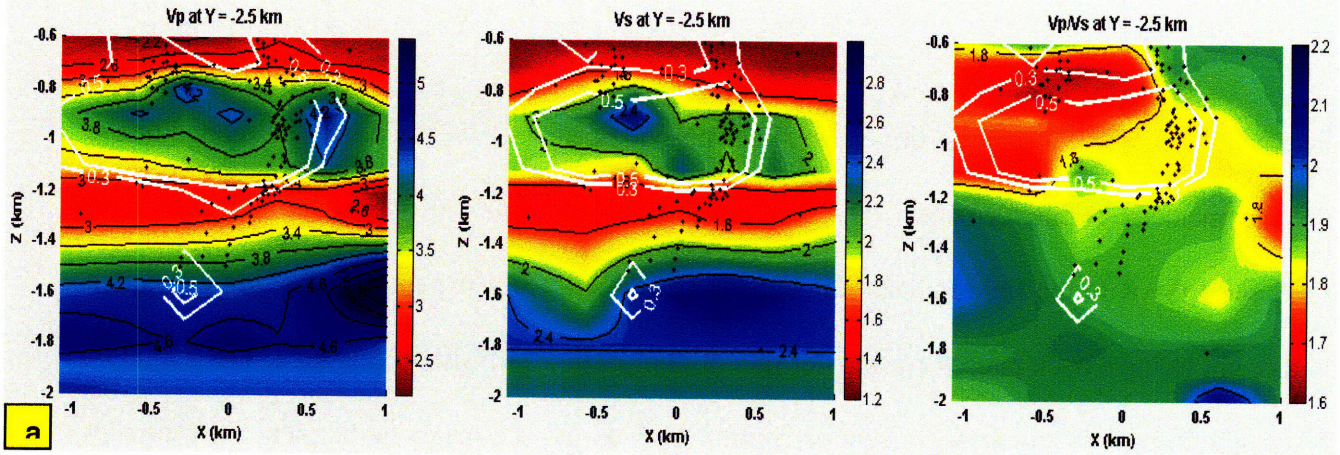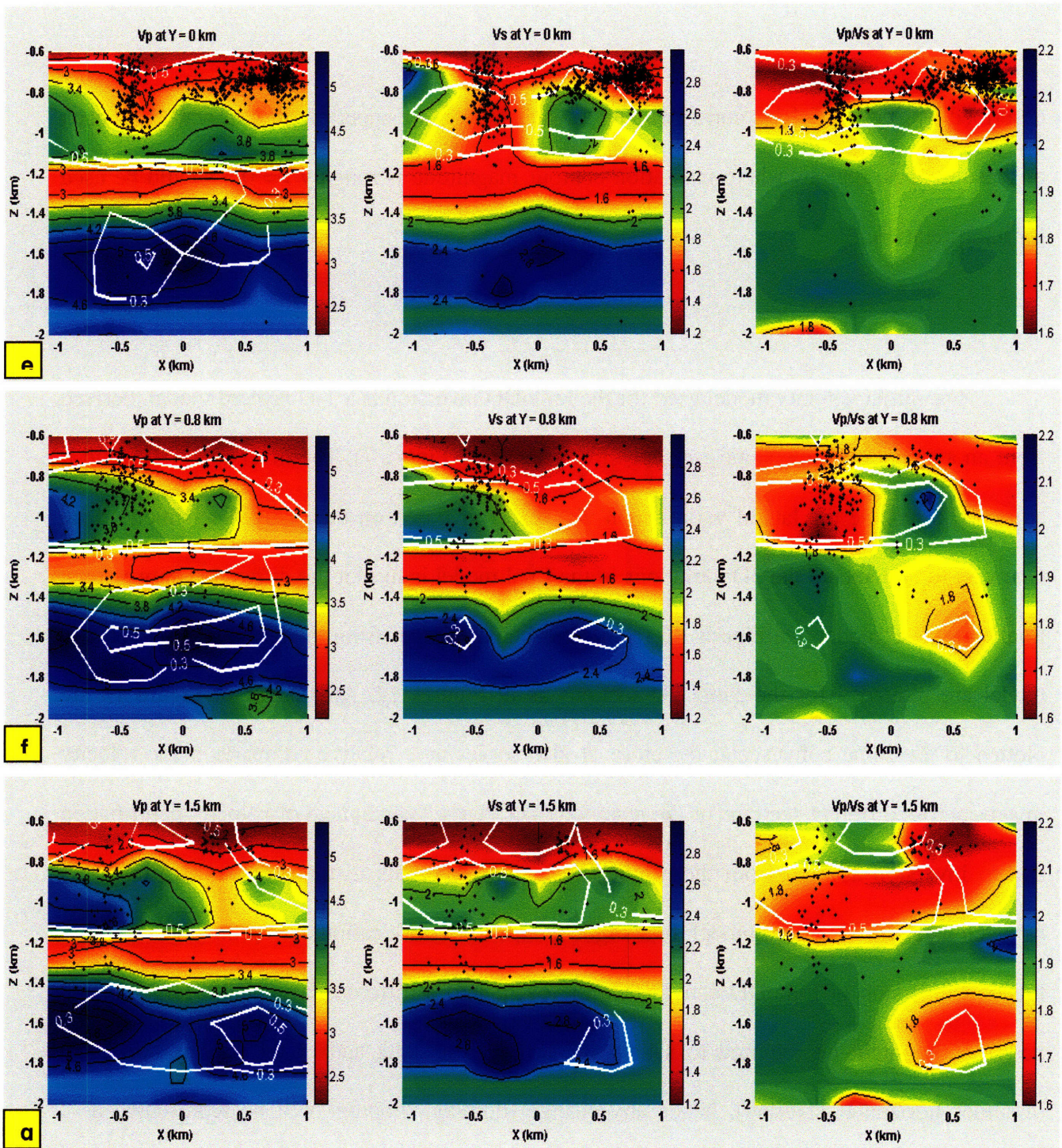
Figure 12 (a-g): 2D images (X-Z section plot) of Vp, Vs, and Vp/Vs (from left to right, in columns) obtained from tomoDD inversion, drawn at different Y-locations of the inversion grid (in different rows). Magnitude scale of the plotted variables for each plot is given by a colorbar next to it. Also shown on the plots in black are the contour lines and labels of the variables. Induced seismicity locations (black dots) within ± 500 m of each section are superimposed on the velocity images. Also, two levels of resolution contours obtained from the resolution test

described by Section 5.4.1.2 corresponding to each section are superimposed in white. On each of these images, regions where resolution contour magnitude is roughly >= 0.3 should be used for interpretation.

The initial velocity model used for the tomoDD inversion is a 1-D layered model, derived from an average of a few sonic well-logs from the field (Figure 7). The inversion is 3D, and it attempts to resolve the lateral variations in the reservoir based on the induced seismicity data. One way to understand the 3D variations in the final model is to plot the difference between the final and initial model. On Figures 13 (a-g), percentage changes from the initial to final velocity model are plotted – for the same 2D sections as in Figures 12. All images of Figure 13 are plotted to the same color scale; therefore, it also serves as a relative comparison for velocity images across different sections of the reservoir. The "large" percentage of velocity perturbation due to inversion as seen from these plots is expected because: a) there exist sharp contrasts between layers in the initial model, b) a slight change in event location during the joint velocity-location inversion of tomoDD could place the event into a different layer and a larger lateral perturbation might be required to satisfy the arrival time data and c) the grid is horizontal (assumes horizontal layering), hence any change (doming, dipping) will be represented as a velocity anomaly. From Figures 13, in general it seems that: i) the Natih formations had been underestimated by the initial model (positive changes in the difference plot) and ii) the Shuaiba formation had been slightly overestimated by the initial model (negative changes in the difference plot). In most of the central part of the reservoir and between the faults, however, the differences between the final and initial models are minimal. Vs differences, in most parts of the reservoir, seem to follow the pattern of Vp.
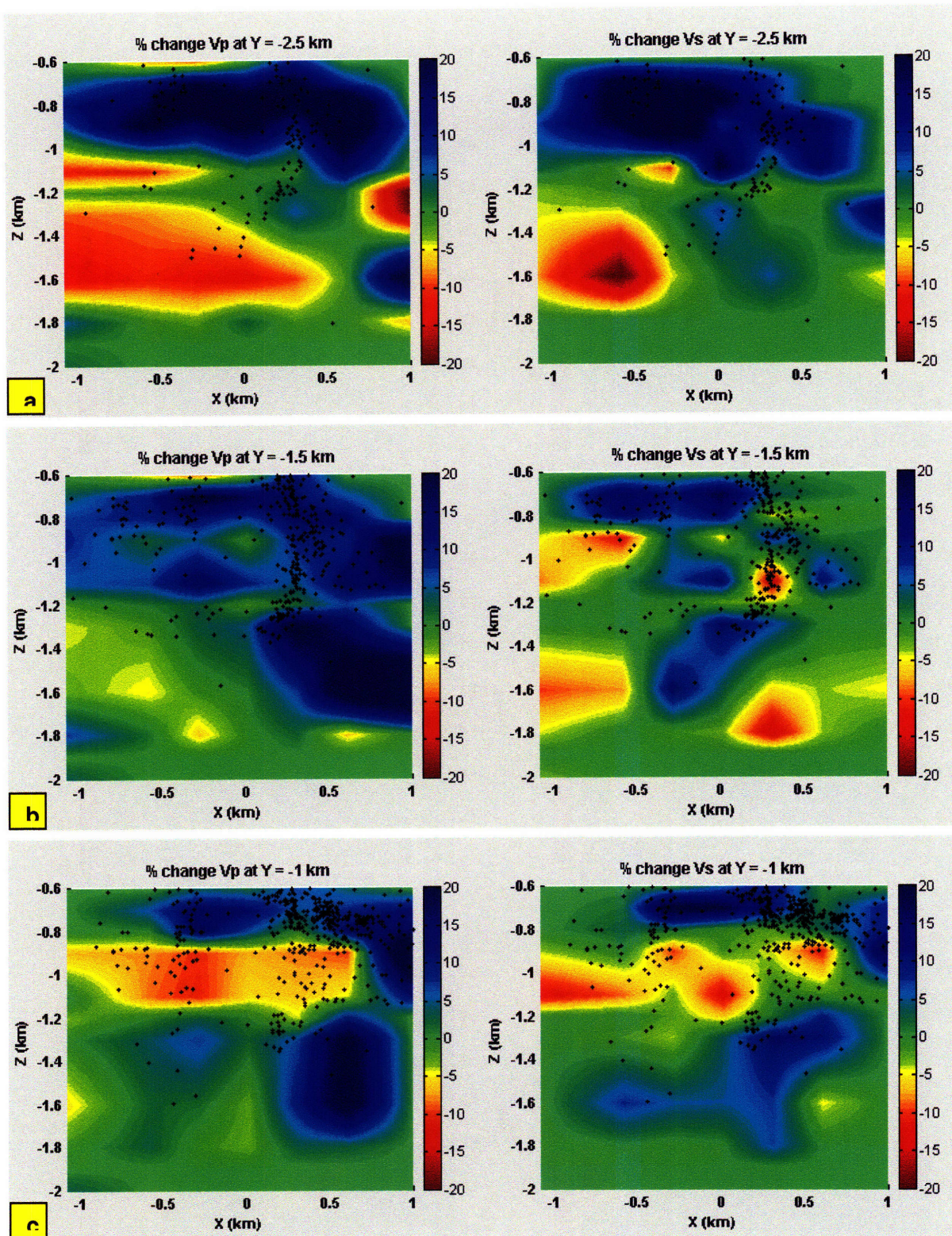
Figure 13 (a-c): Percent change from initial (starting) to final (inverted) velocity model for Vp (left) and Vs (right), shown for different X-Z sections of the reservoir (in different rows).
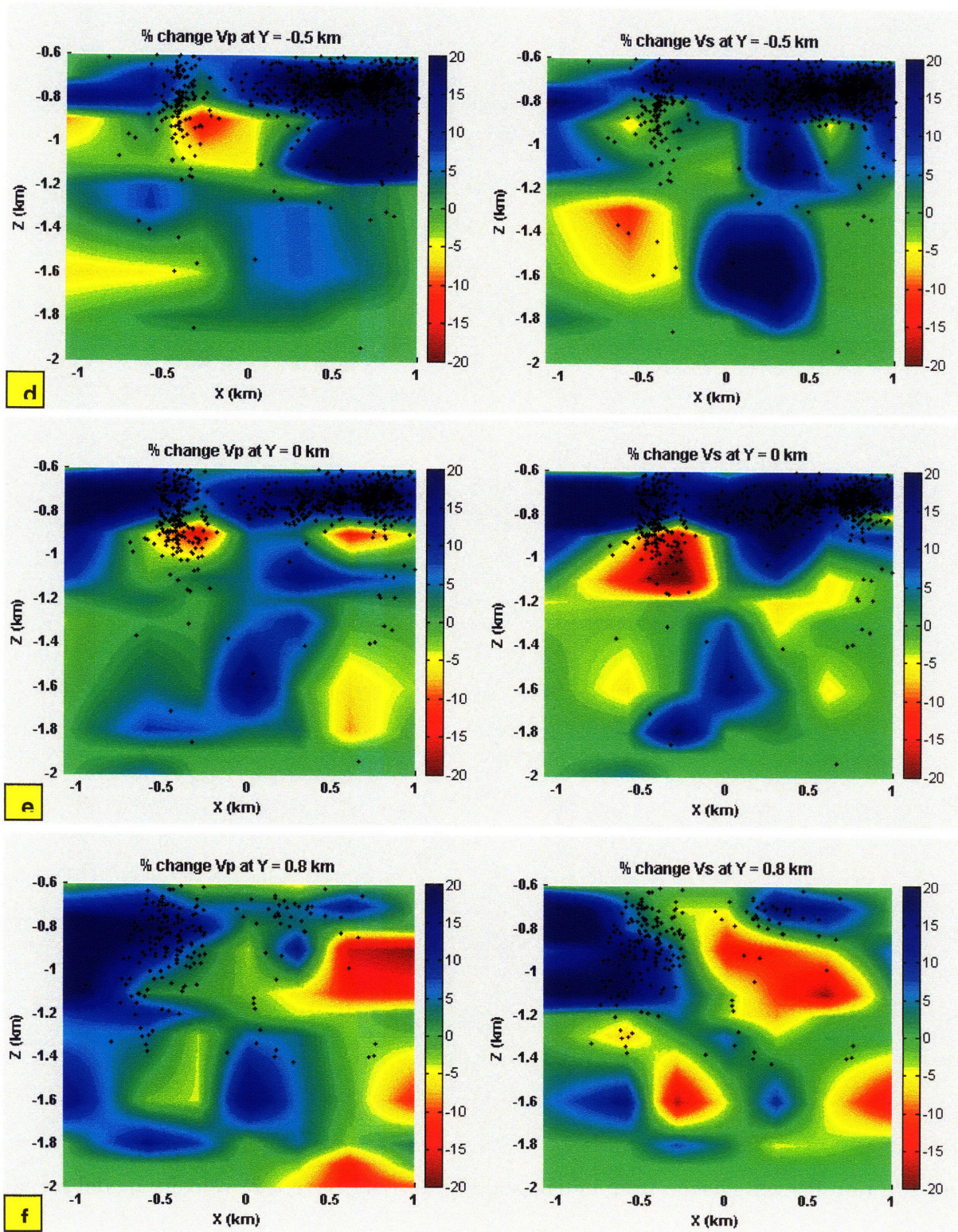
Figure 13 (d-f): Percent change from initial (starting) to final (inverted) velocity model for Vp (left) and Vs (right), shown for different X-Z sections of the reservoir (in different rows).
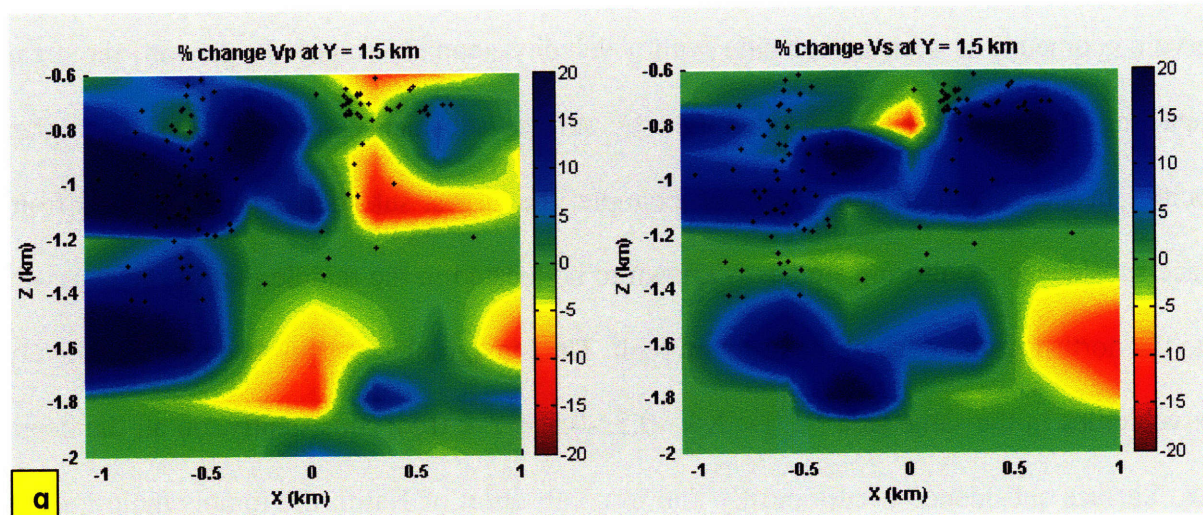
Figure 13 (g): Percent change from initial (starting) to final (inverted) velocity model for Vp (left) and Vs (right), shown for an X-Z section of the reservoir. Induced seismicity locations (black dots) within ± 500 m of each section are superimposed on the difference images.

To get another perspective of the reservoir structure, 2D images of the final (inverted) velocity model obtained for horizontal (X-Y) sections at different depths of the reservoir are also given by Figures 14 & 15. Figures 14 (a-e) show plots of Vp, Vs and Vp/Vs at depths for which we have meaningful resolution – predicted by both checkerboard and resolution matrix tests (Section 5.4.1) – while Figures 15 (a-e) give difference plots for Vp and Vs at the same depths.

Velocity contrast across the two faults in most parts of the inversion area of the reservoir can be identified at all depths from Figures 14 (a-e). The velocity contrasts are visible on and consistent between Vp and Vs plots. The dense "cloud" of events near the break of the fault on the right side of the inversion area in the rotated coordinate system (southern fault in the actual

reservoir geometry) is seen to coincide with a velocity anomaly (high). In general, the areas compacting at a higher rate – as identified by surface subsidence monitoring, show higher velocities in the tomographic images. For example, the largest subsidence bowl reported from surface subsidence monitoring studies is known to be located in the middle part of the reservoir along the north-western edge of the northern fault. The tomographic images also reveal relatively high-velocities in the same area (-1.0 < X < -0.5, -0.5 < Y < 0.5), consistently, on all the depth slices. Surface subsidence occurs mostly due to compaction of Natih; the tomographic images also seem to be consistent with the interpretation of subsidence as they reveal *compact* high-velocity anomaly at the shallower/Natih depths (Figure 14-a & 14-b), with progressive smearing of that anomaly with increasing depth of the reservoir.
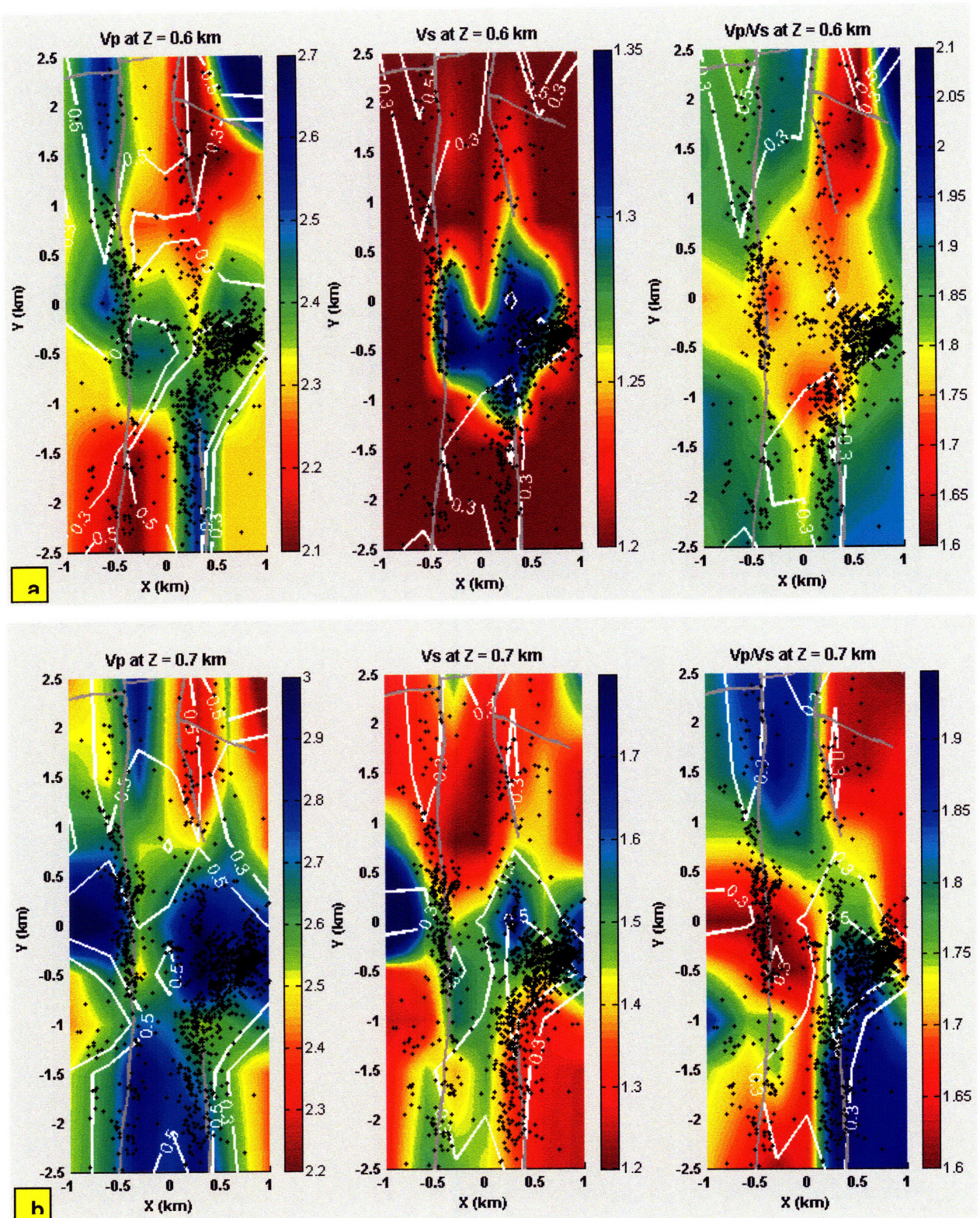
Figure 14 (a-b): 2D images (X-Y section) of Vp, Vs, Vp/Vs (column-wise, from left to right) obtained from tomoDD inversion, showing for two different depths (row-wise).
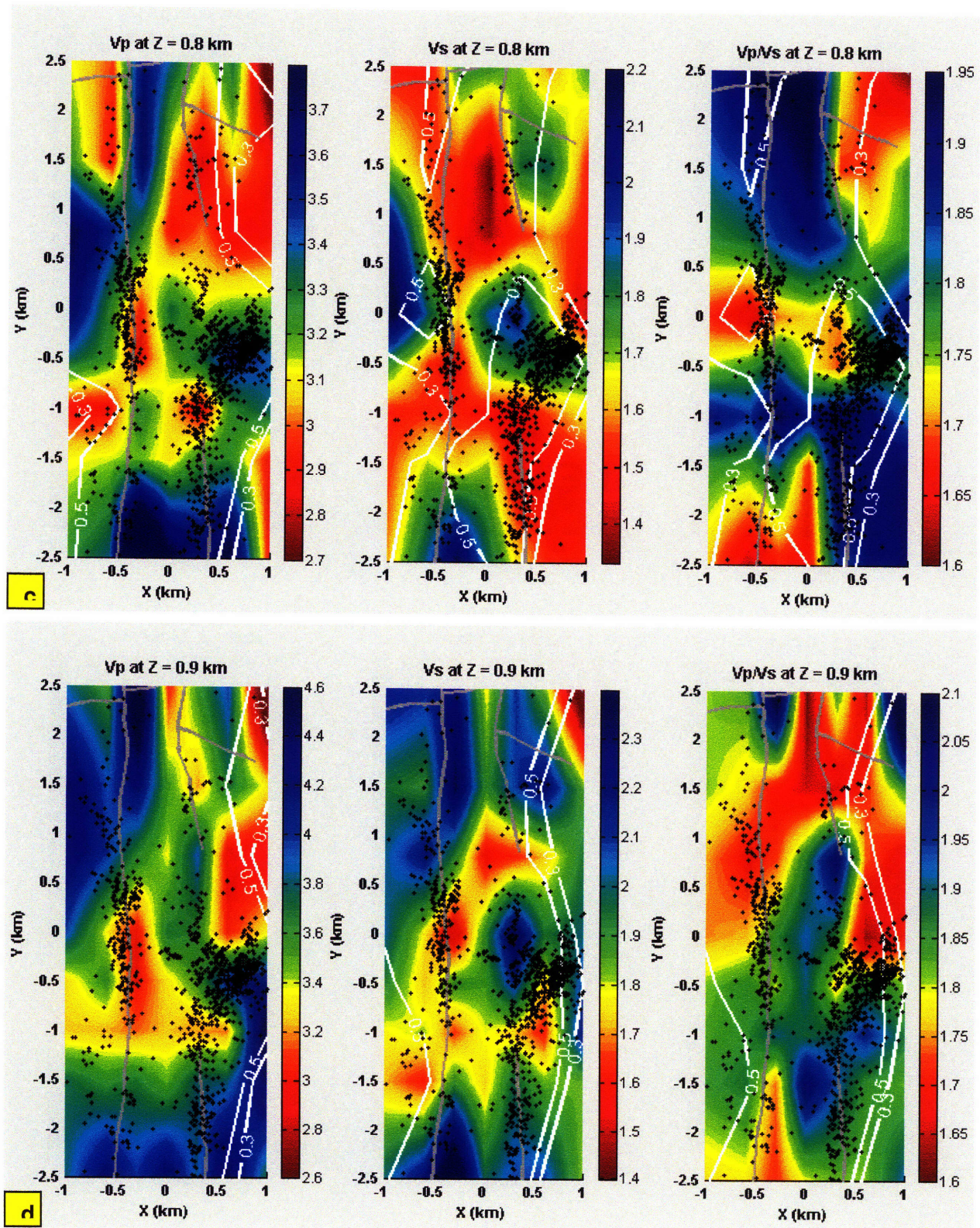
Figure 14 (c-d): 2D images (X-Y section) of Vp, Vs, Vp/Vs (column-wise, from left to right) obtained from tomoDD inversion, showing for two different depths (row-wise).
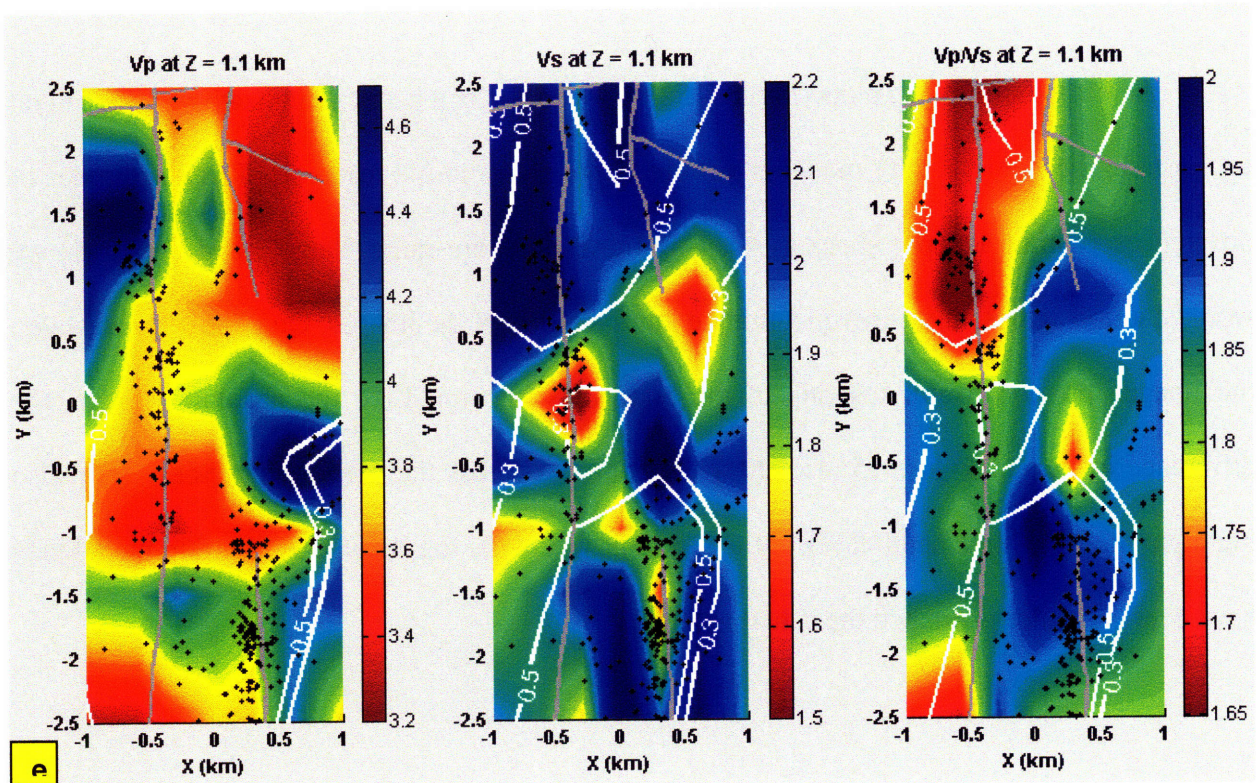
Figure 14 (e): 2D images (X-Y section) of Vp, Vs, Vp/Vs (column-wise, from left to right) obtained from tomoDD inversion, showing for Z=1.1 km. The inversion cannot resolve the velocities well enough below this depth, as predicted by the resolution tests (Section 5.4.1). Superimposed on this and the previous depth slices (a-d) are: preexisting fault maps derived at Natih horizon from surface seismic (grey lines), induced seismicity locations for ± 100 m depth of each section plot (black dots), and the decisive resolution contours obtained from the resolution matrix test (white). As per the resolution matrix test (Section 5.4.1.2), only the regions that have resolution values > 0.3 are considered for interpretation.

As for the difference plots (Figure 15 (a-e)), they offer a better visualization of the lateral contrasts in the final velocity model at various depth levels in the reservoir. The magnitudes of differences (within a depth slice) as seen by these plots are quite "large", and therefore, we would caution against any strict quantitative interpretation of the images. Qualitatively, however, the images provide useful insights to the reservoir structure. Like the absolute images, the difference images of Figure 15 also show the contrasts across the major fault traces. They also highlight areas within a depth layer of the reservoir where the log-derived 1D starting model may have over- or under-estimated the actual velocity.

% change Vp at Z = 0.6 km   % change Vs at Z = 0.6 km

% change Vp at Z = 0.7 km   % change Vs at Z = 0.7 km
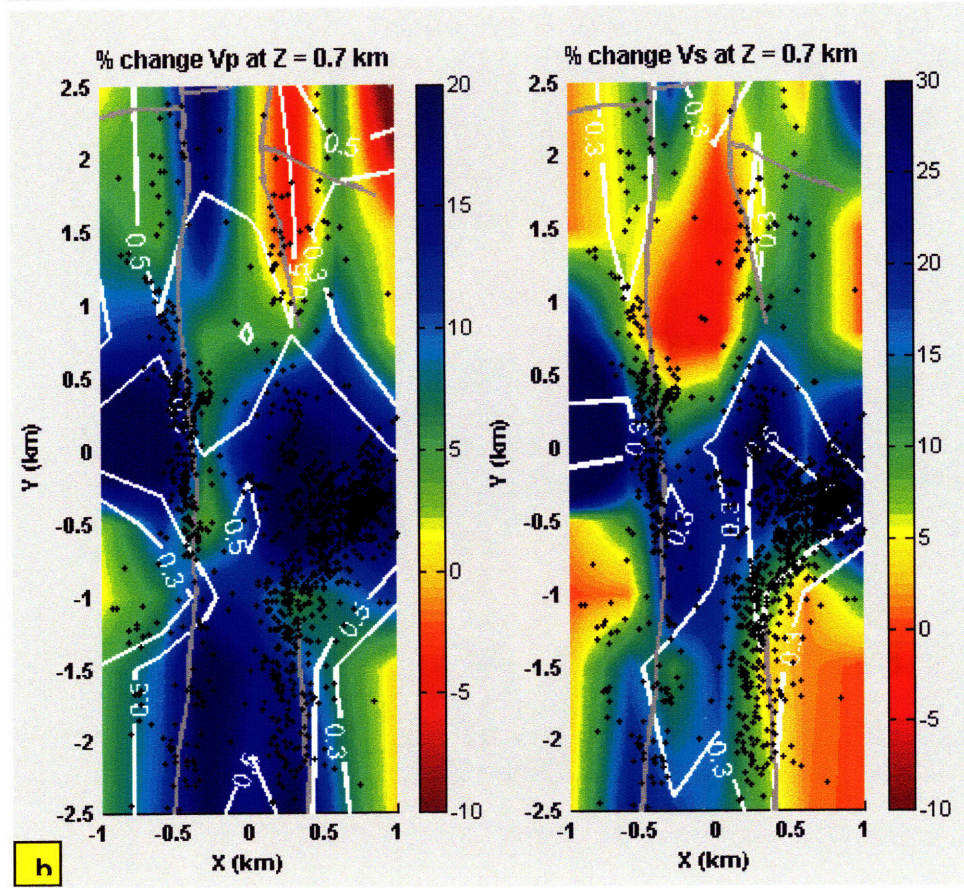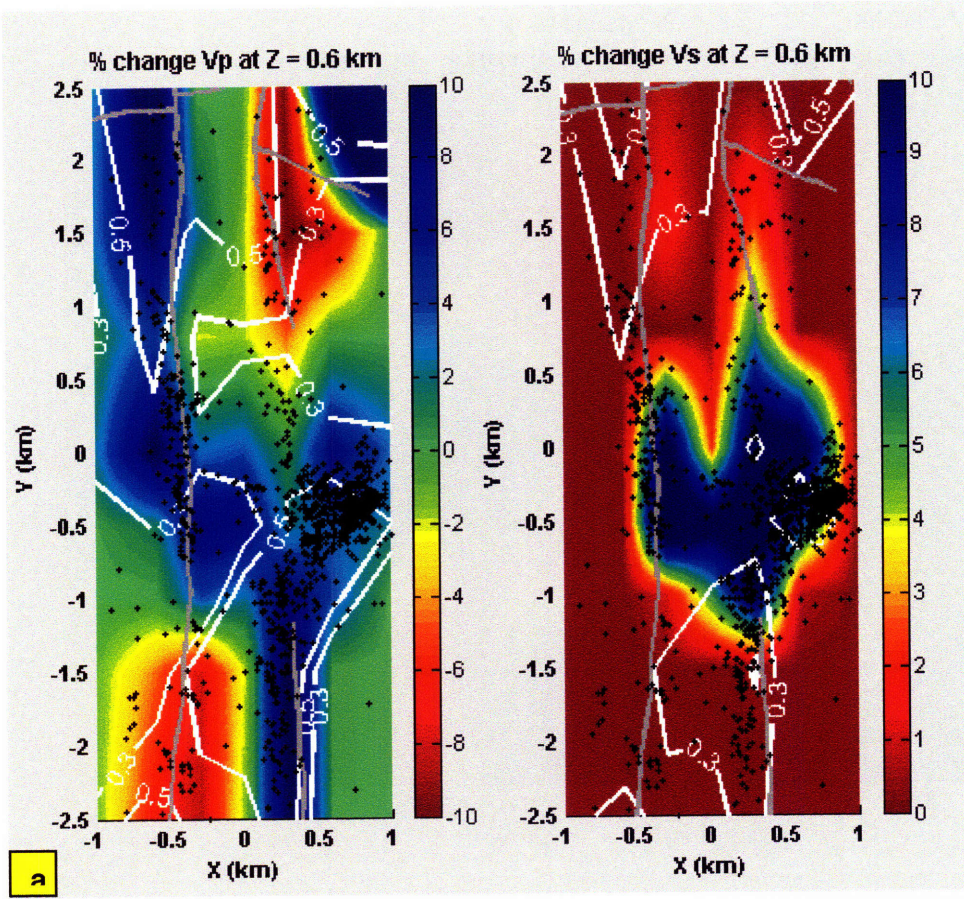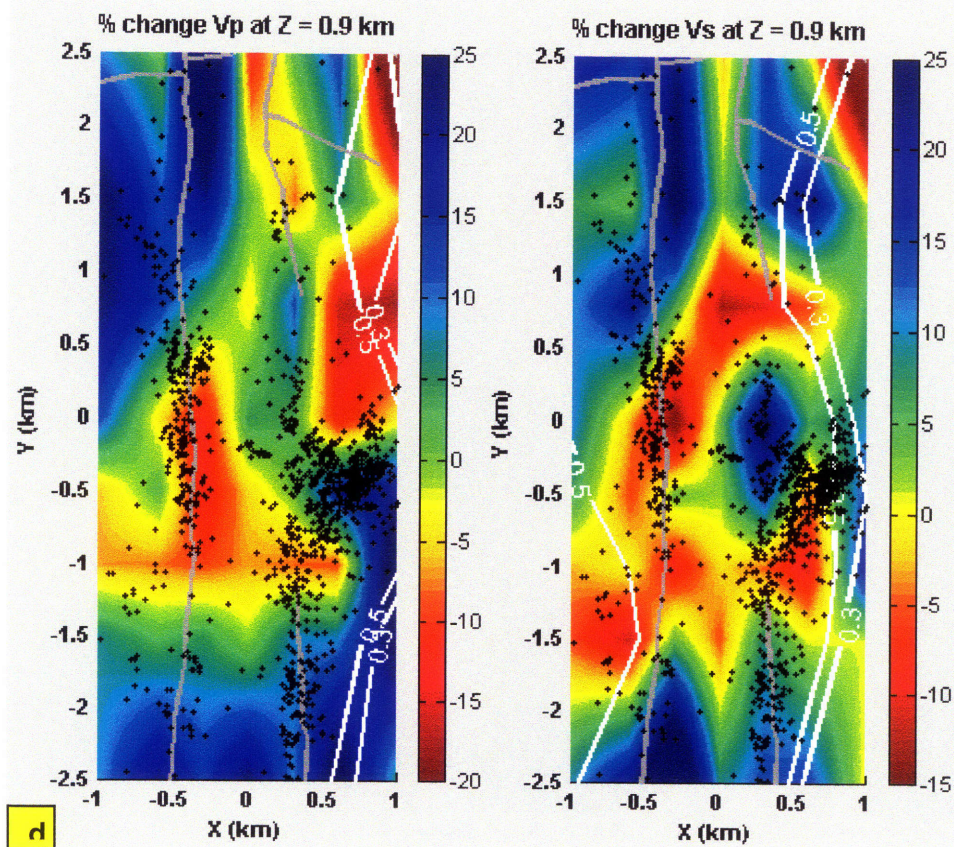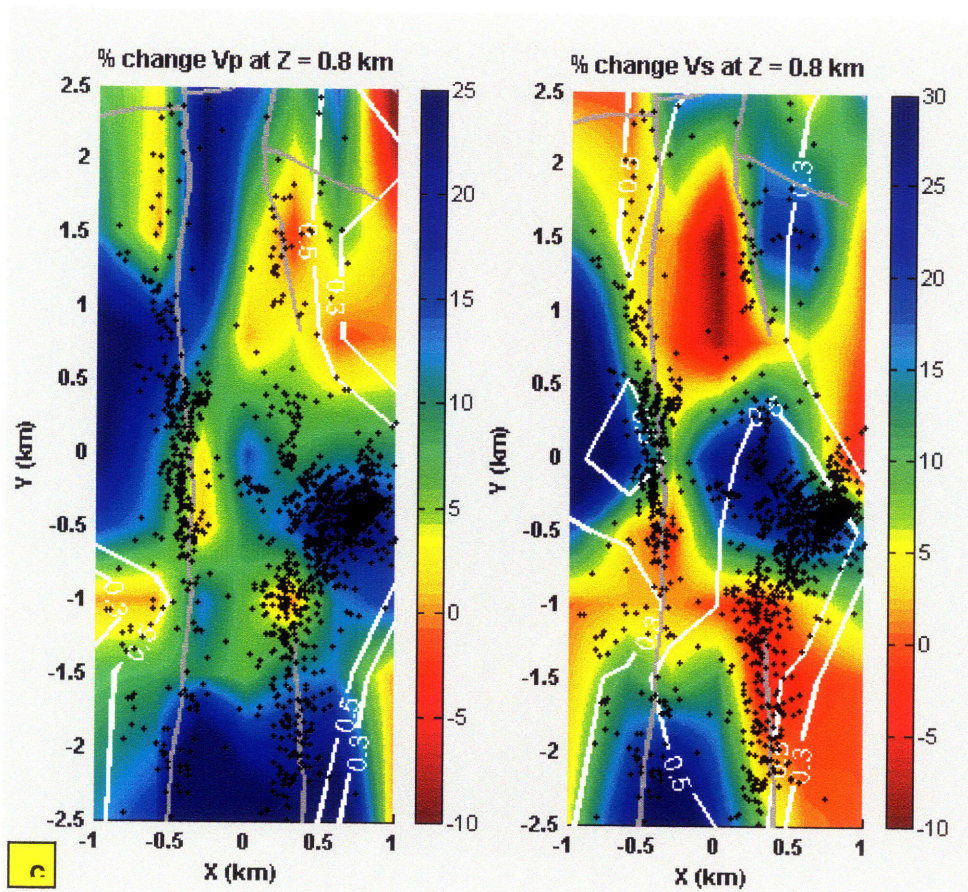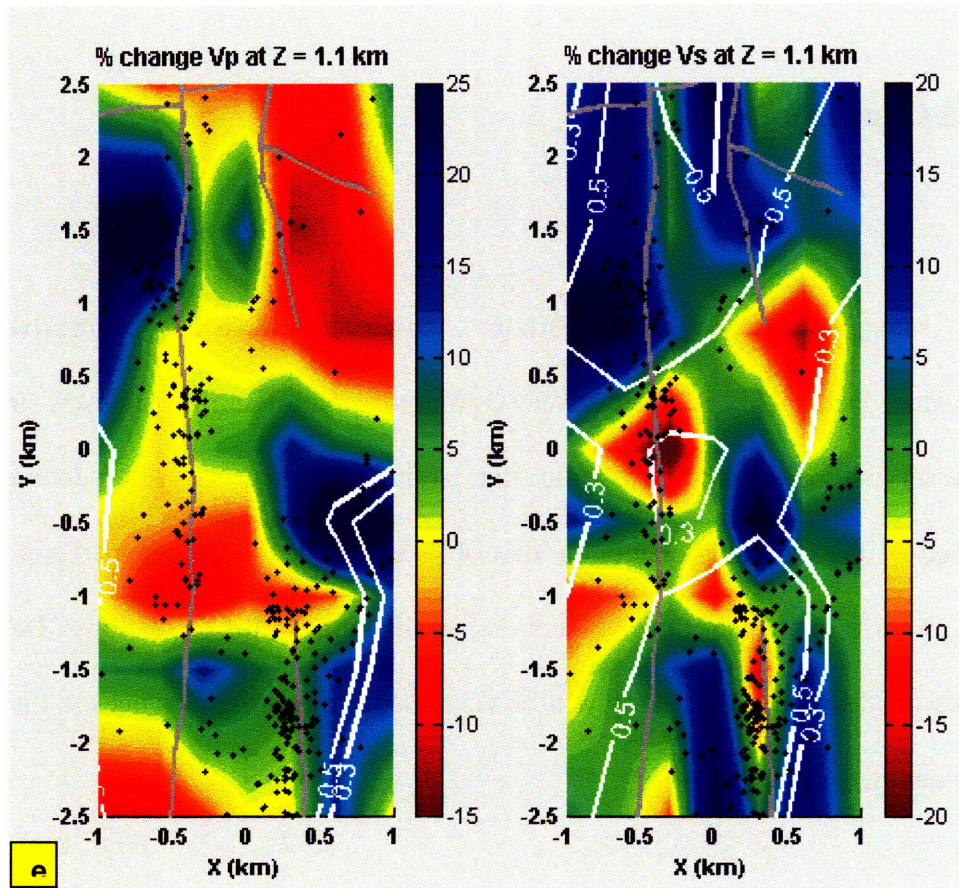
Figure 15 (a-e): X-Y plots of percent change in Vp (left) and Vs (right) at different depth nodes. The percent change is calculated from the difference between initial (starting) and final (inverted) velocity models in each inversion grid. Superimposed on the plots are: preexisting fault maps derived at Natih horizon from surface seismic (grey lines), induced seismicity locations for ± 100 m depth of each section plot (black dots), and the decisive resolution contours obtained from the resolution matrix test (white). As per the resolution matrix test (Section 5.4.1.2), only the regions that have resolution values > 0.3 are considered for interpretation.

5.5 Discussions and Conclusions

Tomographic imaging of hydrocarbon reservoirs using passive seismic/microseismic/induced seismicity data is not very common in the oil and gas industry. In fact, application of reservoir-scale passive seismic tomographic methods at a producing petroleum field described in this study is probably the first of its kind. The results obtained from this study show much promise for further development and application of this technology. The challenges faced and lessons learned in this study will be very useful in making advances in this *new type* of reservoir imaging technique.

Out of the two different induced seismicity data sets available for this study, the near-surface network data could not be used for velocity imaging because of the source-receiver geometry. It was found that the ray coverage was not adequate to resolve the velocity of the reservoir layers with the induced seismic events recorded by the near-surface/shallow seismic network. However, the joint location-velocity inversion of the double-difference tomography method did serve the purpose of improving relative accuracy of the event locations. The comparison between four different location methods shown by Figures 5 establishes the importance of multiple/relative event locations in the analysis of induced seismicity. While a quantitative estimation of location uncertainty is not feasible, the better lineation of events obtained from both double-difference methods, as compared to the two single-event location methods, indicates a higher relative accuracy of events within specific fault zones. In terms of both epicenter maps and depths, the faults seem to be better defined by either of the multiple-

event location methods (Figures 5.a, 5.b and 5.c: green and magenta dots) than the better one of the two single-event location methods (Figures 5.a, 5.b and 5.c: red dots). Among the two multiple-event location methods, the double-difference with tomography method (Figure 5.a, 5.b and 5.c: magenta dots) is better in terms of correlation of seismicity with faults – the seismic event locations show better lineation along the fault traces and are less scattered. Nevertheless, some shifts between fault traces and seismic locations are still observed in the double-difference solutions, indicating that the absolute locations may not be well determined by this method. Although the differential times have the ability to determine the absolute locations under certain circumstances, yet in most cases good relative locations are obtained using only differential times. Use of differential times derived from cross-correlation of event waveforms and use of finite difference method for travel time calculation in sedimentary layers help improve the relative location accuracy in this case.

The induced seismicity data acquired by the deep-borehole network were deemed suitable for conducting a complete tomography study using the double-difference tomography method. The region that could be reasonably imaged using this data was between ~0.7 – 1.1 km, covering all of Natih (Natih A, Natih B-E) and the Nahr-Umr formation (oil overburden). The double-difference tomography method used in this study provided reliable estimates of event locations and velocity models. Except for a few places, the relocated events did not seem to show much improved accuracy over the initial locations, due to two possible reasons: i) the initial locations are already accurate and ii) the more accurate differential travel times from waveform cross-correlation were not used for the relocation (unavailable during the course of this study). As for velocity images, the tomography method yields reasonable estimates of velocities in

places where there is good resolution as predicted by the resolution tests. However, because of frequent layering and large contrasts in velocity between adjacent layers, caution must be exercised in interpreting the final velocity images quantitatively. Nevertheless, together the 2D slices taken at various planes (given by Figures 12, 13, 14, and 15) provide useful information about the 3D reservoir structure and at the least a qualitative description of the velocity contrasts within a layer and across different layers in the reservoir. In the central part of the reservoir and at Natih depth slices, the velocity discontinuities seem to align with the preexisting fault traces.

To achieve more accurate results from induced-seismicity tomography, the existing tomography method needs to be improved. For example, adaptive/non-uniform gridding technique to adequately model the shape of the layer boundaries needs to be incorporated. Finer grid spacing and some additional regularization scheme based on a-priori geologic information could also be useful in improving the inversion results. Nevertheless, with the existing double-difference tomography (tomoDD) method we were able to produce images of certain parts of the reservoir showing reasonable structural features. Another major application of induced seismicity tomography would be to interpret the structural and velocity changes with time. If passive seismic monitoring is carried out long enough in a field and data such as that described in this study (deep-borehole network) can be acquired over a significant portion of the reservoir, there is potential to carry out 4D tomography using the induced seismicity data. The current limitations in the tomography code/method will not be critical if only changes in the reservoir velocities over time are targeted for imaging.

5.6 References

Aki, K., A. Christoffersson, and E. S. Husebye (1977), Determination of the three-dimensional structure of the lithosphere: *J. Geophys.Res.* 82, 277-296.

Aster, R. C., B. Borchers, and C. H. Thurber (2005). Parameter estimation and inverse problems, Elsevier Academic Press, Burlington, MA.

Berryman, J. G. (2000). Analysis of approximate inverses in tomography I. Resolution analysis of common inverse, *Optimization and Engineering*, 1, 87–115.

Du, W., C. H. Thurber, and D. Eberhart-Phillips (2004), Earthquake relocation using cross-correlation time delay estimates verified with the bispectrum method, *Bull. Seismol. Soc. Am.*, 94, 856-866.

Eberhart-Phillips, D. (1990), Three-dimensional P and S velocity structure in the Coalinga region, California, *J. Geophys. Res* .95, 15343-15363.

Eberhart-Phillips, D. (1993), Local earthquake tomography: earthquake source regions. In: H.M. Iyer and Irahara, Editors, *Seismic Tomography: Theory and Practice*, Chapman and Hall, New York, 613–643.

Humphreys, E. and R. W. Clayton (1988), Adaptation of back projection tomography to seismic travel time problems, *J. Geophys. Res.*, 93, 1073–1085.

Larsen, R. M. (1998), Lanczos bidiagonalization with partial reorthogonalization, Department of Computer Science, Aarhus University, Technical Report, DAIMI PB-357, September 1998.

Lomax, A., J. Virieux, P. Volant and C. Berge (2000), Probabilistic earthquake location in 3D and layered models: Introduction of a Metropolis-Gibbs method and comparison with linear locations, in *Advances in Seismic Event Location* Thurber, C.H., and N. Rabinowitz (eds.), Kluwer, Amsterdam, 101-134.

219

Minkoff, S. E. (1996), A computationally feasible approximation resolution matrix for seismic inverse problems, *Geophys. J. Int.,* 126, 345–359.

Nikias, C. L. and M.R. Raghuveer (1987), Bispectrum estimation: a digital signal processing framework, *Proc. IEEE* 75, 867–891.

Nikias, C. L. and R. Pan (1988), Time delay estimation in unknown Gaussian spatially correlated noise, *IEEE Trans Acoust. Speech Signal Process,* 36: 1, 706–1, 714.

Pratt, R. G. and C.H. Chapman (1992), Traveltime tomography in anisotropic media-II. Application, *Geophys. J. Int.,* 109, 20–37.

Sarkar, S. and M. Nafi Toksöz (2008), Location of and Monitoring with Induced Earthquakes in Oil and Gas Fields, *70th EAGE Conference & Exhibition incorporating SPE EUROPEC, Rome, Italy.*

Schaff, D. P., G. H. R. Bokelmann, G. C. Beroza, F. Waldhauser, and W. L. Ellsworth (2002), High-resolution image of Calaveras Fault seismicity, *J. Geophys. Res.,* 107, 2186, doi:10.1029/2001JB000633.

Thurber, C. H. (1983), Earthquake locations and three-dimensional crustal structure in the Coyote Lake area, central California, *J. Geophys. Res.* 88, 8226–8236.

Thurber, C. H. (1993), Local earthquake tomography velocities and Vp/Vs—theory. In: H.M. Iyer and K. Hirahara, Editors, *Seismic Tomography*, Chapman & Hall, London, 20, 563–580.

Thurber, C. H. and D. Eberhart-Phillips (1999). Local earthquake tomography with flexible gridding, Comp. Geosci., 25, 809–818.

Thurber, C. H., S. Roecker, K. Roberts, M. Gold, L. Powell, and K. Rittger (2003), Earthquake locations and three-dimensional fault zone structure along the

creeping section of the San Andreas fault near Parkfield, CA: Preparing for SAFOD, *Geophys. Res. Lett.*, 30(3), 1112, doi:10.1029/2002GL016004.

Toomey, D. R. and G. R. Foulger (1989), Tomographic inversion of local earthquake data from the Hengill–Grensdalur central volcano complex, Iceland. *J. Geophys. Res.* 94, 17497–17510.

Vasco, D. W., L. R. Johnson, and O. Marques (2003), Resolution, uncertainty, and whole Earth tomography, *J. Geophys. Res.,* 108(B1), 2022.

Wagner L. S., S. Beck, and G. Zandt (2005), Upper mantle structure in the south central Chilean subduction zone (30° to 36°S), *J. Geophys.* Res., 110, B01308, doi:10.1029/2004JB003238.

Walck, M. C. (1988), Three-dimensional Vp/Vs variations for the Coso region, California. *J. Geophys. Res.* 93 (1988), 2047–2052.

Waldhauser, F., and W. L. Ellsworth (2000), A double-difference earthquake location algorithm: Method and application to the northern Hayward fault: *Bulletin of the Seismological Society of America*, 90, 1353-1368.

Wolfe, C. J. (2002), On the mathematics of using difference operators to relocate earthquakes, *Bull. Seism. Soc. Am.* 92, 2879-2892.

Yao, Z. S., R. G. Roberts and A. Tryggvason (1999), Calculating resolution and covariance matrices for seismic tomography with the LSQR method, *Geophys. J. Int.,* 138, 886–894.

Zhang, H., and C. H. Thurber (2003), Double-Difference Tomography: The Method and Its Application to the Hayward Fault, California, *Bull. Seism. Soc. Am,* 93 (5), 1875-1889.

Zhang, H. and C. H. Thurber (2007). Estimating the model resolution matrix for large-seismic tomography problems based on Lanczos bidiagonalization with partial reorthogonalization, *Geophys. J. Int.* 170: 337–345.

Zhang, H. and C. H. Thurber (2008), Strategies to solve for a better Vp/Vs model around the SAFOD site using P and S arrival times, *Geophys. Res. Lett.*, (in preparation).

Zhang, J. and G. A. McMechan (1995). Estimation of resolution and covariance for large matrix inversions, *Geophys. J. Int.*, 121, 409–426.

Chapter 6

Conclusion

The objective of this thesis was to apply existing and new methods for reservoir characterization and monitoring at a petroleum field in Oman using reservoir-induced seismicity data. The data analyzed for this thesis are by far the largest (both in terms of size and duration) studied induced seismicity dataset in the history of reservoir-scale passive seismic monitoring in the oil and gas industry. The data used for this thesis were acquired by two different networks in the field: i) a near-surface network consisting of shallow (~150 m below surface) borehole installations of 3-component broadband sensors at 6 different locations and ii) a deep-borehole network consisting of 5 wells at different locations with 8 levels of 4-component sensors installed between ~ 750 – 1300 m depths (below surface) in each borehole. The shallow network, which is now in its eighth year of operation, has been collecting induced seismicity data since November 1999; on the other hand the deep network only recorded data during February 2002 – August 2003. The deep network covered a much smaller area than the shallow network, however due to its sensors' proximity to the gas and oil reservoirs it detected many more events than the shallow network. The events detected by the deep network allowed for a much detailed fault and fracture mapping and reservoir characterization in the region between the minimum and maximum depths of its borehole sensor positions. The resolution offered by the shallow network was not as fine as that of the deep network; however, with passive seismic data from the shallow network event detection and reservoir characterization was possible for a much wider area in the field and at shallower reservoir depths such as the overburden. Moreover, continuous data

acquisition over a long period of time by the shallow network offers a unique opportunity for some meaningful time-lapse interpretation of induced seismicity.

Both detectability and locatability of induced events have been greatly reduced in recent years due to degradation of the shallow network performance. Some of the problems are discussed in Appendix B. During processing of the raw field data for this study, state-of-health (SOH) data of the sensors were also looked at and some of the major problems and troubleshooting suggestions were communicated to PDO. In an effort to revitalize and improve the passive seismic monitoring in this field, recommendations were made to PDO for adding a few stations to the existing network. Some of the design details for this proposed "new" network are given by Appendix C. A network consisting of stations both near surface and at depths would greatly help improve the event locations – especially focal depths.

For this thesis, induced seismicity data for the period November 1999 – February 2007 from the shallow network data, and for October 2002 – August 2003 from the deep network data were analyzed. With large data gaps during the ~ seven year period, about 1300 event data were retrieved and located from the shallow network, whereas out of 15,800 event data received for the 11-month period from the deep network, 5400 events were located. During locations of these events, significant improvements were made in the location method to improve accuracy of event locations. With improved accuracy of the located events, the study focused on identifying faults and fractures in the field and characterization of reservoir using the induced events. The following provides a summary of the key findings of this dissertation work:

224

- Due to presence of alternating low and high velocity layers in the reservoir, a detailed velocity model was required to improve the focal depth accuracy of induced events. We used available well-logs to constrain the major layer boundaries and derived a layered velocity model for the reservoir. A set of events from the shallow network, located during a previous study, was relocated with this "new" velocity model and significant improvements were made in their depth locations.

- For event location from the shallow network, a location method was devised to improve the accuracy of event locations for this study. With the more detailed velocity model and finite-difference method to calculate the forward travel times, the inversion strategy was based on minimizing station-pair-differences of the arrival time data and using exhaustive grid search to find the global optimum solution. Due to the complex nature of wave propagation in shallow sedimentary layers, differentiating pure S-wave arrivals from converted phases from the seismograms seemed very difficult – imposing additional uncertainty in the arrival time data. To accurately locate the events recorded by the shallow network, the safest approach was to exclude the highly uncertain S-phase data and use the station-pair-differencing method to locate events that produced "identifiable" P-phase arrivals at minimum 4 stations of the network. The station-pair-differencing method combined with exhaustive grid-search was very fast and efficient, and produced reasonably accurate event hypocenters as validated by the locations of known repeating events (*multiplets*).

- The primary cause of induced seismicity in the field is attributed to the compaction of the Natih gas formation. High concentration of events in and around the gas formation and strong correlation between monthly gas production and seismicity rate provide further evidence to support this inference. Locations from both shallow and deep network show similar event distribution in the field and lead to the same interpretation about the cause of induced seismicity. Surface subsidence data from leveling, GPS and InSAR monitoring in the field show good correlation with the induced seismicity data. Water injection into the Shuaiba oil formation is also responsible for inducing seismicity in the field, but to a much lesser extent as compared to gas production.

- Seismicity is mostly confined in the major NE-SW fault corridor of the field. 11 months of deep-network data and seven years of shallow-network data reveal that the general pattern and overall distribution of seismicity in the field has not changed much over time. Detail analysis of event hypocenters show strong correlation with existing fault maps. New features are also identified from extensive location study and mapping of the events – some of them could be faults that were previously unmapped, and some are fractures created due to overpressurization in the rocks and/or stress perturbation. The south-western side of the major NE-SW fault corridor shows more seismicity between the two faults in recent years, revealing a few structures *oblique* to the major fault direction.

- Detailed depth analysis of the events with time reveals ongoing large scale fault reactivation in the field. The entire field – all the way from the shallow overburden to the

base of the oil reservoir – has been showing evidence of fault slip. Depth locations of the induced events provide useful information about fault dips and for mapping fault planes at depths. Short-term tracking of the event locations with time can be very useful in identifying flow paths or barriers in the reservoir; however, due to limited access to local production/injection data of the field, this application of induced seismicity could not be used to its full potential in this study.

- Location accuracies of events recorded by the shallow-network and initially located by single-event location method are further improved by using a relative event location technique that minimizes differential travel times of event pairs at common stations. High-fidelity differential travel time data were produced from waveform cross-correlation between similar event pairs. Improvements in relative accuracies of events within clusters are achieved and better correlations with faults are thus observed.

- Reservoir imaging carried out for this dissertation work – using passive/induced seismic data recorded by the deep-network – shows encouraging results in identifying structures and velocity changes within reservoir layers. Although 3D tomography using the double-difference tomography method used in this study demonstrates great value of induced seismicity data and unfolds a new horizon in reservoir characterization application, there is further scope for improvement in the method to make it better-suited for petroleum reservoir applications.

Appendix A

On the Uncertainty and Errors of Induced Event Locations

The accuracy of located events is evaluated based on estimates of formal uncertainty. In order to determine uncertainty, most location algorithms usually use one of the following two methods: 1) F-statistic, where the *a posteriori* residual distribution is mapped to a location confidence ellipsoid (Flinn 1965), or 2) Chi-square statistic, where *a priori* uncertainty for phase picking and traveltime prediction are mapped through the location algorithm to produce a coverage ellipsoid (Evernden 1969). The theories behind these techniques require compliance with basic statistical assumptions: Gaussian, zero mean, uncorrelated error processes. However, a number of studies suggest that these assumptions are violated in most seismic locations. Picking error tends to have "heavy" tails (Buland 1986) and may be multimodal. The mean of the traveltime prediction errors is typically not zero and traveltime prediction errors are typically correlated for similar ray paths (e.g. Myers & Schultz 2000).

In this appendix, we show a couple of examples for uncertainty estimates of event locations derived using NonLinLoc. With the NonLinLoc method, the "optimal" hypocenter solution for an event is actually the maximum likelihood (or minimum misfit) point of the complete, non-linear location PDF for that event hypocenter estimated by NonLinLoc. The significance and uncertainty of this maximum likelihood hypocenter cannot be assessed independently of the complete solution PDF (http://alomax.free.fr/nlloc).

228

For traditional Gaussian case, the variance-covariance matrix, which characterizes the location uncertainty, may be obtained from the gridded values of the normalised location PDF or from samples of this function (Tarantola and Valette, 1982; Sen and Stoffa,1995). As a measure of location uncertainty, NonLinLoc reports 68% confidence ellipsoid obtained from singular value decomposition (SVD) of the variance-covariance matrix following Press *et al.* (1992). The Gaussian estimators and resulting confidence ellipsoid are likely to be good indicators of the uncertainties in the location only in the case where the complete, non-linear PDF has a single maximum and has an ellipsoidal form (http://alomax.free.fr/nlloc).

Figures A.1 and A.2 show the maximum likelihood hypocenters plots for two events (Ev # 3 and Ev # 6: Table 2.2 in the main text) along with their 68% confidence ellipsoids obtained from NonLinLoc outputs. The following table summarizes the length of the semi-axes of the two confidence ellipsoids:

Event #	Semi-axis 1 length (km)	Semi-axis 2 length (km)	Semi-axis 3 length (km)
3	8.24e-02	8.96e-02	1.39e-01
6	1.67e-01	2.04e-01	1.44

It is seen from Figure A.1 that event # 3 is located by data from 5 stations (VA1 through VA5), which provide a good azimuthal coverage for the event. With reasonably accurate picks and good station coverage the error ellipsoids are expected to be small. The location accuracies of such "well-located" events in the field are within 100 – 200 meters, in all three directions. Figure A.2 shows a skewed and relatively larger error ellipsoid for the epicenter (and to some

229

extent for the depth) uncertainty of event #6. This is expected because of the poor station/data

coverage for this event. Data from station VA5 and VA3 were unavailable for this event.

Although a new station VA6 provided data for this event, the effect of large azimuthal gap on

one side of the event could not be mitigated. Nevertheless, the maximum likelihood hypocenter

estimates are quite good for both of these events. Since they both belong to the same *multiplet* set

(Figure 2.7 in the thesis), their locations should be almost identical. Figures A.1 and A.2 show

that the maximum likelihood locations of these two events are quite close.
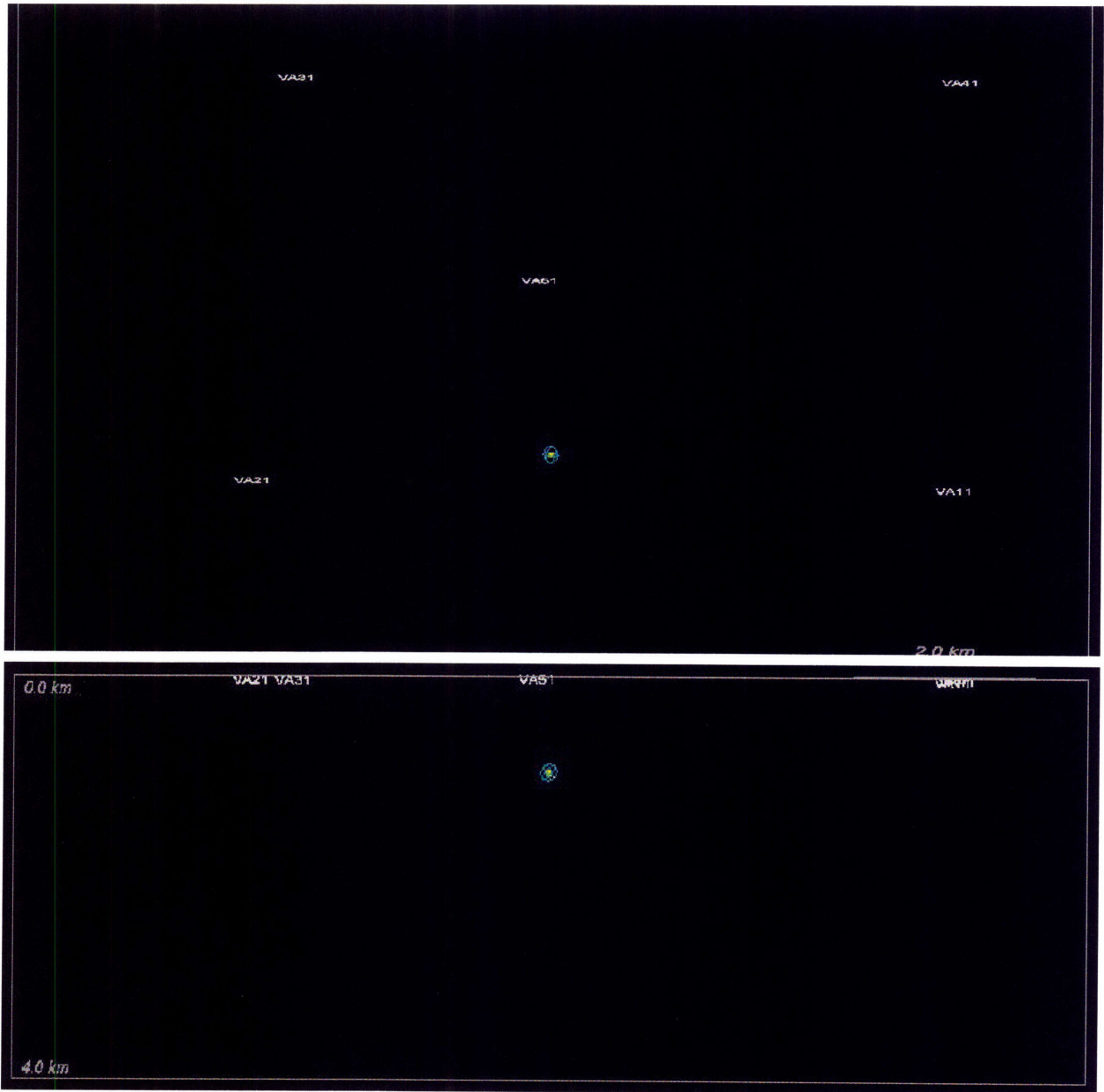
Figure A.1: NonLinLoc L-2 Gaussian estimation of maximum likelihood hypocenter estimate (yellow dot) of an event and corresponding confidence ellipsoid (blue). The upper plot shows the epicenter with dimensions of the two axes being 12 km by 12 km. The lower window shows a vertical cross-section (depth vs. X) plot, with dimensions of the two axes being 4 by 12 km.
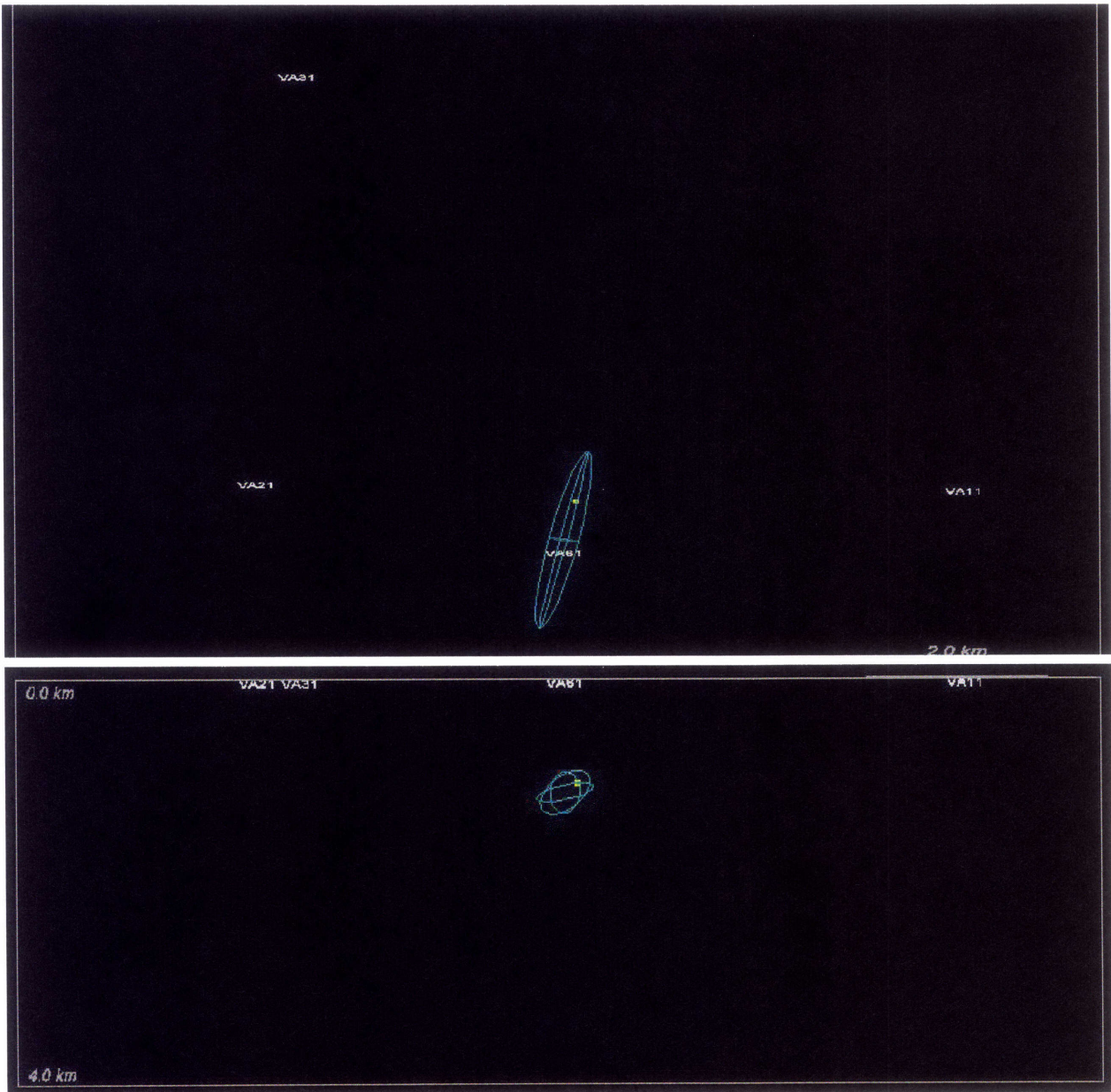
Figure A.2: NonLinLoc L-2 Gaussian estimation of maximum likelihood hypocenter estimate (yellow dot) of an event and corresponding confidence ellipsoid (blue). The upper plot shows the epicenter with dimensions of the two axes being 12 km by 12 km. The lower window shows a vertical cross-section (depth vs. X) plot, with dimensions of the two axes being 4 by 12 km.

We also show comparison between L-2 and L-1 norm minimization from our station-pair-differencing location method (Figure A.3). The two norms yield almost identical minimum residual hypocenter solutions. This demonstrates the robustness of our location method.

New-Loc-Method Results: Comparsion btwn L-1 norm (x) and L-2 norm (.) solutions
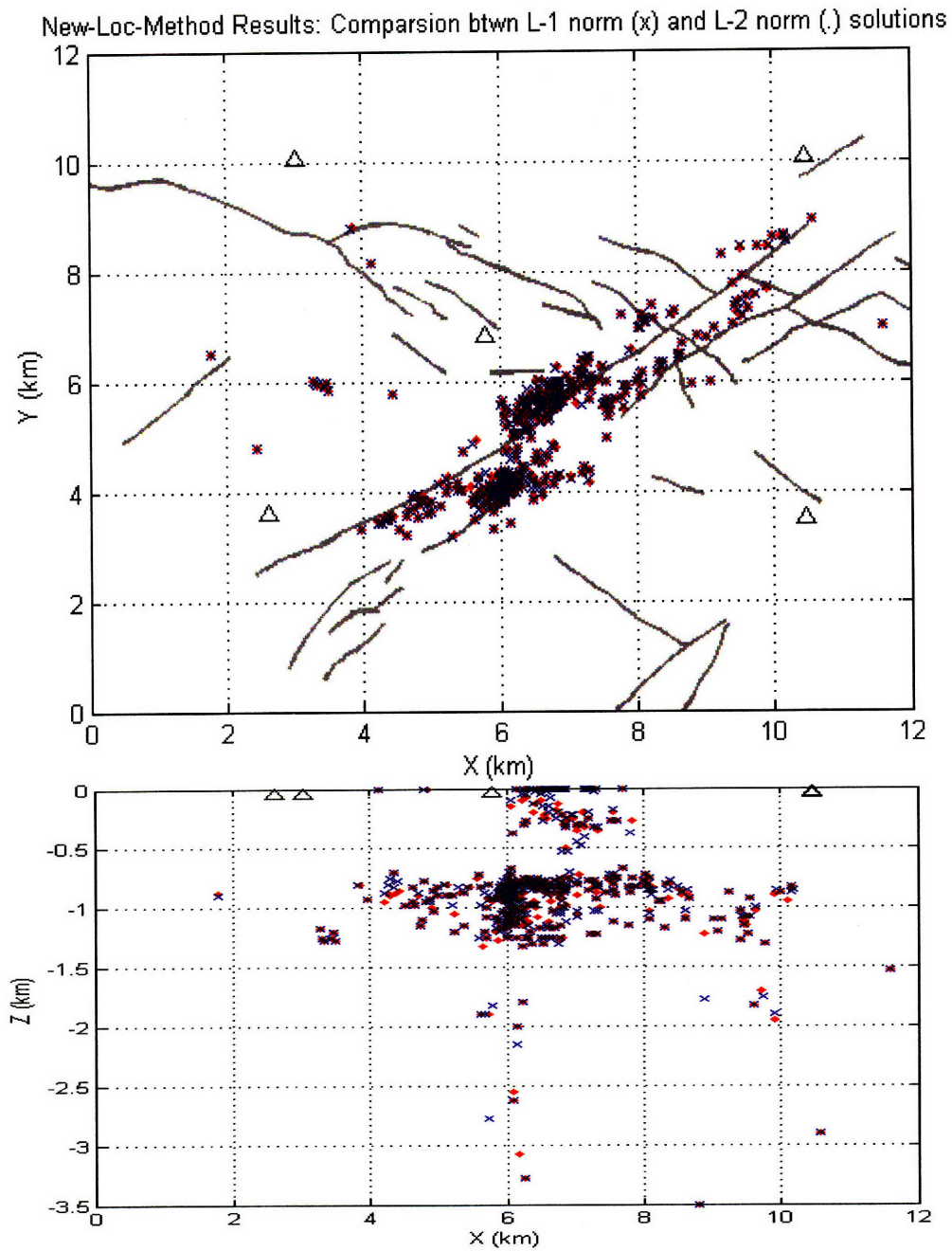
Figure A.2: Comparison between L-2 and L-1 norm solutions (event locations) obtained by the Station-pair-differencing location method.

References

Buland, R., (1986), Uniform reduction error analysis, *Bull. seism. Soc. Am.*, 76, 217–230.

Evernden, J.F., (1969), Precision of epicentres obtained by small numbers of world-wide stations, *Bull. Seism. Soc. Am.,* 59, 1365-1398.

Flinn, E.A., (1965), Confidence regions and error determinations for seismic event location, *Rev. Geophys.,* 3, pp. 157–185.

Myers, S.C., and C.A. Schultz (2000), Improving sparse network seismic location with Bayesian kriging and teleseismically constrained calibration events, *Bull. seism. Soc. Am.,* 90, 199–211.

Press, W.H., S.A. Teukolosky, W.T. Vetterling, and B.P. Flannery (1992), *Numerical recipies in C: the art of scientific computing* or *Numerical recipies in FORTRAN: the art of scientific computing,* Cambridge University Press, Cambridge.

Sen, M., and P.L. Stoffa (1995), *Global optimization methods in geophysical inversion,* Elsevier, Amsterdam, 281.

Tarantola, A., and B. Valette (1982), Inverse problems = quest for information., *J. Geophys.,* 50, 159-170.

Appendix B

A Brief Evaluation of the PDO Seismic Monitoring Network: Its Degradation in Recent Years

In this section, we describe some of the difficulties faced during processing of seismic data from the shallow seismic network.

The following observations are noted from analyzing microseismic data acquired by PDO network during ~ 05/20/2005 – 05/08/2006.

During this period, number of seismic stations acquiring data at a given time did not generally exceed 3. Almost all the stations had interruptions in data acquistion, and number of stations observing an event during this period was 2 – 3, at best.
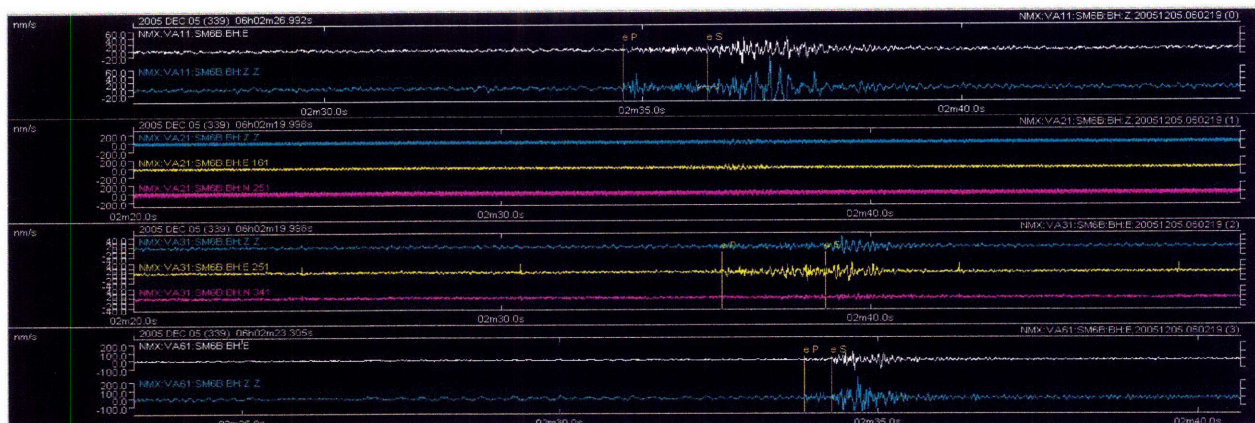
The network maintenance and certain calibrations seemed inadequate. In addition to insufficient data, variation of background noise type and level compounded the difficulty of

earthquake data analysis and phase identification.
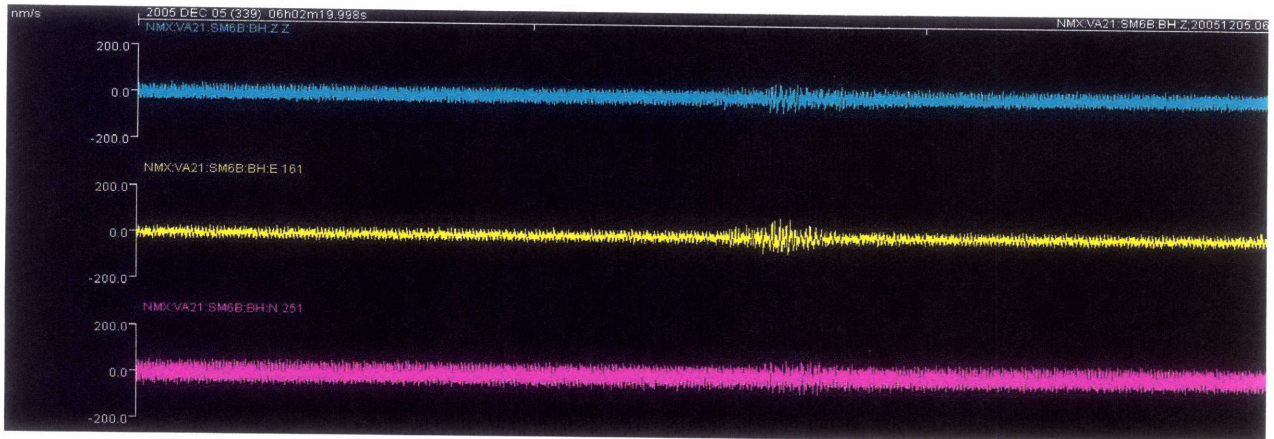
Examples of different background noise types:-
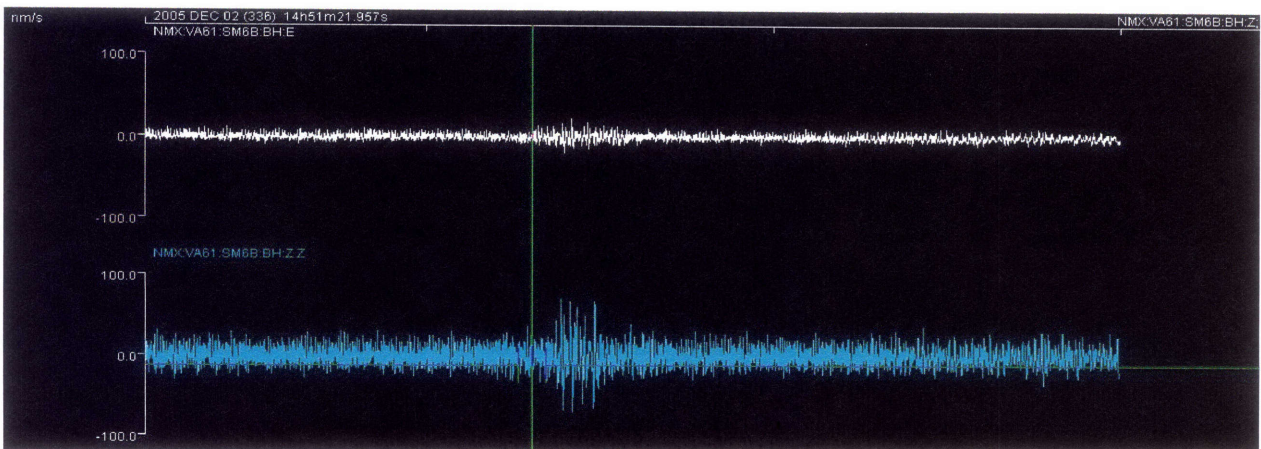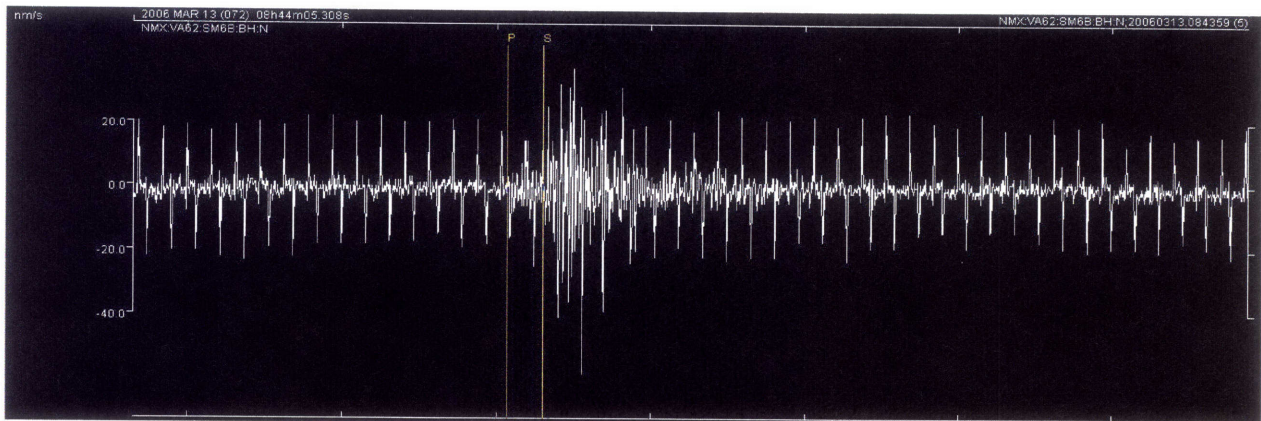
In many instances, some components of the three-component seismograms did not function
properly.
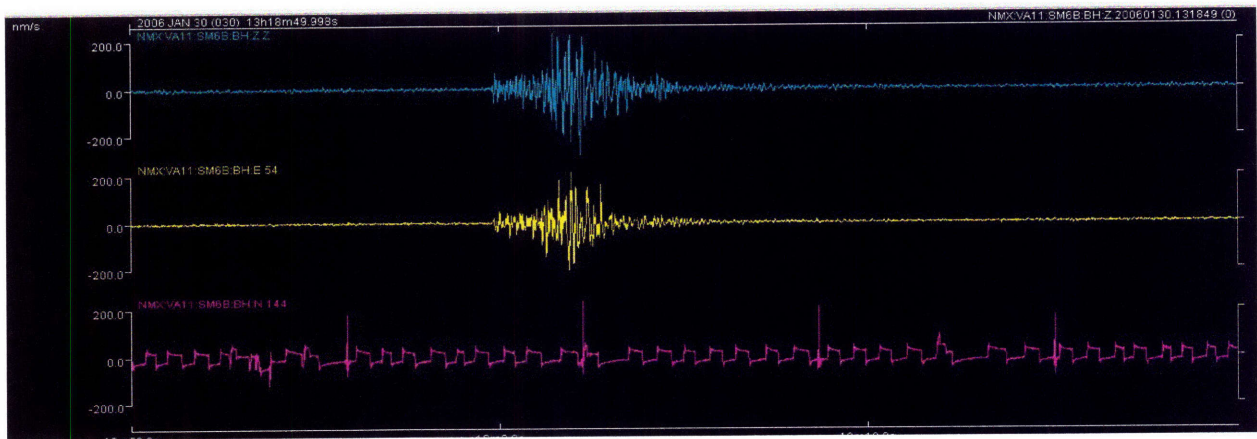
Example of one horizontal component not working properly when an event was recorded:-
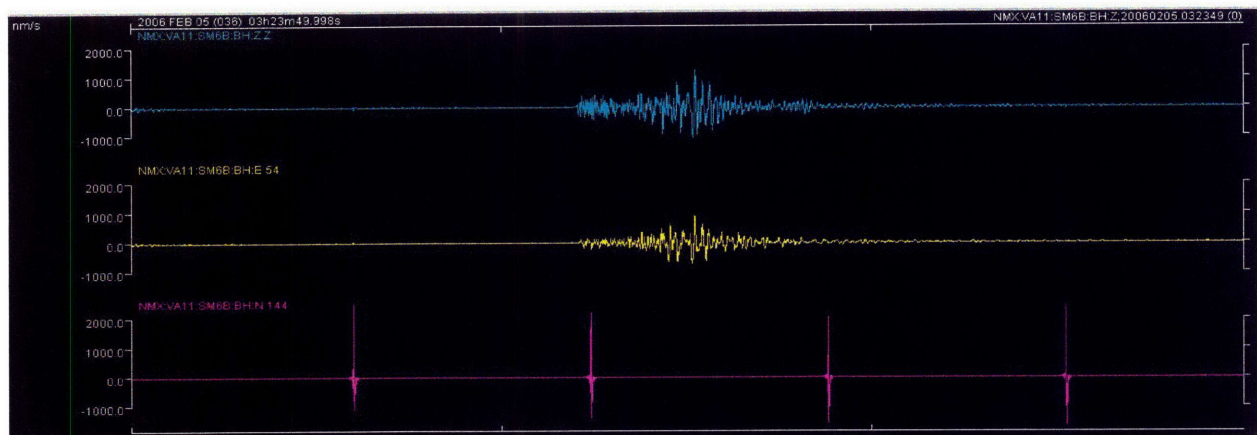
Example of none of the components working properly when an event was recorded :-
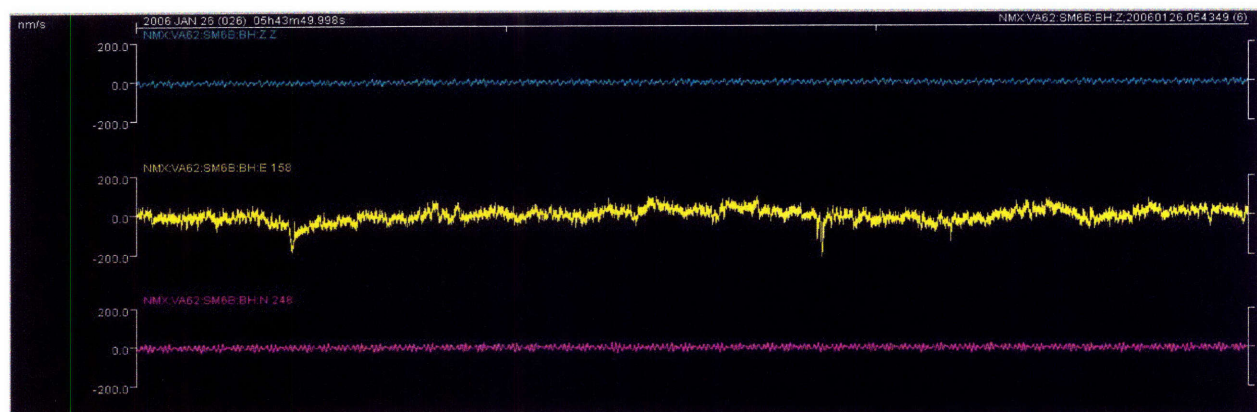
Clock synchronization of the sensors was found problematic.
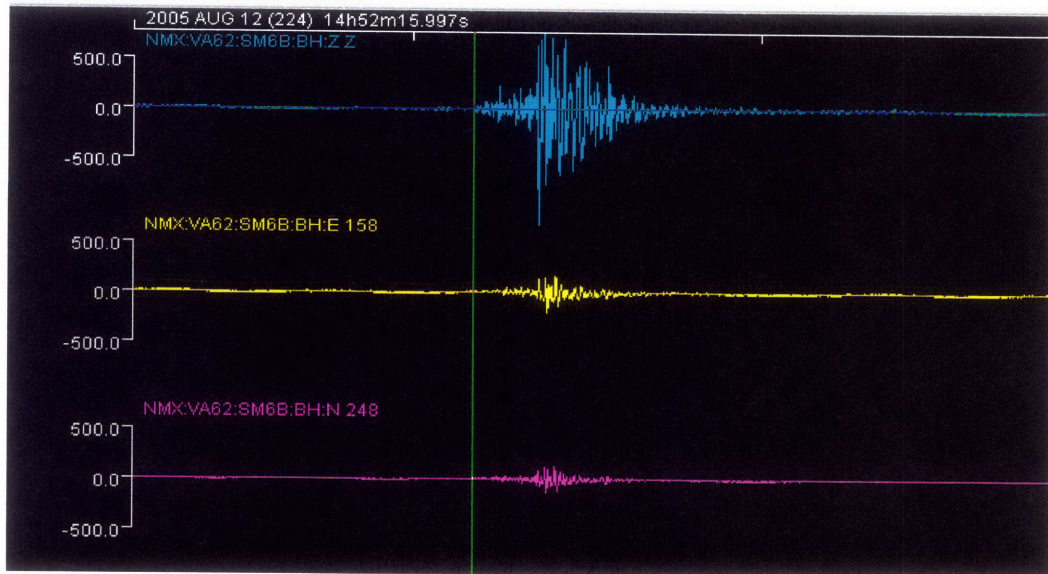
For most of the events, high level of background noise made it extremely difficult to identify P (and S) phases and therefore arrival times required for earthqauke location could not be picked accurately. In general, the data quality was not satisfactory.
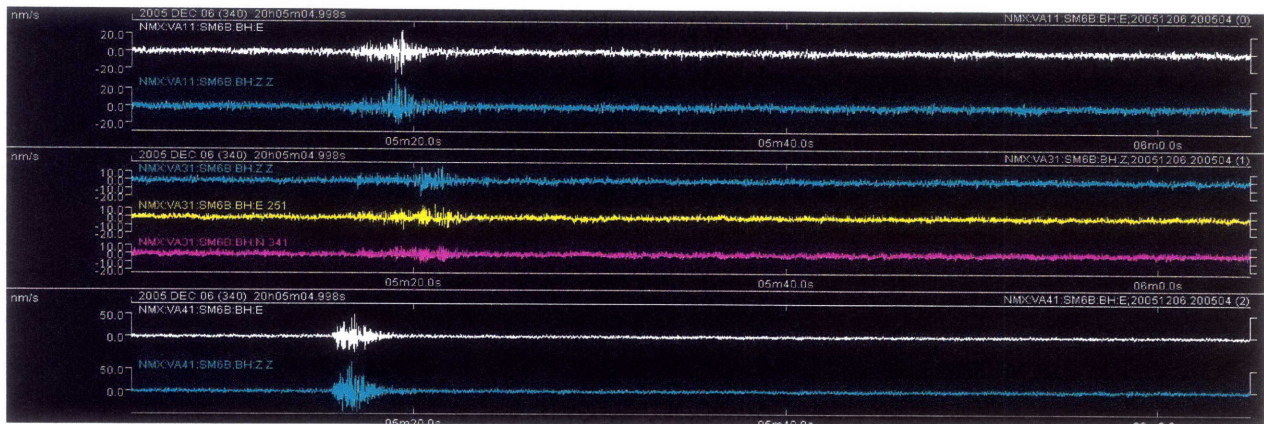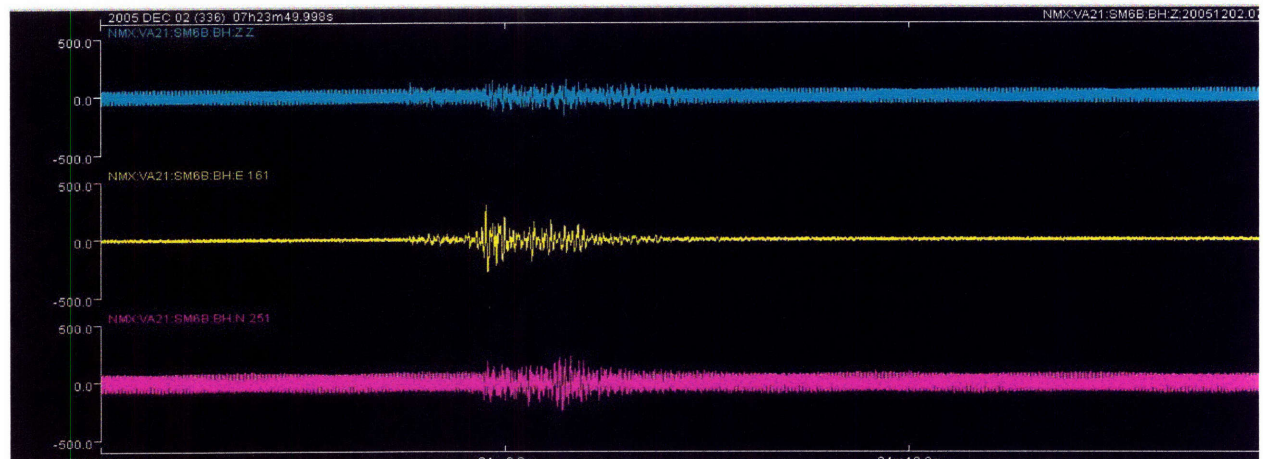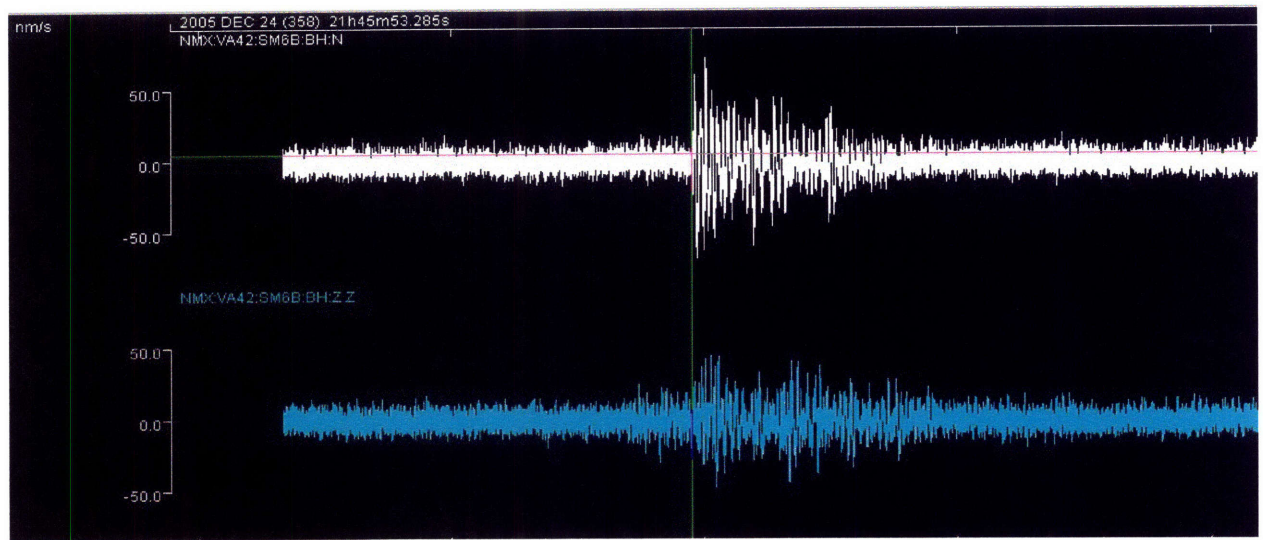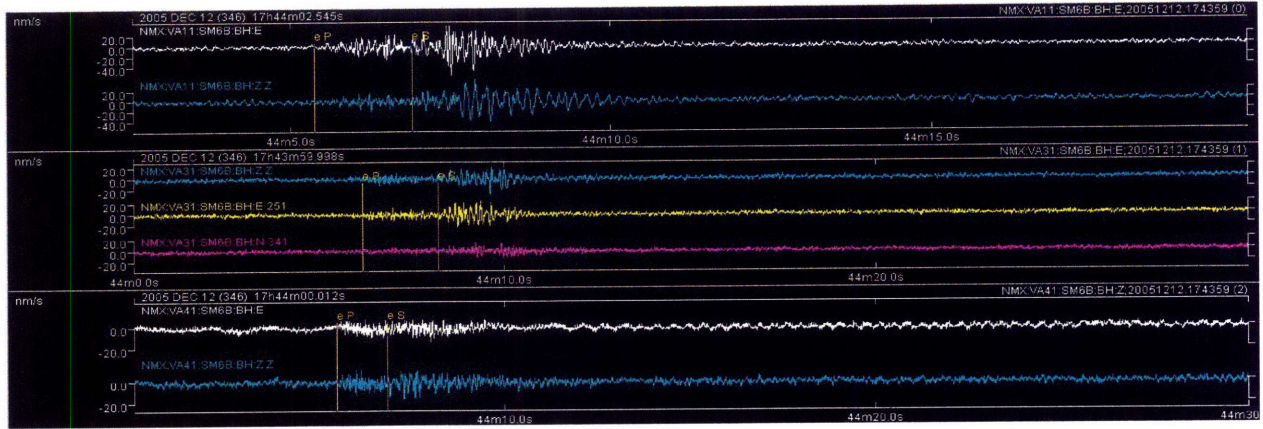
Since only 2 to 3 stations were reporting event data during this period, the accuracy of earthqauke locations suffered heavily due to existing seismic network gaps.

To cite an example, out of 52 events detected during the period 08/10/2005 – 10/04/2005, only 2 events had good data quality and adequate number of arrivals to locate them properly. Since P and S-arrivals from these two events could be read with reasonable certainty, the epicenter solutions were also reasonably accurate. The epicenters of these two events are shown by the following plot :-
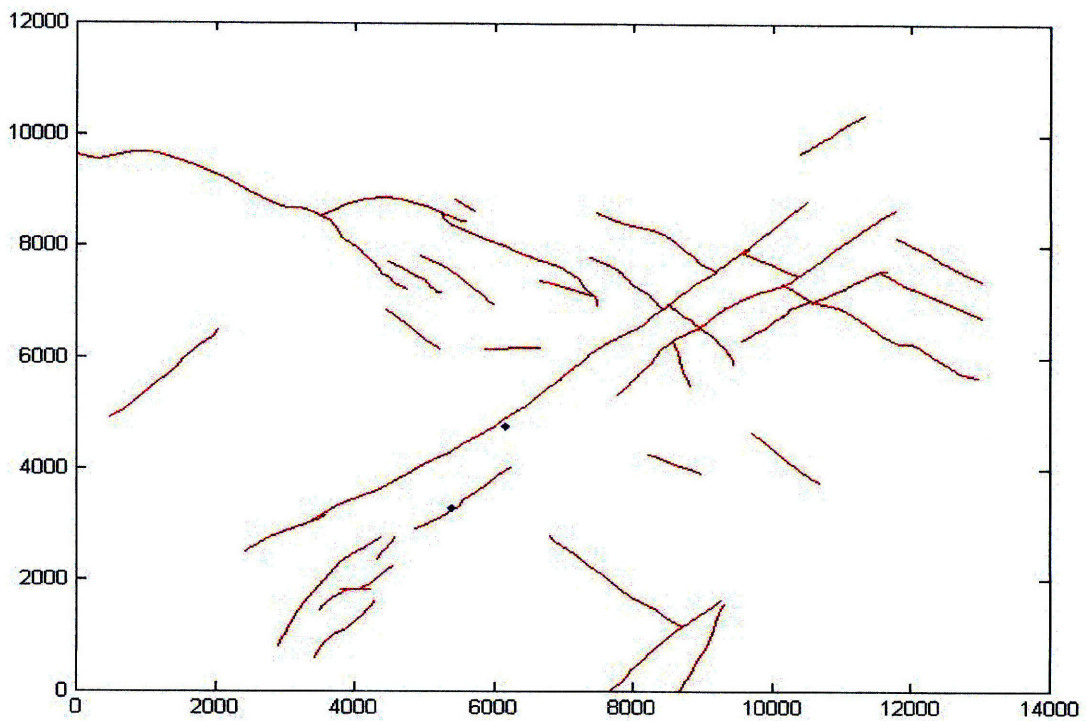
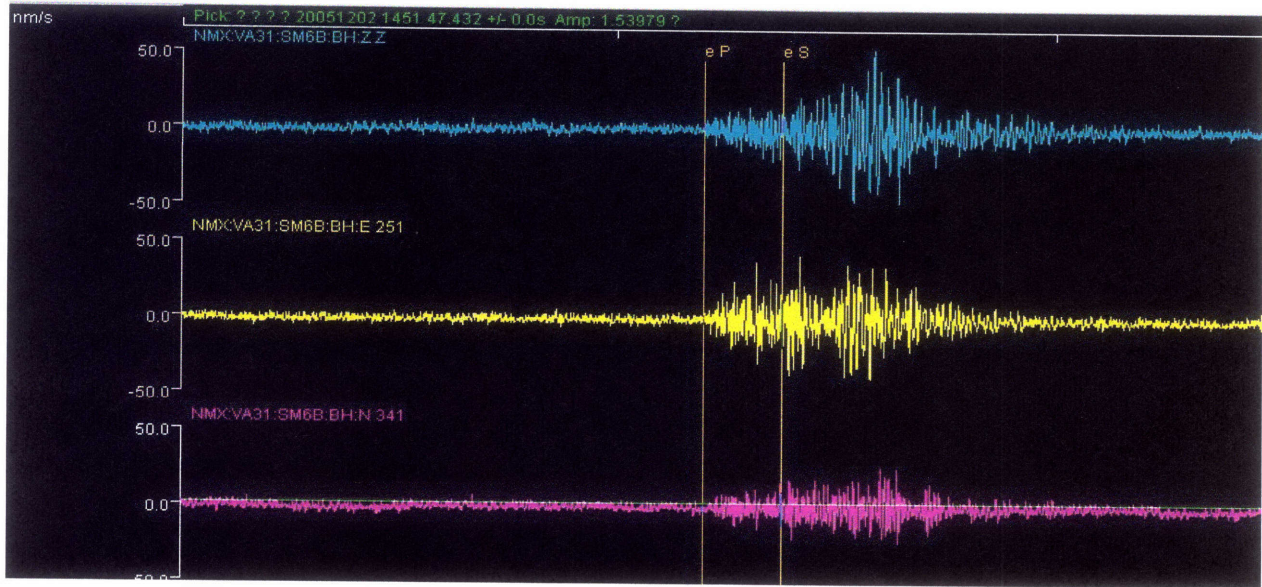Stations used in locating earthquakes :-
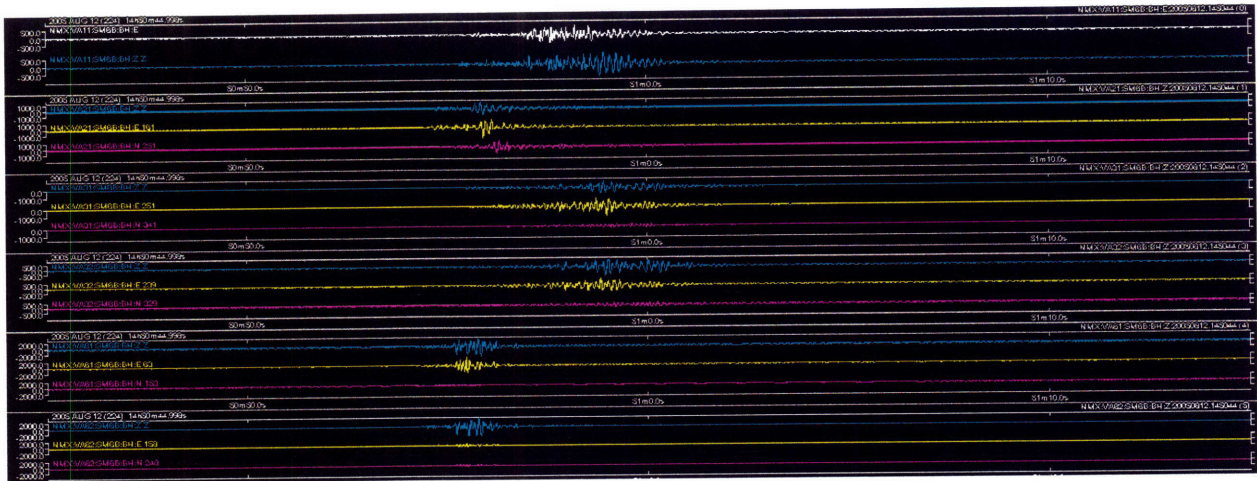
An example of good data quality :-
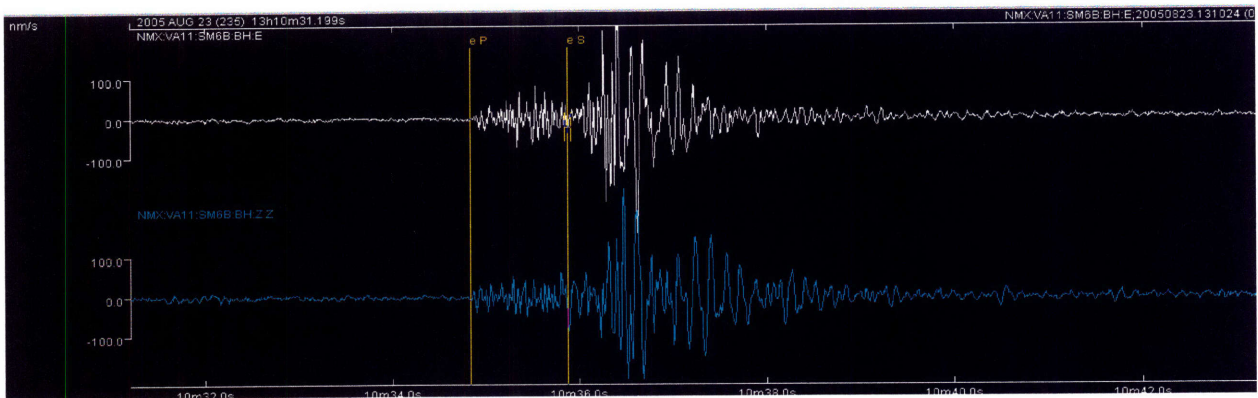
However, a large number of event data looks like the following :-
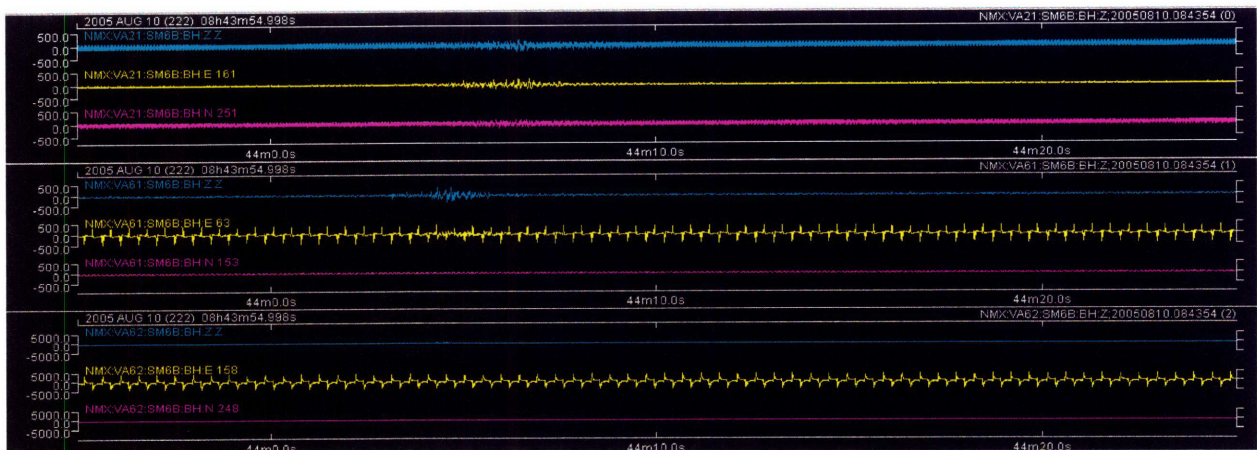
Some events had quite different source mechanisms, and the S-phase readings were extremely difficult for these events. These events were mostly located outside the known major faults.
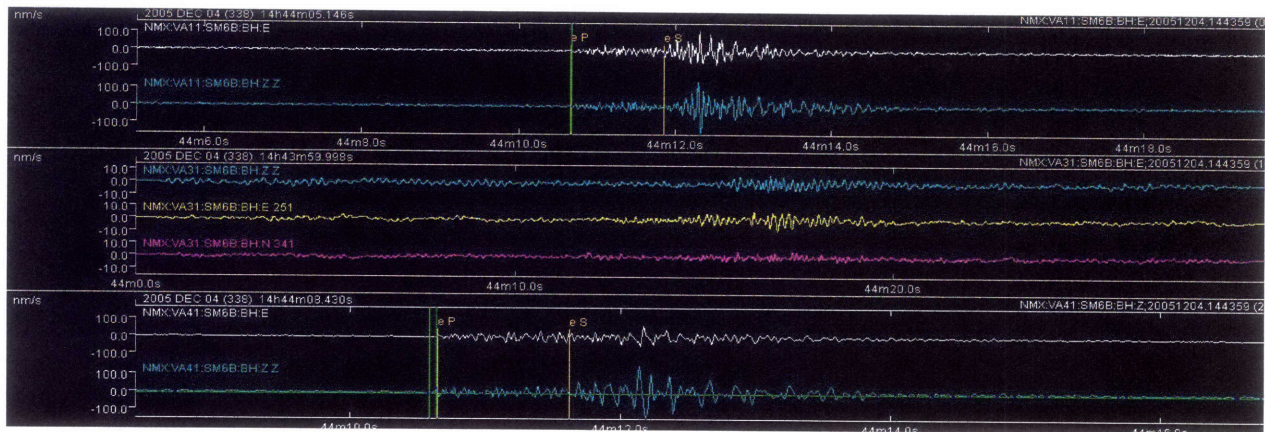
Conclusion: A THOROUGH TECHNICAL EVALUATION OF THE STATUS OF THE SENSORS AND TROUBLESHOOTING ARE REQUIRED, AND DATA QUALITY NEEDS TO BE IMPROVED, IN ORDER TO LOCATE EVENTS IN FUTURE WITH REASONABLE CERTAINTY.

Appendix C

Design of a New Network for Passive Seismic Monitoring at the Petroleum Field in Oman

The existing PDO near-surface seismic network consists of 6 shallow installations – VA1, VA2, VA3, VA4, VA6 and VA7. The status of this PDO seismic network, individual station performances and various data acquisition issues have been discussed in great details by Appendix B. Although not all among the six originally-in-place stations are known to record seismic data in a consistent manner, yet for the purpose of this network design study we would assume that these six stations form the "existing" seismic network, and any new station that might be recommended as a result of this study would be in addition to these existing stations. The purpose of this network design study is to analyze whether or not the existing stations are adequate to reasonably characterize the microseismicity in the field, and if they are not adequate what is the minimal number of new stations required to capture the microseismicity and what would be their optimal installation locations in the field.

A series of synthetic tests is performed for this network design study. For these tests, a ~ 12 km by 12 km area, which is thus far known to contain most of the microseismicity in the field, is selected. The depth of our study extends down to 4 km below surface. For this study we take six earthquakes in the field, locations (epicenters and depths) of which we assume to know:-

Eq. #	Easting (m)	Northing (m)	Depth (km)
1	399500	2449500	1.0
2	395500	2446000	1.0

243

3	402000	2452000	1.0
4	399500	2449500	3.0
5	395500	2446000	3.0
6	402000	2452000	3.0

The locations of these events were selected such that each represents a potential zone of active seismicity in the field, and among them they span the entire zone of interest.

The workflow for the synthetic study can be summarized as follows:-

1. For every event-station pair, we calculate synthetic P- and S-wave travel times (using a 3D Eikonal finite difference scheme of Podvin and Lecomte[11] (1991).

2. We invert the travel times (using a non-linear, probabilistic, grid-search type inversion scheme by Lomax, et. al[12], (2000)) to find the maximum likelihood hypocenters for each of these events.

3. We compare the inversion results (hypocenters) with the actual/modeled hypocenters of the synthetic events.

4. We add noise to the synthetic travel time data computed by step-1, and repeat the procedure (steps 2 – 3).

The results of the synthetic tests with relevant figures are given in the following.

---

[11] **Podvin, P. and Lecomte, I., 1991**, Finite difference computation of traveltimes in very contrasted velocity models: a massively parallel approach and its associated tools., *Geophys. J. Int.*, **105**, 271-284.

[12] **Lomax, A., J. Virieux, P. Volant and C. Berge, 2000.** Probabilistic earthquake location in 3D and layered models: Introduction of a Metropolis-Gibbs method and comparison with linear locations, in *Advances in Seismic Event Location* Thurber, C.H., and N. Rabinowitz (eds.), Kluwer, Amsterdam, 101-134.

[On the figures to follow, different symbols are used to denote different attributes :-

Black Lines ——————— *=> Faults*

Blue Circles O   *=> Actual/modeled locations of the synthetic events*

Red Crosses ✕

             => Inverted locations of the synthetic events

Green Triangles ▲ *=> Original/Existing near-surface seismic stations*

Magenta Triangles ▲ *=> Proposed New near-surface seismic stations*

Black Diamond =>◆Proposed New seismic station at depth

The (0, 0) of the figures correspond to Easting 392000 (m) and Northing 2444000 (m) of the UTM coordinate system. MSL is used for depth = 0.

Network Analysis: Data with no Noise

When there is no error (commonly termed as "noise") present in the data, the existing network can adequately resolve the locations of the microseismic events (*Figure 1.a*). Addition of new seismic stations yields equivalent, if not slightly better, results (*Figure 1.b*). Looking at these results, one might think that installation of new seismic stations may not be required in this field. However, practically it is almost NEVER the case when data will be noise free. We will show by some of the following examples the effects of noise in the inversion for hypocenters and how the existing network stacks up against the new/proposed network in determining the event locations.
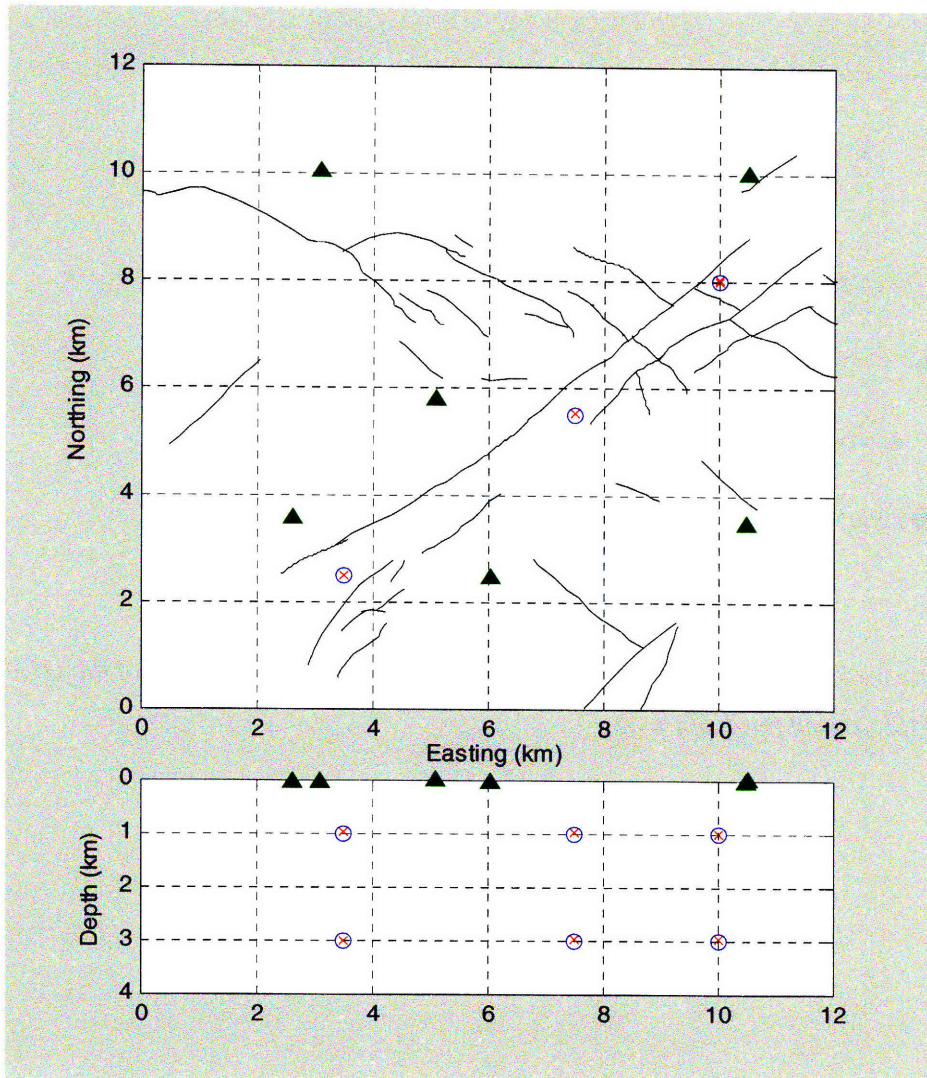
Figure 1.a : Actual event locations compared with locations determined by the EXISTING network, for noise-free data.
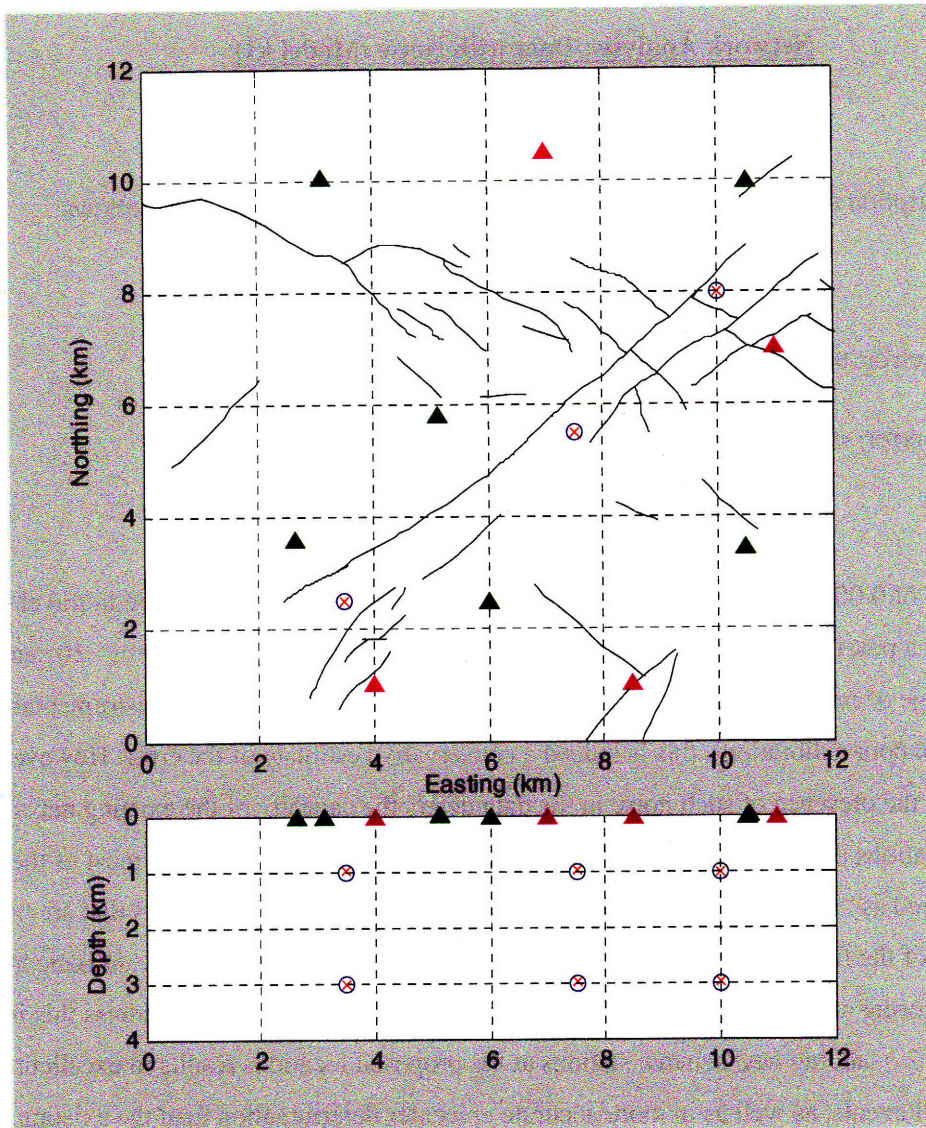
Figure 1.b : Actual event locations compared with locations determined by the proposed NEW network, for noise-free data.

Network Analysis: Data with Noise (Model #1)

The statistical description of the noise added to the travel time data for this case is as follows:

P-wave travel time error: *mean ~ 0, std ~ 0.04*

S-wave travel time error: *mean ~0, std ~ 0.08*

For a sampling rate of 0.008 sec/samples of the current instrumentation, this error range in travel time data corresponds to a possible mis-identification of first-P wave arrivals by ~ 5 samples (~ 10 samples for S-picks). For the type of microseismic data seen in Yibal and issues with the current instrumentation (low signal to noise ratio, poor calibration), this is indeed a conservative estimate of the error. However, as seen by *Figure 2.a*, the presence of such noise in the data deters the capacity of the existing network in determining the locations of some of the events. The epicenters (X-Y coordinates) for most of the events can still be considered as "satisfactorily" resolved, but the depth locations of the events that are on the North-Eastern side of the field are poorly resolved. Depth uncertainty is a very significant issue in the microseismic monitoring at the field, and therefore new stations should be added to address this issue. As we show by *Figure 2.b*, adding new seismic stations at the proposed locations results in excellent depth determination for all events, as well as in more accurate epicenter determination than the existing network.
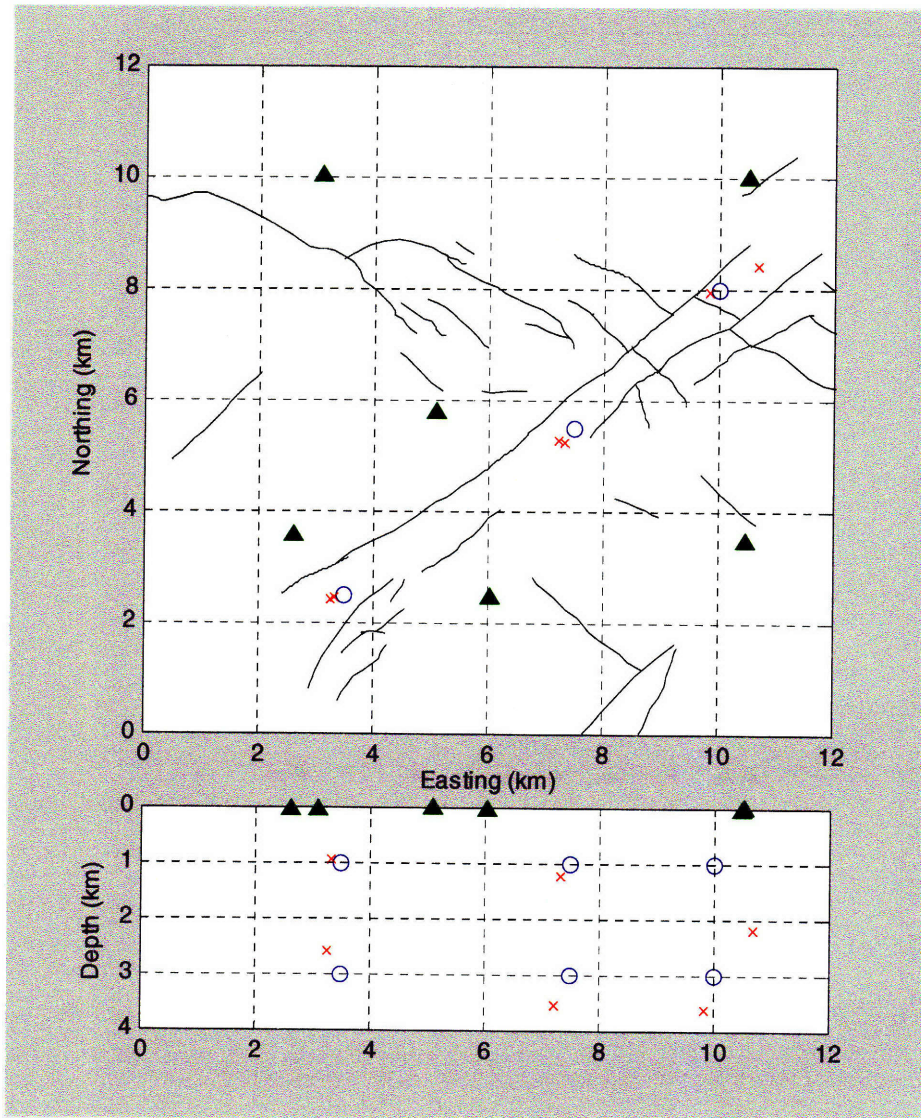
Figure 2.a : Actual event locations compared with locations determined by the EXISTING network, for "realistically-minimal" noisy data.
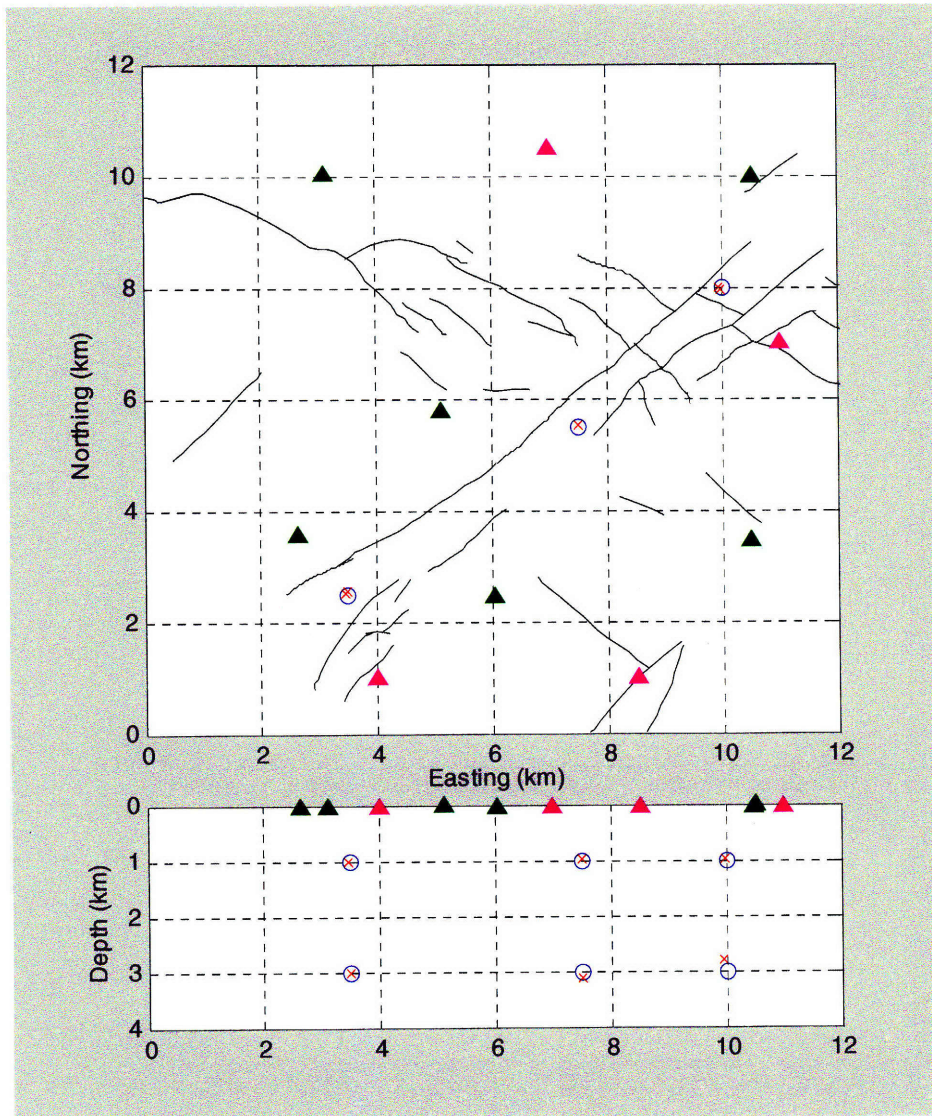
Figure 2.b : Actual event locations compared with locations determined by the NEW network, for "realistically-minimal" noisy data. Significant improvement in event locations due to addition of new stations is observed.

Network Analysis: Data with Noise (Model #2)

The statistical description of the noise added to the travel time data for this case is as follows:

P-wave travel time error: *mean ~ 0, std ~ 0.08*

S-wave travel time error*: mean ~0, std ~ 0.16*

Although for a data sampling rate of 0.008 sec/samples, this error model is quite high, yet from our experience in analyzing the Yibal microseismic data, we have seen that it is not very unlikely to pick (both P and S) phases with errors in this range. As expected, such errors in data will adversely affect the hypocenter determination, and as seen by *Figure 3.a* the epicenter and depth accuracy of the inverted locations suffer severely. However, adding new stations greatly improves the location accuracies (*Figure 3.b*).
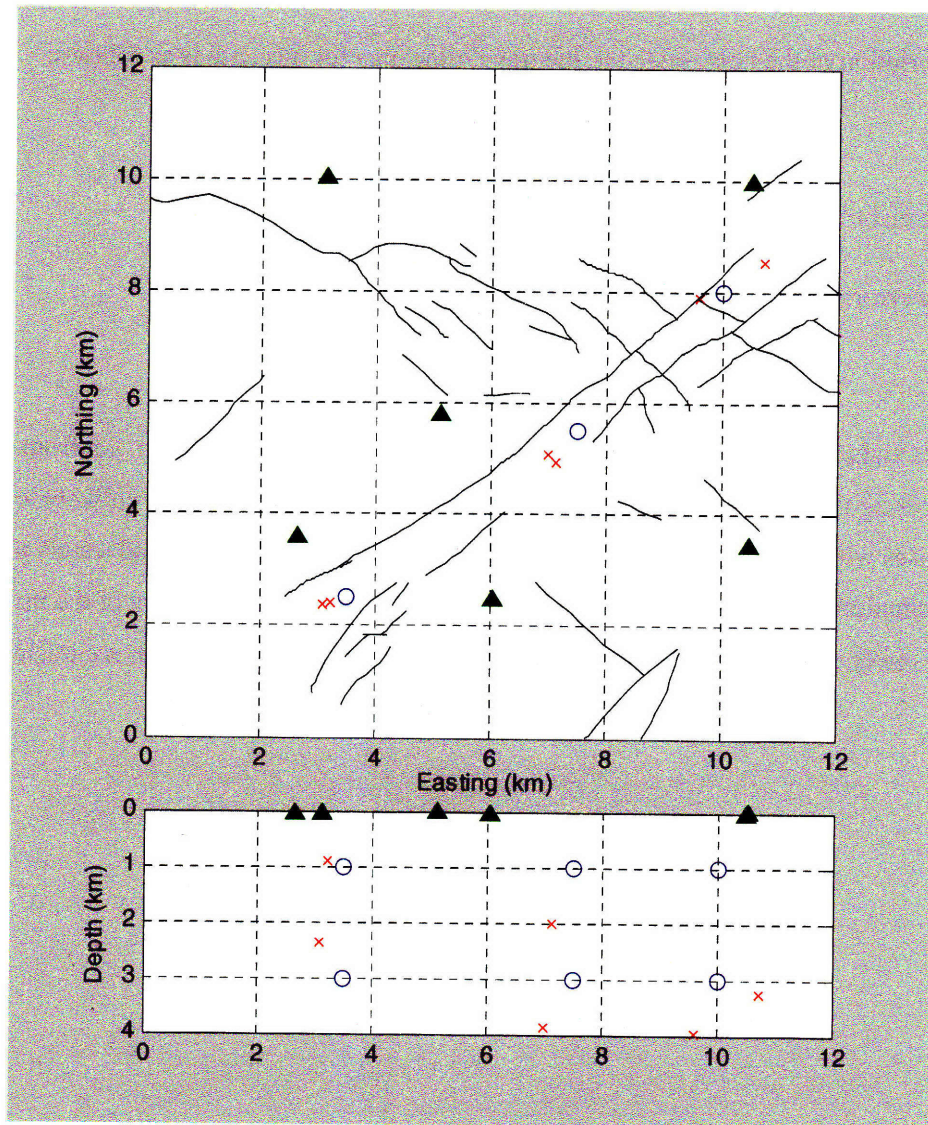
251

Figure 3.a : Actual event locations compared with locations determined by the EXISTING network, for "highly-noisy" data.
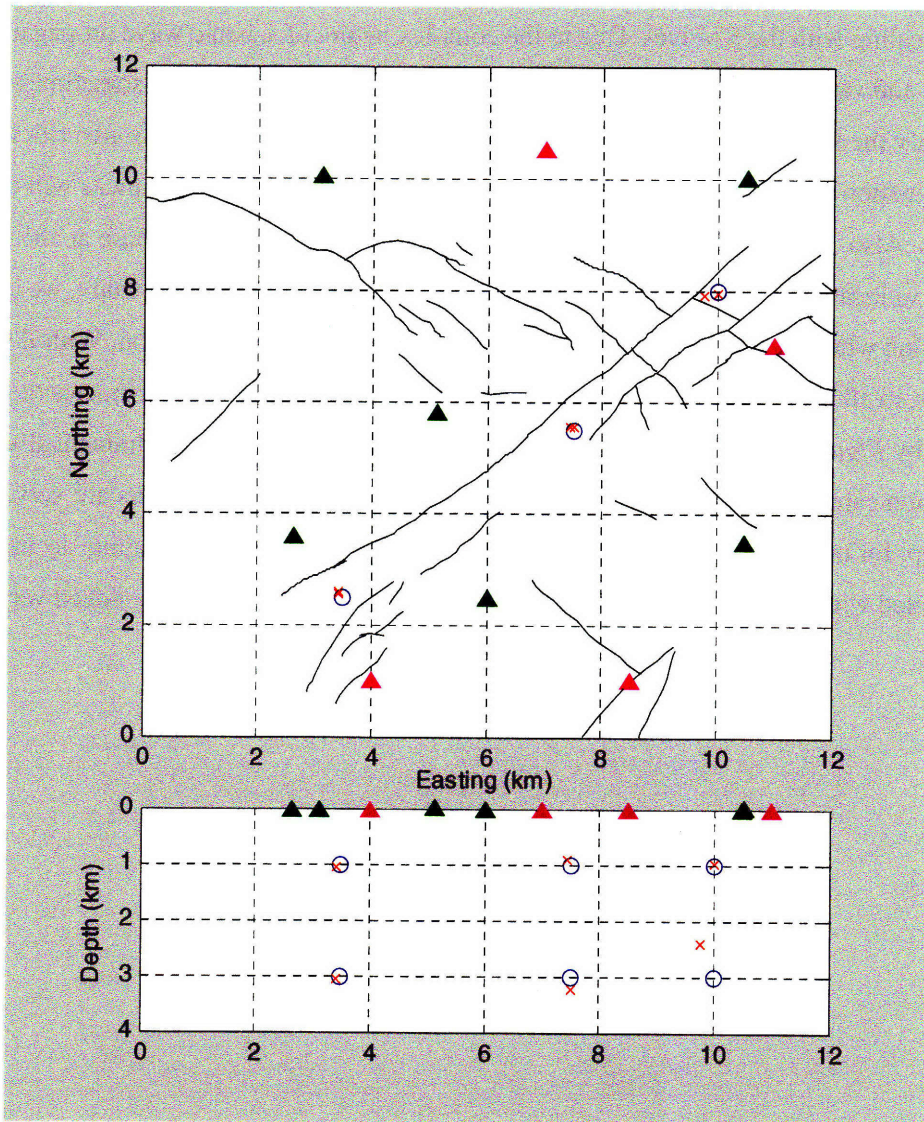
Figure 3.b : Actual event locations compared with locations determined by the NEW network, for "highly-noisy" data. Significant improvement in event locations due to addition of new stations is observed.

During our microseismic data processing and analysis for the field over the years, we have been faced with difficulty in dealing with the S-waves. Due to the complex nature of seismic wave propagation in sedimentary layers and various phase conversions that take place in these layers, it is sometimes very hard to accurately identify the first-S wave arrival from the seismograms. Although S-picks are critical for hypocenter determination - especially for depth determination, however inaccurate S-picks will adversely affect the solutions. Also, sometimes it is simply not possible to identify the first S-phase at all! In such situations, one has to locate the events with available P-arrival time data only. In this study, we also simulate this situation which is very often faced during the microseismic event location. With P-only data (*noise model #2*) from all of the stations of the existing network, how severely the accuracies of locations suffer can be seen by *Figure 4.a*. But, adding new stations at the proposed locations dramatically improves the location capacity of the network. As seen by *Figure 4.b*, all the epicenters are very well resolved, and except for one event with minor uncertainty, all the depth locations are quite accurate. For events that are located with highly-noisy P-only data, such a high level of accuracy is indeed very promising.
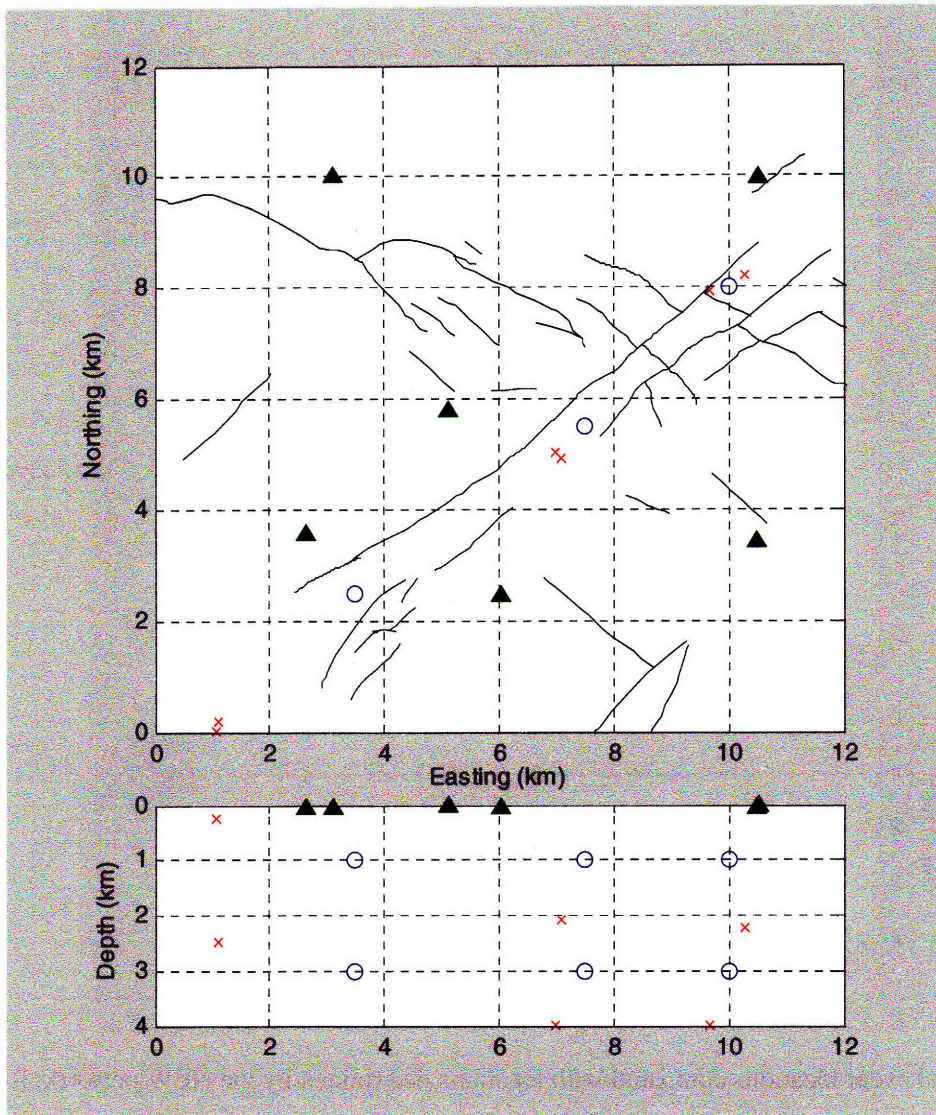
Figure 4.a: Actual event locations compared with locations determined by the EXISTING network, for P-only "highly-noisy" travel time data. The maximum likelihood epicenter and depth solutions from the inversion almost reduce to artifacts as opposed to carrying any significance.
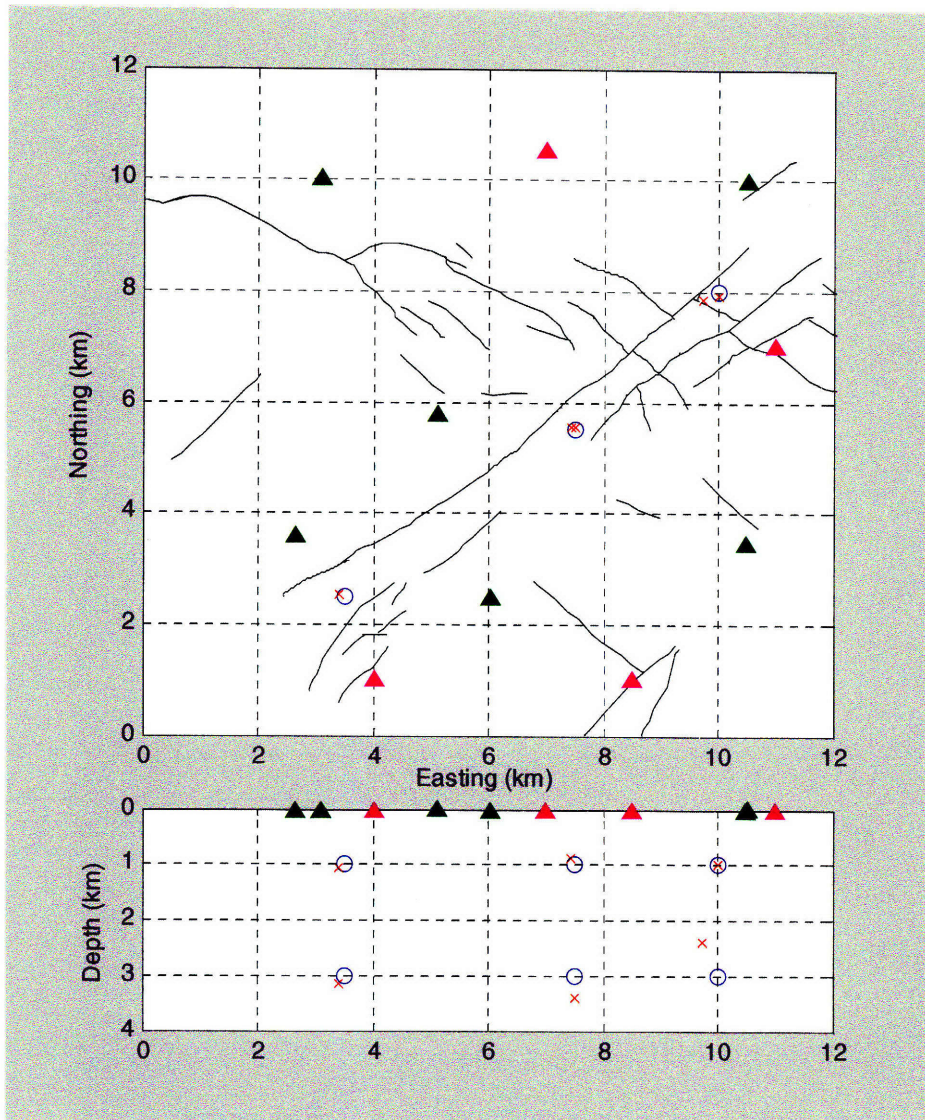
Figure 4.b: Actual event locations compared with locations determined by the NEW network, for P-only "highly-noisy" travel time data. Addition of new stations to the existing ones has a dramatic effect on the improvement of accuracy of the maximum likelihood hypocenters computed by the inversion routine.

Network Analysis: Adding stations at depth

In our study, it was found that adding (borehole) stations at depth gives better control on depth estimates of seismic event locations. Having stations at various depth levels in the reservoir will serve with a few advantages, such as – 1) detectability of the network will increase: very small magnitude events that cannot be recorded by the surface network will be seen by the deep stations, 2) high signal to noise ratio will help us obtain better picks for both P and S-phases, thus reducing the error in travel time, 3) uncertainty in depth estimates of the microseismic events will reduce significantly.

For our synthetic experiment, we evaluated the effect of only one seismic station at depth. As for the station location, we chose the coordinates of well Y080 (part of the erstwhile ABB deep network) at a depth of ~ 1 km (below the mean sea level).

The results of our study indicate that by adding the deep station improvements in depth accuracy from inversion can be achieved. To give an example, we compare the case given by *Figure 3.a* to the following. By adding just a deep station to the existing network, significant improvements in depth locations are achieved, as shown by the following figure.
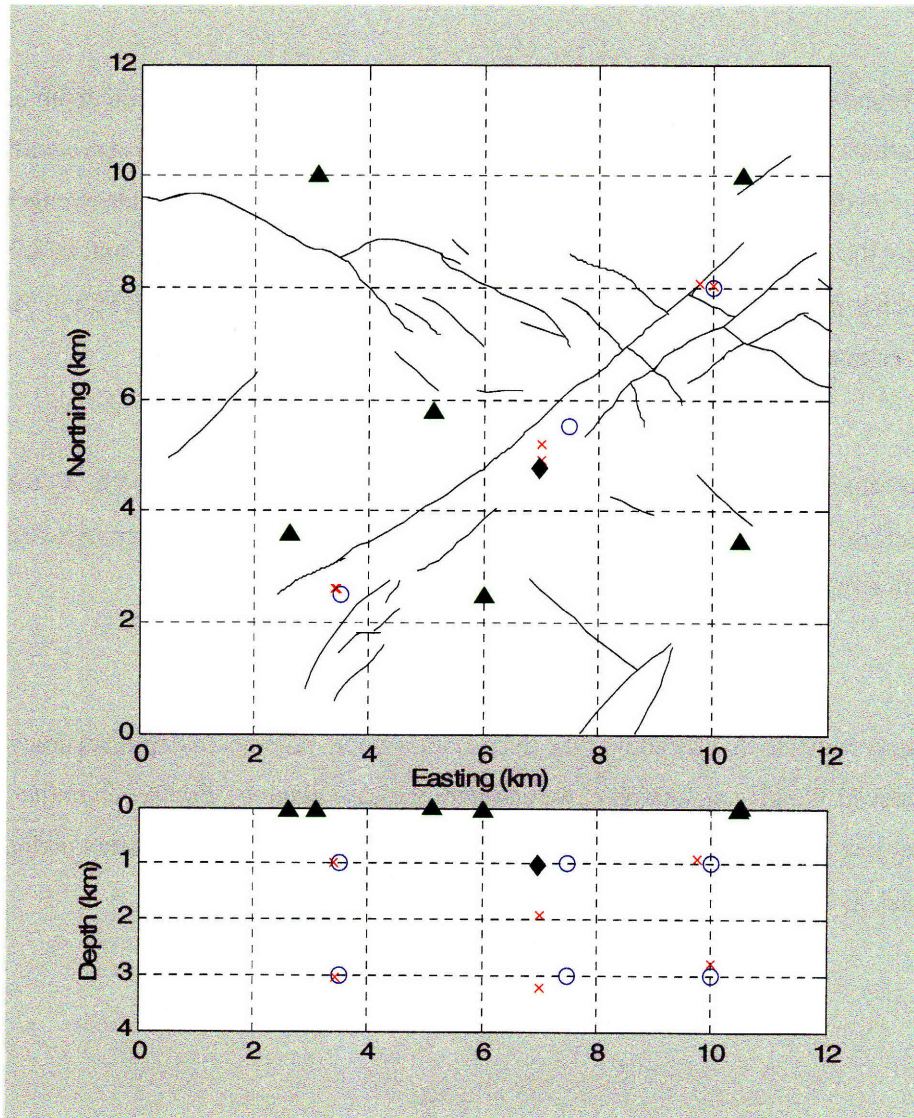
Figure 5.a : Actual event locations compared with locations determined by adding a DEEP station to the EXISTING network, for "highly-noisy" data. Although there are some errors in epicenter estimations, reduction in depth uncertainties for most of the events are significant as compared to a scenario in which the deep station did not exist (*Figure 3.a*).

In another example, we show how the deep station may further aide the depth determination even when the near-surface network provides a good basis for location estimates:-
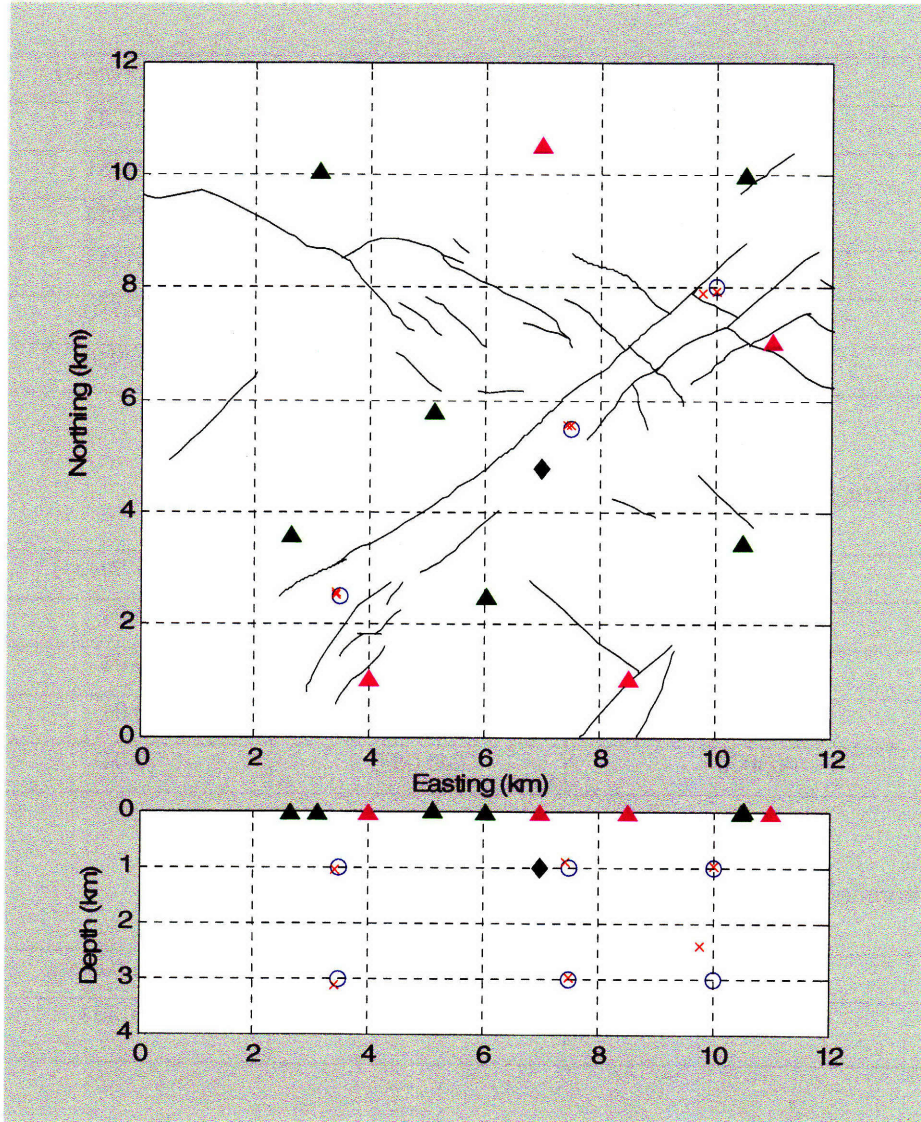

Figure 5.b : Actual event locations compared with locations determined by a network comprised of EXISTING near-surface stations, proposed near-surface NEW stations, and a proposed DEEP station, for P-only "highly-noisy" travel time data. This figure can also be compared with *Figure 4.b* to see how the addition of deep station has improved the accuracy of depth estimates for most of the events.

Coordinates of seismic stations discussed in this study

EXISTING / ORIGINAL near-surface stations

Station ID	Easting (m)	Northing (m)	Depth (km ss)
VA1	402475.18	2447431.58	0.04287
VA2	394638.02	2447563.05	0.04481
VA3	395109.21	2454022.23	0.05054
VA4	402521.5	2453969.65	0.03433
VA6	398033.994	2446459.036	0.04750
VA7	397118.009	2449772.018	0.02950

NEW / PROPOSED near-surface stations

Station ID	Easting (m)	Northing (m)	Depth (km ss)
VAN1	400500	2445000	0.04
VAN2	396000	2445000	0.04
VAN3	399000	2454500	0.04
VAN4	403000	2451000	0.04

PROPOSED deep-borehole stations

Station ID	Easting (m)	Northing (m)	Depth (km ss)
Y080	398969.5	2448769.96	1.01733